The role of mitochondria in dietary lipid processing by enterocytes

Inaugural-Dissertation
zur
Erlangung des Doktorgrades
der Mathematisch-Naturwissenschaftlichen Fakultät
der Universität zu Köln

vorgelegt von
Chrysanthi Moschandrea

aus Kreta, Griechenland

Köln, 2022

Berichterstatter: Prof. Dr. Manolis Pasparakis
Prof. Dr. Thomas Langer
Prof. Dr. Jan Riemer

This is a dissertation accepted by the Faculty of Mathematics and Natural Sciences of the University of Cologne.

Tag der mündlichen Prüfung: 03.06.2022

Zusammenfassung

Das intestinale Epithel besteht aus einer einzigen Schicht säulenförmiger Epithelzellen, die wichtige Funktionen bei der Nährstoffaufnahme und der Regulierung des Stoffwechsels erfüllen und eine strukturelle Barriere zwischen luminalen Mikrobiota und den Immunzellen der Schleimhaut bilden. Mitochondrien sind vor allem für ihre Funktion bei der Energieerzeugung bekannt, sind aber auch an der Regulierung zahlreicher zellulärer Prozesse beteiligt, darunter Stoffwechsel-, Immun- und Stressreaktionen. Eine mitochondriale Dysfunktion wird mit dem Altern und einer stetig wachsenden Zahl menschlicher Krankheiten in Verbindung gebracht. Patienten mit Mutationen, die die Funktion der Mitochondrien beeinträchtigen, zeigen häufig eine Vielzahl von gastrointestinalen Symptomen wie dramatischen Gewichtsverlust, Darmdysmotilität und Pseudoblockade sowie starke Bauchschmerzen, die mit Unterernährung einhergehen. Die Funktion der Mitochondrien im Darm und insbesondere beim Transport und der Sekretion von Lipiden im Darm ist jedoch nach wie vor kaum bekannt. Um die Rolle der Mitochondrien im Darm zu untersuchen, haben wir Mäuse mit einer intestinalen Epithelzellen (IEZ)-spezifischen Ablation von DARS2 erzeugt, die als DARS2$^{\text{IEZ-KO}}$-Mäuse bezeichnet werden. DARS2 ist eine mitochondrienspezifische Aspartyl-tRNA-Synthetase, die die mitochondriale Translation der 13 mtDNA-kodierten OXPHOS-Untereinheiten fördert. Ein Mangel an DARS2 führt letztlich zu einer sehr ausgeprägten Dysfunktion der Atmungskette. DARS2$^{\text{IEZ-KO}}$-Mäuse wurden in den erwarteten Mendelschen Verhältnissen geboren, entwickelten aber postnatal einen spontanen Phänotyp, der sich durch starken Gewichtsverlust, Hypoglykämie und Gedeihstörung äußerte. Die histologische Untersuchung des Darmgewebes dieser Mäuse ergab eine gestörte Gewebearchitektur, die mit einer Beeinträchtigung der epithelialen Stammzellen, der Proliferation und Differenzierung sowie einer massiven Anhäufung von Lipiden in großen Lipidtropfen einherging. Die Verabreichung von Tamoxifen an fünf aufeinanderfolgenden Tagen führte zur Ablation von DARS2 in den IEZs von erwachsenen Dars2$^{\text{fl/fl}}$ Villin-*CreER*$^{\text{T2-}}$Mäusen (DARS2$^{\text{tamIEZ-KO}}$-Mäuse). Auffallend ist, dass nur die Enterozyten des proximalen Dünndarms, die für die effiziente Aufnahme, Mobilisierung und den Transport von Nährstoffen aus der Nahrung, einschließlich Fetten, zuständig sind in DARS2$^{\text{tamIEZ-KO}}$-Mäuse mit großen Lipidtropfen (lipid droplets, LD) übersät waren.

Darüber hinaus wurden Mäuse mit IEZ-spezifischer Ablation von Succinat-Dehydrogenase (SDHA), die Teil von CII der Elektronentransportkette ist und zusätzlich als Enzym des TCA-Zyklus dient, sowie Mäuse, denen der Cytochrom-c-Oxidase-Assemblierungsfaktor Häm A: Farnesyltransferase (COX10) fehlt, der ein Assemblierungsfaktor von CIV in den IEZs ist, eingesetzt. Sowohl SDHA$^{\text{IEZ-KO}}$- als auch COX10$^{\text{IEZ-KO}}$-Mäuse wiesen einen ähnlichen Phänotyp wie DARS2 $^{\text{IEZ-KO}}$-Mäuse auf. Diese Mäuse wiesen ein deutlich reduziertes Körpergewicht auf, überlebten nicht über das Alter von vier Wochen hinaus und zeigten eine massive LD-Anreicherung in den Enterozyten. Zusammengenommen zeigten diese Befunde, dass ein Mitochondrienmangel zu einer Anhäufung von LD in Enterozyten führt, was darauf hindeutet, dass der Verlust der Mitochondrienfunktion den Transport von Nahrungsfetten beeinträchtigt. Die von den Enterozyten aufgenommenen verdauten Lipide werden wieder verestert und zu triglyceridreichen Lipoproteinen zusammengesetzt, vor allem in Form von Chylomikronen (CM), die dann in den Blutkreislauf abgegeben werden, um periphere Organe mit Lipiden zu versorgen. Interessanterweise verhinderte die Fütterung mit einer fettfreien Diät die Fettakkumulation in LDs in Enterozyten von DARS2$^{\text{tamIEZ-KO}}$-Mäusen, was zeigt, dass die in DARS2-defizienten Enterozyten beobachtete Lipidüberladung in erster Linie auf Nahrungsfett zurückzuführen ist. Darüber hinaus zeigten postprandiale Studien, dass der DARS2-Mangel in den IEZs den Transport von Nahrungsfetten zum Plasma und zu den peripheren Organen erheblich beeinträchtigt. Transmissionselektronenmikroskopische Untersuchungen ergaben darüber hinaus einen deutlichen Mangel an reifen Chylomikronen in DARS2-defizienten Enterozyten, der mit einer völligen Desorganisation des Golgi-Apparats einherging, was darauf hindeutet, dass ein gestörter ER-Golgi-Transport die Ursache für eine beeinträchtigte Chylomikronenproduktion und -sekretion ist. Insgesamt haben unsere Ergebnisse eine wesentliche Funktion der Mitochondrien bei der Regulierung der Chylomikron-Produktion und des Fetttransports in Enterozyten aufgezeigt, ein Mechanismus, der für das Verständnis der intestinalen und ernährungsbedingten Defekte bei Patienten mit mitochondrialen Erkrankungen relevant ist.

Abstract

The intestinal epithelium consists of a single layer of columnar epithelial cells, which perform important functions in nutrient absorption and metabolic regulation, and form a structural barrier between the luminal microbiota and mucosal immune cells. Mitochondria are best known for their function in energy production, but they are also involved in the regulation of multiple cellular processes including metabolic, immune and stress responses. Mitochondrial dysfunction is associated with ageing and a steadily increasing number of human diseases. Patients with mutations affecting mitochondrial function often present with a multitude of gastrointestinal symptoms including dramatic weight loss, gut dysmotility and pseudo-obstruction and severe abdominal pain that are associated with malnutrition. However, the function of mitochondria in the intestine and specifically in intestinal lipid trafficking and secretion remains poorly understood. To study the role of mitochondria in the intestine, we generated mice with intestinal epithelial cell (IEC)-specific ablation of DARS2, referred to as DARS2$^{\text{IEC-KO}}$ mice. DARS2 is a mitochondrial specific aspartyl - tRNA synthetase, essential for facilitating mitochondrial translation of the 13 mtDNA - encoded OXPHOS subunits. Deficiency in DARS2 ultimately leads to a very prominent respiratory chain dysfunction. DARS2$^{\text{IEC-KO}}$ mice were born in the expected Mendelian ratios, but developed a spontaneous postnatal phenotype, manifested by severe weight loss, hypoglycemia and failure to thrive. Histological examination of intestinal tissues from these mice revealed perturbed tissue architecture accompanied by impaired epithelial stemness, proliferation and differentiation and a massive accumulation of lipids within large lipid droplets (LDs). Tamoxifen administration on five consecutive days induced DARS2 ablation in IECs of adult Dars2$^{\text{fl/fl}}$ Villin-*CreER*$^{\text{T2}}$ mice (DARS2$^{\text{tamIEC-KO}}$ mice). Histologically, only the enterocytes of the proximal small intestine that are capable of facilitating efficient uptake, mobilization and transport of dietary nutrients, including fats were engorged with large LDs in DARS2$^{\text{tamIEC-KO}}$ mice. Moreover, mice with IEC specific ablation of succinate dehydrogenase (SDHA), which is part of CII of the electron transport chain and additionally serves as enzyme of the TCA cycle, as well as mice lacking the cytochrome c oxidase assembly factor heme A: farnesyltransferase (COX10) that is an assembly factor of CIV in the IECs, were studied. Both SDHA$^{\text{IEC-KO}}$ and COX10$^{\text{IEC-KO}}$ mice demonstrated a similar phenotype to mice with DARS2 deficiency in IECs. These mice exhibited markedly reduced body weight, did not survive beyond the age of four weeks and displayed massive LD accumulation in enterocytes. Together, these findings showed that mitochondrial deficiency caused LD accumulation in enterocytes, suggesting that loss of mitochondrial function causes impaired transport of dietary lipids. Digested lipids taken up by enterocytes are re-esterified and assembled into triglyceride-rich lipoproteins primarily in the form of chylomicrons (CMs), which are then released in the circulation to supply peripheral organs with lipids. Interestingly, feeding with a fat-free diet prevented fat accumulation in LDs in enterocytes of DARS2$^{\text{tamIEC-KO}}$ mice, showing that the lipid overload observed in DARS2-deficient enterocytes derives primarily from dietary fat. In addition, postprandial studies revealed that DARS2 deficiency in IECs significantly impaired dietary lipid transport to the plasma and peripheral organs. Furthermore, transmission electron microscopy revealed a distinct lack of mature chylomicrons in DARS2-deficient enterocytes concomitant with a total disorganization of the Golgi apparatus, suggesting that defective ER to Golgi trafficking underlies impaired chylomicron production and secretion. Taken together, our results revealed an essential function of mitochondria, in regulating chylomicron production and dietary lipid transport

in enterocytes, a mechanism that could potentially explain the intestinal and nutritional defects observed in patients with mitochondrial diseases.

Table of contents

Abbreviations

ACAT1	acyl-CoA:cholesterol acyltransferases
ACC1	Acetyl-CoA carboxylase
ACLY	ATP citrate lyase
ACSLs	fatty-acyl-CoA synthetases
ADP	Adenosine diphosphate
AGPATs	acylglycerolphosphate acyltransferases
ALP	Alkaline phosphatase
AMP	Adenosine monophosphate
AMPs	Antimicrobial peptides
Apaf-1	apoptotic protease-activating factor 1
ApoB48	Apolipoprotein B48
ARS	Aminoacyl- tRNA synthetases
ATGL	adipose triglyceride lipase
ATF4	activating transcription factor 4
ATP	Adenosine triphosphate
Bax	BCL-2-associated X protein
Bak	BCL-2 antagonist/killer
BAT	brown adipose tissue
BN-PAGE	Blue native polyacrylamide gel electrophoresis
BSA	Bovine serum albumin
BCAAs	branched chain amino acids
Bcl-2	B-cell lymphoma 2
CACT	carnitine- acylcarnitine translocase
CARD	caspase activation and recruitment domains
Ca^{2+}	calcium
CBCs	crypt-base columnar stem cells
CC3/8	Cleaved caspase 3/8
CCK	cholecystokinin
CD	Crohn’s disease
CD36	cluster of differentiation
CEs	Cholesterol esters
CGN	*cis* Golgi network
CI, II, III, IV, V	Complex I, II, III, IV, V
CL	cardiolipin
CLDs	Cytoplasmic lipid droplets
CMs	Chylomicrons
CO_2	carbon dioxide
COPII	coat complex type II
COX	Cytochrome c oxidase
COX/SDH	Cytochrome c oxidase/succinate dehydrogenase
CPT1	carnitine palmitoyltransferase 1
CPT2	carnitine palmitoyltransferase 2
CRD	Chylomicron retention disease
Cre	Bacteriophage P1 derived site-specific recombinase
Cu	copper
DAB	3,3′-Diaminobenzidine
DAG	diacylglycerol
DARS2	Aspartyl – tRNA synthetase
DGAT	diacylglycerol acyltransferases
DNA	Deoxyribonucleic acid
ddH_2O	Double distilled water
DKO	Double knockout
Drp1	Dynamin-related protein 1
dsRNA	double - stranded RNA
e^-	electrons
EF-Tu, -Ts, -G1	mitochondrial elongation factor Tu, -Ts, -G1
EGF	epidermal growth factor
EM or TEM	Electron microscopy or Transmission electron microscopy

ER	Endoplasmic reticulum
ETC	Electron transport chain
FAs	Fatty acids
FABP1,2	Fatty acid binding protein 1,2
FADH2	Flavin adenine dinucleotide
FAO	Fatty acid oxidation
FASN	Fatty acid synthase
FATP4	fatty acid transport protein 4
Fe-S	Iron – sulfur
FGF	fibroblast growth factor
FFAs	Free fatty acids
FFD	Fat-free diet
FMN	flavin mononucleotide
G3P	Glycerol-3-Phosphate
GDP	Guanosine diphosphate
GI	gastrointestinal
GPAT	glycerol-3-phosphate acyltransferases
GSEA	Gene set enrichment analysis
GTP	Guanosine triphosphate
GUF1	GTP Binding Elongation Factor
H^+	protons
HDL	High - density lipoprotein
HFD	High-fat diet
HSL	hormone sensitive lipase
HIF-1a	hypoxia-inducible factor-1α
H&E	Haematoxylin & eosin
H_2S	hydrogen sulfide
H_2O_2	hydrogen peroxide
HSP	heavy strand promoter
HSP60	heat shock protein 60
IBD	Inflammatory Bowel Diseases
IBM	Inner boundary membane
IECs	Intestinal epithelial cells
IHC	Immunohistochemistry
IF	Immunofluorescence
IMM	Inner mitochondrial membrane
IMS	Intermembrane space
IRF3/7	interferon regulatory factor 3 and 7
ISCs	Intestinal stem cells
ISR	integrated stress response
KO	knockout
LAL	lysosomal acid lipase
LBSL	leukoencephalopathy with brainstem and spinal cord involvement and lactate elevation
LCFAs	long-chain fatty acids
LDs	Lipid droplets
LDL	Low - density lipoprotein
Lgr5	Leucine-rich repeat-containing G-protein coupled receptor 5
LPAATs	lysophosphatidic acid acyltransferases
LPCAT3	lysophosphatidylcholine acyltransferase-3
LRPPRC	leucine-rich pentatricopeptide repeat cassette
LPL	lipoprotein lipase
LPLs	lysophospholipids
LSP	light strand promoter
mRNA	messenger RNA
MAG	monoacylglycerol
MAVS	mitochondrial antiviral signaling
MCU	mitochondrial calcium uniporter
MDA-5	melanoma differentiation - associated gene 5
MELAS	mitochondrial encephalomyopathy, lactic acidosis, and stroke - like episodes

MERRF	myoclonus epilepsy with ragged red fibers
MFN1,2	Mitofusin 1,2
MGAT	Monoacylglycerol acyltransferase
MGL	monoacylglycerol lipase
MERCSs	mitochondrial – ER contact sites
MIGA2	mitoguardin 2
MICOS	mitochondrial contact site and cristae organizing system
mtDNA	mitochondrial DNA
mtSSB	mitochondrial single strand binding protein
mtPIC-1,2	preinitiation step 1
MTRF1L	mitochondrial peptide chain release factor 1 – like
mtRRF1	mitochondrial ribosome recycling factor 1
MTP	microsomal TAG transfer protein
MOMP	Mitochondrial outer membrane permeabilization
MPC	Mitochondrial Pyruvate Carrier
NADH	Reduced nicotinamide adenine dinucleotide
NCD	Normal chow diet
NCR	non-coding region
NF-κB	Nuclear transcription factor - κB
NH_3	ammonia
NPC1L1	Niemann-Pick C1-like 1
OAA	oxaloacetate
OGFTT	Oral glucose – fat tolerance test
OFTT	Oral fat tolerance test
O_H	H-strand origin of replication
O_L	L-strand origin of replication
Olfm4	Olfactomedin 4
OMM	Outer mitochondrial membrane
OPA1	Optic atrophy 1
ORA	Over-representation analysis
ORO	Oil Red O
OXPHOS	Oxidative phosphorylation
PA	phosphatidic acid
PAS	Periodic acid-Schiff
PC	phosphatidylcholine
PCR	Polymerase chain reaction
PCs	Paneth cells
PCTV	Pre-chylomicron transport vesicle
PDH	pyruvate dehydrogenase
PDMs	peridroplet mitochondria
PE	phosphatidylethanolamine
PHB1	prohibitin 1
PHDs	prolyl hydroxylases
PFA	Paraformaldehyde
PG	phospatidylglycerol
PI	phosphatidylinositol
Pi	inorganic phosphate
PKCζ	protein kinase C zeta
PLs	Phospholipids
PLIN2,5	Perilipin 2,5
POLγ	DNA-polymerase gamma
POLRMT	mitochondrial RNA polymerase
PPARa	Peroxisome Proliferator Activated Receptor Alpha
Pre-CM	Pre-chylomicron
Q	ubiquinone
QH_2	ubiquinol
RC	Respiratory chain
RIG-I	retinoic acid - inducible gene I
RNA	Ribonucleic acid
ROS	Reactive oxygen species

rRNA	ribosomal RNA
RT	Room temperature
RT-PCR	Reverse transcription polymerase chain reaction
SAR1B	Secretion associated Ras related GTPase 1B
SCs	supercomplexes
SDS	Sodium sulfate
SDH	succinate dehydrogenase
SDM	strand displacement model
SEM	Standard error of the mean
SI	Small intestine
SIRT3	Sirtuin 3
SNARE	[soluble NSF (N-ethylmaleimide-sensitive fusion protein attachment protein receptor]
SR-BI	scavenger receptor class B type I
ssDNA	single-stranded DNA
SVIP	small valosin-containing protein/p97-interactive protein
TA	Transit amplifying
TAGs	Triacylglycerols
TCA	Tricarboxylic Acid
TFAM	mitochondrial transcription factor A
TFB2M	mitochondrial transcription factor B2
TEFM	mitochondrial transcription elongation factor
TGN	*trans* Golgi network
TOM	translocase of the outer mitochondrial membrane
TIM	translocases of the inner mitochondrial membrane
TLRs	Triaclyceride – rich lipoproteins
tRNA	transfer RNA
UC	Ulcerative colitis
UPRmt	mitochondrial unfolded protein response
VAMP7	vesicle-associated membrane protein 7
VDAC	voltage - dependent anion channel
VLDLs	Very low-density lipoproteins
WAT	white adipose tissue
WT	wild type

Abbreviations of units

%	percent	sec	seconds
°C	Degree Calcius	l	litter
bp	Base pair	ml	milliliter
cm	centimeter	ul	microliter
um	micrometer	rpm	Rounds per minute
nm	nanometer	rcf or g	Relative Centrifugal Force
M	molar	V	Volt
mM	millimolar	A	Amper
uM	micromolar	W	Watt
nM	nanomolar	kDa	Kilodalton
g	grams		
mg	milligram		
ug	microgram		
ng	nanogram		
h	hours		
min	minutes		

Table of figures

List of tables

1. Introduction

1.1. Multifaceted mitochondria

Mitochondria, etymologically originate from the “mitos” (thread) and khondrion or khondros” (granule), derived from the endosymbiotic relationship between an autonomous α-proteobacterium with a proto-eukaryotic host tightly associated with Asgard Archaea. The transition from an anaerobic pre-mitochondrial endosymbiont into a fully established mitochondrial organelle required a vast amount of genetic, structural and physiological alterations during thousands steps of evolution (Kurland and Andersson 2000, Spang, Saw et al. 2015). Mitochondria are unique, double – membrane structures located in the cytoplasm of every eukaryotic cell, apart from red blood cells, that widely range in shape and number.

1.1.1. Mitochondria structure and functions

Mitochondria are organized into two membranes constituting phospholipid bilayers, the outer and inner mitochondrial membrane (OMM and IMM) that are clearly kept apart from each other owing to the perimitochondrial or intermembrane space (IMS) (Figure 1).

The OMM not only encloses the mitochondrial organelle in order to distinctly separate it from the cytosol, but also coordinates critical, diverse activities. Free diffusion of small, uncharged molecules including ions, metabolites and proteins less than 5 kDa is mediated via porins, such as the voltage - dependent anion channel (VDAC) located on the OMM. Constrastingly, precursor proteins frequently bigger than 5 kDa are selectively imported into mitochondria upon associating with the translocase of the outer mitochondrial membrane (TOM). Upon passing through the TOM, precursor proteins holding an N-terminal cleavable presequence or multiple integral signals enter the IMM via translocases of the inner mitochondrial membrane TIM23 and TIM22, respectively (Kühlbrandt 2015, Ellenrieder, Dieterle et al. 2019).

Additionally, OMM plays the role of a platform for the initiation of cell signalling pathways, in particular response to viral infections and Bcl-2-regulated apoptosis. Notably, innate antiviral immunity is mediated via the adaptor protein mitochondrial antiviral signaling (MAVS), that comprising caspase activation and recruitment domains (CARD) and it is anchored on the OMM. Upon sensing double - stranded RNA (dsRNA) derived from RNA viruses, melanoma differentiation - associated gene 5 (MDA-5), as well as RNA helicases retinoic acid - inducible gene I (RIG-I), associate with MAVS via CARD - CARD homotypic interactions. This interaction activates both the transcription factors interferon regulatory factor 3 and 7 (IRF3/7) and nuclear transcription factor - κB (NF-κB), eventually driving the expression of proinflammatory cytokines and type I interferons that trigger a defense mechanism against the virus (Seth, Sun et al. 2005, Ren, Ding et al. 2020). In the context of Bcl-2-regulated apoptosis, the pro-apoptotic effector protein BCL-2-associated X protein (Bax) and BCL-2 antagonist/killer (Bak) tightly control the permeabilization of the OMM (MOMP). Of note, under stress conditions, Bax (predominantly cytosolic) and Bak (anchored in the OMM), are accumulated and subjected into conformational changes and oligomerization on the OMM in apoptotic foci that eventually disrupts the integrity of the membrane, hence releasing cytochrome c that prompt the activation of the caspases 9 and 3 through the apoptotic protease-activating factor 1 (Apaf-1) (Cosentino and García-Sáez 2017).

Remarkably, OMM is markedly involved in the establishment of physical contacts between mitochondria and other organelles. One of the most well - described interaction is among mitochondria and endoplasmic reticulum (ER) at the mitochondrial – ER contact sites (MERCSs). MERCSs enable sustained tunneling of calcium (Ca^{2+}) into mitochondria via VDAC on the OMM and mitochondrial calcium uniporter (MCU) at the IMM. Phospholipid (mainly phosphatidylcholine, PC and phosphatidylethanolamine, PE) biosynthesis that abundantly constitute cellular membranes is also mediated at the MERCSs upon efficient lipid exchange among the two organelles (Rowland and Voeltz 2012). Beyond MERCSs, mitochondria are closely associated with lipid droplets (LDs). Under conditions of acute stress, autophagy – derived LDs undergo lipolysis via the activity of cytoplasmic lipases to liberate fatty acids (FAs). These FAs are shuttled into mitochondria that are in close proximity with LDs and there are efficiently processed for the purpose of energy production (Rambold, Cohen et al. 2015). However, recent studies have demonstrated that FA surplus can be mediated in a reverse direction owing to provide protection to mitochondria against lipotoxicity, caused by LD overload. Additionally, peridroplet mitochondria (PDMs) within brown adipose tissue (BAT) cells, which binding to LDs is regulated by perilipin 5 (PLIN5), contribute to the growth of LDs by supplying them with ATP or citrate for triacylglycerol (TAG) synthesis or *de novo* lipogenesis, respectively. On the contrary, cytoplasmic mitochondria (CM) are primarily specialized for performing fatty acid oxidation (FAO) in order to maintain the energy homeostasis (Benador, Veliova et al. 2018). Likewise, in differentiating white adipose tissue (WAT) cells mitoguardin 2 (MIGA2), which is located on OMM, serves as the physical link between mitochondria and LDs. MIGA2 stimulates the TAG synthesis from non-lipid-derived precursors in the ER, concurrently supporting lipid storage within LDs (Freyre, Rauher et al. 2019). Lastly, the network of OMM interactions extended to several other subcellular compartments, rendering mitochondria capable of establishing membrane contact sites with lysosomes, endosomes, peroxisomes, melanosomes as well as plasma membrane (Giacomello, Pyakurel et al. 2020).

The IMM constitutes a highly impermeable membrane structured into the inner boundary membrane (IBM), that goes in parallel to the OMM at a distance of 20nm and the cristae membrane. The IBM controls the import of metabolites, ions, adenosine triphosphate (ATP) and adenosine diphosphate (ADP) from the cytoplasm, whereas cristae considered as inward folds of the IMM intensely shaped to maximize the surface for cellular energy demands. The interface between IBM and cristae is bounded by cristae junctions, which are stabilized by a multi-subunit complex named as mitochondrial contact site and cristae organizing system (MICOS) that addionally connect the OMM with the IMM. Importantly, cistae harbors the electron transport chain (ETC) complexes and the ATP synthase, thus are primarily implicated in the generation of the main cellular energy source, ATP through oxidative phosphorylation (OXPHOS). The innermost part of the mitochondria is designated as matrix encompassing numerous copies of the mitochondrial DNA (mtDNA) and the complete machinery for facilitating replication, transcription and translation of the mtDNA - encoded proteins. Moreover, matrix harbors versatile enzymes involved in the Tricarboxylic Acid Cycle (TCA), formation of iron – sulfur (Fe-S) clusters and FAO (Kühlbrandt 2015, Giacomello, Pyakurel et al. 2020, Mannella 2020) (Figure 1).

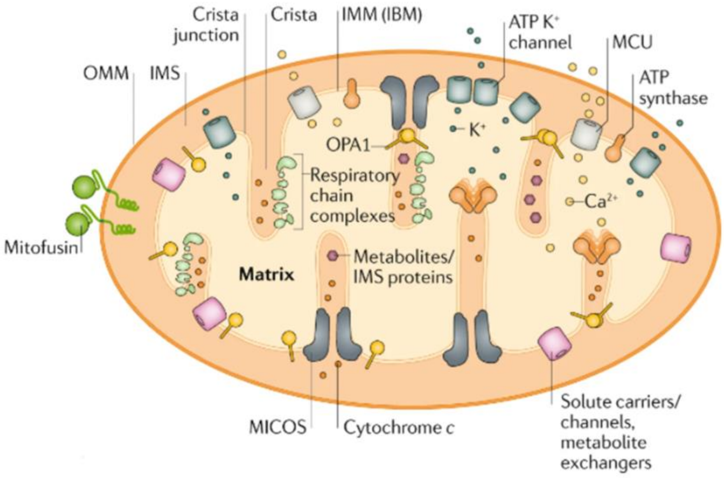

Figure 1. The structural organization of the mitochondria.

Mitochondria are enclosed by two membranes, the outer mitochondrial membrane (OMM) and the inner mitochondrial membrane (IMM), which is composed of the inner boundary membrane (IBM) and mitochondrial cristae. The OMM allows the diffusion of small molecules, the IBM accomodates numerous transporters for the exchange of metabolites and ions, while cristae hosts respiratory chain complexes and ATP synthase for mediating oxidative phosphorylation (OXPHOS). See text for elaborate description. Abbreviations: OPA1, Optic atrophy-1 mitochondrial dynamin like GTPase, MICOS, mitochondrial contact site and cristae organizing system, MCU, mitochondrial calcium uniporter. Adapted and modified from (Giacomello, Pyakurel et al. 2020).

Mitochondria are extremely dynamic organelles and do not exist independently of each other. Mitochondria promote coordinated behavior, being able to form giant networks through coordinated cycles of fission and fusion and ultrastructural remodelling of the membrane based on cell demands (Collins, Berridge et al. 2002). Mitofusins 1 and 2 (MFN1 and MFN2) carries out mitochondrial fusion of the OMM, while Optic atrophy 1 (OPA1) performs IMM fusion. Mitochondrial fusion is controlled by the coordinated balance between the long, uprocessed form of OPA1 (L-OPA1) and the soluble, short OPA1 (S-OPA1), that derives from L-OPA1 after beeing proteolytically cleaved (Westermann 2010). On the other hand, OMM fission is facilitated by dynamin-related protein 1 (DRP1). OXPHOS, nutrient availabitity and stress responses alter morphology of mitochondria, rendering them fragmented or hyperfused (Wai and Langer 2016).

Mitochondria coordinate numerous metabolic pathways critical for bioenergetics and biosynthesis of macromolecules comprising nucleotides, amino acids, fatty acids and heme. Essential metabolic hub for the generation of energy using diverse fuel sources such as carbohydrates, fats and proteins is considered to be the TCA, also known as Krebs of citric acid cycle (Nunnari and Suomalainen 2012). Depending on the oxygen availability (aerobic conditions) pyruvate, generated from glycose via cytoplasmic glycolysis, enters IMM though the Mitochondrial Pyruvate Carrier (MPC). Upon entry, pyruvate can be converted either to acetyl-CoA via pyruvate dehydrogenase (PDH), giving rise to one molecule of the reducing agent NADH (reduced nicotinamide adenine dinucleotide) or alternatively to oxaloacetate (OAA) with the activity of pyruvate carboxylase (PC). Alternative sources of acetyl-CoA is the FAO, branched chain amino acids (BCAAs) including valine, leucine, isoleucine catabolism and oxidation of ketone bodies. Acetyl-CoA goes into the TCA cycle where is subjected to a chain of chemical reactions in order to be oxidized to carbon dioxide (CO_2) with the simultaneous release of one FADH2 (flavin adenine dinucleotide), one GTP (guanosine triphosphate) equivalent and three NADH. The electron donors NADH and FADH2 eventually supply the respiratory chain complexes CI and CII, respectively (Akram 2014, Spinelli and Haigis 2018).

TCA cycle not only confers to catabolic pathways, but also orchestrates anabolic functions. TCA cycle intermediates utilized as building blocks of biosynthetic purposes in the cytosol such as purine, purimidine and porphyrin synthesis or act as signaling molecules regulating chromatin modifications, hypoxic responses or DNA methylation. In particular, citrate, via ATP citrate lyase (ACLY), gives rise to acetyl CoA and latterly operates the fatty acid synthesis pathway or the mevalonate pathway for cholesterol production. Acetyl-CoA can also alter the epigenetic landscape by promoting acetylation of histones. Strikingly, succinate is involved in a process named as pseudohypoxia due to the suppression of prolyl hydroxylases (PHDs) and the consequent induction of hypoxia-inducible factor-1α (HIF-1α) (Martínez-Reyes and Chandel 2020).

Mitochondria are also regarded as the primary site of FAO. Acyl-CoA synthases (ACS) convert long-chain fatty acids derived from the diet to fatty acyl-CoAs. Long-chain fatty acyl-CoAs are not capable of crossing the IMM. Therefore, they are subjected to esterification via the carnitine palmitoyltransferase 1 (CPT1) to generate acylcarnitines that move through the IMM by the carnitine- acylcarnitine translocase (CACT). Lastly, acylcarnitines are reconverted to acyl-CoAs in a process mediated by carnitine palmitoyltransferase 2 (CPT2) in the mitochondria matrix. Acyl-CoAs undergo a series of enzymatic reactions catalyzed by chain length specific acyl-CoA dehydrogenases to ultimate yield 2 carbon shortened acyl-CoAs, one acetyl-CoA that powers TCA cycle, as well as one NADH and one $FADH_2$ molecule to supply the ETC (Houten and Wanders 2010).

Aside from the abovementioned myriad functions entailing ATP generation, Ca+ buffering, heme, amino acid and phospholipid biosynthesis, synthesis of Fe-S clusters, mitochondria have critical functions for cell survival, programmed cell death and inflammation and emission of cell intrinsic danger signals (Galluzzi, Kepp et al. 2012, Tait and Green 2012). What is more, mitochondria are intimately linked to the management of metabolic by-products, such as clearance of ammonia (NH_3) produced during the catabolism of amino acids and nucleotides via the urea cycle to evade toxicity, hydrogen sulfide (H_2S) and sequestration of reactive oxygen species (ROS). Beyond the deleterious effects of ROS, hydrogen peroxide (H_2O_2) has been involved in the propagation of signalling cascades promoting cellular proliferation and differentiation. It is now unambiguous that mitochondria and their pleiotropic functions play a fundamental role in the cellular homeostasis (Figure 2).

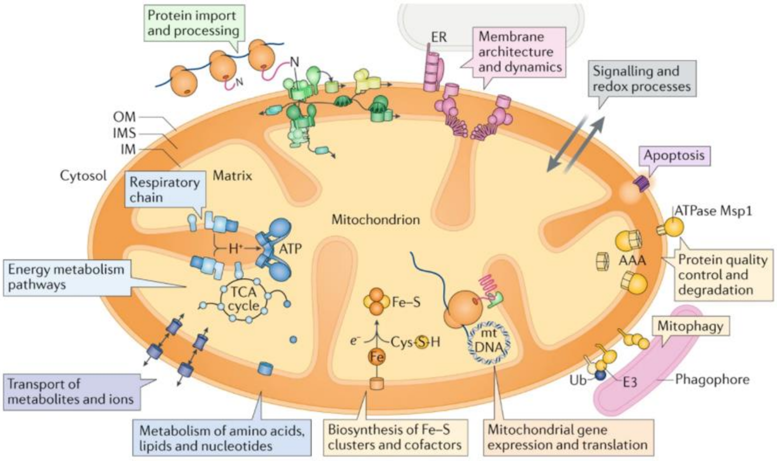

Figure 2. Mitochondria are essential players in the coordination of a multitude of cellular functions.

The figure summarizes the wide range of diverse functions that have been connected with mitochondrial organelles. Mitochondria are typically described as the powerhouses of the cells, since they produce ATP via OXPHOS. It is becoming progressively evident that mitochondria modulate pathways crucial for the viability of the cell comprising quality control of mitochondrial proteostasis, ROS formation, programmed cell death, iron-sulfur cluster biosynthesis and numerous others. See text for elaborate description. Abbreviations : OM, outer mitochondrial membrane, IMS, intermembrane space, IM, inner mitochondrial membrane,TCA, tricarboxylic acid, ATP, adenosine triphosphate, Fe-S, iron-sulfur clusters, Fe, iron, Cys-S-H, cystein thiol, mt DNA, mitochondrial DNA, Ub, ubiquitin, E3, ubiquitin-protein ligase, AAA, ATP-dependent proteases, ER, endoplasmic reticulum. Adapted from (Pfanner, Warscheid et al. 2019).

1.2. Electron Transport Chain (ETC) - Oxidative phosphorylation (OXPHOS)

ETC comprises a chain of oxidation and reduction reactions catalyzed by versatile protein complexes residing at the IMM that receive high energy electrons from the NADH and $FADH_2$ electron donors. Electrons (e^-) move through the carriers and ultimately captured by molecular oxygen to generate water. The passage of e^- stimulates the movement of protons (H^+) away from the matrix and into the IMS, hence building up the proton (electrochemical) gradient. Proton gradient facilitates the motive force of the H^+-ATP synthase to generate ATP from ADP, eventually engaging ETC with OXPHOS in line with the chemiosmotic coupling hypothesis as stated by Peter D. Mitchell in 1961 (Mitchell 1961) (Gilkerson, Selker et al. 2003).

The ETC contains four major IMM-embedded protein complexes; NADH oxidoreductase (NADH dehydrogenase or complex I, CI), succinate dehydrogenase (complex II or CII), ubiquinol cytochrome c reductase (complex III or CIII), and cytochrome c oxidase (complex IV, CIV). The four complexes are followed by F_1F_o ATP synthase (often referred to as complex CV or CV). Additionally, the water - soluble cytochrome c and coenzyme Q (CoQ or ubiquinone, Q) are important components of the ETC (Papa, Martino et al. 2012).

The OXPHOS system is initiated with the donation of two e^- from an NADH molecule to an acceptor group lying in the vertical component of the L-shaped multisubunit CI, known as flavin mononucleotide (FMN), thus leading to $FMNH_{2,}$ (reduced form). The movement of e^- is achieved through a series of Fe-S clusters ([2Fe–2S] and [4Fe–4S]) to latterly transferred to ubiquinone (Q), which is converted to its fully reduced state, ubiquinol (QH_2) after the uptake of two H^+ from the matrix. CI finally utilizes the e^- to pump four H^+ into the IMS. In parallel, CII oxidizes succinate to fumarate with the concomitant generation of $FADH_2$ by succinate dehydrogenase, an enzyme that is part of both CII and TCA cycle. $FADH_2$ remained attached to the CII and donates two e^- to a chain of Fe-S clusters ([2Fe–2S], [4Fe–4S], and [3Fe–4S]) that ultimately transferred to Q, resulting in QH_2. Unlike CI, e^- transfer from $FADH_2$ to Q does not release sufficient amounts of energy to drive the pumping of H^+ across the IMM, rendering CII as the only respiratory complex that does not act as an H^+ pump. Following CI and CII, e^- shuttle from QH_2 to cytochrome c, so-called Q-cycle. The Q-cycle starts with the binding of QH_2 to CIII that directs the movement of e^- through two distinct routes. The first e^- goes through the 2Fe-2S group of the Rieske center, moves onto the heme group of cytochrome $c_{1,}$ effectively acquired by the cytochrome c that freely diffuse away to reach CIV. The second e^- passes through the heme group of cytochrome b and taken up by Q, which is now partially reduced to another state, named as semiquinone free radical ($Q^{\cdot -}$). Afterwards, another QH_2 molecule carries a second pair of e^- to the CIII in a similar manner and gets oxidized to Q, simultaneously reducing a second cytochrome c and pumping two H^+ into the IMS. Overall, the net gain of a single Q-cycle is the reduction of two molecules of cytochrome c, the oxidation of two QH_2 molecules into Q with the concomitant release of four H+ and finally the reduction of one Q molecule to QH_2 that allows the recycling of e^- and their reuse for the same process. The tunneling of e^- terminates at the CIV, which is the final e^- acceptor. CIV consists of two heme groups, heme *a*, heme a_3 and three atoms of copper, Cu_A/Cu_A and Cu_B. Two reduced cytochrome c molecules bind to the CIV and transfer two e^- that move through the Cu_A/Cu_A center and heme *a* to heme a_3 and Cu_B. After receiving one e^-, heme a_3 and Cu_B are in their fully reduced state and ready to accept an O_2 molecule, disengage two e^- and build a peroxide bridge. Oxidation of two more reduced molecules of cytochrome c permits the movement of two additional e^- accompanied by the uptake of two H^+ ions from the matrix to ultimately break the peroxide bridge between heme a_3 and Cu_B. The collapse of the peroxide bond gives rise to two separate structures of heme a_3 and Cu_B that are associated with hydroxide groups (heme a_3 – OH and Cu_B – OH). Afterwards, two more H^+ ions are obtained from the matrix that oxidize heme a_3 and Cu_B, thus regenerating their original oxidized state and release two water molecules (Fontanesi, Soto et al. 2006, Papa, Martino et al. 2012, Read, Bentley et al. 2021).

At the end of this process, CIV pumps out four H^+ ions from the matrix to the IMS, thus establishing the necessary proton gradient. This particular electrochemical gradient powers the rotational motor mechanism of the ATP synthase. ATP synthase contains two major regions; the F_1 (catalytic unit) and the F_0 (H^+ pump). F1 part is mainly hydrophilic and lies into the mitochondrial matrix. It composed of a hexameric ring structure made by a combination of three α and three β polypeptide chains ($\alpha_3\beta_3$) that predominantly bind ADP and inorganic phosphate (Pi) to catalyze the ATP synthesis. The remaining polypeptide chains γ and ε organized to form the central stalk that interacts with the hexameric ring and rotates, thus enabling the synthesis and release of ATP, whereas δ subunit stabilizes the hexameric ring and prevents it from rotating. On the contrary, the IMM-embedded F_0 is particularly hydrophobic and arranged into a ring-like structure composing of c subunits, which allows the channeling of H^+ from the IMS to the matrix. Additionally, there is a single a subunit bound on the outside of the c ring that forms an arm with two b subunits and the δ subunit, thus holding the F_1 with the F_0 together. Therefore, only c ring and the γε stalk constitute the rotating region of the ATP synthase, while the remaining subunits belong to the stationary part. The β subunit is primarily responsible for the ATP synthesis, which depends on the interconversion between its tense, open and loose state coordinated by the rotation of the γ subunit in a binding – change mechanism. ADP and Pi are closely associated to form ATP (tense) that is released allowing the binding of the next ADP/Pi (open). At the loose state, ADP and Pi get fully trapped. β subunit changes from the tense to the open state upon 120^o in the counter clockwise rotation of the γ subunit, hence promoting ATP release. The open β subunit is now accessible from a new set of ADP/Pi and another rotation of the γ subunit on the same direction leads to loose state (Jonckheere, Smeitink et al. 2012) (Figure 3).

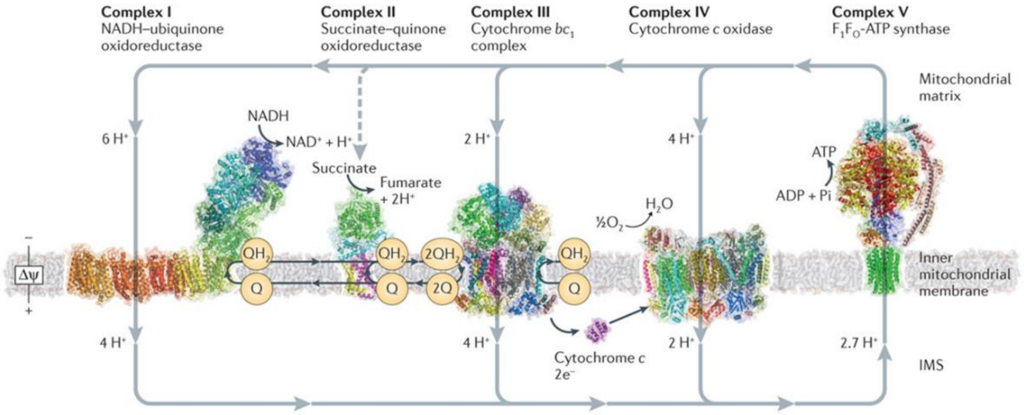

Figure 3. The electron transport chain (ETC) of mitochondria.

The four major complexes of the respiratory chain (RC), Complex I to Complex IV, pump protons (H^+) into the intermembrane space (IMS) in order to produce an electrochemical gradient sufficient to trigger the F_1F_0- ATP sythase for ATP generation. Electrons (e^-) delivered by NADH and $FADH_2$ move across the complexes aiming to reach cytochrome c and reduce molecular oxygen (O_2) to water (H_2O). See text for elaborate description. Abbreviations : Δψ, membrane potential, Q, ubiquinone, QH_2, ubiquinol, ADP, adenosine diphosphate, Pi, inorganic phosphate. Adapted from (Sazanov 2015).

It has been initially proposed that ETC complexes are structurally organized based on two leading models; the “fluid-state” or “random collision” and the “solid-state” model (Hackenbrock, Chazotte et al. 1986). As far as the “fluid-state model is concerned, ETC complexes and redox components are freely and continuously diffused in the IMM and random collision of the complexes determines the transport of the electrons. On the contrary, solid-state model refers to assembly of individual ETC complexes in large, multi-enzyme structures termed as supercomplexes (SCs) (Hackenbrock, Chazotte et al. 1986). The idea of the “fluid-state” as the exclusive model of organization was refuted after the analysis of mitochondrial proteins using blue native polyacrylamide gel electrophoresis (BN-PAGE), which substantiated the existence of SCs. However, particular fractions of distinct ETC complexes were not united together into the SCs, implicating a third model so-called “plasticity” model where individual ETC complexes go along with SCs (Acin-Perez and Enriquez 2014, Javadov, Jang et al. 2021). Complexes I, III and IV can be associated to build SCs in different stoichiometry, thus primarily forming CI/CIII$_2$, CI/CIII$_2$/CIV$_{1\text{-}4}$ (respirasome), and CIII$_2$/CIV$_{1\text{-}2}$. In particular, almost 85% of CI, 55 - 65% of CIII and only 15-25% of CIV is present into SCs, whereas CII is typically not detected as part of the SCs (Wu, Gu et al. 2016), (Guo, Zong et al. 2017). Initially, it has been stated that the assembly of these supramolecular structures is advantageous for the cell as they not only govern channeling of the substrates Q pool and cytochrome c for higher speed and efficiency of electron transport, but also diminish production of ROS by impeding leukage of electrons. However, this still remains controversial (Fedor and Hirst 2018). Noteworthy, SCs guard the structural and functional integrity of the individual complexes and halt uncontrolled aggregation of proteins in the IMM (Milenkovic, Blaza et al. 2017).

1.2.1. Succinate dehydrogenase A (SDHA)

As it has been already mentioned, succinate dehydrogenase (SDH) or CII, is one of the smallest ETC complexes that resides at the IMM and does not directly contribute to proton pumping into the IMS. Additionally, it serves as enzyme of the TCA cycle which oxidizes succinate to fumarate, hence indirectly involved in the proton motif force. SDH constitutes a heterotetrameric complex, encompassing four nuclear – encoded subunits (SDHA-D). SDHA and SDHB belongs to the hydrophilic domains of the complex that are associated with the membrane – anchored hydrophobic domains, SDHC and SDHD (Figure 4). SDHA is a flavoprotein that carries catalytic activity, allowing the binding and oxidation of succinate to fumarate via deprotonation at the FAD binding site. A functional SDH requires crucial assembly factors that regulate each single step of the assembly process, named as SDHAF1, SDHAF2, SDHAF3, and SDHAF4. In particular, SDHAF1 coordinates the Fe-S centers insertion within the SDH, as well as iron homeostasis. Similarly, SDHAF3 actively participates in the maturation of Fe-S subunits and offers protection from oxidative stress. SDHAF2 controls the covalent incorporation of FAD into SDHA via interaction with dicarboxylate. On the other hand, SDHAF4 functions as a chaperone in the formation of SDH holocomplex by mediating SDHA and SDHB heterodimer and additionally defending against ROS damaging effects (Na, Yu et al. 2014, Van Vranken, Bricker et al. 2014, Sharma, Maklashina et al. 2020). Loss of SDHA in embryonic and adult myocytes (*Sdha*$^{\mathrm{MKO}}$) results in decreased body weight, severe muscle atrophy at 3 weeks of age and eventually lethality at 4.5 weeks of age. On the other hand, deletion of SDHA in the heart (*Sdha*^{HKO}) caused lethality between 16 and 21 days of age, accompanied by a severe cardiomyopathy (Hofsetz, Trifunovic et al. 2019). Mutations either in the individual SDH subunits or in the assembly factors have been manifested in several human pathologies, comprising of hereditary or sporadic malignancies, such as gastrointestinal stromal tumours (GIST), paraganglioma and pheochromocytoma (PGL/PHEO) and renal carcinomas (RCC). Previous studies have proposed that most of the patients with Leigh syndrome carrying familiar germline mutations within the SDHA gene, which was frequently linked to severe cardiomyopathy (Horváth, Abicht et al. 2006, Jain-Ghai, Cameron et al. 2013). In SDH-deficient tumours, high elevated levels of succinate have been reported. Interestingly, succinate accumulation mediates inhibition of prolyl hydroxylases (PHDs) that eventually stabilize hypoxia inducible factor 1a (HIF-1a) leading to a pseudo-hypoxic state, common signature of PGL/PHEO tumours (Pollard, El-Bahrawy et al. 2006). Importantly, increased expression of the oncogene Myc resulted in deactivation of SDHA via acetylation by inducing proteosomal degradation of sirtuin 3 (SIRT3) deacetylase. SDHA suppression consequently prompt the accumulation of succinate that in turn resulted in enhanced histone methylation (H3K4me3) and expression of tumour-specific genes and Myc-deregulated cancer progression (Li, Huang et al. 2020). Interestingly, another study has demonstrated that patients with persistent polyclonal B cell lymphocytosis (PPBL) exhibited accumulation of fumarate as well as protein succination due to a SDHA gain-of-function, which subsequently triggered an inflammatory phenotype via the KEAP1-Nrf2 system (Burgener, Bantug et al. 2019). A recent study proposed that reduction of SDHA in IECs increased their sensitivity to cytotoxicity driven by T-cells, hence exacerbating the severity of gastrointestinal diseases mediated by T-cells, including autoimmune IBD, alloimmune gastrointestinal chronic graft – versus – host disease (GI-GVHD), and iatrogenic CTLA-4Ig - induced colitis (Fujiwara, Seike et al. 2021).

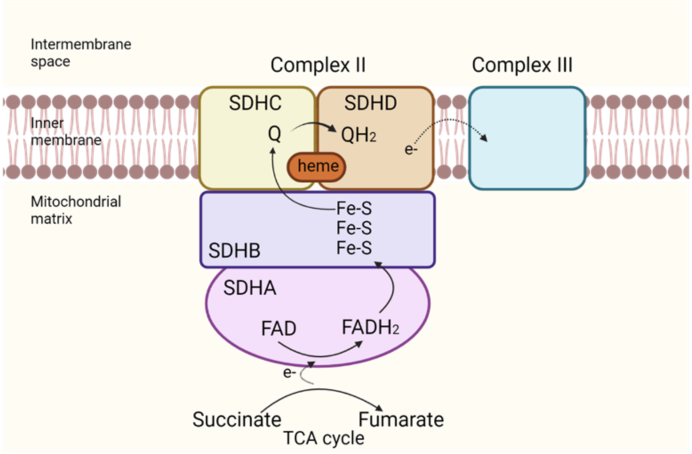

Figure 4. Assembly of succinate dehydrogenase complex (SDH).

Scheme depicting the structural organization of SDH complex, residing at the IMM. SDH interconnects TCA cycle with OXPHOS and oxidizes succinate to fumarate, concomitantly reducing ubiquinone to ubiquinol. See text for elaborate description. Abbreviations : Q, ubiquinone, QH_2, ubiquinol, FAD, flavin adenine dinucleotide, $FADH_2$, reduced flavin adenine dinucleotide, Fe-S, iron-sulfur cluster. Image inspired by (Moreno and Santos 2020) and created by BioRender.

1.2.2. Cytochrome C Oxidase Assembly Factor HemeA: Farnesyltransferase (COX10)

The mammalian cytochrome *c* oxidase (COX) complex comprising of 13 subunits, the mitochondrial encoded catalytic subunits that constitute the core of the enzyme; COX1 COX2 and COX3 or alternatively called as MT-CO1, MT-CO2 and MT-CO3 and the structural, assessory nuclear encoded subunits located at the periphery of the central core; COX4, COX5a, COX5b, COX6a, COX6b, COX6c, COX7a, COX7b, COX7c and COX8 (Tsukihara, Aoyama et al. 1996). Recently, it has been shown that COX contains one more subunit, called NDUFA4 or COXFA4, which was previously considered as part of CI (Pitceathly and Taanman 2018). As it has been described above, COX consists of two heme groups, heme *a*, heme a_3 and three atoms of copper, Cu_A/Cu_A and Cu_B.The copper center Cu_B, and the heme moieties a_3 and *a* resides at the COX1, whereas COX2 bears the binuclear Cu_A center. The assembly process of the mammalian COX enzyme is a highly coordinated process that additionally requires auxiliary proteins which are not part of the complex, such as LRPPRC (leucine-rich pentatricopeptide repeat cassette), Surf1, SCO1 and SCO2, COX10 and COX15 (Figure 5). Surf1 participates in the early assembly steps of CIV, assisting the maturation of heme a_3-Cu_B, whereas LRPPRC implicated in the stability of COX1 and COX3 mRNAs. Copper (Cu^{2+}) is transferred from COX17 either to SCO1 and SCO2 or to COX11. Subsequently, binuclear Cu_A is delivered into the COX by SCO1 and SCO2 , whereas COX11 transfer the Cu_B center. Lastly, COX10 and COX15 catalyze heme biosynthesis. COX10 (heme A: farnesyltransferase cytochrome c oxidase assembly factor 10) is a protoheme IX farnesyltransferase that farnesylates the vinyl group of heme *b* at C2 position in order to convert it into heme *o*. Heme *o*, via COX15, is subsequently converted to heme *a* (Antonicka, Leary et al. 2003). As lipophilic anchor, the farnesyl chain of heme a holds the prosthetic group in the right position within complex IV (Mogi, Saiki et al. 1994). Deficiency of COX10 is predicted to impair enzyme biogenesis at the earliest stage by interfering with synthesis of heme *a* cofactor.

Missense mutations in the COX10 gene have related to a spectrum of clinical presentations, including anemia and Leigh syndrome, as well as leukodystrophy and tubulopathy (Valnot, von Kleist-Retzow et al. 2000, Antonicka, Leary et al. 2003, Coenen, van den Heuvel et al. 2004). Up to date, numerous mouse models of COX10 ablation have been reported. COX10 deletion in skeletal muscle leads to an isolated CIV deficiency, recapitulating progressive mitochondrial myopathies that have been connected to deficiency of cytochrome c (Diaz, Thomas et al. 2005). These mice developed slowly progressive myopathy and a severe CIV deficiency at 3 months of age. In a cell culture model, COX10 deletion has shown to lead to a combined CI deficiency, as well. In a mouse skin fibroblast model, loss of COX10 lead to an inability to assemble CIV and a pronounced loss of CI (Diaz, Fukui et al. 2006). Nephron epithelial – specific deletion of COX10 (*Cox10*$^{\Delta/\Delta}$) results in prenatal and postnatal lethality with renal failure. The majority of mice with loss of COX10 in the nephron died before reaching 20 weeks of age. *Cox10*$^{\Delta/\Delta}$ mice analysed at 2-3 months of age, showed reduced body weight and exhibited severe focal segmental glomerulosclerosis (FSGS) with almost all glomeruli exhibit segmental scars, tubulointestitial damage and fibrosis (Baek, Gomez et al. 2018). Moreover, liver-specific COX10 knockout mice displayed reduced body weight and premature death between 45-65 days of age. Additionally, they exhibited hepatomegaly and a pale-coloured liver indicating steatosis (“fatty liver”) (Diaz, Garcia et al. 2008). Specific-deletion of COX10 in the mouse endothelium resulted in embryonic lethality at E12.5 due to impaired vascular development. However, there was no effect on the survival of the adult mice upon tamoxifen-induction of the COX10 ablation for up to 100 days, suggesting that COX10 is not essential for adult vascular homeostasis (Schiffmann, Werthenbach et al. 2020). Neuron-specific loss of COX10 (COX10 cKO) resulted in life span shortening and death between 8-12 months. COX10 cKO exhibited decreased body weight after 4-5 months of age, accompanied by severe cortical neurodegeneration (Diaz, Garcia et al. 2012). Finally, specific deletion of COX10 in oligodendrocytes and Schwann cells caused severe peripheral nervous system neuropathy, characterized by demyelination, which resulted in muscular atrophy and paralysis by 9 months of age (Fünfschilling, Supplie et al. 2012).

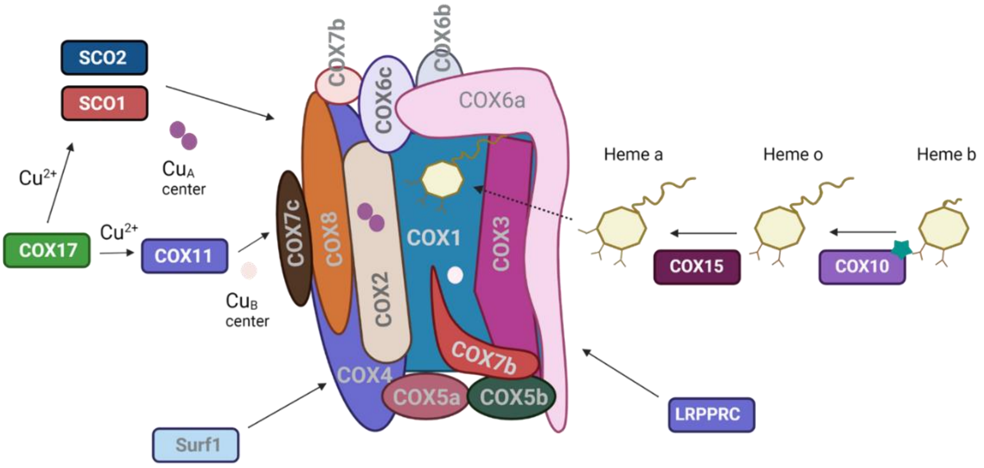

Figure 5. The assembly of the mammalian cytochrome c oxidase (CIV).

Scheme illustrating the mt-encoded catalytic subunits (COX1, COX2, COX3), the nuclear-encoded subunits (COX4, COX5a, COX5b, COX6a, COX6b, COX6c, COX7a, COX7b, COX7c and COX8) and the assessory proteins (COX10, COX15, LRPPLRC, SCO1, SCO2, COX17, COX11 and Surf1) of the CIV of the ETC. The COX10 assemly factor, labelled with the green star, mediates heme a biosynthesis. Image inspired by (Diaz 2010) and created by BioRender.

1.3. Mitochondrial genome – Replication, Transcription and Translation

Mitochondria possess their own genome containing 37 genes, which encodes 13 polypeptides for the OXPHOS complexes I, III, IV and V subunits that are embedded in the IMM, as well as 22 transfer RNAs (tRNAs) and two ribosomal RNAs (rRNAs) required for mitochondrial translation. In particular, *ND1-ND6* and *ND4L*; seven CI subunits, *Cyt b*; one CIII subunit, COX I, COX II and COX III; three CIV subunits and *ATP6*, *ATP8*; three subunits from CV, are encoded by the mt DNA, while CII is solely nuclear – encoded. The fact that only 13 out of 1500 mitochondrial proteins are mtDNA - encoded, whereas the rest are encoded by nuclear DNA further strengthen the endosymbiotic theory of mitochondria origin (Schon, DiMauro et al. 2012).

Mitochondrial DNA (mtDNA) is an intron – free, circular, double - stranded DNA (dsDNA) molecule, with 16.6 kb in size in mammals that is present in 2 - 10 copies per mitochondrion and varies from 100 to 10.000 copies per cell, depending on its energy requirements. The mtDNA follows a uniparental pattern of inheritance, since it is exclusively transmitted through the female germ line due to the increased presence of mtDNA copy number within oocytes. The uniparental inheritance hampers the spreading of deleterious mutations that can be transmitted by biparental inheritance of cytoplasmic genomes. Interestingly, pathogenic mtDNA mutations can occur and lead to a spectrum of severe mitochondrial disorders determined by a certain level of a mutant mtDNA load, so-called threshold effect (Wallace 2007).

The majority of mtDNA - related diseases triggered by a wide spectrum of mutations. In particular, myoclonus epilepsy with ragged red fibers (MERRF) and mitochondrial encephalomyopathy, lactic acidosis, and stroke - like episodes (MELAS) are attributed to point mutations in tRNA genes. On the other hand, neuropathy, ataxia and retinitis pigmentosa (NARP syndrome), as well as Leber Hereditary Optic Neuropathy (LHON) caused by mtDNA mutations in protein coding genes, while Kearns - Sayre Syndrome (KSS) and Pearson Marrow - Pancreas Syndrome (PMPS) induced by mtDNA deletions (DiMauro and Schon 2008). A primordial germ cell, which gives rise to the mature oocytes, might contain a mixture of distinct mtDNA copies including wild-type and mutant mtDNA or only identical copies of mtDNA that is described as heteroplasmy and homoplasmy, respectively. Therefore, mitotic segregation of mtDNA generates daughter cells that composed of markedly different levels of mtDNA heteroplasmy. However, there a strong selection in the germline which significantly eliminate putatively detrimental mtDNA mutations from being transmitted (Lightowlers, Chinnery et al. 1997), (Klucnika and Ma 2019).

MtDNA comprises two strands, the heavy (H) strand rich in guanines and the light (L) strand with high composition of cytosines. Additionally, it contains a 1kb non-coding region (NCR) that accommodates the H-strand origin of replication (O_H), the heavy and light strand promoter (HSP, LSP), the displacement loop (D-loop) region and the termination-associated sequence (TAS). The L-strand origin of replication (O_L) resides 11 kb downstream of the O_H. The H-strand of the mtDNA encodes the majority of transcripts such as 12 mRNAs, two rRNAs and 14 tRNAs, whereas L-strand accounts for encoding eight tRNAs and one mRNA. MtDNA replication is initiated based on the strand displacement model (SDM) which requires DNA-polymerase gamma (POLγ), mitochondrial single strand binding protein (mtSSB) and TWINKLE DNA helicase. The mtSSB insulates single-stranded DNA (ssDNA) from nucleases, whereas TWINKLE specifically unwinds dsDNA following 5’ to 3’ direction, thus rendering the mtDNA template accessible for replication with high – fidelity by POLγ at the mitochondrial replication fork (Gustafsson, Falkenberg et al. 2016, Falkenberg 2018).

The mtDNA transcription machinery composed of the essential components; mitochondrial RNA polymerase (POLRMT), mitochondrial transcription factor A and B2 (TFAM and TFB2M, respectively), and mitochondrial transcription elongation factor (TEFM). TFAM belongs to the high – mobility group box (HMG) proteins and it constitutes an accessory factor of mitochondrial transcription, as well as a shielding protein, since it mediates packaging of mtDNA into 100nm in diameter structures, termed as nucleoids (Kanki, Nakayama et al. 2004). Mitochondrial transcription begins with the recruitment of the POLRMT at the transcription start site, process mediated by TFAM which inserts a sharp 180^o bend of the DNA upstream of LSP and HSP. Afterwards, TFB2M is brought in close vicinity to the pre - initiation complex and incurs efficient DNA duplex melting, thus leading to formation and stabilization of the open initiation complex. TFB2M and TFAM subsequently dissociate from the complex, allowing TEFM to take over and activate the elongation process. POLRMT is now able to synthesize primary polycistronic transcripts that undergo further processing in order to produce tRNAs, mRNAs and rRNAs (Hillen, Morozov et al. 2017, Ramachandran, Basu et al. 2017)

Mitochondrial translation is a tightly coordinated process that considerably differs from the cytoplasmic translation and it is highly dependent on proteins encoded by the nuclear DNA. Mitochondrial ribosomes or mitoribosomes are assembled into a large 39S subunit (mtLSU), entailing 48 proteins encoded by the nucleus and the 16S rRNA, and into a small 28S (mtSSU) subunit, that contains the 12S rRNA and 30 nuclear – encoded proteins (Greber and Ban 2016).

Initiation of translation consists of two steps, preinitiation step 1 (mtPIC-1) and 2 (mtPIC-2) until the formation of the complete initiation complex (Amunts, Brown et al. 2015). The mtPIC-1 begins with the dissociation of the mitoribosome into mtLSU and mtSSU subunits and involves the initiation factor MTIF3. Main function of MTIF3 is not only to impede the premature association of the two subunits of the mitoribosome, but also to facilitate the correct placing at the peptidyl (P) site of the mtSSU of the start codon AUG or AUA of the mRNA. Afterwards, a mitochondrial - specific aminoacyl-tRNA synthetase (ARS2), termed as MARS2 is responsible for loading methionine to a corresponding tRNA (tRNA^{Met}). The tRNA^{Met} is further processed by mitochondrial methionyl-tRNA formyltransferase (MTFMT) in order to generate the formylated methionine (fMet). Subsequently, during the mtPIC-2 step fMet-tRNA^{Met} binds with the mRNA at the mtSSU with the aid of the initiation factor MTIF2 in a GTP - dependent process. Upon mRNA codon - tRNA anticodon interaction, mtLSU is recruited and binds to the mtSSU and MTIF2/3 are released, thus giving rise to the complete initiation complex (Suomalainen and Battersby 2018).

The elongation phase implicates four major factors; mitochondrial elongation factor Tu (EF-Tu), Ts (EF-Ts), G1 (EF-G1 or GFM1) and GTP Binding Elongation Factor (GUF1). Amino acid – charged tRNA is transferred to the aminoacyl (A) site of the mtSSU through its interaction with EF-Tu and GTP. Upon efficient pairing of mRNA codon - tRNA anticodon, the EF-Tu is liberated via GTP hydrolysis, thus generating EF-Tu · GDP. Regeneration of EF-Tu · GTP is mediated by EF-Ts that efficiently exchanges GDP for GTP. The 3' end of the aminoacyl- tRNA is carried into the mtLSU P center, hence enabling the addition of an amino-acid into the newly - synthesized polypeptide. Hydrolysis of the GTP that is bound to EF-G1 or GFM1 induces the translocation of the ribosome and the moving of the peptidyl-tRNAs from A and P site to ultimately P and exit (E) tRNA binding site, which is the weakest one, thus allowing the release of the tRNA and the induction of a new elongation cycle. Interestingly, GUF1 is capable of promoting back - translocation of the mitoribosome in order to block potential amino acid misincorporation (Smits, Smeitink et al. 2010, Mai, Chrzanowska-Lightowlers et al. 2017, D'Souza and Minczuk 2018, Suomalainen and Battersby 2018, Ferrari, Del'Olio et al. 2021).

Mitochondrial translation is completed once the mitochondrial peptide chain release factor 1 – like (MTRF1L) identifies a termination codon, such as UAA or UAG, leading to the release of the nascent polypeptide. Lastly, mitochondrial ribosome recycling factor 1 (mtRRF1) and 2 (mtRRF2 or EF-G2mt) trigger the disassembly of mtSSU and mtLSU and together with the mt-mRNA and deacylated mt-tRNA are ready to reinitiate the translation machinery (Rorbach, Richter et al. 2008) (Figure 6).

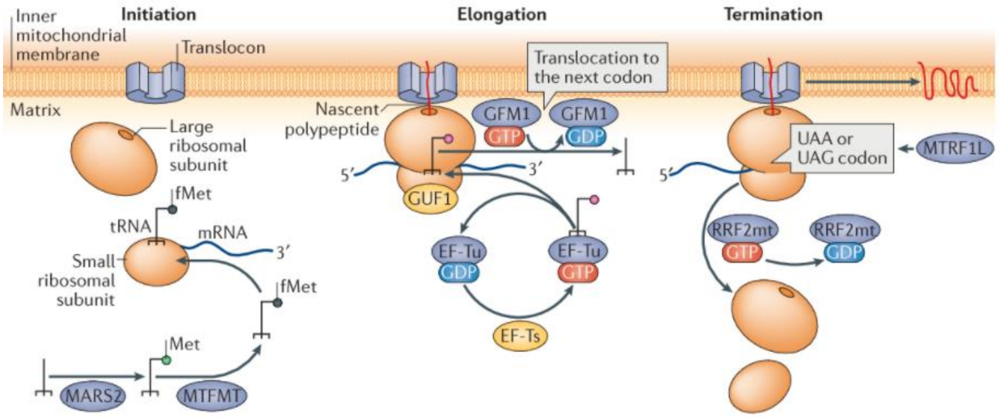

Figure 6. The process of mammalian mitochondrial translation.

Scheme summaring the process of mitochondrial protein synthesis inluding the steps; initiation, elongation and termination on mitochondrial ribosomes and the essential components involved in each step. See text for elabolate description. Abbreviations: Met, methionine, fMet, formylated methionine, MTFMT, methionyl-tRNA formyltransferase, MARS2, mitochondrial methionine – tRNA ligase, GFM1, mitochondrial elongation factor G, GUF1, GTP binding elongation factor, EF-Tu, mitochondrial elongation factor Tu, EF-Ts, mitochondrial elongation factor Ts, RRF2mt, mitochondrial ribosome releasing factor 2, MTRF1L, mitochondrial peptide chain release factor 1-like. Adapted and modified from (Suomalainen and Battersby 2018).

1.3.1. Aminoacyl - tRNA synthetases and related diseases

Aminoacyl - tRNA synthetases (ARS) are a group of highly conserved, specialized enzymes that are responsible for catalyzing the initial step of protein synthesis, designated as tRNA charging or loading. This two-step reaction initiates with the binding of an amino acid and a molecule of ATP on a specific ARS, hence forming an aminoacyl adenylate intermediate with the subsequent release of a pyrophosphate. The second step continues with the attachment of a cognate tRNA to the ARS. Then, the activated amino acid is transferred to the tRNA, while an AMP molecule is liberated. The tRNA is ultimately charged and ARS is released for the next aminoacylation reaction (Diodato and Ghezzi 2014, Sissler, González-Serrano et al. 2017). Beyond the anticodon-binding domain, ARS carry an editing domain to facilitate deacylation of amino acids that have not been properly charged during protein synthesis. ARS are categorized into (a) cytoplasmic (ARS), (b) mitochondrial (ARS2) and (c) bifunctional (dual localization of KARS and GARS that charge $tRNA^{Lys}$ and $tRNA^{Gly}$. The mitochondrial ARS are nuclear encoded and a mitochondrial targeting sequence (MTS) guide them into mitochondria. This MTS is subsequently cleaved upon ARS import. In total, 19 ARS have been reported, with one ARS accounting for charging $tRNA^{Glu}$ and $tRNA^{Pro}$ in the cytoplasm. Noteworthy, cytoplasmic QARS is absent from mitochondria. Therefore, $tRNA^{Gln}$ is firstly mischarged with glutamic acid instead of glutamine and then, tRNA-dependent aminotransferases mediate its conversion to glutamine (Nagao, Suzuki et al. 2009). Dominant and recessive mutations in ARS have been intimately linked to a wide spectrum of pathologies including leukoencephalopathies (AARS2, DARS2, EARS2, and WARS2), Perrault syndrome (HARS2, LARS2), Charcot-Marie-Tooth disease (GARS and KARS) and cardiomyopathies (KARS, GARS and AARS2) (Sissler, González-Serrano et al. 2017).

1.3.2. Aspartyl – tRNA synthetase (DARS2)

DARS2 is a mitochondrial specific class II aminoacyl - tRNA synthetase, which covalently attaches aspartic acid to its corresponding tRNA, allowing the synthesis of 13 mtDNA-encoded proteins that are components of respiratory complexes (Scheper, van der Klok et al. 2007) (Figure 7). Therefore, deficiency of DARS2 inhibits protein translation of the mtDNA-encoded OXPHOS subunits, leading to a severe respiratory chain deficiency. The first described mutation in mtAsp-RS or *DARS2* gene has been identified in patients suffering from an autosomal recessive disease, termed as leukoencephalopathy with brainstem and spinal cord involvement and lactate elevation (LBSL). LBSL predominantly manifested by spasticity, cognitive decline and impaired movement coordination along with high lactate accumulation in the white matter (Scheper, van der Klok et al. 2007). Overall, almost 60 mutations have been discovered to be distributed over the *DARS2* gene. The reported cases correspond to patients heterozygous for DARS2 mutations with a splice site mutation in one allele and a deletion, missense or nonsense mutation in the other allele. Surprisingly, seven LBSL patients carrying a homozygous DARS2 mutation, which is compatible with life but the phenotypic spectrum has not been fully characterized so far (van Berge, Hamilton et al. 2014), (Finsterer and Zarrouk-Mahjoub 2017). Complete loss of DARS2 results in embryonic lethality at embryonic day 8.5 (E8.5), proposing that DARS2 is an indispensable protein for embryonic development in mice (Dogan, Pujol et al. 2014). Tissue-specific DARS2 ablation causes robust respiratory chain deficiency in heart and skeletal muscle. However, cardiomyocytes exclusively elicit adaptive stress responses, such as mitochondrial unfolded protein response (UPRmt), prior to respiratory chain deficiency. Perturbed proteostasis activates cell intrinsic and systemic metabolic changes, including autophagy inhibition, enhanced mitobiogenesis and high upregulation of the mitokine FGF21. On the contrary, skeletal muscles seems to a protective mechanism through a higher proteostatic buffering capacity and a slower turnover of mitochondrial transcripts (Dogan, Pujol et al. 2014). Interestingly, severe cardiomyopathy induced by DARS2 ablation could be significantly ameliorated upon depletion of the mitochondrial matrix protease CLPP, while the lifespan of the mice deficient in both DARS2 and CLPP (DKO) was remarkably extended without impacting the UPRmt (Seiferling, Szczepanowska et al. 2016). Additionally, mice lacking DARS2 in adult forebrain hippocampal neurons ($Dars2^{NEKO}$) and myelin-producing cells ($Dars2^{MYKO}$) exhibited a strong mitochondrial dysfunction. Notwithstanding, $Dars2^{NEKO}$ displayed a massive cell loss, which progressively leads to degeneration of cortex and hippocampus. Contrastingly, there was no signs of neuroinflammation in the $Dars2^{MYKO}$ mice and the number of oligodendrocytes together with the myelin production appeared to be unaffected (Aradjanski, Dogan et al. 2017). Moreover, mice with specific ablation of DARS2 in Purkinje cells (PCs) present motor skill deterioration at 15 weeks of age accompanied with robust OXPHOS dysfunction, dramatic loss of PCs and severe neuroinflammation (Rumyantseva, Motori et al. 2020). Strikingly, it has been recently demonstrated that loss of DARS2 in myeloid cells compromises wound closure upon skin injury. Early – phase skin wound pro-inflammatory macrophages (MFs) devoid of DARS2 are unable to generate mtROS and consequently promote HIF-1 stabilization, hence impeding proper vascular response and optimal progression of wound healing (Willenborg, Sanin et al. 2021). Seemingly, each tissue differentially copes with mitochondrial dysfunction induced by loss of DARS2 via activating distinct stress responses or promoting systemic metabolic alterations. Remarkably, analysis of clinical data obtained from patients with hepatitis B virus (HBV) – associated hepatocellular carcinoma (HCC) recognized the nuclear factor of activated T-cells 5 (NFAT5) as a tumor suppressor in HCC that negatively regulates DARS2. Infection with HBV blocked NFAT5 expression and prompted DARS2 upregulation, which in turn enhanced HCC tumorigenesis via hindering HCC cell apoptosis (Qin, Li et al. 2017).

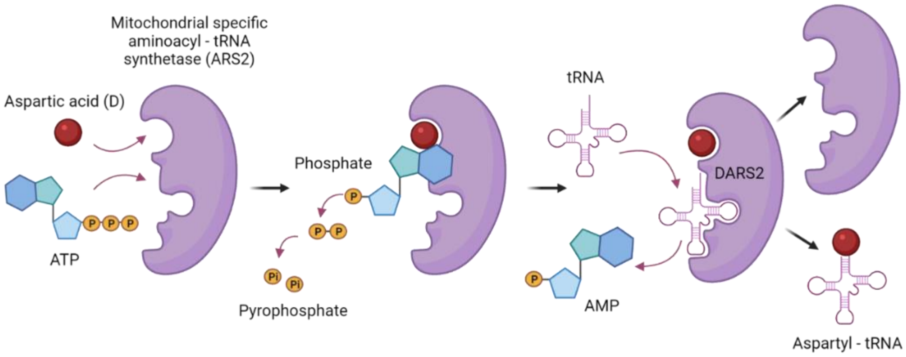

Figure 7. Aminoacylation reaction of DARS2.

DARS2 facilitates loading of aspartic acid (D) to each corresponding tRNA in a two-step catalytic reaction that utilizes ATP. Abbreviations: ATP, adenosine triphosphate, AMP, adenosine monophosphate. Image inspired by (Rajendran, Kalita et al. 2018) and created by BioRender.

1.4. Anatomy and function of the gastrointestinal tract

The mammalian gastrointestinal (GI) tract or digestive tract begins with the oral cavity, esophagus and stomach and continues with the intestinal tract, including the small and the large intestine. The small intestine (SI) is initiated from the pyloric sphincter of the stomach and extended to the ileocaecal valve. It is subdivided from cranial to caudial into three distinct segments; duodenum and jejunum (proximal SI) and ileum (distal SI) (Figure 8). The SI mainly accounts for the digestion of the food and the absorption of dietary nutrients, such as carbohydrates, lipids, proteins and vitamins. In particular, each of the small intestinal regions specifically contributes to these processes. Duodenum, the shortest division of the SI is located right after the stomach and performs the enzymatic digestion of the food-derived components. Jejunum, the middle section of the SI, is predominantly involved in the absorption of nutrients from the diet and their transport via the bloodstream into the peripheral organs of the body. The ileum constitutes the terminal region of the SI, which mainly accomplishes the uptake of bile salts, vitamin B12 and undigested content from the jejunum (Lema, Araújo et al. 2020).

On the other hand, the large intestine or colon consists ascending colon (proximal), descenting colon (distal) and rectum. The essential function of the colon is the reabsorption of water and electrolytes (bicarbonate, sodium and chloride) from the faeces. In addition, the colon contains a rich microbial community consisting primarily of commensal bacteria, which perform critical metabolic and immune functions including the production of short-chain fatty acids by fermenting non-absorbed carbohydrates from the diet (Treuting, Valasek et al. 2012, Mowat and Agace 2014) .

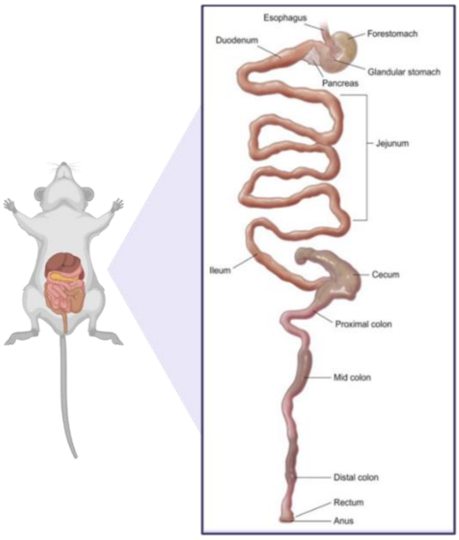

Figure 8. Anatomy of the mouse gastrointestinal (GI) tract.

Schematic representation of the mouse GI tract starting from the esophagus and ending up to the rectum. GI tract obtained from (Treuting, Valasek et al. 2012). Image created by BioRender.

1.4.1. Cellular architecture and function of the intestinal epithelium

The gastrointestinal wall consists of numerous, uniquely seperated layers; the mucosa, submucosa, muscularis externa and serosa/adventitia, as indicated by a cross section through the SI from the outside to the inside part. The outer surface of the intestine, termed as serosa or adventitia, is composed of loose connective tissue that provides protection against friction damage during the propagation of luminal content along the tract (peristalsis). The muscularis externa constituted by the outer longitudinal and the inner circular smooth muscle layer and modulates peristaltic movements via coordinated contractions of the myenteric plexus. The thin layer of connective tissue arranged below the muscle layers is called submucosa and comprises of blood and lymphatic vessels, as well as nerves protruding the mucosa. Mucosa is designated as the inner lining of the gastrointestinal wall and branched into three compartments; the muscularis mucosa, the lamina propria and the intestinal epithelium. Muscularis mucosa keeps the mucosa and submucosa apart, lamina propria is abundant in lymphoid nodules, capillaries, nerve endings and accomodates numerous immune cells and lastly intestinal epithelium composed by a single layer of polarized epithelial cells that constitute a physical barrier seperating the intestinal mucosa from the large bacterial communities residing in the intestinal lumen (Liao, Zhao et al. 2009, Mowat and Agace 2014). Therefore, intestinal epithelial cells (IECs) beyond the regulation of the digestive processes, play a critical role in the host defense by preventing the interaction between microbiota and immune cells.The structural organization of the intestinal epithelium markedly differs among the small intestine and colon.

Small intestine is organized into continuous villous and crypt units. Villi are characterized as finger-like projections into the lumen comprising of postmitotic cells that sustain a broad brush border surface for nutrient absorption. The length of the villi gradually alters as going down the intestinal tract. In particular, duodenum exhibits longer villi compared to the ileum. On the contrary, crypts of Lieberkühn constitute invaginations of the intestinal wall that harbor the epithelial stem cell and proliferation compartment (Beumer and Clevers 2021) (Figure 9a). Intestinal epithelial cells undergo rapid self-renewal every 4 to 5 days, a process strictly controlled by intestinal stem cells (van der Flier and Clevers 2009). These stem cells are known as crypt-base columnar stem cells (CBCs) and are related to the specific expression of the cell surface marker leucine-rich repeat-containing G protein-coupled receptor 5 (LGR5). Additionally, CBCs constitute the active population of intestinal stem cells found at the bottom of the crypts (Barker, van Es et al. 2007).

Besides the LGR5+ CBCs cells, +4 cells residing at the fourth position of the crypt base are considered as a quiescent, reserve stem cell population that mobilized to reconstitute the stem cell niche upon epithelial injury, such as stress, irradiation or chemotherapeutic agents. However, it has been recently reported that stemness can be restored by dedifferentiation of both secretory and absorptive progenitors to promote intestinal regeneration (Tetteh, Farin et al. 2015, Gehart and Clevers 2019). The CBCs undergo assymetric division once per day generating one new stem cell at the crypt bottom and a transient amplifying (TA) cell (or rapidly proliferating progenitor), which follows 4-5 rounds of cell division and migrates upwards the villus compartment (Karmakar, Deng et al. 2020). The progenitor cells continue to move towards the villus tip, where they undergo differentiation into specialized IEC subtypes depending on Notch signalling.

Active Notch signals favors the absorptive fate, while lack of Notch signalling promotes the secretory lineage. The absorptive progenitors give rise to enterocytes or M (microfold) cells, determined by high BMP (bone morphogenetic protein) signals or RANKL (receptor activator of nuclear factor kappa B ligand) presence, accordingly. Enterocytes comprise 80% of the total IECs and form a brush border with numerous microvilli that account for nutrient absorption from the gut lumen and transport to the blood vessels. M cells largely cover the lymphoid follicles, such as Peyer’s patches that consist of B- and T-lymphocytes, macrophages and dendritic cells and trigger an antigen – specific immune response by promoting selective antigen endocytosis and presentation (Gehart and Clevers 2019).

On the contrary, secretory progenitors differentiate into four distinct cell types including Tuft, Goblet, Paneth or enteroendocrine cells. This cell type specification is governed by interleukins (IL4, IL13), Wnt signalling or epidermal and fibroblast growth factor (EGF, FGF). Particularly, an environment rich in Wnt and FGF signals results in Paneth cell fate, whereas low levels of Wnt and absence of EGF or presence of IL4 and IL13 promotes either enteroendocrine or Goblet cell differentiation path, accordingly. Lastly, IL4 and IL13 are additionally considered as drivers of Tuft cell formation (Clevers 2013, Gehart and Clevers 2019).

Tuft cells constitute a rare population of chemosensory bottle – shaped IEC that exclusively secrete IL-25 and coordinate type 2 immune responses against helminth parasitic infections in the intestine (Schneider, O’Leary et al. 2019). On the other hand, Goblet cells comprising the most abundant IEC subpopulation that contain secretory granules laden with highly glycosylated mucins. They expell mucins, Fc-γ binding protein (Fcgbp), trefoil factor 3 (TFF3) and resistin-like molecule-β (RELMβ) in order to generate a dynamic mucus layer, which protects against mechanical forces and bacterial encroachment, thus maintaining gut defence and homeostasis (Barker 2014, Ali, Tan et al. 2020). Enteroendocrine cells are located scattered throughout the intestinal epithelium with occurrence of less then 1%. Their principal role is to release peptide hormones including ghrelin, cholecystokinin, glucagon-like-peptides, serotonin, gastrin and somatostatin, hence orchestrating appetite, gastric emptying and food ingestion (Barker 2014).

Finally, Paneth cells (PCs) characterized as a long-lived IEC population with a self-renewing rate of 6-8 weeks. Unlike the other mature intestinal epithelial cell types, PCs do not follow upward flow during the migratory path, thus ending up at the bottom of the intestinal crypt intercalated among Lgr5+ CBCs. Mature PCs are critically involved in the regulation of innate immunity and the intestinal microbiota via the production of antimicrobial peptides (AMPs) like lysozyme, angiogenin-4, C-type lectin regenerating islet-derived protein IIIγ (RegIIIγ), secretory phospholipase A2 (sPLA2), and cryptdins/defensins. Due to their intimate contact with the Lgr5+ CBCs, PCs supply vital signals, including EGF, TGF-α, Wnt (Wnt3) and Notch (Dll4) ligands and cyclic ADP ribose (cADPR) to support the intestinal stem cell (ISC) niche (Sato, van Es et al. 2011, Ali, Tan et al. 2020). As soon as the terminally differentiated IECs approach the tip of the intestinal villus after the continuous turnover of the intestinal epithelium every 4-5 days, they detach from the surrounding extracellular matrix (ECM) and lose contact with neighbouring cells, consequently leading to luminal shedding. This is facilitated by a process of programmed cell death termed as anoikis (Delgado, Grabinger et al. 2016).

As opposed to the small intestine, colonic epithelium surface is relatively flat and devoid of the typical villi. However, it is structurally organized into multiple deep crypts harboring the stem cell compartment and the TA region in close proximity. Colon is immensely populated by Goblet cells that continuously supply mucus to sustain the inner and outer colonic mucus layer. On the other hand, it lacks Paneth cells which are rather replaced by the functional equivalent deep secretory cells (DSCs) indicated by REG4 that provide Notch ligands and EGF but not Wnt ligands (Sasaki, Sachs et al. 2016) (Figure 9b).

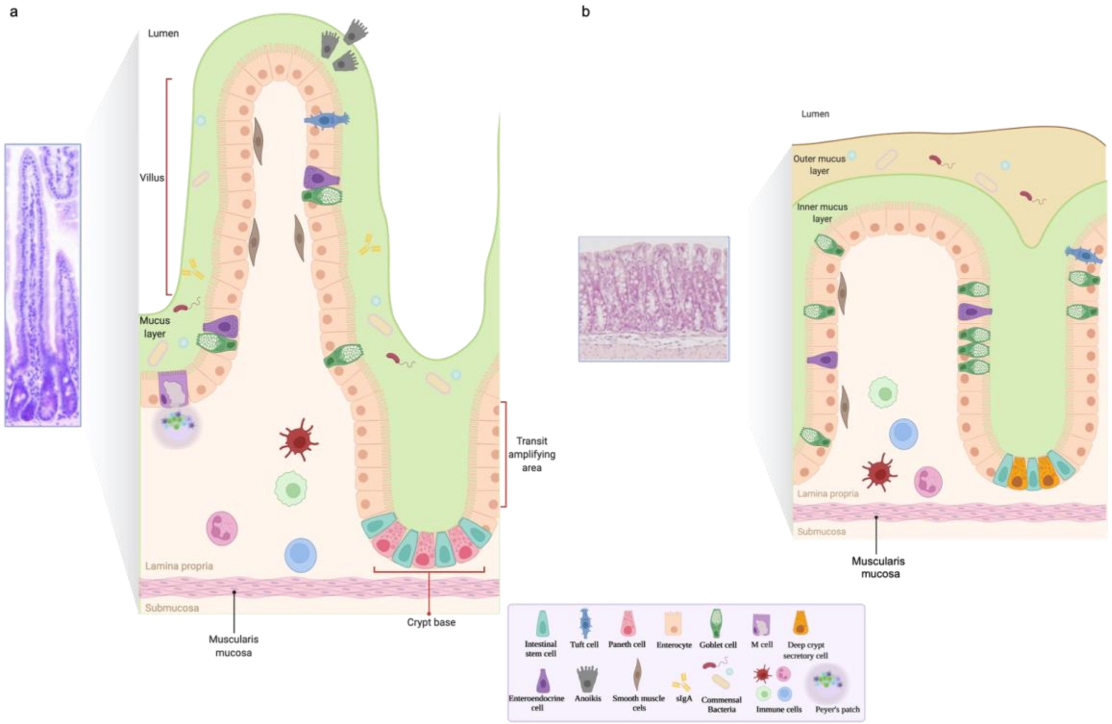

Figure 9. The structure of small intestinal and colonic epithelium

(a, b) Schematic representation of the small intestinal (a) and colonic (b) epithelium. The small intestine is structured into crypts and villi. Crypts harbor crypt base columnar stem cells and give rise to intestinal epithelial cell (IEC) absorptive and secretory lineages that undergo several cycles of proliferation in the transit amplifying (TA) area. Villus is populated by terminally differentiated IEC subtypes including enterocytes, enteroendocrine cells, Goblet cells, Tuft cells, M cells, whereas

Paneth cells move downwards to the crypt upon differentiation. Polarized IECs form a monolayer which functions as a barrier from the luminal contents. Mucus is an additional protection from the commensal bacteria and pathogens. The colonic epithelium is organized into crypts, containing deep crypt secretory cells and stem cells and is covered by a double layer of epithelium – attached mucus, the inner and the outer mucus layer. Every icon illustrated in the scheme is clearly described within the table. See text for elabolate description. Image created by BioRender.

1.5. Intestinal dietary fat absorption, mobilization and secretion

1.5.1. Digestion and emulsification of dietary lipids

Dietary lipids are predominantly composed of non-polar lipids, such as TAGs and cholesterol esters (CE), as well as polar phospholipids (PLs). Besides the diet-derived lipids, ingested fat also originate from endogenous sources, such as bile (mostly cholesterol and phospholipids) (Shiau, Popper et al. 1985).

Digestion of dietary lipids starts in the mouth by lingual lipase and continues in the stomach with the help of both lingual and gastric lipase. These lipases mostly hydrolyse ester bonds of TAGs to produce 1,2-diacylglycerols and fatty acids, facilitating partial fat emulsification into fine lipid droplets of 0.5 mm diameter (Cheng, Mah et al. 2020). The release of “acidic chyme” into the intestinal lumen, stimulates the secretion of the digestive hormones cholecystokinin (CCK) and secretin by the intestinal enteroendocrine cells.

CCK induces secretion of the bile from the gallbladder. Bile is primarily synthesized in the liver and consists of cholesterol derivatives glycine or taurine conjugated bile salts that function as emulsification agents. In addition, CCK leads exocrine pancreas to produce a pancreatic juice enriched in pancreatic lipase and its co-factor colipase, cholesterol esterase and phospholipase A2. In line with CCK, secretin activates bicarbonate release from the pancreatic duct, promoting the pH neutralization of the incoming chyme to allow proper digestion by the pancreatic enzymes (Whitcomb and Lowe 2007, Gribble and Reimann 2019) .

Pancreatic lipase aids the hydrolysis of TAGs into 2-monoacylglycerol (2-MAG) and fatty acids, cholesterol esterase contributes to the hydrolysis of cholesterol esters to produce free cholesterol and fatty acids, whereas phospholipase A2 carries out the digestion of phospholipids (dietary and biliary-derived) to yield lysophospholipids and free fatty acids. The poorly soluble lipid breakdown products diffuse across the unstirred water layer as mixed micelles to reach the duodenal enterocyte microvilli surface (Iqbal and Hussain 2009).

1.5.2. Intestinal uptake of fatty acids, cholesterol and lysophospholipids

As soon as the mixed micelles approach the enterocyte’s apical membrane, the lipid content included in the micelle carrier is liberated to facilitate entry into the enterocyte as single monomers. Depending on the concentration gradient, fatty acids can be either passively diffused through the microvilli of the enterocyte, or actively transported by highly-specialized integral membrane proteins (Cifarelli and Abumrad 2018).

The most widely accepted view in the literature is that short and medium-chain fatty acids (SCFAs/MCFAs), 2-MAG and lysophospholipids can be efficiently taken up by diffusion, whereas long-chain fatty acids (LCFAs) with 16-20 carbon atoms and cholesterol often require protein-mediated transport. In principle, the classic transmembrane proteins involved in the intestinal FA uptake consists of the cluster of differentiation (CD36/FAT), fatty acid transport protein 4 (FATP4) / solute carrier family 27 member 4 (SLC27A4) and the fatty acid-binding protein plasma membrane (FABPpm) (Yen, Nelson et al. 2015).

CD36/FAT is a fatty acid translocase, abundantly expressed on the villi enterocytes of both duodenum and jejenum that mediates binding with a broad repertoire of ligands, including LCFAs. *Cd36*-deficient mice exhibited defective absorption of [^{3}H]-oleate (C18:1) and [^{14}C] cholesterol in proximal primary enterocytes (Nassir, Wilson et al. 2007), as well as chylomicron synthesis and secretion (Nauli, Nassir et al. 2006). Moreover, de-phosphorylation of CD36 induced by intestinal alkaline phosphatase (IAP), enhanced the rate of LCFA uptake, which was further augmented by high-fat diet in mouse enterocytes in vitro (Lynes, Narisawa et al. 2011).

FATP4/SLC27A4 is strongly present on the apical enterocyte border and has been initially implicated in the uptake of LCFAs by the intestine. Inhibition of FATP4 expression with antisense oligonucleotide treatment in freshly isolated enterocytes significantly reduced the uptake of oleate and palmitate, but the effect was rather dependent on its acyl CoA synthetase activity (Stahl 2004). Despite the findings *in vitro*, no remarkable fat malabsorption phenotype was apparent upon FATP4 knockdown *in vivo* or after treatment of mice with FATP4 inhibitors, weakening the notion of a primary function of FATP4 in intestinal lipid uptake (Blackburn, Guan et al. 2006, Shim, Moulson et al. 2009). Later studies suggested differential localization of FATP4 in the ER, where it participates in the esterification of fatty acid through rapid conversion into acyl-CoA for subsequent TAG synthesis (Niot, Poirier et al. 2009).

The peripheral membrane protein FABPpm, which shares similarity with the mitochondrial aspartate aminotransferase, has been initially described to participate in the intestinal FA uptake. However, the role of both FATP4 and FABPpm in dietary fat absorption as a transport proteins remains debatable, rendering CD36/FAT as the best well-described transporter of fatty acid in enterocytes so far (Yen, Nelson et al. 2015).

LCFA uptake can be also facilitated intracellularly with the aid of cytosolic fatty-acid binding proteins (FABPc). In the proximal enterocytes, FABP1 (liver-FABP/L-FABP) and FABP2 (intestinal-FABP/I-FABP) are highly expressed. Their main function is to sequester free fatty acids aiming to eliminate fatty-acid induced toxicity and deliver them into specific cell compartments. FABP1 has been also implicated in chylomicron trafficking, since *L-Fabp*$^{-/-}$ mice exhibited markedly impaired intestinal lipid secretion despite normal rates of lipid uptake (Neeli, Siddiqi et al. 2007).

Free cholesterol absorption by the intestine is facilitated by Niemann-Pick C1-like 1 (NPC1L1), a glycosylated protein abundantly located on brush-border enterocyte membrane microdomains, by a clathrin-mediated endocytosis. Upon microdomain internalization, cholesterol is liberated in the endocytic machinery in order to be transported into intracellular compartments (Jia, Betters et al. 2011). Deficiency of NPC1L1 in mice substantially diminished cholesterol absorption. In addition, treatment of NPC1L1 knockout mice with ezetimibe, therapeutic agents that block biliary and dietary uptake of cholesterol, did not further impact the levels of absorption, suggesting the crucial role of NPC1L1 in this process (Altmann, Davis et al. 2004). Additionally, scavenger receptor class B type I (SR-BI) has been engaged with plasma membrane cholesterol sensing. *In vitro* studies have demonstrated that apolipoprotein B trafficking necessitates the association of SR-BI with plasma cholesterol upon exposure to postprandial micelles (Saddar, Carriere et al. 2013). Finally, overexpression of SR-BI in the intestine boosted the uptake of ^{14}C-cholesterol and ^{3}H-triolein, albeit the unaffected cholesterol and FA absorption upon total SR-BI ablation in mice (Mardones, Quiñones et al. 2001) (Bietrix, Yan et al. 2006). ATP-binding cassette subfamily G member 5 (ABCG5) and ABCG8 heterodimer constitute the cholesterol efflux transporters in the liver and intestine that participate in the elimination of cholesterol within enterocytes and hepatocytes, respectively. In particular, the heterodimer transporter act by secreting dietary excessive cholesterol into the gut lumen or directly into the bile and through impeding the uptake of the harmful phytosterols (sitosterols). In the liver, cholesterol can be also eliminated by being converted into bile acids. Intestinal-specific ablation of ABCG5 and ABCG8 in mice (*I-G5G8*$^{-/-}$) leads to enhanced uptake of plant sterols, while cholesterol absorption maintained unaltered. Additionally, both hepatic and intestinal G5G8 transporter markedly participates in excretion of cholesterol into the feces (Wang, Mitsche et al. 2015).

The majority of the peripheral cells of the body prevent the build-up of intracellular unwanted cholesterol through the reverse cholesterol pathway and the hepatobiliary secretion of cholesterol into the feces. However, removal of cholesterol can be additionally achieved by the transintestinal cholesterol excretion (TICE) into the lumen of the intestine via ABCG5-ABCG8 transporters upon being absorbed from circulating plasma lipoproteins at the basolateral site of the enterocytes (Temel and Brown 2015).

1.5.3. Intracellular processing of absorbed lipids by the intestine

To date, two major pathways has been assigned to execute the re-esterification of TAGs at the ER membrane upon enterocyte entry of the digestive products in a postprandial state; the Monoacylglycerol acyltransferase (MGAT or Mogat) pathway and the Glycerol-3-Phosphate (G3P) pathway, that utilize MAG or G3P as initial acceptors of the acyl group, accordingly. Both pathways are active in the intestine, however the MGAT pathway is the predominant one, being responsible for 80% of newly synthesized TAGs (Pan and Hussain 2012).

The MGAT pathway is initiated with the acylation of monoacylglycerol (MAG) by fatty acyl-CoA (FA-CoA), produced from the activation of FA through the action of fatty-acyl-CoA synthetases (ACSLs), to form diacylglycerol (DAG). The reaction is performed by monoacylglycerol acyltransferases (MGAT) enzymes. The group of MGAT enzymes is composed of three isoforms; MGAT1, MGAT2 and MGAT3 and is localized in the ER. MGAT2 is abundantly expressed in both murine and human intestine, specifically in the villi of the proximal part. On the other hand, MGAT3 is only found in the ileum of human intestine (Shi and Cheng 2009). Mice globally deficient in MGAT2 (*Mogat2*$^{-/-}$) or lacking MGAT2 in the intestine (*Mogat2* (IKO)), exhibited blockade in the uptake and re-esterification of MAG and delay in the delivery of dietary fat into the circulation after feeding with high-fat diet (HFD) (Yen, Cheong et al. 2009, Tsuchida, Fukuda et al. 2012). However, the decreased secretion rate of TAG in response to fat load was reverted in the *Mogat2*$^{-/-}$ mice after introducing the MOGAT2 human gene under the intestinal-specific villin promoter (Gao, Nelson et al. 2013). The final step in the TAG re-synthesis process is the conversion of DAG into TAG via acylation, reaction catalysed by diacylglycerol acyltransferases (DGAT) enzymes. The two well-described DGAT isoforms which are expressed in the murine small intestine, are DGAT1 and DGAT2. Both enzymes localized on the ER membrane, while DGAT2 is tightly associated with cytoplasmic lipid droplets (CLDs) and mitochondria (Chitraju, Walther et al. 2019). Whole body *Dgat1*-deficient mice display normal fat absorption. However, they show highly elevated levels of TAG species in the proximal small intestine and slower release of dietary fats into the circulation upon high-fat feeding, in sharp contrast to their control littermates. Intestine-specific DGAT1 expression in the *Dgat1*-deficient mice ameliorates the phenotype by diminishing the accumulation of CLDs within the enterocytes and restoring the delayed secretion rate of TAGs (Lee, Fast et al. 2010, Harris, Haas et al. 2011). DGAT1 is the only isoform expressed in human small intestine, where homozygous mutations have been correlated with congenital diarrheal disorder. Interestingly, DGAT1 inhibitors have been employed for treating hypertriglyceridemia. However, they were not well-tolerated owing to severe diarrhea, as a prominent side effect (DeVita and Pinto 2013). On the other hand, *Dgat2*-deficient mice cannot survive beyond twenty-four hours, due to skin defects and rapid dehydration. While overexpression of DGAT2 in the intestine raise the secretion of TAGs, no such beneficial effect was apparent in *Dgat1*-deficient mice, proposing distinct functions of DGAT1 and DGAT2 (Uchida, Slipchenko et al. 2013).

The acylation of glycerol-3-phospate (G3P) to produce lysophosphatidic acid (Lyso-PA or LPA) by glycerol-3-phosphate acyltransferases (GPATs) is the first step of the G3P pathway. The four well-described isoforms have different subcellular localization with GPAT1 and GPAT2 to be found on the mitochondria outer membrane, while GPAT3 and GPAT4 to be abundant on the ER membrane of both human and murine small intestine. *Gpat3*$^{-/-}$ mice present accumulation of TAGs in gut epithelia and declined TAG secretion upon administration of an oral lipid bolus comparable to the intestinal phenotype observed in *Dgat1*$^{-/-}$ mice (Khatun, Clark et al. 2016). The second step of the pathway includes the acylation of the LPA to phosphatidic acid (PA) by acylglycerolphosphate acyltransferases (AGPATs) or lysophosphatidic acid acyltransferases (LPAATs). To date, three isoforms of AGPATs have been identified in the small intestine; AGPAT2, -4 and -8. PA can be also synthesized by DAG kinases (DGKs) upon DAG phosphorylation or by phospholipase D (PLD) after hydrolysis of phosphatidylcholine (PC). PA is further utilized as substrate for the production of amphipathic glycerolphospholipids that constitute components of cell membranes or surfaces of lipids and lipoproteins. In principle, PA is converted to cytidine diphosphate diacylglycerol (CDP-DAG) to subsequently yield phosphatidylinositol (PI), which is directly aimed for the generation of phosphatidylinositol (3, 4, 5)-trisphosphate (PIP3), phospatidylglycerol (PG) and cardiolipin (CL). Following this step, DAG is generated by dephosphorylation of the PA from phosphatidic acid phosphatases (PAPs) or lipins. Among the three characterized isoforms, lipin 1, 2 and 3, only the last two are predominantly expressed in the small intestine. Lipin 2/3- deficient mice display elevated levels of PA and PC, modifying membrane phospholipid composition. Hence, *Lpin2/3*-KO mice show fully-filled with enlarged TAG-rich lipid droplets intestinal villi, due to defective pre-chylomicron assembly and chylomicron secretion (Zhang, Csaki et al. 2019). DAG function as a precursor of phosphatidylcholine (PC), phosphatidylethanolamine (PE) and TAGs (Bond 2017, Lee and Ridgway 2020). Ultimately, the last acylation step of DAG into TAG is shared between the two enzymatic pathways that facilitate re-esterification of TAGs.

The free cholesterol that has been absorbed by the enterocytes undergoes esterification, a process carried out by acyl-CoA:cholesterol acyltransferases (ACAT) enzymes, such as ACAT1 and ACAT2, to form CEs that are subsequently integrated in the core of lipoprotein particles. ACAT2 is highly dominant in the murine and human intestine. ACAT2 knockout mice (ACAT2$^{-/-}$) reveal lessened absorption of cholesterol and composition of CEs in the apoB-containing lipoproteins upon feeding with a diet full of cholesterol, cholic acids and TAGs (Repa, Buhman et al. 2004, Nguyen, Sawyer et al. 2012). Esterification of lysophospholipids is conveyed by acyltransferases to provide phospholipids. In particular, lysophosphatidylcholine is converted to phosphatidylcholine with the help of lysophosphatidylcholine acyltransferase-3 (LPCAT3). Intestinal-specific deletion of LPCAT3 leads to growth retardation and postnatal lethality with an intestinal pathology mostly manifested by high amounts of lipid droplets within the enterocytes and lower TAG release in the plasma. The reduction in the rate of lipoprotein secretion in the *Lpcat3*$^{-/-}$ mice has been attributed to the unsuccessful incorporation of arachidonic acid into the intracellular membranes, eventually affecting their phospholipid composition and lipid mobility through them (Hashidate-Yoshida, Harayama et al. 2015, Rong, Wang et al. 2015).

1.6. Destinations of the intestinal lipids upon processing

The newly synthesized intestinal lipids in the ER membrane are either assembled into lipoproteins, particularly chylomicrons (CMs) and subsequently released into the circulation or temporarily retained as cytoplasmic lipid droplets (CLDs) in the cytosol of the enterocytes (Figure 10).

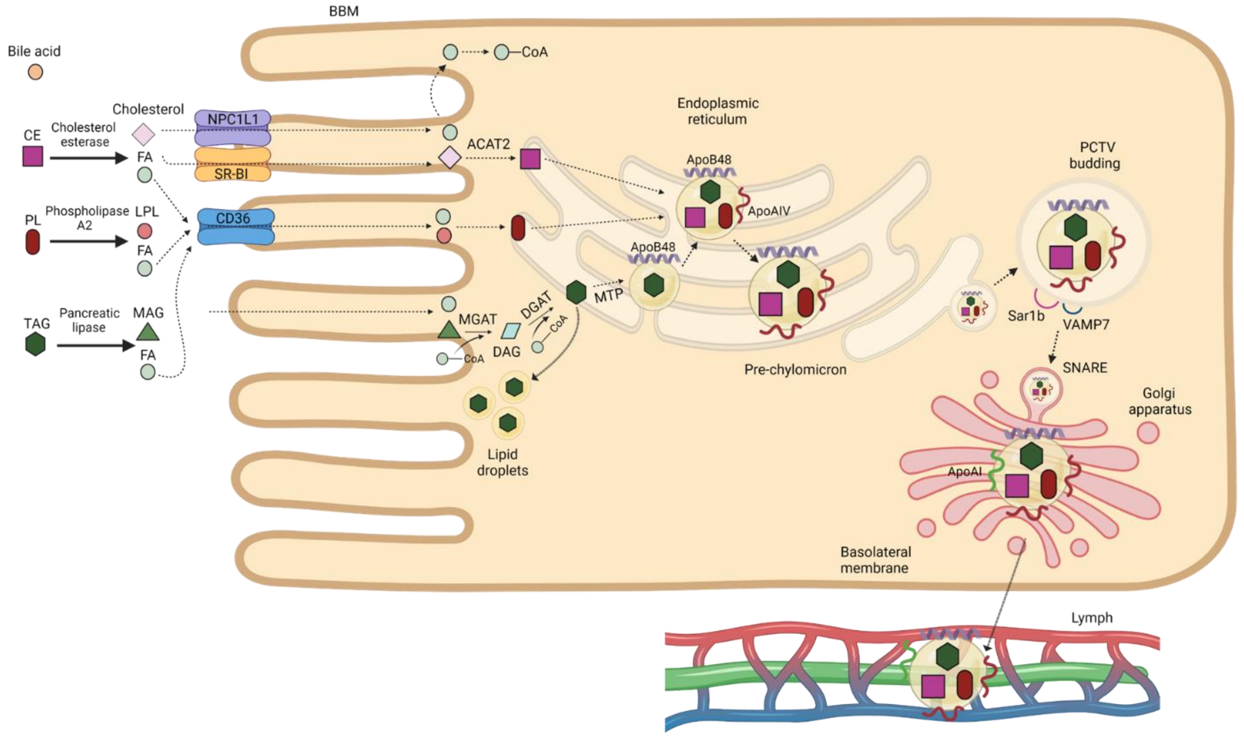

Figure 10. The complete process of the intestinal lipid absorption and transport.

Schematic representation of lipid uptake from the lumen and secretion into the lymph in the form of chylomicrons. In the intestinal lumen, dietary lipids comprising of triacylglycerols (TAGs), phospholipids (PLs) and cholesteryl esters (CE), as well as endogenously produced lipids are broken down by pancreatic enzymes, thus giving rise to cholesterol, monoacylglycerols (MAGs), lysophospholipids (LPLs) and fatty acids (FAs). Their transport across the brush border membrane (BBM) of the enterocyte is performed via passive diffusion or by the action of fatty acid transporters. Upon entry, re-esterification of the lipid products takes place with the aid of MGATs, DGATs and ACATs leading to the fully assembled TAGs, CEs and PLs. Subsequently, lipids are transferred to the ER in order to be packaged via a MTP-mediated process into pre-chylomicrons with ApoB48 or they temporarily stored as lipid droplets. Pre-chylomicrons are then transported in a pre-chylomicron transport vesicle (PCTV) to the *cis*-Golgi. PCTV gets fused with the Golgi, in a process headed by Sar1b and SNARE proteins. After acquiring ApoA1, mature CMs leave the *trans*-Golgi in Golgi-derived vesicles and subsequently secreted into the lymphatic circulation. Abbreviations: NPC1L1, Niemann Pick C1-like 1, SR-BI, scavenger receptor class B type I, CD36, cluster of differentiation 36, ACAT2, acyl CoA:cholesterol acyltransferase enzyme 2, MGAT, monoacylglycerol acyltransferase, DAG, Diacylglycerol, DGAT, Diacylglyceride acyltransferase, MTP, microsomal triglyceride transfer protein, Apo-B48, -AIV, -AI, apolipoprotein -B48, -AIV, -AI, Sar1b, secretion-associated, Ras-related GTPase 1B, VAMP7, vesicle-associated membrane protein 7, SNARE, soluble N-ethylmaleimide sensitive-factor attachment protein receptor. Image was inspired by (Ko, Qu et al. 2020) and created by BioRender.

1.6.1. Chylomicrons (CMs)

1.6.1.1. Chylomicron assembly

Chylomicron particles are synthesized in a two-step process in the inner ER membrane, starting with the nascent primordrial CM assembly. Primordial CM contains a neutral lipid core made of TAGs and CEs, which is enclosed by a phospholipid monolayer with surface lipoproteins and free cholesterol (Mansbach and Siddiqi 2010).

A pivotal nonexchangeable structural component of CM is apolipoprotein B48 (ApoB48), a truncated form of the full-length ApoB (ApoB100). Each CM carries out only one molecule of ApoB48, as its unique signature. Complete loss of ApoB in mice is embryonic lethal at embryonic day 10 to 12, due to the inability of yolk sac to transport lipid nutrients to the embryo. Mice with intestinal epithelial cell-specific deletion of ApoB fail to thrive due to malabsorption of fats. These mice display enterocytes fully filled with CLDs and greatly lack chylomicron-containing Golgi cisternae (Young, Cham et al. 1995, Kim and Young 1998). In humans, familiar hypobetalipoproteinemia (FHBL) is caused by missense or frame-shift mutations of the ApoB gene resulting in ApoB truncation (Figure 11). This truncated ApoB protein impairs assembly and plasma concentration of ApoB-containing lipoproteins released from the enterocytes and hepatocytes, ultimately leading homozygote patients to develop among other severe symptoms, hepatic steatosis and intestinal fat malabsorption (Hooper, Robertson et al. 2007). The intestine is capable of constitutively synthesized ApoB48-containing lipoproteins the size of which varies based on the bulk of ingested lipids being packaged during the postprandial state. However, ApoB48 can be directed towards ubiquitination - proteosomal degradation in the absence of adequate lipid amounts and insufficient lipidation (Mansbach and Siddiqi 2010).

Lipidation of ApoB is mediated by the microsomal TAG transfer protein (MTP) in both the intestine and the liver. MTP is a heterodimeric intracellular lipid transfer protein that contains an active subunit of 97 kDa carrying lipid transfer activity and a smaller 58 kDa subunit which forms disulfide bonds and stabilize the MTP complex. Physical interaction of MTP with ApoB48 contributes to protein folding and structural configuration of ApoB48 for its proper lipidation (Hussain, Rava et al. 2012). Finally, the dense ApoB48-containing primordial CM expands its core with TAGs either through direct fusion with an ApoB48-free ER luminar lipid droplet or by utilization of TAGs originated from hydrolysis and re-esterification of luminar lipid droplets to ultimately generate the pre-chylomicron (pre-CM) (Mansbach and Gorelick 2007). In mice, whole body knockout of *Mttp* results in embryonic lethality at embryonic day 9.5 to 10.5 due to inhibited lipoprotein synthesis and delivery to the embryo from the yolk sac of the mother. Mice lacking MTP in the intestine reveal fat-laden enterocytes, similarly to the intestinal specific *ApoB*-deficient mice accompanied by lowered secretion of CMs and steatorrhea (Raabe, Flynn et al. 1998), (Hussain, Rava et al. 2012). Abetalipoproteinaemia is a rare disorder elicited by mutations in the large subunit of MTP resulting in inadequate lipidation of ApoB48 and ApoB100 and hence, failure in the CM and VLDL production by intestine and liver in humans, respectively (Figure 11). Homozygote patients present various complications including hepatic steatosis, diarrhoia, low levels of fat-soluble vitamin E and neurological disturbances (Tarugi, Averna et al. 2007). Currently, specific MTP inhibitors have been developed for decreasing the levels of plasma TAGs and LDL cholesterol in patients suffering from homozygous familial hypercholesterolemia (Mera, Odani et al. 2011).

Lastly, apolipoprotein AIV (ApoA-IV) is further incorporated in the pre-CM within the ER. Mice deficient in ApoA-IV fed with chow diet or challenged with HFD for 8 weeks display normal lipid absorption and secretion, but affect CM particles composition and metabolism. In particular, ApoA-IV KO mice release larger CMs from the intestine into the lymph, whose clearance from the circulation is remarkably delayed (Kohan, Wang et al. 2015).

1.6.1.2. COPII-mediated ER-to-Golgi transport

ER is a dynamic and multisystemic organelle. It is organized into a network of flattened, stacked sheets enriched with ribosomes (rough ER) and tubular structures with no bound ribosomes on them (smooth ER). In mammalian cells, the trafficking of the secretory cargo of newly synthesized proteins from the rough ER to the ER-Golgi intermediate compartment (ERGIC), to the Golgi apparatus and ultimately to the extracellular space, is a coat complex type II (COPII) - mediated dependent process. COPII are typically 60-80 nm spherical vesicles, whose budding is initiated from specialized domains of the ER membrane, reported as transitional ER or ER-exit sites (ERES) (McCaughey and Stephens 2018).

The conventional COPII assembly starts at ERES with the binding of Sec12, which is an ER transmembrane protein and guanine nucleotide exchange factor (GEF) to Sec16, enabling GDP from the small secretion - associated RAS - related GTPase 1 (Sar1) to BE exchanged to GTP. Inactive Sar1-GDP is converted to its activated form Sar1-GTP, which eventually engages the inner layer COPII components Sec23 and Sec24 heterodimers to generate the pre-budding complex as a cup-shaped ER region. Sec24 carries multiple binding sites in order to facilitate interaction with cargo proteins and recruits the outer layer COPII components Sec13 and Sec31 heterotetramers. On the other hand, interaction of Trk-fused gene (TFG) with Sec23 on the outer COPII coat leads to the production of a matrix for efficient formation of COPII components. Addionally, Sec23 functions as GTPase-activating protein or GTPase-accelerating protein (GAP) for Sar1 GTP hydrolysis, which is boosted upon Sec13/Sec31 interaction. At this stage, cargo proteins are further accumulated and the COPII vesicle expands in size. Ultimately, COPII vesicles bud off from the ER upon conformational changes of Sar1 GTP through GTP hydrolysis, outer coat is disassembled and merge with ERGIC/Golgi compartments. COPI-coated vesicles perform recycling of the non-targeted to the Golgi cargo, back to the ER membrane (Saito, Maeda et al. 2017, McCaughey and Stephens 2018). However, incorporation of large cargo, such as procollagen (>300nm) and prechylomicrons (100-500nm) within plain COPII-coated vesicles of 60-80 nm in diameter, remains quite challenging. Export of large procollagen with relatively flexible fibrils from the ER is governed by COPII carriers of 150nm and supported by Hsp47 chaperone that plays a crucial role as an adaptor of the cargo receptor transport and Golgi Organization 1 (TANGO1), that is inseparably associated with cutaneous T-cell (cTAGE5). TANGO1/cTAGE5 regulates taking up of the procollagen, expansion of the COPII prebudding complex and fusion with the ERGIC membrane. Large procollagen that lacks flexibility can be encapsulated in distinct COPII carriers of >350nm in diameter partially bound to the ER or transported to the ERGIC via a tunnel-like pathway (McCaughey and Stephens 2019).

1.6.1.3. Chylomicron trafficking

To exit the ER, newly formed prechylomicrons with an average size of 250nm require specialized transport vesicles, which are considered to be more extended than classical protein cargo-containing vesicles, designated as pre-chylomicron transport vesicles (PCTVs). The PCTV complex leaves the ER surface with the assistance of a four-protein complex including ApoB48, CD36, FABP1 and vesicle-associated membrane protein 7 (VAMP7) (Figure 12). Firstly, a 70kDa part of the ApoB48 becomes exposed on the cytosolic side of the ER, rendering it vulnerable for attack by proteinases. However, the vesicular membrane that covers the pre-CM does not allow further degradation (Siddiqi, Saleem et al. 2010). FABP1 constitutes a member of a heteroquatromeric protein complex that contains Sec13, Sar1b and small valosin-containing protein/p97-interactive protein (SVIP) that resides in the cytosol. FABP1 is not able to bind to the ER as long as is integrated within the multiprotein complex. However, phosphorylation of SAR1B GTPase by protein kinase C zeta (PKCζ) disengage monomeric FABP1 from the complex in a process that requires ATP, allowing its binding to the ER and consequently the initiation of PCTV budding (Neeli, Siddiqi et al. 2007, Siddiqi and Mansbach 2008, Siddiqi and Mansbach 2012). Interestingly, it has been shown that CD36 KO or L-FABP (FABP1) KO mice display considerably diminished PCTV production (Siddiqi, Saleem et al. 2010).

Besides FABP1, SAR1B GTPase is undoubtedly an essential player in the regulation of CM secretion. In humans, biallelic mutations in the *SARA2* or *SAR1B* gene have been connected to the development of a rare, autosomal recessive congenital disorder, known as chylomicron retention disease (CRD) or Anderson's disease (Figure 11). Exploring the genetic defects of 60 patients that have been diagnosed so far with CRD, unravelled several frameshifts, slice site, nonsense and missense mutations on the *SAR1B* gene, giving rise to truncated or dysfunctional SAR1B protein. In particular, these mutations specifically disturbed interaction of SAR1B GTPase with the COPII machinery, through altering its affinity for GTP and GDP (Jones, Jones et al. 2003, Charcosset, Sassolas et al. 2008). In CRD, CM are normally assembled, but the maturation and transport across the secretory system of the enterocytes is utterly hampered. Therefore, the phenotype of the CRD patients manifested by fully loaded enterocytes with LDs, complete lack of CMs and ApoB48 in the blood circulation after a fatty meal, shortage of fat-soluble vitamins and essential fatty acids, as well as strinkingly low levels of total cholesterol and HDL/LDL-cholesterol. Consequently, heterozygous patients do not show any symptoms in strong contrast to the homozygous ones that fail to thrive since they suffer from steatorrhoea, vomiting, swelling of the abdomen and ocular and neurological abnormalities. Treatment of those patients based on limitations of the fat intake and supplementation with essential fatty acids and fat-soluble vitamins (Levy 2015, Ben Ameur, Aloulou et al. 2016, Ferreira, Ramos et al. 2018, Levy, Poinsot et al. 2019).

Over the last years, multiple *in vivo* and *in vitro* studies have tried to gain insight into the unrecognized aspects of the CRD disorder. In particular, loss of *Sar1b* in zebrafish larvae using an antisense oligonucleotide resulted in abundant retention of ingested dietary lipids within enterocytes after high-fat feeding and significantly diminished clearance of LDs upon fasting. Additionally, *Sar1b* is pivotal for the uptake of cholesterol by enterocytes and the proper development of the digestive tract and exocrine pancreas in the zebrafish model (Levic, Minkel et al. 2015).

Homozygous *Sar1b*$^{-/-}$ mice die at late gestation, wheres heterozygous mice with mutated or deleted *Sar1b* exhibit severe gastrointestinal abnormalities. Specifically, SAR1B KO (*Sar1b*$^{del/+}$) and mutated (*Sar1b*$^{mut/+}$) mice fail to secrete CM upon intragastric administration of [^{14}C]-triolein and revealed notably diminished levels of total cholesterol, HDL-cholesterol and TAGs in the plasma and markedly reduced protein levels of MTP and ApoB. In addition, *Sar1b*$^{mut/+}$ show augmentation of the TAG fecal content, indicating intestinal fat malabsorption. Lastly, ablation of *Sar1b* greatly impaired intestinal lipid homeostasis without affecting liver lipid metabolism (Auclair, Sané et al. 2021). *Sar1b* transgenic mice (*Sar1b*$^{+/+}$) challenged with HFD boosted the secretion of CM, but elicited metabolic complications such as hepatic steatosis, insulin insensitivity and dyslipidemia (Levy, Spahis et al. 2014). Likewise, overexpression of *Sar1b* in Caco-2/15 cells markedly increase both esterification and release of TAGs, CE and PLs, as well as CM secretion. Additionally, biogenesis of ApoB48 together with enzymatic activity of MGAT, DGAT and MTP was detected to be greatly elevated upon *Sar1b* overexpression (Levy, Harmel et al. 2011). Notwithstanding, deletion of *SAR1B* induced by the zinc finger nuclease technoque in Caco-2/15 cells, did not completely abolished CM production, suggesting that increased levels of its paralogue SAR1A might compensate for the loss of SAR1B*.* On the other hand, total ablation of both SAR1A and SAR1B resulted in a full abrogation of CM output and HDL cholesterol, infering that both proteins are vital for CM trafficking (Sané, Seidman et al. 2017). Another recent study has demonstrated that double knockout of *SAR1A/B* in Caco-2/15 cells significantly impact enterocyte lipid homeostasis by augmenting fatty acid β-oxidation (amplified PPAR-a and PGC1A transcription factor gene expression) and reducing lipogenesis (decreased mRNA levels of *ACC* and *FASN*, as well as protein levels of SREBP-1c). In response to combined depletion of *SAR1A/B*, antioxidant defense was collapsed, leading to lipid peroxidation accompanied with induced inflammatory response (Sané, Ahmarani et al. 2019).

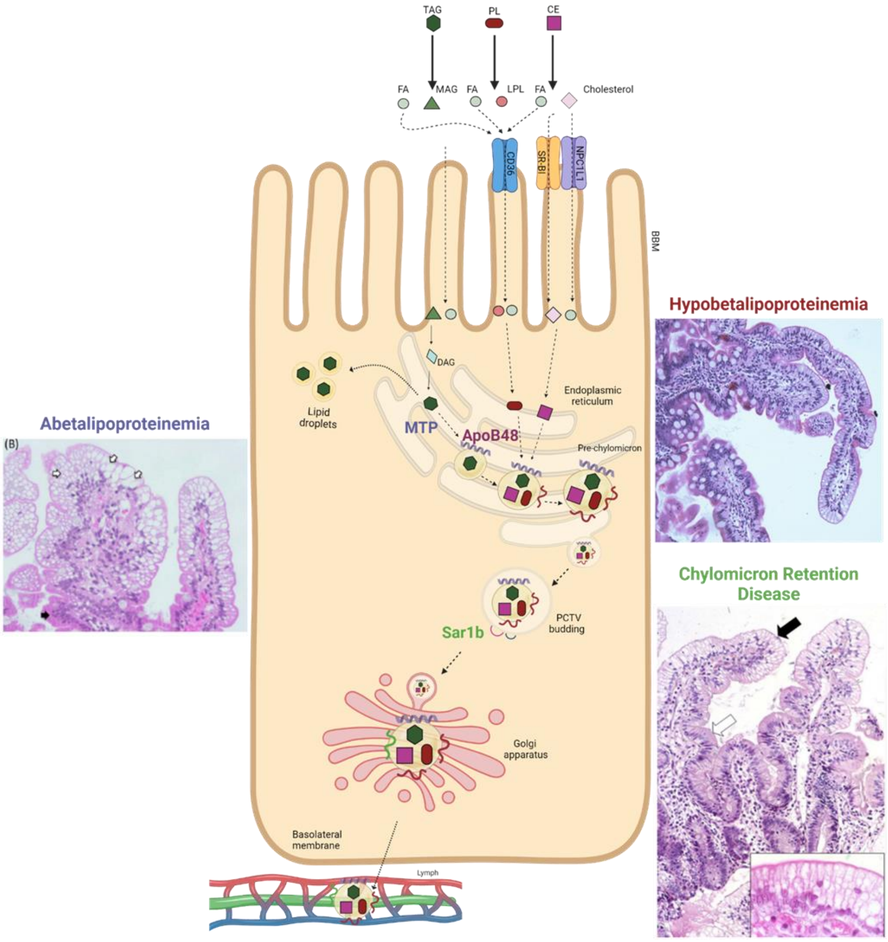

Figure 11. The diseases related to defective lipid transport by the enterocytes.

Schematic representation of the dietary lipid trafficking by enterocytes highlighting the key proteins that are closely associated with three autosomal recessive Mendelian cases. Impaired assembly of the nascent chylomicron (CM) due to inactivating mutations in the genes encoding either MTP or ApoB48 results in the development of Abetalipoproteinemia or Hypobetalipoproteinemia, respectively. Defective COPII-coated vesicular transport of pre-chylomicrons (pre-CMs) from ER to

Golgi owing to mutations in the gene encoding Sar1b leads to chylomicron retention disease (CRD) or Anderson disease. The effect of all three diseases is massive lipid droplet overload within enterocytes. The pictures illustrating the respective diseases were obtained from: (Peretti, Sassolas et al. 2010, Desomer, De Vos et al. 2015, Di Filippo, Collardeau Frachon et al. 2019). Image was created by BioRender.

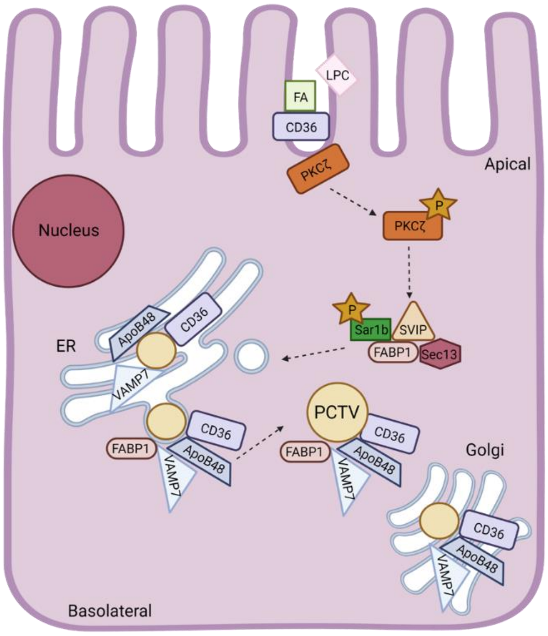

Figure 12. The formation and budding of the pre-chylomicron transport vesicle (PCTV)

Schematic representation of the proteins required for the generation of the PCTV in the ER, budding from the ER for subsequent transport to the Golgi. LPC activates protein kinase zeta (PKC-ζ) in order to promote Sar1b phosphorylation that constitutes one of the components of a cytosolic heteroquatromeric protein complex comprising of SVIP, Sec13 and FABP1. Phosphorylation of Sar1b liberates FABP1 that subsequently binds to ER. In the ER, CD36, VAMP7, FABP1 and ApoB48 induce the PCTV budding. PCTV fuses with the Golgi membrane and release the pre-chylomicron for further processing and maturation within the Golgi. Abbreviations: FA, fatty acids, LPC, lysophosphatidylcholine, CD36, cluster of differentiation 36, Sar1b, secretion-associated, Ras-related GTPase 1B, FABP1, fatty acid binding protein 1, SVIP, small VCP Interacting Protein, VAMP7, vesicle-associated membrane protein 7, P, phosphorylation. Image was inspired by (Cifarelli and Abumrad 2018) and created by BioRender.

1.6.1.4. Chylomicron maturation

The Golgi apparatus is an immensely dynamic organelle mainly involved in the sorting, modifying and trafficking of intracellular protein, lipids and carbohydrates. Its structure is uniquely and tighly organized into flattened saccules, named as cisternae that piled up to generate Golgi stacks. Tethering of individual Golgi stacks lead to the assembly of the compact Golgi ribbon. Golgi complex is highly polarized and arranged into two faces, the *cis* Golgi network (CGN) and the *trans* Golgi network (TGN). CGN captures the incoming cargos from the ER, while TGN is the site where cargo is sorted and targeted to the endolysosomal system, plasma membrane or destined for secretion to the extracellular space (Boncompain and Perez 2013, Saraste and Prydz 2019).

After leaving the ER membrane, PCTVs are directly targeted to the *cis*-Golgi. Despite the fact that PCTV budding is COPII-independent, docking of PCTV with the Golgi relies on COPII proteins (Siddiqi, Gorelick et al. 2003). In particular, Sec24C is predominantly needed for PCTV-Golgi fusion, while Sec23 is required in a lesser extent (Siddiqi, Siddiqi et al. 2010). Another pivotal player on the fusion process of PCTV with the Golgi is considered to be the VAMP7. VAMP7 has been initially identified in the *trans*-Golgi network region, facilitating endolysosomal vesicular trafficking (Advani, Yang et al. 1999). Later studies have illustrated that VAMP7 is mostly localized in the intestinal ER and particularly concentrated on the PCTVs. Antibody-mediated blockage of VAMP7 resulted in absolute shutdown of the PCTV budding activity (Siddiqi, Mahan et al. 2006). The tethering of PCTVs to the *cis*-Golgi is controlled by the soluble N-ethylmaleimide-sensitive factor (NSF) attachment protein receptor (SNARE) complex. This complex is generated by the pairing of vesicle membrane SNARE (v-SNARE), that guide the transport vesicles to their destination, with the target membrane SNARE (t-SNARE) located on the target membrane. In particular, one out of the four stable helices of the SNARE complex found on the v-SNARE and the other three, on the t-SNARE. VAMP7 acts as v-SNARE to drive the PCTV towards the Golgi, where it engages with the t-SNAREs of the *cis*-Golgi membrane; syntaxin 5, RBET1 and VTI1a to liberate the pre-CM cargo into the lumen of the Golgi (Siddiqi, Siddiqi et al. 2006).

In the Golgi, pre-CMs will be further processed to mature CMs through undergoing two additional modifications. Firstly, pre-CM acquires apolipoprotein A-I (Apo-AI), which is only binds to the pre-CM within Golgi lumen, despite its ER synthesis and subsequently ApoB48 is subjected to glycosylation (Mansbach and Siddiqi 2016). Despite the fact that MTP is also localized in the Golgi, it has been initially proposed that mature CMs do not undergo further lipidation in the Golgi lumen, as indicated by the absence of size expansion (Siddiqi, Siddiqi et al. 2006). Mature chylomicrons are now ready to exit the trans-Golgi into large secretory vesicles and being exocytosed at the basolateral membrane of the enterocyte.

1.6.1.5. Chylomicron secretion

As soon as mature CMs released from the Golgi, they are directed towards the basolateral membrane of the enterocyte. Following exocytosis, CMs journey to the lacteals through the villous lamina propria, subsequently enter the mesenteric lymphatic vessels, then the lymph nodes and the thoracic duct to ultimately move at the left subclavian vein into the blood circulation. It has been proposed that uptake of CM into the tip of the lacteals is facilitated by size exclusion via porous intercellular junctions in a paracellular way (Dixon 2010). In mice, ablation of the transcription factor pleomorphic adenoma gene-like 2 (*Plagl2*) might change the compositional properties of CMs, hence causing their accumulation in the lamina propria due to their inability to pass through the lacteals. The *Plagl2*$^{-/-}$ mice are capable of releasing a small fraction of CM into the circulation that cannot be adequately taken up by peripheral organs, inevitably leading to fat malabsorption and neonatal death (Van Dyck, Braem et al. 2007).

Therefore, size exclusion is not the only factor impacting the CM passage from the lamina propria to the lacteals and it seems to be dependent on more complex and dynamic mechanisms. Nitric oxide (NO) – dependent modulation of intestinal blood flow and vasodilation coordinated by neural signals upon glucose ingestion, as well as alterations in the level of supplied oxygen to the enterocytes are also considered potent regulators of CM mobilization (Xiao, Stahel et al. 2018).

Additionally, vascular endothelial growth factor A (VEGF-A) seems to significantly contribute to the CM drainage into the lacteals. Increased activation of the VEGF-A/VEGFR2 signalling axis modifies the pattern of the junctions between the intestinal blood endothelial cells (ECs) and the lymphatic endothelial cells (LECs) from an open state (button) to a close state (zipper), eventually blocking the CM movement into the lymphatic capillaries (Zhang and Zarkada 2018). The role of VEGF-C/VEGFR3 has been highlighed in the process of intestinal lipid absorption and mobilization, as well. Mice lacking *Vegfc* exhibit severe atrophy of the intestinal lymphatic vessel and elevated contents of cholesterol and fatty acids in the feces, thereafter inducing defective dietary fat absorption (Nurmi, Saharinen et al. 2015). Likewise, mice carrying an inactivating mutation of the tyrosine kinase motif of the VEGFR3 (Chy mice), present increased TAG content within their enterocytes, while diminished levels of TAGs in the plasma, impacting their transport to peripheral tissues (Shew, Wolins et al. 2018).

Other studies have demonstrated that constant remodelling and regeneration of intestinal lymphatics, which is controled by Notch signaling through Notch ligand delta-like protein 4 (DLL4), as well as adrenomedullin signaling via calcitonin receptor-like receptor (CLR) highly impact dietary fat absorption. In particular, inducible ablation of *Dll4* in lacteals markedly affect their length and adherent junction plasticity, hence distorting the efficient CM uptake and transport (Bernier-Latmani, Cisarovsky et al. 2015).

Similarly, mice lacking lymphatic *Calcrl* exhibit dilated lacteals due to increased storage of lipids within the submucosal area or the centre of the villus, compromising lymphatic vasculature integrity and ineluctably CM handling in the intestine (Davis, Kechele et al. 2017). Lastly, intestinal lipid drainage is immensely dictated by the flow of lymph in the lymphatic vessel of the intestine to the circulation through an active pumping force by lacteal smooth muscle cell contractions (Xiao, Stahel et al. 2018, Cifarelli and Eichmann 2019, Xiao, Stahel et al. 2020).

1.6.1.6. Uptake of chylomicrons and other lipoproteins by peripheral tissues and its clearance from the circulation

The newly formed mature CMs delivered in the systemic circulation, obtain three additional apolipoproteins; ApoC-II, ApoC-III and ApoE from circulating high density lipoprotein (HDL). As the CMs move across the capillaries, they are processed by lipoprotein lipase (LPL), which hydrolyzes TAGs to distribute fatty acids and glycerol to the peripheral tissues. Parenchymal cells of the myocardium, skeletal muscle and adipocytes are responsible for the synthesis of LPL, which is expelled out of these cells and moved to the luminal surface of the endothelial cells. Transport, stabilization and tethering of LPL to the capillary endothelium is facilitated by lipase maturation factor 1 (LMF1) and glycosylphosphatidylinisitol anchored high density lipoprotein binding protein 1 (GPIHBP1). LPL is activated with the aid of the co-factor ApoC-II and enhanced by ApoA-V, while inhibited via ApoC-III. LPL activity is further regulated by angiopoietin-like protein 3 (ANGPTL3) and 4 (ANGPTL4), as well as insulin. FFAs that liberated by LPL-mediated hydrolysis of TAGs contained within CMs either enter muscle cells in order to be oxidized for energy production or taken up by adipose tissue for re-esterification into TAGs and subsequent storage, whereas glycerol mainly ends up in the liver. Additionally, another fate of the released FFAs is the non-esterified fatty acids (NEFAs) pool through the spillover pathway. NEFAs can be subsequently absorbed by the liver or other peripheral tissues (Lambert and Parks 2012). Delipidation of CMs and removal of ApoA and ApoC promotes their size reduction leading to smaller, functionally-devoid particles, named as chylomicron remnants. However, deattachment of ApoC-II prevents LPL activation, ultimately impeding further breakdown of TAGs. ApoA and ApoC become parts of other lipoproteins, such as high-density lipoprotein (HDL). Chylomicron remnants are enriched on ApoE and ApoB48 and mostly composed of CEs. With the help of ApoE, that constitutes the ligand recognized by the LDL receptor or the LDL receptor-related protein

1 (LRP1), and the hepatic lipase, which degrades membrane phospholipids, CM remnants bind to the surface of hepatocytes via heparan sulphate proteoglycans (HSPG) and get internalized. Inside the liver, remnant CMs are degraded by the lysosomes in order to be recycled. Therefore, liver takes up CM remnants, resulting in its clearance from the circulation. The transport of dietary lipids in the form of CMs from the intestine to the peripheral tissues, including liver, muscles and adipose tissues is known as exogenous lipoprotein pathway (Masuda and Yamashita 2017), (Julve, Martín-Campos et al. 2016).

The liver is the primary organ for very low-density lipoprotein (VLDL) production. A nascent VLDL particle is enriched in TAGs and CEs and composed of ApoB-100. Similarly to intestinal ApoB-48, lipidation of ApoB-100 in the liver is facilitated by MTP. VLDLs are secreted from the hepatocytes and momentarily associate with circulating HDL to acquire ApoC-II and ApoE. LPL breaks down the TAGs contained within the VLDLs, leading to the release of FFAs and glycerol and subsequently the generation of VLDL remnants, named as intermediate density lipoproteins (IDL). IDL particles interact with LDL or LRP1 receptor via ApoE, hence partially taken up by the liver. Transfer of ApoE to the circulating HDL and hydrolysis of the remaining TAG content within IDL by hepatic lipase give rise to LDL particles, which largely comprise of CEs. LDL particles removal from the circulation is predominantly mediated by the liver and in a lesser extent by other extrahepatic tissues. LDL clearance is dictated by the activity of the hepatic LDL receptors that strongly affected by the levels of cholesterol in the hepatocyte. The delivery of the lipids synthesized in the liver into the peripheral extrahepatic tissues is considered as the endogenous lipoprotein pathway (Dallinga-Thie, Franssen et al. 2010, Tiwari and Siddiqi 2012).

Circulating HDL particles are largely involved in the reverse cholesterol pathway. The essential, structural protein of HDL is the Apo-AI, which is produced primarily by the liver and partly by the intestine. Apo-AI moves into the bloodstream and picks up free cholesterol. The immature nascent HDL particle receives free cholesterol either from enterocytes, hepatic and extrahepatic cells via the ATP-binding cassette transporter (ABCA1), whose expression is highly regulated by liver X receptor (LXR) agonists or from circulating CMs, VLDLs and LDLs. Initially, these particles show a disk-like shape due to the unesterified form of cholesterol. However, conversion of free cholesterol to CEs is achieved by LCAT enzyme and co-factor Apo-AI, promoting the maturation of the HDL particle and its shape modification into a more spherical one. Mature HDL can further exchange cholesterol for TAGs via the cholesteryl ester transfer protein (CETP) from ApoB-containing lipoproteins. The slightly altered HDL is able to bind to the surface receptor SR-BI and selectively transfer the cholesterol into the liver, whereas TAGs can also be absorbed by the liver via the activity of hepatic lipase. Finally, the remnant HDL is filtered by the glomeruli in the kidneys to ultimately recycle the Apo-AI (Ben-Aicha, Badimon et al. 2020). Besides HDL, cholesterol (free and esterified) is additionally secreted with ApoB-containing CMs. However, combined intestinal-specific deletion of MTP with global ACAT2 ablation diminished secretion of cholesterol in both CMs and HDL particles, suggesting that they do not rely on the same cholesterol pool for their formation. Therefore, circulating HDLs are not able to utilize accumulated free cholesterol upon depletion of both ACAT2 and MTP. Similarly, simultaneous intestinal MTP and ABCA1 deficiency markedly decreased the cholesterol absorption and secretion, proposing a synergistic effect of CM and HDL pathway in this process (Iqbal, Boutjdir et al. 2014)

1.6.2. Cytoplasmic lipid droplets (CLDs)

1.6.2.1. Cytoplasmic lipid droplet synthesis, growth and functions

Cytoplasmic lipid droplets (CLDs) are constituted of a hydrophobic core mainly composed of TAGs and CEs, coated by a polar phospholipid monolayer studded with a variety of associated proteins that control synthesis and catabolism of CLDs. The prevailing model of LD biogenesis is considered to be the ER budding. Accumulation of newly formed TAGs within the inner and outer leaflets of the ER bilayer membrane drives the budding of the nascent LDs with PL monolayer synthesized by the cytosolic ER membrane leaflet. In any cell type, the emergence of the LDs into the cytosol to give rise to CLDs is a unidirectional, tightly controlled process affected by altered ER membrane surface tension owing to assymetrical phospholipid composition and recruitment and binding of CLD-related proteins (Olzmann and Carvalho 2019). Upon budding, growth of CLDs is mediated by two mechanisms; fusion of smaller CLDs or expansion of existing CLDs through increased synthesis of TAGs on the surface of CLDs. Local TAG synthesis is facilitated via ER-LD bridges that allow relocalization of TAG synthesis enzymes from the ER to LDs and newly formed PC, as the most abundant PL required for LD monolayer (Wilfling, Haas et al. 2014). In sharp contrast to the other cell types, nascent LDs are capable of budding off not only into the cytosol, but also into the ER lumen for the generation of luminal LDs (LLDs), subsequently utilized for CM assembly in both enterocytes and hepatocytes (Beilstein, Carrière et al. 2016). A recent study has revealed that DGAT1 and DGAT2 exhibit non-redundant functions in the regulation of dietary fat absorption by directing ER-budded TAGs towards subcellular pools in the enterocytes. In particular, DGAT1 mainly facilitates synthesis of TAGs destined for ApoB-free LLDs, whereas DGAT2 favors distribution of TAGs both in ApoB-containing CMs and CLDs (Hung, Carreiro et al. 2017).

After a fat-rich meal, ingested lipids are stored as CLDs for up to 12 hours in murine jejenal enterocytes (Zhu, Lee et al. 2009). Interestingly, in human gut almost 10-12% of TAGs derived from previous meals are incorporated into new CMs within a time frame of 20 minutes upon the consumption of a second meal, while the enteric lipid pool is able to serve CM appearance and secretion for up to 16 hours following the last fat intake (Chavez-Jauregui, Mattes et al. 2010). The small intestine purposefully keep this regulatory pool of TAGs within CLDs in intracellular spaces or preformed lipoprotein particles in extracellular spaces for prolonged periods of time. The potential benefits might be to either avoid the exposure of the enterocytes to toxic free FA or prevent the deleterious attack of the extraintestinal tissues with a high amount of postprandial plasma TAGs. The small intestine ultimately promote mobilization and packaging of the reserved lipids into CM particles in response to multiple stimuli to ensure stable supply of the organs with fat between the meals (Xiao, Stahel et al. 2018). Due to their hydrophobic environment, CLDs can additionally retain xenobiotic compounds and hydrophilic vitamins beyond lipid storage. Moreover, cyclooxygenase-2 (COX2), that mediates synthesis of proinflammatory eicosanoids, including leukotrienes and prostaglandins, resides on the CLDs in enterocytes, strongly indicating that CLDs might serve as site for initiation of lipid-mediated inflammatory signaling pathways (Beilstein, Carrière et al. 2016).

1.6.2.2. Cytoplasmic lipid droplet associated proteins in enterocytes

A distinct set of proteins that are closely associated with CLDs have been identified to modulate both CLD storage and mobilization. The perilipins (PLIN), PLIN2 or adipocyte related protein (ADRP) or adipophilin, as well as PLIN3 or alternatively named as Tip47, are among the most predominant CLD-associated proteins in the intestine. PLIN3 is found attached on the CLDs only after challenging with an acute fat bolus, while is solely localized in the cytosol during fasting, suggesting that PLIN3 is related with transient storage of lipids. On the other hand, PLIN2 is preferentially associated with prolonged lipid storage, considering that it is constitutively present on the CLDs under conditions of chronic high-fat feeding (Lee, Zhu et al. 2009). Ablation of PLIN2 in mice markedly diminished detrimental long-term effects of high-fat feeding and attenuates diet-induced obesity. In addition, whole body *Plin2*-knockout mice display reduced number of accumulated intestinal CLDs, increased excretion of TAGs in their feces while the composition and biodiversity of microbial communities was largely affected upon feeding with either HF or LF diet (Frank, Bales et al. 2015).

Cell death inducing DFFA-like effector B (CIDEB) has a dual localization to both CLDs and ER and indirectly influences CLD storage by promoting TAGs mobilization towards CM assembly. Mice lacking *Cideb* exhibit greatly abrogated intestinal secretion of TAGs, smaller CM particles and fat-laden enterocytes (Zhang, Wang et al. 2014).

Furthermore, the milk fat globule epidermal growth factor–like 8 (MFGE8) has been linked to CLD metabolism. Mfge8 interacts with αvβ3 and αvβ5 integrins to trigger a PI3 kinase/mTORC2/PKCζ–dependent pathway and boost TG hydrolase activity. Therefore, augmented CLD hydrolysis liberates FFAs that used as substrates for CM synthesis upon acute or chronic fat challenge. Mice lacking *Mfge8* or the αvβ3 and αvβ5 integrins show perturbed hydrolase activity, hence resulting in excessive TAGs stored within CLDs in enterocytes (Khalifeh-Soltani, Gupta et al. 2016).

Lastly, ablation of transmembrane 6 superfamily member 2 (TM6SF2) in a zebrafish model leads to enhanced hepatic and intestinal CLD accumulation and disturbed dietary fat clearance after HFD. Similarly, CLD accumulation was apparent upon silencing *TM6SF2* in human Caco-2 cells, overall suggesting its function as potential promoter of CLD mobilization (O'Hare, Yang et al. 2017).

1.6.3. Catabolism of cytoplasmic lipid droplets in enterocytes

Lipolysis is the enzymatic process that involves hydrolysis of ester bonds of TAGs, CEs and PLs to release FFAs. Gastrointestinal lipolysis assists dietary fat absorption by the intestine, intravascular lipolysis accounts of the breakdown of circulating TAG-rich plasma lipoproteins (VLDLs and CMs) to supply parenchymal organs with FFAs, whereas intracellular lipolysis enables liberation of FFAs and glycerol from stored CLDs. Thus, hydrolysis of TAGs generates glycerol and FAs, while hydrolysis of CEs and PLs yields free cholesterol and FAs, as well as lysophospholipid and FAs respectively. In enterocytes, CLD catabolism is orchestrated by either cytoplasmic TAG lipolysis or a form of macroautophagy described as lipophagy and thoroughly control quantity and rate of dietary fat absorption (D'Aquila, Hung et al. 2016, Zechner, Madeo et al. 2017).

1.6.3.1. Cytoplasmic TAG lipolysis

Cytoplasmic hydrolysis is initiated with the hydrolysis of TAG into DAG and FA via adipose triglyceride lipase (ATGL), encoded by patatin-like phospholipase domain containing 2 (*PNPLA2*) gene, with the aid of its co-activator comparative gene identification-58 (CGI-58). Complete loss of ATGL in mice strongly affects lipolysis that contributes to massive TAG deposition in many tissues, as well as enterocytes rendering the mice susceptible to obesity. Likewise, intestinal specific deletion of ATGL in mice fed with chow or high-fat diet leads to enhanced TAG accumulation in the proximal enterocytes and delayed absorption of cholesterol, while the secretion rate of TAGs was comparable to the control mice (Haemmerle, Lass et al. 2006). This observation from the *iAtgl*-deficient mice together with the downregulation of peroxisome proliferator a (PPARa) target gene expression involved in fatty acid oxidation (FAO), propose that ATGL is not directly implicated in the TAG release into the circulation via CM particles (Obrowsky, Chandak et al. 2013). In sharp contrast, despite the excessive TAG storage within CLDs in mice specifically lacking *Cgi-58* in the intestine, *iCgi-58*-deficient mice display significant fat malabsorption, indicated by steatorrhea and lower levels of TAGs in the circulation upon feeding and diminished intestinal FAO, proposing that CGI-58 is indispensable for CM production in a ATGL-independent manner. In humans, loss of CGI-58 is related to the development of the Chanarin-Dorfman Syndrome, which is manifested by unusual deposition of CLDs in liver, skin, intestine and leukocytes (Lass, Zimmermann et al. 2006). According to a recent publication, intestinal ATGL and CGI-58 are responsible for the catabolism of basolaterally-derived lipids and not the alimentary ones. Mice with double deletion of ATGL and CGI-58 specifically in the intestine do not exhibit impaired apical lipid absorption and CM synthesis. In addition, iDKO mice present enhanced intracellular CLD accumulation 2 hours upon administration of the oral lipid load, but not in the early phase of dietary lipid absorption and low-fat feeding is not sufficient to diminish the CLD presence, postulating a basolateral origin of those lipids (Korbelius, Vujic et al. 2019).

The second step of TAG hydrolysis is facilitated by the hormone sensitive lipase (HSL), encoded by *LIPE* gene, and generates MAG and FA from DAG. Mice with intestinal specific ablation of HSL present with increased levels of CEs, whereas the rest of the lipid species, including TAGs were not markedly affected. While TAG secretion is not impaired in *iHSL*-deficient mice, a total reduction in the cholesterol biosynthesis was observed, indicating that HSL might not be necessary for TAG metabolism, but essential for cholesterol metabolism instead (Obrowsky, Chandak et al. 2012).

At the final step, MAG is hydrolyzed into glycerol and FA through monoacylglycerol lipase (MGL), encoded by *MGLL* gene. Mice with complete absence of MGL appeared leaner compared to control mice upon LFD with alleviated insulin and glucose sensitivity, whereas postprandial lipemia was greatly attenuated after challenge with HFD. MGL$^{-/-}$ mice show augmented MAG species in the small intestine and considerably delayed fat absorption (Douglass, Zhou et al. 2015). Transgenic mice with overexpression of MGL in the intestine developed an obese phenotype, characterized by a whole body energy imbalance and elevated plasma and hepatic TAGs when fed with HFD (Chon, Douglass et al. 2012).

1.6.3.2. Lipophagy

Lipophagy is a subtype of macroautophagy, which involves the degradation of CLDs mediated by lysosomal acid lipase (LAL). In particular, small CLDs or parts of larger CLDs are initially recruited and engulfed by LC3-II-positive phagophores. Lipoautophagosome carrying CLD cargo subsequently fuses with late endosomes or lysosomes to give rise to autolysosomes. LAL performs hydrolysis of TAGs and CEs into glycerol, cholesterol and FAs within the optimal pH 4.5 – 5 of the autolysosome. However, lysosomes can directly interact with “primed” CLDs via a Ras-related protein called Rab7a, ultimately releasing non-esterified FAs in the cytosol (Zechner, Madeo et al. 2017). In human, total loss of LAL is associated with Wolman syndrome, whereas partial loss of LAL leads to CE storage disease. Patients with Wolman syndrome show excessive TAGs and CEs accumulation both in their liver and intestine, thus suffering from malabsorption and diarrhea (Ko, Qu et al. 2020). Analogously, total depletion of LAL in mice contributed to an identical phenotype to the one observed in patients, accompanied with a complete loss of white and brown adipose tissue, that eventually decreased the lifespan of those mice (Du, Heur et al. 2001).

1.7. Metabolic fates of fatty acids in enterocytes

Fatty acids taken up by the apical or basolateral side of the enterocytes or released from catabolism of CLDs can be re-esterified for lipoprotein synthesis or mebrane biogenesis, oxidized via mitochondrial beta-oxidation or function as signalling molecules. It has been initially described that the metabolic destiny of the FAs in the enterocytes is determined by the site of entry in mice and rats. In particular, apically absorbed lipids mostly constitute CLDs and contribute to the CM assembly. On the other hand, basolateral lipids derived from the circulation, including hepatic – VLDLs, CM remnants and FFAs from white adipose tissue (WAT) or vascular lipolysis, can be also taken up by the enterocytes but preferentially directed for β-oxidation, ketogenesis and phospholipid synthesis (Storch, Zhou et al. 2008). Binding specificity of FABP1 and FABP2 highly orchestrate the partioning of intestinal fatty acids among secretory or oxidative pathways. FABP1 leads FAs to the oxidative route, whereas FABP2 preferentially guides FAs towards TAG synthesis (Lagakos, Gajda et al. 2011). Additionally, organelle compartmentation might be considered as a crucial regulator of the differential metabolic fate of the FAs, since ER is located in close proximity to the apical side of the enterocyte, whereas mitochondria are predominantly abundant at the basolateral membrane (Korbelius, Vujic et al. 2019). These findings highlight the presence of two distinctly dynamic storage pools of CLDs within the enterocytes and the existance of a lipid secretion/re-uptake cycle (Figure 13).

Another publication has shown that intestinal FAO is primarily activated upon ingestion of high dietary fats, despite the fact that FAs are not the preferable fuel source of enterocytes. A plausible explanation for the induction of FAO would be to fulfill the increased energetic demands of the enterocytes for facilitating absorption of large lipid quantities (Kondo, Minegishi et al. 2006). FAO can be mediated by polyunsaturated FAs (PUFAs) via activation of the transcription factor PPARa. Intestinal – specific PPARa activation enhanced FAO, but markedly eliminated TAG storage within CLDs and ultimately available substrates for CM secretion (D'Aquila, Hung et al. 2016).

Surprisingly, a recent study focused on mice with overexpression of the human apolipoprotein C-III (ApoC-III) underlined a notable decline in the CM secretion due to blockage of the basolateral lipid substrate transport (BLST) pathway. Excessive ApoC-III on the plasma TLRs impedes the uptake of TLRs via the low density lipoprotein receptor (LDLr), hence redirecting the CLDs from the chylomicron synthetic machinery to mitochondrial oxidation (Li, Rodia et al. 2019). FAs can be ligands for other transcription factors, such as liver X receptor (LXR) or hepatocyte nuclear factor alpha (HNFa) in the intestine and by PPARa activation or by trigger signalling pathways, eventually regulating intestinal homeostasis and dietary fat absorption. For instance, arachidonic acid mediates synthesis of eicosanoids via the cyclo-oxygenase pathway and promotes strong inflammatory responses in gastrointestinal mucosa (D'Aquila, Hung et al. 2016).

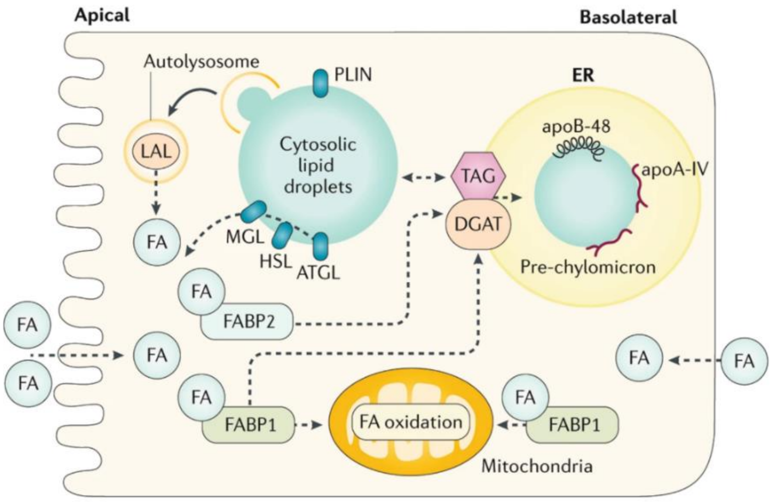

Figure 13. Intestinal lipids follow different metabolic routes depending on the site of entry

Schematic representation of the metabolic fate of fatty acids (FA) according to their entry into the enterocytes. Apically derived FA are directed towards chylomicron formation, whereas FA taken up from the basolateral side are utilized for fatty acid oxidation and phospholipid synthesis. FABP1 guides FA to oxidative pathways in contrast to FABP2 that promotes TAG synthesis. Abbreviations: LAL, lysosome acidic lipase, FABP1,2, fatty acid binding protein 1,2, TAG, triacylglycerol, DGAT, Diacylglycerol acyltransferase, PLIN, perilipin, MGL, monoacylglycerol lipase, HSL, hormone sensitive lipase, ATGL, adipocyte triglyceride lipase. Image obtained from (Ko, Qu et al. 2020)

1.8. Regulation of chylomicron production and cytoplasmic lipid droplet metabolism in enterocytes.

Numerous systemic factors that positively or negatively regulate assembly of nascent CMs or rapid release of pre-formed lipoproteins stored in the have been described so far. Oral glucose ingestion is considered to have a stimulatory effect on the mobilization of enteral pool of lipids depots. Upon consuming a high-fat liquid meal, healthy patients were subjected to oesopho-gastro-duodenoscopy (OGD), which revealed increased lipid accumulation within jejunal enterocytes and lamina propria. Oral administration of glucose solution five hours after the fat-load was sufficient to markedly diminish the retained lipid droplets and elicit a robust raise in the plasma TAGs and CM TAGs. However, ingested glucose did not have any impact on the lipid mobilization after 10 hours delayed fasting, most likely due to the lower quantities of CLDs within the enterocytes (Robertson, Parkes et al. 2003).

Untargeted proteomic analysis of the duodenal biopsies upon glucose ingestion unravelled multiple proteins being significantly altered. Predominantly, upregulation of ethanolaminephosphotransferase 1 (EPT1) and downregulation of syntaxin-binding protein 5 (STXBP5). Increased levels of EPT1, which mediates synthesis of PE, suggests potential modification in the membrane composition of the CMs that might boost their secretion. On the other hand, reduced amount of STXBP5 promotes the activity of syntaxin 5 to regulate the docking of the pre-CM to the *cis*-Golgi for maturation and secretion (Robertson, Parkes et al. 2003, Xiao, Stahel et al. 2019).

In addition, direct intraduodenal infusion of the monosacharides glucose and fructose stimulated intestinal triglyceride-rich lipoprotein (TLR) CM production in a group of healthy male patients (Xiao, Dash et al. 2013). Furthermore, intravenous infusion of either glucose or intralipid/heparin solution, which elevated plasma FFAs, could efficiently enhance CM production in human subjects, suggesting that basolateral supply of lipids might also participate in the mobilization process (Xiao, Stahel et al. 2018).

Another notable stimulus of the transient lipid storage pool is termed as “cephalic phase response” or sham feeding, which involves chewing but not swallowing of the food. A consumption of second high-fat meal that comes after a previously ingested high-fat meal is sufficient to elicit a high peak in plasma CMs. This process rapidly initiated within 10-30 min, inadequate time frame for the newly absorbed nutrients to reach the intestinal lumen, proposing movement of a pre-existing lipid pool owing to an orosensory perception of fats by activation of oral taste receptors (Chavez-Jauregui, Mattes et al. 2010).

Release of certain hormones is thought to be among the important regulatory cues of CM secretion. Gut peptides; glucagon - like peptide 1 (GLP-1) and 2 (GLP-2) are secreted from the intestinal enteroendocrine L-cells upon nutrient ingestion and differentially influence CM particle synthesis. Subcutaneous injection of GLP-2 in a group of healthy lean men that subjected to continuous intraduodenal feeding robustly enhanced the output of presynthesized ApoB48-containing CMs (Dash, Xiao et al. 2014). Similarly, GLP-2 triggered postprandial CM production in mice and hamster by augmenting mesenteric arterial blood flow via increased activity of nitric oxide (NO) (Hsieh, Trajcevski et al. 2015). Finally, GLP-2 and particularly a GLP-2 analogue named teduglutide, is considered beneficial for restoring defective nutrient absorption in patients with short bowel syndrome (Jeppesen, Pertkiewicz et al. 2012).

On the contrary, administration of GLP-1 analogue; exendein- 4 or dipeptidyl peptidase IV (DPPIV) inhibitor; sitagliptin, that are normally implemented for type 2 diabetes treatment, eliminated postprandial secretion of CMs in mice and hamsters (Hsieh, Longuet et al. 2010). In a similar way, sitagliptin attenuated postprandial lipemia by profoundly reducing ApoB-48 - containing lipoprotein particles in healthy males (Xiao, Dash et al. 2014). Acute inhibition of intestinal lipoprotein secretion and depleted levels of non-esterified fatty acids were also observed upon GLP-1 infusion in healthy male volunteers in response to a solid test meal owing to delayed emptying of the gastic content (Meier, Gethmann et al. 2006). Following studies revealed that GLP-1 might exert its inhibitory action on CM secretion by stimulating sympathetic pathways and melanocortin-4 receptors (MC4Rs) (Farr, Taher et al. 2016). Besides GLP-1, pancreatic hormone insulin robustly suppressed intestinal ApoB48 and hepatic ApoB100-containing lipoproteines in healthy humans under continuous fed state by partial reduction of circulating FFA (Pavlic, Xiao et al. 2010). Moreover, administration of high doses of polyphenol resveratrol in obese men, as well as bariatric surgery was associated with an remarkable decline in the production rates of TLR ApoB-48 and ApoB-100 (Dash, Xiao et al. 2015).

Emerging evidences have indicated that the expression of numerous proteins, including ApoB, ApoA-IV, and MTP governed by circadian rythms and exhibit diurnal variation that affects intestinal lipid absorption. It has been shown that deficiency of ApoAIV in mice diminished the levels of plasma TAGs at night and upon food administration during the day, most likely by controling the binding of the transcription factors forkhead box protein A2 and O1 (FOXA2 and FOXO1) on the *Mttp* promoter. Thus, ApoAIV strongly affect the expresion of MTP to assist packaging and secretion of lipoproteins by the intestine (Pan, Munshi et al. 2013).

Several studies have emphasized on the connection between intestinal microbiota diversity/abundance and response to the dietary lipids by the host. Germ-free mice fed with a HF diet did not develop obesity, owing to profoundly defective lipid absorption and digestion, enhanced intestinal FAO and increased TAGs in the stool. In addition, transplantation of jejunal microbiota from HFD-fed and not from LFD-fed conventional mice to germ-free mice was sufficient to augment lipid absorption (Martinez-Guryn, Hubert et al. 2018). Disturbance of the gut flora by antibiotic administration in rats completely abolished the activation of intestinal mucosal mast cells (MMCs), that release histamine and mast-cell protease II, subsequently decreasing gut permeability and lymph flow in response to dietary fats. Therefore, those rats exhibited dramatically blunted lipid absorption and CM secretion, accompanied by eliminated output of ApoB48, ApoA-I and ApoA-IV in the lymph (Sato, Zhang et al. 2016).

Intestinal lipid metabolism and dynamics of CLDs can be regulated via Hedhehog (Hh) signaling, which is essential for the development of the gastrointestinal tract. In utero or postnatal administration of an anti-hh monoclonal antibody severe fat malabsorption concomitant with fatty stool and enterocytes massively stuffed with CLDs. Despite the unaltered levels of MTP or ApoB, reduced reduced levels of Apo-AIV in the plasma might also indicate impaired CM secretion (Wang, Nassir et al. 2002).

Lastly, there are other described factors including superoxide dismutase 1 (SOD1), carboxylesterase 1 (CES1) and proprotein convertase subtisilin/kexin type 9 (PCSK9) that impact intestinal lipid absorption and secretion, as revealed by *in vivo* studies. Mice lacking the scavenger of superoxide radicals, SOD1 display enterocytes loaded with CLDs and decreased MTP activity and postprandial plasma TAGs upon challenging with high-fat feeding (Kurahashi, Konno et al. 2012). On the other hand, mice deficient in the hydrolase CES1 are severely hyperlipidemic, since CM clearance from the circulation is significantly delayed, owing to their irregular size and composition (Quiroga, Lian et al. 2012). Oppositely, ablation of PCSK9 in mice, which naturally inhibits LDL receptor, is related to secretion of larger CMs that can be cleared at a faster rate from the circulation, attenuating postprandial lipemia (Le May, Kourimate et al. 2009).

Taken together, numerous determinants including nutrition, microbiota, hormones, circulating components, circadian rhythms, transcription factors and signaling pathways that substantially regulate CM production and secretion, as well as CLD metabolism in the intestine.

1.9. Mitochondria dysfunction is closely associated with the pathophysiology of the Inflammatory Bowel Diseases (IBDs)

Mitochondrial dysfunction has been linked to ageing and a steadily increasing number of human diseases (Trifunovic and Larsson 2008). Previous research findings presented evidence of an association between the perturbation of mitochondrial function and the pathophysiology of multifactorial, idiopathic conditions of the gastrointestinal tract, with increasing prevalence in the developing world, known as Inflammatory Bowel Diseases (IBD). Ulcerative colitis (UC) and Crohn’s disease (CD) that fall under the IBD spectrum, predominantly manifested by chronic or relapsing gastrointestinal inflammation. In particular, under inflammatory conditions of IBDs production of mucus and antimicrobial peptides are reduced, rendering the intestinal epithelium susceptible to the luminal antigens (Indriolo, Greco et al. 2011, Khor, Gardet et al. 2011).

Interestingly, markedly diminished activity of the mitochondrial respiratory chain complexes, CII, CIII and CIV have been frequently descibed both in the mucosal biopsies derived from UC patients compared to healthy individuals and experimental mouse model of dextran sulfate sodium (DSS) - induced colitis (Sifroni, Damiani et al. 2010, Santhanam, Rajamanickam et al. 2012). Recent studies have demonstrated that ablation of methylation-controlled J protein (MCJ) that endogenously inhibits complex I activity, aggravated murine experimental colitis by enhancing the release of proinflammatory cytokines, such as *Il1b* involved in the intestinal permeability and via alterations in the microbiota composition and bile acid production (Pascual-Itoiz, Peña-Cearra et al. 2020).

Moreover, structurally abnormal mitochondria, swollen with irregular cristae, and reduced expression of mitochondrial proteins were detected in the colonic mucosa of UC patients (Hsieh, Shih et al. 2006). Damaged mitochondria with defects in the respiratory chain activity lead to decreased levels of ATP generation as well as a build-up of cellular ROS. Aberrant accumulation of ROS and RNS (reactive oxygen and nitrogen species, respectively), occurred due to inability of the cell to efficiently detoxify them with the assistance of antioxidant enzymes, such as catalase, glutathione peroxidase as well as superoxide dismutase. This results in increased mtDNA damage and lipid peroxidation, which could trigger NLRP3 inflammasome activation, rendering the intestinal epithelium permeable to bacteria and luminal antigens and triggering intestinal inflammation (Gillespie, Pastukh et al. 2009, Lee and Hüttemann 2014). Indeed, DSS-induced colitis was highly ameliorated in mice treated with MitoQ, a mitochondrial ROS scavenger via blocking activation of the NLRP3 inflammasome and subsequent maturation of IL-1b and IL-18 (Dashdorj, Jyothi et al. 2013). Likewise, mice deficient in the multidrug resistance-1 (*MDR1*), which is an efflux transporter highly dependent on ATP, shown an accumulation of perturbed mitochondria and boosted mtROS generation that accelerated colitis. Interestigly, administration of MitoQ in *Mdr1*-deficient mice effectively weaken the development of colitis (Ho, Aird et al. 2018). Remarkably, strains of conplastic mice that exhibited enhanced levels of OXPHOS and ATP, displayed augmented epithelial regenerative potential and less susceptibility to DSS or TNBS (trinitrobenzene sulfonate) - associated colitis (Bär, Bochmann et al. 2013). Another study has unveiled diminished activity of complex I and complex IV in human IBD colon, while colonocytes with depleted mtDNA (ρ^0 cells) triggered TNF-a-induced expression of IL-8 in an AMP-activated protein kinase (AMPKa2) – dependent manner (Heller, Penrose et al. 2017). It has been well – described that colonic epithelial cells rely on short chain fatty acid (SCFA) butyrate as their main source of energy. Notably, patients with UC revealed 80% reduction in the activity of mitochondrial acetoacetyl CoA thiolase, a crucial enzyme for catalyzing butyrate oxidation, presumably due to high mtROS production (Santhanam, Venkatraman et al. 2007).

The preservation of tight junction integrity, which is critical for the gut barrier, is a highly energy - demanding process. Compromized integrity results in increased bacterial translocation and immune cell infiltration and it has been correlated to impaired mitochondrial function (Novak and Mollen 2015). Loss of an intestinal – released mucin, named as mucin 2 (*Muc2*), results in spontaneous colitis. *Muc2*-deficient mice remarkably present with unhealthy mitochondria, depleted ATP content and significantly diminished oxygen consumption rates (OCR) (Borisova, Achasova et al. 2020). Moreover, disruption in mitochondrial biogenesis and bioenergetics in mice upon ablation of PGC-1a dramatically disturbed the intestinal barrier, ultimately exacerbating DSS-induced colitis and intestinal inflammation (Cunningham, Vincent et al. 2016). Impaired colonic differentiation of the Goblet cells and mucus production and has been recently described in patients with remissing UC with the defects being driven by the mitochondrial protein p32, which maintains proper OXPHOS activity. In a similar manner, following mutation of ATP8, a subunit of the mitochondrial ATP synthase, mice displayed reduced levels of p32, mitochondria impairment and malfunctioning Goblet cells, imbalancies that have been restored upon switching to a low glucose nutritional intervention (Sünderhauf, Hicken et al. 2021).

Activation of the mitochondrial unfolded protein response (UPR^{mt}), that promotes the recovery of mitochondrial proteostasis upon strong mitochondrial dysfunction via activation of mitochondrial proteases and chaperones, has been implicated in the pathogenesis of IBDs. In particular, it has been previously demonstrated that IEC – specific deletion of activating transcription factor 4 (ATF4) in mice resulted in spontaneous enterocolitis accompanied by suppressed expression of antimicrobial peptides from ileal PCs and the glutamine transporter, solute carrier family 1 member 5 (SLC1A5), eventually infuencing the glutamine uptake from the intestine (Hu, Deng et al. 2019).

Previous studies proposed the active involvement of prohibitin 1 (PHB1) in the pathogenesis of IBDs. PHB1 resides at the IMM and implicated in the proper assembly of the ETC. Strikingly, patients suffering from active IBD shown lessened levels of PHB1, whereas overexpression of PHB1 in mice eliminated oxidative stress and ameliorated DSS-induced colitis (Theiss, Vijay-Kumar et al. 2009). Later studies have demonstrated that PHB1 associates with the phosphorylated at serine 727 (S727) signal transducer and activator of transcription 3 (Stat3), hence impeding mitochondrial perturbations in the intestinal epithelium (Han, Yu et al. 2014). Consistently, mice deficient in PHB1 specifically in IECs (*Phb*$^{i\Delta IEC}$) presented with mitochondrial dysfunction and Opa1 upregulation that subsequently resulted in considerable alterations in the phenotype of the Paneth cells and in the development of spontaneous ileitis (Jackson, Panopoulos et al. 2020). Collectively, these discoveries desipher the undoubted link between mitochondria function and the progression of IBDs. The above-mentioned studies indicate that IBD therapies should focus on mitochondria. Precise manipulation of mitochondria either by boosting the mitochondrial respiration or via abolishing the mtROS and oxidative stress paving the way for promising interventions.

1.10. Mitochondria play an indisputable role in the maintenance of intestinal epithelial homeostasis

Several studies have supported the crucial role of mitochondrial function in the maintenance of intestinal stemness and homeostasis in mice. According to their position along the crypt-villus axis, IECs exhibit distinct metabolic profiles to fulfil their energetic needs. Glycolysis is the preferable pathway of stem cells located at the bottom of the crypts for ATP production, whereas differentiated cells strongly rely on OXPHOS and a fully functional respiratory chain (Cho, Kwon et al. 2006, Tormos, Anso et al. 2011). It has been previously shown that PCs boost ISC proliferation by augmenting synthesis of NAD+ and thus upregulating the activity of NAD+ - dependent protein deacetylase SIRT1 and mammalian target of rapamycin complex 1 (mTORC1) signalling in the neighbouring ISCs under conditions of caloric restriction (CR) (Igarashi and Guarente 2016). Another study has revealed that PCs sustain ISC renewal by fuelling them with lactate. Lgr5+ CBCs strongly depend on mitochondrial activity, whereas PCs undergo glycolysis to produce lactate. Lactate is eventually converted to pyruvate, which functions as the substrate for mitochondrial OXPHOS in the Lgr5+ CBCs. Finally, enhanced OXPHOS triggers activation of p38 MAPK signalling through ROS that ultimately promote differentiation (Rodriguez-Colman, Schewe et al. 2017). Lastly, aged PCs impair regenerative potential of the intestinal epithelium via the generation of Notum, an inhibitor of Wnt signaling. Increased mTORC1 signaling in aged PCs blocks PPAR-α activity, thereby elevating Notum expression and hindering stemness (Pentinmikko, Iqbal et al. 2019). Additionally, IEC-specific ablation of heat shock protein 60 (HSP60) triggered CHOP - independent UPR^{mt} activation, resulting in defective mitochondrial respiration accompanied by considerably impaired IEC proliferation and stemness (Berger, Rath et al. 2016). Likewise, loss of HSP60 specifically in ISCs drives notable disturbance of mitochondria functionality that severely impacts ISC niche and expression of *Lgr5* in the intestinal cryps, ultimately conferring to the differentiation towards aberrant, degranulated Paneth cells (Khaloian and Rath 2020).

1.11. Aim of the project

To date, there is a significant gain of knowledge on the crucial role of mitochondria in the pathophysiology of Inflammatory Bowel Diseases and several emerging studies aim to fully elucidate the connection between mitochondria function and maintenance of intestinal epithelial homeostasis. However, the role of mitochondria in regulating nutrient absorption and transport by enterocytes remains poorly understood. This study aims to shed some light on how mitochondria are implicated in the processing and transport of dietary lipids by the intestine, which is relevant for the better understanding of the mechanisms causing severe gastrointestinal complications and particularly malabsorption and failure to thrive in some patients with mitochondrial diseases.

2. Materials and Methods

2.1. Materials

The chemicals and reagents used in this study were purchased from the indicated suppliers with the provided catalog numbers and described in Table 1. Buffers and solutions described in the Table 2 were prepared with double-distilled water (ddH_20). The kits used in the study are presented in the Table 3.

Table 1 Reagents and Chemicals used in this study.

Reagents & Chemicals	Company (Catalog number)
Acetic acid	VWR (36289.AE)
Acetone	AppliChem (161007)
Acetonitrile 99% LC-MS grade	Thermo Fisher Scientific (51101)
Acrylamid/Bis solution	Serva (10688.01)
Agarose ultra-pure	Biozym (840004)
Ammonium persulphate (APS)	Sigma Aldrich (A3678-100G)
Albumin from bovine serum (BSA)	Biorad (500-0006)
Aquatex (aqueous mounting agent)	Sigma Aldrich (108562)
β-mercaptoethanol	Sigma Aldrich (M7522)
Bromophenol blue	Merck (B5525)
Bradford reagent	Merck (B6916)
Catalase from bovine liver	Sigma Aldrich (C9322)
Chloroform	VWR (22711290)
cOmplete^{TM} Mini Protease Inhibitor Cocktail Tablets	Sigma Aldrich (4693124001)
Coomassie Brilliant Blue R-250	Merck (B7920)
Corn oil	Sigma Aldrich (C8267)
Cytochrome C from bovine heart	Sigma Aldrich (C2506)
DAPI (4',6-Diamidin-2-phenylindol, Dihydrochlorid)	Thermo Fisher Scientific (D1306)
Deoxynucleotides (dNTPs)	Invitrogen (10297-117)
3,3′-Diaminobenzidine tetrahydrochloride hydrate (DAB)	Sigma Aldrich (D9015)
Digitonin, high purity	MERCK (300410)
Dimethyl sulfoxide (DMSO)	AppliChem (A3672,0050)
Dithiothreitol (DTT)	VWR (A2948-0025)
Dodecyl-β-maltosicyl (DDM)	Roth (CN26.2)
Dulbecco's phosphate-buffered saline (DPBS)	Gibco (14190144)
ECL Western Blot detection reagent	GE Healthcare (RPN2132)
ECL Western Blot detection reagent	Thermo Fisher Scientific (34095)
Entellan	Merck Millipore (107960)
Eosin solution	Sigma Aldrich (1098442500)
Ethanol absolute	AnalR Normapur (20821-321)

Ethidium bromide 0.025%	Carl Roth (HP47.2)
Ethylenediaminetetraacetic acid (EDTA)	JT-Baker (8993-01)
Ethylene-bis(oxyethylenenitrilo)tetraacetic acid (EGTA)	MERCK (E3889)
Fluoromount-G	Southern Biotech (0100-01)
GoTaq® qPCR Master Mix	Promega (A6001)
Glycerol	VWR (24386-298)
Glycine	VWR (101196X)
Hematoxylin, Mayer’s	Sigma Aldrich (MHS32)
4-2-hydroxyethyl-1-piperazineethanesulfonicacid (HEPES)	Thermo Fisher Scientific (15630-056)
Hydrogen Peroxide (H2O2) 30%	MERCK (1072090250)
Hydrochloric acid (HCl) 37%	AppliChem (A2427-2500)
Isopropanol (2-Propanol)	AppliChem (A3928)
LysC (Lysyl Endopeptidase, Mass Spectrometry Grade)	Wako Chemicals USA (121-05063)
Methanol	Sigma Aldrich (494437)
Magnesium Chloride Hexahydrat ($MgCl_2$)	VWR (1.05833.1000)
Milk Powder	Serva (42590.02)
Monopotassium phosphate (KH_2PO_4)	Sigma Aldrich (P5655)
Nitrogen (liquid)	Sigma Aldrich (N4638)
Nitrotetrazolium blue (NTB)	Sigma Aldrich (N6876)
Normal goat serum	Biozol (VEC-S-1000)
Paraformaldehyde (PFA)	AppliChem (A3813)
Phenazine methosulphate (PMS)	Sigma Aldrich (P9625)
Phosphatase inhibitor cocktail tablets (PhosSTOP)	Roche (4906837001)
Phosphate buffered saline (PBS) (without Ca^{2+} and $Mg^{2+)}$	Gibco (14190-094)
Pierce™ 660 nm Protein Assay	Thermo Fisher Scientific (22660)
Plus DNA Ladder (1 Kb)	Thermo Fisher Scientific (10787026)
Potassium chloride (KCl)	MERCK (P3911)
Potassium hydroxide (KOH)	MERCK (221473)
Ponceau S Solution	VWR (A2935.0500)
Power SYBR™ Green PCR Master Mix	Thermo Fisher Scientific (4367659)
Primer / DNA Oligo	Integrated DNA Technologies IDT
Proteinase K	Roche (3115852)
Protein-marker V PeqGOLD	Peqlab (27-2210)
Random hexamer primers	Invitrogen (48190-011)
Red-Taq DNA Polymerase 2X MasterMix	VWR (733-2131)

Restore Western Blot stripping buffer	Thermo Fisher Scientific (21059)
RNase OUT	Invitrogen (10777-019)
RNase H from E. coli	Thermo Fisher Scientific (AM2293)
Sodium Azide (NaN3)	Merck (S2002)
Sodium chloride (NaCl)	VWR (7647-14-5)
Sodium dodecyl sulfate (SDS)	Millipore (817034.1000)
Sodium hydroxide pellets (NaOH)	AppliChem (AP131687.1210)
Sodium deoxycholate	MERCK (D6750)
Sodium succinate	Sigma Aldrich (S2378)
Sodium phosphate dibasic (Na_2HPO_4)	Sigma Aldrich (S9763)
Sodium phosphate dibasic dihydrate (Na2HPO4 · 2H2O)	Sigma Aldrich (71643)
Sodium phosphate monobasic (H_2NaO_4P)	Sigma Aldrich (74092)
Sucrose	Sigma Aldrich (S0389)
SuperScript III Reverse Transcriptase	Invitrogen (18080-044)
SuperSignalTM West Pico Chemiluminescent substrate	Thermo Fisher Scientific (34080)
TaqMan™ Gene Expression Master Mix	Thermo Fisher Scientific (4369542)
Taqman probe	Thermo Fisher Scientific / Life Technologies
Tamoxifen ≥99%	Sigma Aldrich (T5648)
Tetramethylethylenediamine (TEMED)	Serva (35925)
Tissue-Tek® O.C.T. Compound	Hartenstein Laborversand (TTEK)
Tris(hydroxymethyl)aminomethan (Tris)	VWR (103156X)
Tris(hydroxymethyl)aminomethan Hydrochlorid (Tris HCl)	VWR (85.827.297)
Tris HCL/Base	VWR (443864E)
Triton X-100	AppliChem (A4975-0500)
Trizol reagent	Invitrogen (15596-018)
Trypsin	Promega (V5111)
Tween-20	Sigma Aldrich (P1379-500)
L-Valine-d8	Cambridge Isotope Laboratories (NC0894143)
Xylol	VWR (APPC251769.2714)

Table 2 Buffers and solutions used in this study

Buffers & Solutions	Composition
Tail lysis buffer for lysis of the mouse tails 0.1mg Proteinase K (10mg/ml in 50mM Tris, pH 8.0) per 200ul tail lysis buffer per sample	Tris-HCl (pH 8.5) 100mM EDTA 5mM SDS 0.2% (w/v) NaCl 200mM
RIPA buffer for intestinal epithelial cells (IECs) lysis	Tris-HCl (pH 8.0) 10mM NaCl 140mM EDTA 1mM Triton X-100 1% (v/v) Sodium deoxycholate 0.1% (w/v) SDS 0.1% (w/v)
Running buffer for immunoblotting	Tris-Base 25mM Glycine 192mM SDS 0.1% (w/v)
Transfer buffer for immunoblotting	Tris-Base 25mM Glycine 192mM Methanol 20% (v/v)
SDS polyacrylamid gel for immunoblotting	10% resolving gel (20ml) 6.7ml 30% Acrylamide mix 5ml Tris (pH 8.8) 1.5M 0.2ml APS 10% (w/v) 0.2ml SDS 10% (w/v) 0.008ml TEMED 7.9ml H_2O 5% stacking gel (10ml) 1.7ml 30% Acrylamide mix 1.25ml Tris (pH 6.8) 1M 0.1ml APS 10% (w/v) 0.1ml SDS 10% (w/v) 0.01ml TEMED 6.8ml H_2O
Blocking buffer for immunoblotting	Non-fat dry milk 5% (w/v) in PBST 0.1% (v/v) (1x PBS + Tween-20)
1x PBS (pH 7.3)	NaCl 137mM KCl 2.7mM $Na_2HPO_4 \cdot 7H_2O$ 4.3mM KH_2PO_4 1.4mM
5x Laemmli loading buffer	Tris-HCl (pH 6.8) 250mM SDS 10% (w/v) Glycerol 50% (v/v) Bromophenol blue 0.01% (w/v) β-Mercaptoethanol 10% (v/v)
Blocking buffer for Immunohistochemistry (IHC) and Immunofluorescence (IF)	1x PBS Bovine serum albumin (BSA) 1% (w/v) Fish skin gelatin 0.2% (v/v) Triton-X-100 0.3% (v/v) Tween-20 0.05% (v/v)

Endogenous Peroxidase blocking buffer for IHC	NaCitrate 0.04M Na_2HPO_4 0.121M NaN_3 0.03M H_2O_2 3%
Antigen retrieval buffer Or Citrate buffer (pH=6) for IHC	NaCitrate 10mM Tween-20 0.05% (v/v)
Primary antibody dilution buffer for immunoblotting	Non-fat dry milk 5% (w/v) in PBST 0.1% (v/v) or PBST 0.1% (v/v) NaN_3 0.02% (w/v)
Secondary antibody dilution buffer for immunoblotting	Non-fat dry milk 5% (w/v) in PBST 0.1% (v/v)
0.5M EDTA (pH=8)	181.6g of $Na_2EDTA \cdot 2H_2O$ 800ml ddH_2O
25x TAE (Tris/acetate/EDTA) electrophoresis buffer	1210g of Tris-Base 500ml EDTA 0.5M (pH=8) 285.5ml Acetic acid
TEX protease K buffer (pH=8)	Tris-Base 50mM EDTA 1mM Triton-X-100 0.5% (v/v)
PCR reaction mix (per reaction)	12.5ul Taq 2x Mastermix 2ul Primer Mix (1:1 Forward/Reverse primer, 10uM) 10.5ul H20 2ul genomic DNA
Tamoxifen solution for mouse injections	10ml corn oil 100mg Tamoxifen 200ul sterile DMSO
0.1M Phosphate buffer (pH=7)	1.56g H6NaO6P in 50ml ddH_2O 2.83g Na_2HPO_4 in 100ml ddH_2O
0.2M Phosphate buffer (pH=7.4)	3.12g H6NaO6P in 50ml ddH_2O 11.32g Na_2HPO_4 in 200ml ddH_2O
Cytochrome c oxidase (COX) incubation medium	0.8ml DAB 5mM 0.2ml cytochrome c 500uM few grains of catalase
Succinate dehydrogenase (SDH) incubation medium	0.8ml Nitroblue tetrazolium 1.875mM 0.1ml sodium succinate 1.30M 0.1ml Phenazine methosulphate 2mM 0.010ml sodium azide 100mM
Oil Red O solution	0.3g Oil Red O 60ml isopropanol 40ml ddH_20
Mitochondrial isolation buffer (pH=7.6)	Sucrose 100mM KCl 50mM EDTA 1mM TES 20mM fatty acid-free BSA 0.2% (w/v)

Metabolite extraction solution	Methanol 50% (v/v) Acetonitrile 30%(v/v) ddH_20 20% Valine d8 5uM

Table 3 Commercial Kits used in this study

Kits	Company (Catalog number)
Alcian Blue PAS Stain Kit	Abcam (ab245876)
Avidin/Biotin Blocking Kit	Biozol (VEC-SP-2001)
DAB Substrate Kit	Abcam (ab64238)
Fast Red Substrate Kit	Abcam (ab 64254)
ImmPACT DAB Substrate Kit	Biozol (VEC-SK-4105)
Liquid DAB Substrate Chromogen System	DakoCytomation (Code K3466)
Pierce™ Bovine Serum Albumin Standard Pre-Diluted Set	Thermo Fisher Scientific / Life Technologies (23208)
RNA extraction RNeasy mini Kit	Qiagen (74106)
RNase-free DNase set	Qiagen (79254)
SuperScript III cDNA synthesis Kit	Invitrogen (18080-044)
TaqMan® Gene expression Master Mix	Applied Biosystems (4369542)
VECTASTAIN® Elite ABC-Peroxidase Kit	Biozol (VEC-PK-6100)

2.2. Methods

2.2.1. Animal handling and experiments

2.2.1.1. Mouse models, housing and care

The following mouse lines were used: *Dars2*$^{fl/fl}$ (Dogan, Pujol et al. 2014), *Cox10*$^{fl/fl}$ (Diaz, Thomas et al. 2005), *Vil1-Cre* (Madison, Dunbar et al. 2002), *Villin-CreERT2* (el Marjou, Janssen et al. 2004). *Sdha*^{tm2a} mice were obtained from the Knock Out Mouse Project (KOMP) repository (Project ID: CSD48939) and bred to FLP deleter mice(Rodriguez, Buchholz et al. 2000) to delete the FRT-flanked region to generate *Sdha*$^{fl/fl}$ mice. IEC-specific knockout mice were generated by intercrossing mice carrying the respective loxP-flanked alleles, with *Vil1-Cre* or *Villin-CreERT2* transgenic mice. Both female and male mice were included in all groups. Mice of the indicated genotype were assigned at random to groups and mouse studies were performed in a blinded fashion. All mice were maintained in C57BL/6N background. Mice were housed in individually ventilated cages and maintained at the specific-pathogen-free (SPF) animal facilities of the CECAD Research Center of the University of Cologne. Mice were kept under a regular 12h light cycle at 22-24°C, with unlimited access to water and fed with a standard chow diet (Harlan diet no. 2918 or Prolab Isopro RMH3000 5P76) ad libitum. All breedings initiated at the age of 8 weeks between one male and one or two females simultaneously. Ear tags were mainly placed at the 2-week- old litters and mice of the same sex were accommodated in a single cage with maximum 5 animals per cage. Tails biopsies for isolation of genomic DNA and appropriate genotyping were obtained at 2 weeks of age. For the experiments assessing the role of dietary fat, mice, mice were fed with fat-free diet (E15104-3474, ssniff-Spezialdiäten GmbH, Soest, Germany) containing only traces of fat (<0.5%). All animal procedures were conducted in accordance with European, national and institutional guidelines and protocols were approved by local government authorities (Landesamt für Natur, Umwelt und Verbraucherschutz Nordrhein-Westfalen, Germany) and Animal Welfare Officers of University Medical Center Hamburg-Eppendorf and Behörde für Gesundheit und Verbraucherschutz Hamburg, Germany. Animals requiring medical attention were provided with appropriate care and were culled humanely when reaching pre-determined termination criteria to minimize suffering. No other exclusion criteria existed. VillinCreER^{T2} recombinase activity was induced by five consecutive daily intraperitoneal administrations of 1 mg tamoxifen dissolved in corn oil/DMSO. Littermates not carrying the *Vil1-Cre* or *Villin-CreERT2* transgenes were used as controls in all experiments.

2.2.2. Molecular biology

2.2.2.1. Isolation of genomic DNA from tail biopsies

Mice were euthanized with cervical dislocation or with the use of carbon dioxide (CO_2) at the age of 3 weeks, while pups were sacrificed by decapitation 6-7 days upon birth. After euthanasia, a small piece of 2mm from the tail was cut and lysed using 2ul of Proteinase K (10mg/ml) in 200ul of tail lysis buffer overnight at 56°C and 600rpm shaking in an Eppendorf thermocycler. To isolate genomic tail DNA, the next day equal volume of isopropanol was added and the tube was inverted several times. Afterwards, the tube was centrifuged at 11.000g for 1min, the supernatant was removed and 200ul of 70% (v/v) ethanol was carefully added to the pellet for the appropriate washing. After a second centrifugation step at 11.000g for 1min, the supernatant was discarded and the pellet was air-dried at RT for 15 min. Finally, the pellet was resuspended in 100ul of ddH_20 and stored at 4°C.

2.2.2.2. PCR for genotyping

Genotyping was performed by polymerase chain reaction (PCR) using specific primers to amplify allele specific PCR products (table 4). In particular, a PCR mix was prepared following the general scheme described above in table 3 and amplification of genomic DNA was made by thermal cyclers. PCR programs composed of a denaturation, a primer annealing and an extension/elongation step (Table 4).10ul of the PCR reaction products were separated on 2% (w/v) low melting agarose gels with 0.5mg/ml ethidium bromide in 1x TAE buffer at 120mV for 30-40 min and visualized using UV-light and a standard Plus DNA ladder for product size comparison.

Table 4 Primer sequences and PCR programs for genotyping PCRs

Allele	Primer Sequence (5-3')	Expected band size (bp)	PCR program		Cycles
			Temperature	Time	
Dars2 (floxed)	ATGAATTCTAGGCCAGCCAC TGGCAATCTCTTAGGACTAAG	WT: 475 FL: 623	95°C	5 min	
			95°C	30 sec	30x
			60°C	30 sec	
			72°C	45 sec	
			72°C	3 min	

Sdha (floxed)	TGAAGGACAGTAGTCACTAGATCAG TAAAGGAACCTACTGGTGCTCTAAT	WT: 325 FL: 431	94°C 94°C 52°C 72°C 72°C	2 min 30 sec 45 sec 30 sec 2 min	35x
Cox10 (floxed)	GAGAGGAGTCAAGGGGACCT GGCCTGCAGCTCAAAGTGTA	WT: 162 FL: 290	94°C 94°C 63°C 72°C 72°C	3 min 30 sec 40 sec 30 sec 3 min	35x
VillinCre	ACAGGCACTAAGGGAGCCAATG ATTGCAGGTCAGAAAGAGGTCACAG GTTCTTGCGAACCTCATCACTC	WT: 900 Cre: 350	94°C 94°C 67°C 72°C 72°C	3 min 1 min 1 min 1 min 5 min	35x
Villin CreERT2	CAAGCCTGGCTCGACGGCC CGCGAACATCTTCAGGTTCT	TG:300	94°C 94°C 55°C 72°C 72°C	5 min 45 sec 45 sec 45 sec 5 min	30x
Caspase-8 (floxed)	TCCTGTACCATATCTGCCTGAACGCT ATAATTCCCCCAAATCCTCGCATC	WT: 900 FL: 1000 DEL:200	94°C 94°C 62°C 72°C 72°C	3 min 30 sec 30 sec 35 sec 3 min	34x
Mlkl	CATCAAGTTAGGCCAGCTCA TCTGCTGGTTAGCCTCCTTC	WT: 204 DEL:173	94°C 94°C 58°C 72°C 72°C	3 min 30 sec 30 sec 60 sec 3 min	35x
B-actin-Cre	CACGACCAAGTGACAGCAAAT AGAGACGGAAATCCATCGCT	TG:350	94°C 94°C 53°C 72°C 72°C	3 min 30 sec 30 sec 30 sec 2 min	35x

2.2.2.3. RNA isolation from mouse tissues

Small pieces about ~0,5cm were isolated from proximal (post stomach) and distal (prior to caecum) small intestine and colon were dissected and washed with PBS. Afterwards, they were snap frozen on dry ice for RNA expression analysis. Frozen pieces were placed into a vial containing a small number of ceramic beads, 350ul RA1 lysis buffer and 3.5ul β-mercapthoethanol and subsequently disrupted using Precellys 24 tissue homogenizer (Bertin technologies) at 6.000 rpm for 1min. Then, the tubes were centrifuged for 5min at 14.000 rpm at 4°C and the supernatant was transferred in a fresh 1.5ml eppendorf tube. Isolation of RNA was ultimately performed using a NucleoSpin RNA isolation kit (Macherey Nagel Ref. 740955.250) according to manufacturer's instructions. In order to digest genomic DNA, rDNAse (provided by manufacturer) was added and incubated at RT for 45min. RNA was eluted in 60ul RNAse-free H_2O. RNA concentration and purity was assessed by a NanoDrop Spectrophotometer (Thermo Fisher Scientific) and RNA was kept at -80^{o}C until further use.

2.2.2.4. cDNA synthesis and quantitative RT-PCR

cDNA was prepared using Superscript III cDNA-synthesis kit (18080-044, ThermoScientific). In a final reaction volume of 10ul, 500ng - 1ug RNA was mixed with 1ul of 50 ng/uL random hexamer primers and 1ul of 100mM dNTPs. To allow annealing of the primers to mRNA, the reaction mixture was incubated at 65°C for 5 min and then placed shortly on ice. Afterwards, 10ul of cDNA reaction mix composed of 2ul of 10x RT-reaction buffer, 4ul of 25mM $MgCl_2$, 2ul of 0.1M DTT, 1ul of RNase OUT (40 units/ul) and 1ul of SuperScript III polymerase (200 units/ul) was prepared and mixed with the samples for a 20ul total reaction. Reverse transcription was performed using a PCR cycler. The samples were placed 10min at 25°C allowing reverse transcription of the RNA, 50min at 50°C for cDNA synthesis and 5min at 85°C as a heat-inactivation step. RNA was ultimately digested with 1ul of RNaseH for 20min at 37°C. Finally, the cDNA reaction mix was diluted 1:5 in RNAse-free water and subjected to β-actin PCR to confirm efficient cDNA synthesis. Quantitative real-time polymerase chain reaction (qRT-PCR) was performed with TaqMan probes (Life Technologies) or SYBR Green (Thermo Scientific) indicated at Table 5 and 6, respectively. Final volume of each Taqman probe – based qRT-PCR reaction was 10ul, consisting of 5ul TaqMan™ Gene Expression Master Mix, 5ul qRT-PCR primer-probe mix, 2.5ul RNAse-free H_20 and 2ul c DNA. All samples were run in two technical replicates and mRNA expression of each gene was normalized to the expression of the housekeeping gene TATA box binding protein (*Tbp*). For Sybr Green-based qRT-PCR reactions, 6ul of Power SYBR™ Green PCR Master Mix, 1.2ul of 20uM primer mix, 2ul of cDNA and 2.8ul of RNAse-free H_20 were mixed for a final 10ul reaction. All samples were run in two technical replicates and mRNA expression of each gene was normalized to the expression of the housekeeping gene Hypoxanthine-guanine phosphoribosyltransferase (*Hprt1*). RT-qPCRs were carried out on a Quant Studio Real-Time PCR System (Thermo Fisher Scientific) in 384-well plates. The following PCR program was performed, as suggested by the manufacturer: 95°C for 10min (polymerase activation step), 95°C for 10sec (40 cycles), 60°C for 20sec (annealing) and 72°C for 40sec (elongation step). Relative expression of gene transcripts was analysed by using the $2^{-\Delta\Delta Ct}$ method.

Table 5 Taqman probes used for quantitative RT-PCR analysis

Gene	Taqman probe
Olfm4	Mm01320260_m1
Lgr5	Mm00438890_m1
Ascl2	Mm01268891_g1
Tbp	Mm00446973_m1
Prominin-1	Mm00477115_m1
Lrig-5	Mm00456116_m1
Ccl2	Mm00441242_m1
Cxcl1	Mm00433859_m1
Il-1b	Mm00434228_m1
Tnf	Mm00443258_m1
Lyz1	Mm00657323_m1
Defa-rs2	Mm00655851_gH

Ang4	Mm03647554_g1

Table 6 Oligonucleotides used for Sybr-Green based quantitative RT-PCR analysis

Gene	Forward (5’-3’)	Reverse (5’-3’)
Ppara	AACATCGAGTGTCGAATATGTGG	CCGAATAGTTCGCCGAAAGAA
Scd1	GCTCTACACCTGCCTCTTC	CCGTGCTTGTAAGTTCTG
Acc1	GACAGAGGAAGATGGCGTCC	TACAACTTCTGCTCGCTGGG
Srepb1c	CGCGGAAGCTGTCGGGGTAG	AAATGTGCAATCCATGGCTCCGTGGTC
Dgat1	GCCCCATGCGTGATTATT	TCTGTCAGGGCACCCACT
Acat1	CAGGAAGTAAGATGCCTGGAAC	TTCACCCCCTTGGATGACATT
Acox1	TAACTTCCTCACTCGAAGCCA	AGTTCCATGACCCATCTCTGTC
Mgat2	GTGTGGGATTAGGGGGACTT	TCCCTGTTTGTCCTTTGGTC
Mcad	AGGGTTTAGTTTTGAGTTGACGG	CCCCGCTTTTGTCATATTCCG
Ehhadh	ATGGCTGAGTATCTGAGGCTG	GGTCCAAACTAGCTTTCTGGAG
Fasn	GGAGGTGGTGATAGCCGGTAT	TGGGTAATCCATAGAGCCCAG
Pparg	CCTGAAGCTCCAAGAATACCA	GCCTGATGCTTTATCCCCACA
Mttp	TGAGCGGCTATACAAGCTCAC	CTGGAAGATGCTCTTCTCGC
Lipe	AGTGCCTATTCAGGGACAGA	TGGGCGATGTGGTCTTTT
Ppard	GCAGCCTCAACATGGAATGTC	GAGCTTCATGCGGATTGTCC
Mgat1	CTGGTTCTGTTTCCCGTTGT	TGGGTCAAGGCCATCTTAAC
Gpat3	GTGCTGGGTGTCCTAGTGC	AAGCTGATCCCAATGAAAGC
Acly	CAGTCCCAAGTCCAAGATCC	GTCTCGGGAGCAGACATAGT
Hadha	TGCATTTGCCGCAGCTTTAC	GTTGGCCCAGATTTCGTTCA
Acadvl	CTACTGTGCTTCAGGGACAAC	CAAAGGACTTCGATTCTGCCC
Cd36	CTGTGGGCTCATTGCTGG	CGCCACGTCATCTGGGTTT
Cpt2	CAGCACAGCATCGTACCCA	TCCCAATGCCGTTCTCAAAAT
Cidea	TGACATTCATGGGATTGCAGAC	GGCCAGTTGTGATGACTAAGAC
Atgl	GGATGGCGGCATTTCAGACA	CAAAGGGTTGGGTTGGTTCAG
Lpl	ACTCGCTCTCAGATGCCCTA	TTGTGTTGCTTGCCATTCTC
Hprt1	GCCCCAAAATGGTTAAGGTT	TTGCGCTCATCTTAGGCTTT
Apoa1	TATGTGGATGCGGTCAAAGA	ACGGTTGAACCCAGAGTGTC
Apoa2	TACCTCCAGTCAAGCCCAGAG	GACCAGCAGTGCGACCATT
Apoa4	TGCCAAGGAGGCTGTAGAAC	CTTGTTGTGCACCCCATCAG
Apoa5	GTGATGGAGTGTGTAATGGGGA	AGCAGGCATGAGGAATCTGG
Apob	TCCAAAGAGGCCAGTCAAGC	TGCCTGTTCTCAACCAGAGG
Apoc1	GTCCGGAACATTGGAGAGCATA	TCACTTTGCCAAATGCCTCTGA
Apoc2	ATAAAGCCTGCCAACCCACT	AGGAAGAACCGAGACCCCAT
Apoc3	GAACAAGCCTCCAAGACGGT	AGTGATTGTCCATCCAGCCC

Apoe	GCTAAGGACTTGTTTCGGAAGGA	CACTCGAGCTGATCTGTCACC
Sar1b	GCTAAAAAGGCAGGGCTATGG	GGCCGCTGCTAATCGATGTA
Sar1a	GGGCCGTTGTAAGCATCAATA	TTCCAGATTTCTTGTAGAGTCCTAGGA

2.2.2.5. Microarray analysis

Clariom-S mouse microarray analysis (Thermo Fisher Scientific) was performed using 500ng of total RNA per sample. RNA quality was assessed based on RNA integrity number (RIN) and OD260/280 and OD260/230 ratios. RIN value was evaluated using TapeStation4200 and RNA ScreenTapes (Agilent Technologies). Sample exclusion criteria were OD260/280<1.8, OD260/230<1.5 and RIN<6. Any sample that did not follow the given requirements was excluded from the analysis. Labelled cDNA was generated using GeneChip WT PLUS Reagent Kit (Thermo Fisher Scientific) according to manufacturer's instructions followed by hybridization in a Gene Chip Hybridization Oven 645 for 16 h at 45 °C. Gene chips were scanned with the Gene Chip Scanner 7G, whereas the Clariom-S-mouse array (Thermo Fisher Scientific, 902930) was performed in a 169 format following the Fluidics Protocol FS450-0007. Array-quality control was performed using Affymetrix Expression Console or Transcriptome Analysis Console (TAC). Gene expression data (Heat-Cluster) were visualized using R/bioconductor for Z score transformation.

2.2.2.6. Measurement of serum parameters

Blood was collected from the caval vein during sacrifice or from the head after decapitation and was spun down at 13000 rpm for 15 min to collect the sera. Then, serum was diluted 1:5 with 0.9% NaCl. Glucose (GLU2), Triacylglycerol (TRIGL), total cholesterol (CHOL2), high density lipoprotein (HDLC4) and low density lipoprotein (LDLC3) levels were measured in the blood serum of the mice using standard assays in a Cobas C111 Biochemical Analyzer (Roche Diagnostics, Mannheim, Germany).

2.2.3. Histological analysis

2.2.3.1. Tissue preparation

For histological examination of the small intestine and the colon, intestinal tissue was completely removed by cutting the small intestine right after the pylorus and the colon in close proximity to the anus. Afterwards, the intestine was placed into PBS and was cut longitudinally to remove mesenteric fat and luminal content including faeces. Intestinal tissues were rolled up from proximal to distal and with the mucosa facing down on a Petri dish to form a Swiss roll with the help of injection needle. Finally, swiss rolls were transferred either into histology cassettes for o/n fixation in 4% paraformaldehyde (4% PFA) at 4°C or embedded in TissueTek O.C.T (Sakura) within cryomolds on dry ice for frozen sectioning. The next day, cassettes were transferred into fresh 1xPBS and further processed in order to be embedded into paraffin blocks. Paraffin blocks were sectioned with a microtome at 3um thickness, whereas cryomolds were cut via a cryostat (Leica CM1850) at 7-10um thickness.

2.2.3.2. Haematoxylin & Eosin staining of paraffin-fixed tissues

Paraffin-embedded 3 um-thick intestinal tissue sections were deparaffinised with Xylol for 20min. Rehydration was performed by decreasing amount of ethanol solutions for 2min each (100% (v/v) ethanol, 96% (v/v) ethanol, and 75% (v/v) ethanol). Afterwards, sections were washed for 5min in tap H_20. Subsequently, sections were stained for 2min in Meyer's Haematoxylin, quickly washed in tepid tap H_20 for 10sec and differentiated in tap H_2O for 15min. After 15min, sections were additionally washed with ddH_20 for 1min and incubated for 1min in Eosin staining solution. Coloured clouds were disappeared from the slides by placing the sections in tap H_2O for 6 or 7 times. Stained sections were dehydrated using increasing amount of ethanol solutions for 1min each and fixed in Xylol for 1min. Finally, slides were mounted with Entellan.

2.2.3.3. COX/SDH staining of fresh-frozen tissues

Fresh-frozen 7um-thick intestinal sections were sequentially stained for COX and SDH activity. Cryosections were air-dried for 15min and incubated for 45min at 37°C with COX solution (0.8ml of DAB, 0.2ml of 500uM cytochrome c, a few grains of catalase). Then, cryosections were briefly washed with 1xPBS and incubated for 40min with SDH solution (0.8ml of 1.875mM nitrotetrazolium blue, 0.1ml of 1.3M sodium succinate, 0.1ml of 2mM phenazine methosulphate, 0.01ml of 100mM sodium azide) at 37°C. Afterwards, cryosections were shortly washed in ddH_2O. Following dehydration through graded alcohol solutions for 2min (70% (v/v) ethanol, 96% (v/v) ethanol, 100% (v/v) ethanol), the sections were mounted with D.P.X and stored at RT.

2.2.3.4. ORO staining of fresh-frozen tissues

Fresh-frozen sections 10um-thick were fixed in 4% PFA for 15min at RT. Upon fixation, the sections were washed with tap H_2O for 5min and stained with Oil Red O (ORO) in isopropanol/water (60:40) for 15min. For the ORO solution 0.3g ORO was dissolved in 60ml isopropanol o/n with stirring and 40ml tap H_2O was added for the final solution, which was subsequently filtered for immediate use. All sections were quickly rinsed with tap H_2O, counterstained with Haematoxylin for 5 min, washed with tap H_20 for 15min and finally mounted with Aquatex (EMD Millipore).

2.2.3.5. Periodic acid-Schiff staining of intestinal tissue sections

For periodic acid-Schiff (PAS) staining, sections were deparaffinized (as described above) and washed in tap H_2O for 5min. Periodic acid was freshly prepared by mixing 0.04g of periodic acid (Thermo fisher Scientific, 15657060) with 5ml tap H_2O. Tissue sections were incubated with periodic acid for 5-8min and washed two times for 5min in tap H_2O. Afterwards, sections were incubated in Schiff's reagent (VWR, 1090330500) for 5 to 10min. The pink staining of the viscous glycoproteins was obvious after 10min and the reaction was terminated by placing the sections under running tap H_2O for 10min. Nuclei were counterstained with Meyer's Hematoxylin for 2min, samples were washed for 10min under running tap H_2O and dehydrated with ascending series of alcohol for 1min each (70% (v/v) ethanol, 96% (v/v) ethanol, 100% (v/v) ethanol). Finally, the sections were placed in Xylol for 1min and mounted with Entellan.

2.2.3.6. Alkaline phosphatase staining of intestinal tissue sections

Staining for alkaline phosphatase (ALP) was performed using the Fast Red Substrate Kit (Abcam, ab64254) according to manufacturer's instructions. Tissue sections were deparaffinized and rehydrated as has been already described in the previous sections. Samples were rinsed with 20x TBS. Subsequently, 1 drop (40ul) of Fast Red Chromogen was mixed with 3ml of Liquid Fast Red Substrate, immediately added on top of the slides and incubated for 15-20min. The presence of alkaline phosphatase enzyme was observed upon washing the sections with ddH_2O for 1min. Nuclei were counterstained with Meyer's Hematoxylin for 1 min, as usual. Samples were finally properly washed, dehydrated in ethanol solutions and mounted with Entellan.

2.2.3.7. Immunohistochemistry (IHC)

For IHC stainings, tissue sections were deparaffinised and rehydrated in ascending concentration of ethanol (100% (v/v) ethanol, 96% (v/v) ethanol, and 75% (v/v) ethanol). Antigen unmasking was performed by heat-induced antigen retrieval in citrate buffer, TRIS buffer pH=6 for 30 min at 120^{o}C in a pressure steam cooking device or by proteinase K treatment with 10ug/ml Proteinase K in TEX buffer for 10 min at RT. Endogenous peroxidase activity was blocked in peroxidase blocking buffer for 15 min at RT. Afterwards, the sections were washed for 5 min in PBS. In order to block unspecific background, sections were incubated for 60 min with blocking buffer containing 1% Albumin, 0.2% Fish Skin Gelatin, 0.1% Triton X-100, 0.05% Tween- 20 in PBS and 160ul/ml Avidin D from Avidin/Biotin blocking kit (Vector, no. SP-2001). Sections were subsequently incubated with primary antibodies in blocking buffer and 160ul/ml Biotin 4^{o}C o/n. Primary antibodies used in IHC are described in Table 7. Next day, sections were washed 3x for 5 min each in PBS with 0.5% (v/v) Tween-20. Then, sections were incubated for 1hr at RT with biotinylated secondary antibodies purchased from Perkin Elmer and Dako in blocking buffer. Secondary antibodies used are described in Table 8. After washing 3x for 5 min each with 0.5% (v/v) Tween-20 in PBS, sections were incubated with 1:60 Avidin and 1:60 Biotin from ABC Elite Vectastain Kit (Vector, no. PK 6100) in 1x PBS for 30 min at RT. After 3x 5 min washes with 0.5% (v/v) Tween-20, the staining was developed by exposing the sections to DAB Chromogen ImmPACT DAB/DAB Substrate Chromogen System; Vector no SK-4105 (1 drop of DAB Chromogen + 1ml Substrate buffer). Incubation with DAB was adapted for each single staining and remained equal for all the samples. After positive signal, the reaction was terminated by washing the slides in tap H_20. Nuclei were counterstained with haematoxylin for 2 min and dehydrated in descending concentration of ethanol, cleared in Xylol and mounted with Entellan. For image acquisition, the intestinal sections were analyzed using a light microscope (Leica DM4000B, Leica Microsystems, Wetzlar, Germany) or with Hamamatsu slide scanner.

Table 7 List of primary antibodies and appropriate dilutions.

Antigen	Company	Host	Dilution
Ki67	Dako (M724901)	Rat	1:1000
Olfm4	Cell Signaling (D6Y5A)	Rabbit	1:400
CC3	Cell Signaling (9661)	Rabbit	1:1000
CD45	BD Bioscience (30-F11)	Rat	1:500
F4/80	homemade	Rat	1:200
Gr1	BD Pharmingen (1A8)	Rat	1:500
Lysozyme	Dako (F0372)	Rabbit	1:2000

CC8	Cell Signaling (8592)	Rabbit	1:1000

Table 8 List of secondary biotinylated antibodies and appropriate dilutions.

Antigen	Company	Host	Dilution
Biotinylated rat IgG	Vector Laboratories (BA-9400-1.5)	Rabbit	1:1000
Biotinylated rabbit IgG	Vector Laboratories (BA-1000-1.5)	Goat	1:1000
Biotinylated mouse IgG	Vector Laboratories (BA-9200-1.5)	Rabbit	1:1000

2.2.3.8. Immunofluorescence (IF)

For IF stainings, tissue sections were deparaffinised and rehydrated in ascending concentration of ethanol (100% (v/v) ethanol, 96% (v/v) ethanol, and 75% (v/v) ethanol). Antigen unmasking was performed by heat-induced antigen retrieval in citrate buffer, TRIS buffer pH=6 for 30 min at 120°C in a pressure steam cooking device. Then, sections were incubated for 60 min with blocking buffer containing 1% Albumin, 0.2% Fish Skin Gelatin, 0.1% Triton X-100, and 0.05% Tween- 20 in PBS. Sections were subsequently incubated with primary antibodies in blocking buffer. Primary antibodies used in IF are described in Table 9. Next day, sections were washed 3x for 5 min each in PBS with 0.5% (v/v) Tween-20. Then, sections were incubated for 30 min at RT with fluorescent secondary antibodies purchased from Molecular Probes in blocking buffer. Fluorescent secondary antibodies used are described in Table 10. After washing 3x for 5 min each with 0.5% (v/v) Tween-20, nuclei were stained with Hoechst 33342 Blue Fluorescent DNA stain for 10 min, washed for 5 min with PBS and mounted with Vectashield containing DAPI (Vector) and stored at 4°C. For image acquisition, the intestinal sections were analyzed using a TCS SP8 confocal microscope (Inverse, DMi 8 CS, Leica Microsystems).

Table 9 List of primary antibodies and appropriate dilutions.

Antigen	Company	Host	Dilution
Adipophilin/ Perilipin 2	Progen (GP46)	Guinea pig	1:500
TGN38	R&D bio-techne (AF8059-SP)	Sheep	1:200
E-cadherin	BD Biosciences (610182)	Mouse	1:1000

Table 10 List of secondary fluorescent antibodies and appropriate dilutions.

Antigen	Company	Host	Dilution
a-mouse Alexa 488	Molecular Probes Inc. (A-11001)	Goat	1:400
a-rabbit Alexa 594	Molecular Probes Inc. (A-11012)	Goat	1:400
a-rat Alexa 488	Molecular Probes Inc. (A21210)	Rabbit	1:400
a-sheep IgG NorthernLights™ NL557	R&D bio-techne (NL010)	Donkey	1:300

2.2.3.9. Electron microscopy

A piece of 0.5cm proximal small intestinal tissue was fixed o/n in 2%Glutaraldehyde (Merck) and 2% Formaldehyde (Science Services) in 0.1M Cacodylate buffer (AppliChem). Tissues were treated with 1% OsO_4 (Science services) in 0.1M Cacodylate buffer for 2 hours. After dehydration of the sample with ascending EtOH concentrations followed by propylenoxid, samples were embedded in Epon (Sigma-Aldrich) Ultrathin sections (70 nm) were cut, collected onto 100 mesh copper grids (Electron Microscopy Sciences), and stained with uranyl acetate (Plano GMBH) and lead citrate (Sigma Aldrich). Images were captured by a transmission electron microscope (JOEL JEM2100 Plus) at an acceleration voltage of 80 kV, and pictures were acquired using a 4K-CCD camera, OneView (GATAN). The visualization of the electron microscopy (TEM) images that are included in this thesis has been performed in collaboration with the group of Dr. Astrid Schauss from the CECAD Imaging Facility.

2.2.4. Biochemistry

2.2.4.1. Isolation of mitochondria and analysis of mitochondrial respiratory complexes with blue native electrophoresis

Mitochondrial protein concentrations were determined with Bradford reagent (Sigma). 20 μg of mitochondria were lysed for 15 min on ice in dodecylmaltoside (DDM; 5 g/g of protein) for individual respiratory complexes, or digitonin (6.6 g/g protein) for supercomplexes, and cleared from insoluble material for 20 min at 20,000 × g, 4 °C. Lysates were combined with Coomassie G-250 (0.25% final). Mitochondrial complexes were resolved with BN-PAGE using the 4–16% NativePAGE Novex Bis-Tris Mini Gels (Invitrogen) in a Bis-Tris/Tricine buffering system with cathode buffer initially supplemented with 0.02% G-250 followed by the 0.002% G-250.

For Complex I *in-gel* activity: gels were incubated in a buffer containing 0.01 mg/ml NADH and 2.5 mg/ml nitrotetrazolium blue in 5 mM Tris-HCl pH 7.4.

For western blot analysis following BN-PAGE: separated mitochondrial complexes were transferred onto a polyvinylidene fluoride membrane using the wet transfer methanol-free system. Membranes were immunodecorated with antibodies indicated in Table 11, followed by ECL-based signal detection. The small intestine was chopped into small pieces and homogenized with a rotating Teflon potter (Potter S, Sartorius; 20 strokes, 1000 rpm) in a buffer containing 100 mM sucrose, 50 mM KCl, 1 mM EDTA, 20 mM TES, 0.2% fatty acid-free bovine serum albumin (BSA), pH 7.6, followed by differential centrifugation at 850 × g, and 8500 × g for 10 min at 4 °C. Mitochondria were washed with BSA-free buffer and protein concentrations were determined with Bradford reagent. Mitochondria were subjected to blue native polyacrylamide gel electrophoresis (BN-PAGE) followed by western blot analysis or determination of the *in-gel* activity of respiratory complexes.

Table 11 List of primary antibodies and appropriate dilutions used for WB.

Antigen	Company	Host	Dilution
MT-CO1	Molecular Probes Inc. (459600)	Mouse	1:5000
COX4L1	Molecular Probes Inc. (A21348)	Mouse	1:1000
UQCRC1	Molecular Probes Inc. (459140)	Mouse	1:4000
NDUFS1	Proteintech (12444-1-AP)	Rabbit	1:1000
NDUFS2	Abcam (ab96160)	Rabbit	1:1000
NDUFV2	Proteintech (15301-1-AP)	Rabbit	1:1000
UQCRFS1/RISP[5A5]	Abcam (ab147446)	Mouse	1:1000
ATP5A [15H4C4]	Abcam (ab14748)	Mouse	1:3000
SDHA [2E3GC12FB2AE2]	Molecular Probes Inc. (459200)	Mouse	1:5000
NDUFA9	Molecular Probes Inc. (459100)	Mouse	1:1000

2.2.4.2. Isolation of intestinal epithelial cells.

Small intestinal tissue was harvested from mice, washed in DPBS (14190-094, Gibco) to remove faeces and cut longitudinally. Intestinal tissues were incubated in pre-heated 1 mM dithiothreitol (DTT) in DPBS for 10 min at 37°C, while shaking. The supernatant was discarded and the tissues were incubated in pre-heated 1.5 mM EDTA in DPBS at 37°C while shaking. Then, tissues were vortexed for 1 min to disconnect IECs from connective tissues. The tissue pieces were removed and the IEC-containing solution was centrifuged at 1200 rpm for 10 min. Pellets were resuspended in 2 ml of PBS and transferred into 2 ml eppendorf tubes. After another centrifugation for 5 min at 1200 rpm, intestinal epithelial cell (IEC) pellet was frozen at -80°C for further processing.

2.2.4.3. Protein lysate preparation and assessment of protein concentration

IEC pellets were lysed in RIPA lysis buffer (10mM Tris-Cl (pH=8), 140mM NaCl,1mM EDTA, 0.5mM EGTA, 1% Triton X-100, 0.1% sodium deoxycholate, 0.1% Triton X-100, 0.1% SDS). Lysis buffer was supplemented with protease and phosphatase inhibitor tablets (Roche). For lysis, IECs were kept on ice for 30 min and every 10 min the tubes were inverted several times. Then, the solution was centrifuged at 4°C and the supernatant was collected for analysis. Protein concentration was measured using PIERCE 660nm Protein Assay Reagent (22660, Thermo Scientific) and a Bovine Serum Albumin stardard pre-diluted set ranging from 0-2000 µg/ml (23208, Thermo Scientific). Lysates were adjusted to the appropriate concentration. 5x SDS Laemmli loading buffer containing b-mercaptoethanol was added and samples were boiled at 95°C for 10 min at 800 rpm shaking. Samples were placed at -80°C for subsequent SDS gel electrophoresis.

2.2.4.4. Western blot analysis

Cell lysates were separated on SDS–PAGE consisted of a stacking step at 70 V for 30 min in a 5% SDS stacking gel, followed by separation at 120 V in a 10 or 12% resolving gel (table 2). Protein size ladder (26620, Thermo Scientific) was used for size comparison. PVDF membranes (IPVH00010, Millipore) were used for immunoblotting. Membranes were activated in 100% methanol for 1 min prior transfer and soaked in transfer buffer. Wet transfer was performed either at 4°C for 3 hrs at 80 V or at 4°C o/n at 20 V. Afterwards, membranes were stained with Ponceau solution for 1 min and washed in 0.1% (v/v) Tween-20 in PBS. Then, membranes were blocked with 5% milk/0.1% (v/v) Tween-20 in PBS for 1 hr at RT and were probed with primary antibodies indicated in Table 11 and 12 o/n at 4°C. The next day, membranes were washed 3x in 0.1% (v/v) Tween-20 in PBS for 5 min each and incubated with the secondary HRP-linked antibodies, indicated in Table 13, in 5% milk/0.1% (v/v) Tween-20 in PBS for 1 hr. Subsequently, membranes were washed 3x in 0.1% (v/v) Tween-20 in PBS for 5 min each and incubated for 1 min with Amersham ECL Western Blotting Detection Reagent or SuperSignalTM West Pico Chemiluminescent substrate. Membranes were stripped using Restore^{TM} Western Blot Stripping Buffer (21059, Thermo Fisher Scientific) for 15 min at RT and re-probed.

Table 12 List of primary antibodies and appropriate dilutions used for WB.

Antigen	Company	Host	Dilution
DARS2	Proteintech (13807-1-AP)	Rabbit	1:1200
Total OXPHOS Rodent WB Antibody cocktail	Abcam (ab110413)	Mouse	1:1000
Tubulin	Sigma (T6074)	Mouse	1:1000
TOMM70	Sigma (HPA014589)	Rabbit	1:500
β-actin	Santa Cruz (sc-1616)	Goat	1:1000
Perilipin 2	Progen (GP46)	Guinea pig	1:500
FABP2	Proteintech (21252-1-AP)	Rabbit	1:500
FASN	Cell Signaling Technology (3189S)	Rabbit	1:1000
Vinculin	Cell Signaling Technology (13901)	Rabbit	1:1000
Perilipin 4	Sigma (ABS526)	Rabbit	1:1000
ACLY	Cell Signaling (4332S)	Rabbit	1:1000
AceCS1	Cell Signaling (D19C6)	Rabbit	1:1000
ACC1	Cell Signaling (4190)	Rabbit	1:1000
ACADL	Proteintech (17526-1-AP)	Rabbit	1:1000
HADHA	Proteintech (10758-1-AP)	Rabbit	1:1000
EHHADH	Proteintech (26570-1-AP)	Rabbit	1:1000
ACADS	Santa Cruz (sc-365953)	Mouse	1:2000
CPT2	Abcam (ab181114)	Rabbit	1:1000

Table 13 List of secondary HRP-linked antibodies and appropriate dilutions used for WB.

Antigen	Company	Host	Dilution
Anti-Goat Horseradish peroxidase (HRP)-linked	Jackson Immuno Research (705-035-003)	Donkey	1:1000
Anti-Mouse HRP-linked	GE Healthcare (NA931)	Sheep	1:5000
Anti-Rabbit HRP-linked	GE Healthcare (NA934V)	Sheep	1:5000
Anti-rat IgG HRP-linked	Jackson Immuno Research	Goat	1:5000

	(112-035-003)		

2.2.5. Omic analysis

2.2.5.1. Lipidomics

For lipid analyses mouse tissue samples were homogenized in deionized water (10 µl/1 mg wet weight) using the Precellys 24 Homogenisator (Peqlab) at 6.500 rpm for 30 sec. The protein content of the homogenate was routinely determined using bicinchoninic acid.

Sphingolipid (ceramides, sphingomyelins) and cholesterol levels in mouse small intestinal tissue were determined by Liquid Chromatography coupled to Electrospray Ionization Tandem Mass Spectrometry (LC-ESI-MS/MS). For sphingolipid analyses, 50 µl of tissue homogenate was used. Lipid extraction and LC-ESI-MS/MS analysis were performed as previously described. For the determination of cholesterol levels, 25 µl of tissue homogenate were extracted and processed as previously described (Mourier, Motori et al. 2015). Levels of cholesteryl esters (CEs), di- and triacylglycerols (DAGs, TAGs) and glycerophospholipids in mouse small intestinal tissue were determined by Nano-Electrospray Ionization Tandem Mass Spectrometry (Nano-ESI-MS/MS). 10 µl (for DAGs) or 5 µl (for TAGs and CEs) of tissue homogenate was diluted to 500 µl with Milli-Q water and mixed with 1.875 ml of chloroform/methanol/37 % hydrochloric acid 5:10:0.15 (v/v/v). 20 µl of 4 µM d5-TG Internal Standard Mixture I (for TAGs), 15 µl of 256 µM Cholesteryl ester 19:0 (for CEs) or 20 µl of 4 µM d5-DG Internal Standard Mixtures I and II (for DAGs) (Avanti Polar Lipids) were added. Lipid extraction and Nano-ESI-MS/MS analysis of DAGs and TAGs were performed as previously described (Rashid et al, 2019). The detection of CE species was conducted in the positive ion mode by scanning for precursors of m/z 369 Da at a collision energy of 15 eV and with a declustering potential of 100 V, an entrance potential of 10 V, and a cell exit potential of 14 V. Levels of glycerophospholipids (i.e. phosphatidylcholines, -ethanolamines, -inositols, -serines, and -glycerols) were determined by performing extraction and Nano-ESI-MS/MS measurement of 10 µl of tissue homogenate as previously described (Kumar, Bouameur et al. 2015). The lipidomics data included in this thesis have been performed in collaboration with the group of Dr. Susanne Brodesser from the CECAD Lipidomics/Metabolomics facility.

2.2.5.2. Metabolomics

2.2.5.2.1. Metabolite Extraction

Metabolite extraction solution (50% methanol, 30% acetonitrile, 20% water, 5uM valine-d8 as internal standard) was added to (10-20mg) frozen small intestine tissue samples at an extraction ratio of 25ul/mg on dry ice. Samples were then homogenized using a Precellys 24 tissue homogenizer (Bertin technologies). The resulting sample suspension was vortexed, mixed at 4^{o}C in a Thermomixer for 15 min at 1,500 rpm and then centrifuged at 16,000 x g for 20 min at 4^{o}C. The supernatant was collected for LC-MS analysis.

2.2.5.2.2. Metabolite measurement by LC-MS

LC-MS chromatographic separation of metabolites was achieved using a Millipore Sequant ZIC-pHILIC analytical column (5 µm, 2.1 × 150 mm) equipped with a 2.1 × 20 mm guard column (both 5 mm particle size) with a binary solvent system. Solvent A was 20 mM ammonium carbonate, 0.05% ammonium hydroxide; Solvent B was acetonitrile.

The column oven and autosampler tray were held at 40°C and 4 °C, respectively. The chromatographic gradient was run at a flow rate of 0.200 mL/min as follows: 0–2 min: 80% B; 2-17 min: linear gradient from 80% B to 20% B; 17-17.1 min: linear gradient from 20% B to 80% B; 17.1-22.5 min: hold at 80% B. Samples were randomized and analysed with LC–MS in a blinded manner with an injection volume of 5 µl. Pooled samples were generated from an equal mixture of all individual samples and analysed interspersed at regular intervals within sample sequence as a quality control. Metabolites were measured with a Thermo Scientific Q Exactive Hybrid Quadrupole-Orbitrap Mass spectrometer (HRMS) coupled to a Dionex Ultimate 3000 UHPLC. The mass spectrometer was operated in full-scan, polarity-switching mode, with the spray voltage set to +4.5 kV/-3.5 kV, the heated capillary held at 320 °C, and the auxiliary gas heater held at 280 °C. The sheath gas flow was set to 25 units, the auxiliary gas flow was set to 15 units, and the sweep gas flow was set to 0 unit. HRMS data acquisition was performed in a range of *m/z* = 70–900, with the resolution set at 70,000, the AGC target at 1×10^6, and the maximum injection time (Max IT) at 120 ms. Metabolite identities were confirmed using two parameters: (1) precursor ion m/z was matched within 5 ppm of theoretical mass predicted by the chemical formula; (2) the retention time of metabolites was within 5% of the retention time of a purified standard run with the same chromatographic method.

2.2.5.2.3. Data analysis of metabolomic data

Chromatogram review and peak area integration were performed using the Thermo Fisher software Tracefinder (v.5.0). The peak area for each detected metabolite was subjected to the “Filtering 80% Rule”, half minimum missing value imputation, and normalized against the total ion count (TIC) of that sample to correct any variations introduced from sample handling through instrument analysis. Samples were excluded after performing testing for outliers based on geometric distances of each point in the PCA score plot as part of the muma package (v.1.4)(Gaude, Chignola et al. 2013). Afterwards, differential metabolomics analysis was performed. In detail, the R package „gtools“(v.3.8.2) (https://cran.r-project.org/web/packages/gtools/index.html) was used to calculate the Log2FC using the functions „foldchange“and „foldchange2logratio“(parameter base=2). The corresponding p-value was calculated using the R base package stats (v.4.0.5) (https://www.r-project.org/) with the function “t.test” (SIMPLIFY = F). The p-value was adjusted using the stats base function „p.adjust“(method= "bonferroni"). Volcano plots were generated using the EnhancedVolcano package(Blighe, Rana et al. 2021) (v. 1.8.0).

2.2.5.3. Proteomics

2.2.5.3.1. In-solution digestion for MS

Samples for MS analysis were prepared by in-solution digestion. 20 µg of protein were precipitated for at least one hour in four volumes (v:v) of ice-cold acetone and protein pellets were extracted by centrifugation at 13,000 g for 10 min and dissolved in Urea buffer (6 M Urea, 2 M Thiourea in 10 mM HEPES, pH 8.0). Urea-containing samples were reduced by applying tris(2-carboxyethyl)phosphine (TCEP) at a final concentration of 10 mM, alkylated with chloroacetamide (CAA) at a final concentration of 40 mM and incubated for 1 h RT. Samples were then digested with 1 µL LysC for 2h at RT, diluted with 50 mM ABC to a Urea concentration of 2 M, incubated with 1 µL 0.5 mg/mL trypsin overnight at RT, acidified to 1% FA and purified using Stop and Go extraction tips (StageTips)(Rappsilber, Mann et al. 2007).

2.2.5.3.2. MS-based proteome analysis

Proteome samples were analyzed using liquid chromatography tandem mass spectrometry on an Orbitrap Eclipse™ Tribrid™ Mass Spectrometer (Thermo Fisher) with FAIMS Pro device using a combination of two compensation voltages of -50 V and -70 V. Chromatographic peptide separation was achieved on a 50 cm reversed phase nanoHPLC-columns (ID 75 µm, PoroShell C18 120, 2.4 µm) coupled to an EASY-nLC 1200 HPLC system and a binary buffer system A (0.1% FA) and B (80% ACN/0.1% FA). Samples derived from in-solution digestion were measured over a 120 min gradient, raising the content of buffer ACN from 3.2 to 22% over 102 min, from 22 to 45% over 8 min and from 45 to 76% over 2 min. The column was washed with 76% ACN for 8 min. Full MS spectra (300–1,750 m/z) were recorded at a resolution (R) of 60,000, maximum injection time (max. IT) of 20 ms and AGC target of 6e5. The 20 most abundant ion peptides in each full MS scan were selected for HCD fragmentation at nominal collisional energy (NCE) of 30. MS2 spectra were recorded at R = 15,000, a maximum IT of 22 ms, and an AGC target of 1e5. This MS acquisition program was alternatively run for both FAIMS compensation voltages to cover different peptide fractions.

2.2.5.3.3. MS data processing and analysis

The generated MS raw data were analysed using MaxQuant analysis software and the implemented Andromeda software (1.6.14) (Cox and Mann 2008, Cox, Neuhauser et al. 2011). Peptides and proteins were identified using the canonical mouse UniProt database (downloaded 08/2019) with common contaminants. All parameters in MaxQuant were set to the default values. Trypsin was selected as the digestion enzyme, and a maximum of two missed cleavages was allowed. Methionine oxidation and N-terminal acetylation were set as variable modifications, and carbamidomethylation of cysteines was chosen as a fixed modification. The label-free quantification (LFQ) algorithm was used to quantify the measured peptides and the "match between runs" option was enabled to quantify peptides with a missing MS2 spectrum. Subsequent statistical analysis was performed using Perseus (1.5.8.5) software. Potential contaminants and reverse peptides were excluded, and values were log2 transformed. Raw files were assigned to two groups (TG and WT) and proteinGroups were filtered for 4 valid values in at least one group before missing values were replaced from normal distribution (width: 0.3; down shift: 1.3). Welch's Student t-test with S0=0.1 and a permutation-based FDR of 0.01 with 500 randomizations was performed to obtain differentially regulated proteins between the two groups. Identified proteins were annotated with the following Gene Ontology terms: Biological Process, Molecular Function, and Cellular Compartment, and the Reactome Pathway database. Fisher Exact test was conducted on the FDR<0.05 significant protein subset using the Benjamini-Hochberg FDR with a threshold of 0.02. Finally, graphical visualization was achieved using Instant Clue software (Nolte, MacVicar et al. 2018).

2.2.5.3.4. Data visualization

Gene set enrichment (GSE) methods were applied using gene set enrichment analysis (GSEA) and over representation analysis (ORA). In detail, GSEA was performed by using gene sets published on the MsigDB (Reactome, KEGG, Biocarta and Hallmarks) (Subramanian, Tamayo et al. 2005) and by Han et all (Han, Back et al. 2013) (ATF4) using the packages fgsea (Sergushichev 2016) (v.1.16.0) and GSEABase (Morgan, Falcon et al. 2021) (v. 1.52.1). Volcano plots were generated using the EnhancedVolcano package(Blighe, Rana et al. 2021) (v. 1.8.0). The ORA was performed using the “enrich_GO” function (parameters: keyType = "ENTREZID", OrgDb = org.Mm.eg.db, ont = "ALL", pAdjustMethod = "BH", qvalueCutoff = 0.1) of the clusterProfiler package (Yu, Wang et al. 2012) (v. 3.16.1).

The output data are plotted using the “emapplot” function of the enrichplot package (v.1.8.1) (https://www.bioconductor.org/packages/release/bioc/html/enrichplot.html (parameters: pie_scale=1, showCategory=40, layout = "nicely").

2.2.5.3.5. QuantSeq 3’ mRNA sequencing

RNA quality was evaluated based on RNA integrity number (RIN) and OD260/280 and OD260/230 ratios. RIN value was determined using TapeStation4200 and RNA Screen Tapes (Agilent Technologies). Gene expression was determined using QuantSeq 3’ mRNA-Seq Library Prep Kit FWD for Illumina (Lexogen). Sample exclusion criteria were OD260/280<1.8, OD260/230<1.5 and RIN<7. Illumina adapters were clipped off the raw reads using cutadapt with standard parameters and a minimum read length of 35 after trimming (shorter reads were discarded). QuantSeq specific features were deliberately not removed to avoid loss of reads. Trimmed reads were mapped to a concatenation of the mouse genome (Mus_musculus.GRCm38.dna.chromosome.*.fa.gz, downloaded from ftp://ftp.ensembl.org/pub/release-100/fasta/mus_musculus/dna/) and the ERCC92 Spike In sequences (downloaded from https://assets.thermofisher.com/TFS-Assets/LSG/manuals/ERCC92.zip), using subread-align version v2.0.1 with parameters -t 0 -d 50 -D 600 --multiMapping -B 5. Genomic matches were counted using featureCounts with parameters -F "GTF" -t "exon" -g "gene_id" --minOverlap 20 -M --primary -O --fraction -J -Q 30 -T 4. The genome annotation used was Mus_musculus.GRCm38.100.gtf (downloaded from ftp://ftp.ensembl.org/pub/release-100/gtf/mus_musculus/), augmented by entries for the ERCC92 Spike Ins. All analyses were done in R-4.0.0, using functionality of Bioconductor version 3.11.

For differential gene expression analysis, package DESeq2 was used (https://bioconductor.org/packages/release/bioc/html/DESeq2.html).

Pairwise comparisons were performed between genotypes tg and wt (differential_expression_DESeq2_tg_VS_wt.xlsx). Genes were excluded from a DESeq2 run if they had a zero count in more than half of the samples in either of the conditions compared. Note that DESeq2 sets the p-value and the adjusted p-value to NA for genes with too few counts or with extreme outlier counts. Such genes were removed post-analysis from the DESeq2 output. The output tables were augmented by gene symbols and descriptions, derived from the org.Mm.eg.db annotation package via function AnnotationDbi::mapIDs(https://bioconductor.org/packages/release/bioc/html/AnnotationDbi.html). In addition, the raw read counts per gene and sample, as returned by featureCounts, were appended to the rows of each output table. For Gene Ontology over-representation analysis and visualization, Bioconductor version 3.11 package clusterProfiler (http://yulab-smu.top/clusterProfiler-book/) was used with R-4.0.0. The clusterProfiler::enrichGO function was queried with significant genes (pvalue or padj <= 0.05) from one DESeq2 run at a time, using parameters pvalueCutoff =0.05, qvalueCutoff =0.2 and taking annotations from org.Mm.eg.db (OrgDb=org.Mm.eg.db). The distribution of differentially expressed genes was visualized on 32 hand-selected KEGG pathway diagrams (see Table XYZ), using Bioconductor version 3.11 package pathview with R-4.0.0. We made minor modifications to the source code of the package, to improve its handling of multiple query genes mapping to the same diagram node. While the original package version does allow to color a node according to a summarized regulation value (e.g., the mean or median) of multiple mapping genes, nevertheless the node label is always the first mapping gene. This is confusing if the first gene in the list is not representative of the behavior of the remaining genes (e.g., it is down-regulated, while most genes in the list are up-regulated). We added the possibility to label nodes by that gene which actually attains the minimum or maximum regulation among the genes mapping to the node, or by the gene whose regulation is closest to the median regulation. The pathview function can plot any numerical measure of regulation attached to the query genes. Here, we defined Regulation: = -log10 (*padj*) * sign (*log2FoldChange*) where "padj" and "log2FoldChange are the corresponding columns from the DESeq2 output. This "signed exponent of the p-value" takes extreme negative (positive) values for highly significantly down (up)-regulated genes.

2.2.6. Metabolic tracer studies

2.2.6.1. Postprandial glucose and fat tolerance tests

Mice were fasted for 2 hours before receiving an oral gavage of 300 µl of a glucose-lipid-emulsion containing triolein (3.6 g/kg body weight), lecithin (0.36 g/ kg body weight) and glucose (2 g/kg body weight), traced with ^{3}H-triolein (1.4 MBq/kg body weight) and ^{14}C -deoxyglucose (1.7 MBq/kg body weight). After 2 hours, mice were anaesthetized and transcardially perfused with PBS containing 10 U/ml heparin. Organs were harvested, weighed and dissolved in 10x (v/w) Solvable™ (Perkin Elmer), and radioactivity (in dpm) was measured by scintillation counting using a Perkin Elmer Tricarb Scintillation Counter. Uptake of radioactive tracers was calculated per total organ weights.

2.2.6.2. Chylomicron production studies

Mice were injected with Tyloxapol (500 mg in 0.9% NaCl/ kg body weight) to block vascular lipolysis. Then, mice received an oral gavage of a lipid emulsion with triolein (3.6 g/kg body weight) and lecithin (0.36 g/ kg body weight) that are traced with -cholesterol (1.4 MBq/kg body weight) and ^{3}H-triolein (1.7 MBq/kg body weight). Blood was collected from tail vein 30, 60 and 120 min after gavage. Plasma triglycerides were determined by standard colorimetric assays (Roche) and radioactivity was measured by scintillation counting.

2.2.6.3. Plasma parameters

Plasma was generated by centrifugation of EDTA-spiked blood for 10 min at 10,000 rpm at 4°C in a bench top centrifuge. Free glycerol was determined photometrically using the Free Glycerol Reagent (F6428, SIGMA). For lipoprotein profiling, 150µl pooled plasma was diluted with equal amount of FPLC buffer (total 300µl), which was separated by fast-performance liquid chromatography (FPLC) on a Superose 6 10/300 GL column (GE Healthcare) with a flow rate of 0.5 mL/min. Forty fractions (0.5 ml each) were collected and cholesterol/triglyceride concentrations were measured in each one.

2.2.7. Statistical analysis

Data shown in column graphs represent the mean ± S.E.M., as indicated in the figure legends. When data fulfilled the criteria for Gaussian distribution, unpaired Student's t-tests were performed; otherwise the nonparametric Mann–Whitney test was chosen. Multiple pairwise comparisons of groups over time by repeated measures were evaluated by two-way ANOVAs with Bonferroni correction (the corrected *p* values are given for comparison between genotypes at each time point). The number of mice analysed in each experiment is described in the respective figure legends. Statistical analysis was performed with Prism6, GraphPad. $*p \leq 0.05$; $**p \leq 0.01$; $***p \leq 0.005$; $****p \leq 0.001$ for all figures.

2.2.8. Data availability / accessibility

The mass spectrometry proteomics data have been deposited to the ProteomeXchange Consortium via the PRIDE (Perez-Riverol, Csordas et al. 2019) partner repository with the dataset identifier PXD026934. All the results that have been generated and analyzed in this thesis, incuding original microscopic images and raw data from the qRT-PCR, microarray gene expression and RNAseq, as well as lipidomic and metabolomic analysis can be accessed via the server provided by the University of Cologne (nas7.uni-koeln.de and nas9.uni-koeln.de) and allocated to the group of Manolis Pasparakis. Paraffin blocks with mouse biopsies are kept in the Histology lab (CECAD Research Center) that belongs to the group of Manolis Pasparakis. Materials and reagents described in this study are kept in the freezers (-20ºC or -80ºC) or fridges (4ºC) of the lab of Manolis Pasparakis. RNA, cryomolds and intestinal biopsies dissected from mice used in this study are stored in -80ºC freezers of Manolis Pasparakis lab.

3. Results

3.1. Generation and phenotypic characterization of mice with intestinal epithelial cell specific DARS2 ablation.

3.1.1. DARS2$^{IEC\text{-}KO}$ mice develop spontaneous phenotype that results in premature death.

In order to functionally delineate the role of mitochondria in the intestinal epithelial cell (IEC) function and homeostasis, we generated mice lacking DARS2 specifically in IECs. Mice carrying loxP-flanked *Dars2* alleles (*Dars2*$^{fl/fl}$) (Dogan, Pujol et al. 2014) were crossed with *Vil1-Cre* mice (Madison, Dunbar et al. 2002), which express Cre recombinase under the *Villin* promoter (*Dars2*$^{fl/fl}$ *Vil1-Cre,* hereafter referred to as DARS2$^{IEC\text{-}KO}$). Genetic recombination mediated by *Vil1-Cre*, begins in the visceral endoderm at embryonic day 9 (E9), whereas in the whole intestinal epithelium around E12.5 (el Marjou, Janssen et al. 2004). DARS2$^{IEC\text{-}KO}$ mice were born at expected Mendelian ratios (Figure 14a), but developed a spontaneous severe phenotype apparent already early after birth. Immunoblot analysis of total protein extracts from primary IECs from 7-day old DARS2$^{IEC\text{-}KO}$ pups revealed efficient ablation of DARS2 (Figure14b). Mice lacking DARS2 in the intestinal epithelium showed strongly reduced body weight, up to 50% compared to littermate controls. In addition to cachexia, the phenotype is manifesting by watery, bulky and oily feaces (diarrhoea), dehydrated skin, ruffled fur and unstable walking (Figure 14c, d). DARS2$^{IEC\text{-}KO}$ mice failed to thrive and died prematurely within the first 4 weeks of life (Figure 14e), thus indicating that DARS2 plays an important role in maintaining intestinal tissue homeostasis.

a

Dars2$^{fl/fl}$; villinCre tg/wt x Dars2$^{fl/wt}$; villinCre wt/wt	***Dars2*$^{fl/fl}$; villinCre wt/wt**	***Dars2*$^{fl/wt}$; villinCre wt/wt**	***Dars2*$^{fl/fl}$; villinCre tg/wt**	***Dars2*$^{fl/wt}$; villinCre tg/wt**
Expected	47 (25%)	47 (25%)	47 (25%)	47 (25%)
Observed	45 (23,9%)	48 (25,5%)	46 (24,4%)	49 (26%)

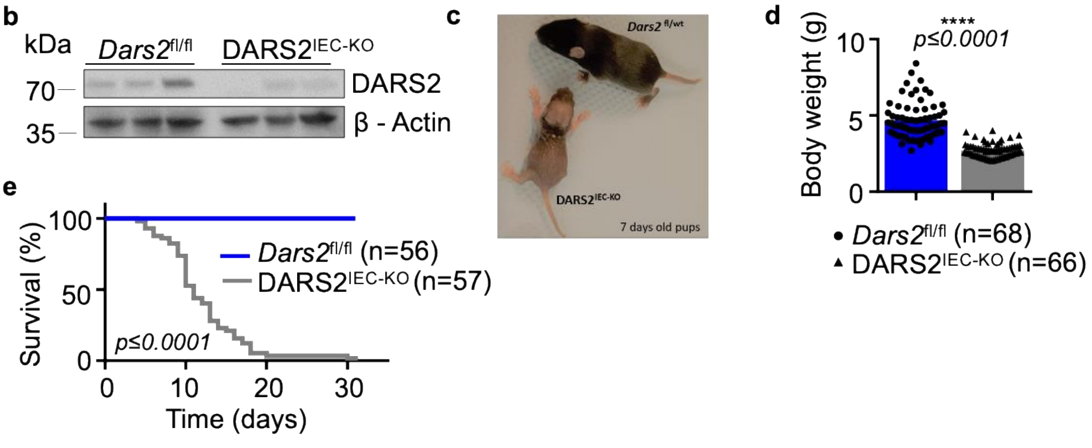

Figure 14. DARS2$^{IEC\text{-}KO}$ mice fail to thrive and show premature lethality.

(a) Table depicting expected and observed absolute number and possibilities of obtained offsprings with the indicated genotypes coming from the breeding of *Dars2*$^{fl/fl}$;VillinCre tg/wt mice with *Dars2*$^{fl/wt}$;VillinCre wt/wt mice, (b) Total protein extracts from primary IECs from 7-day-old *Dars2*$^{fl/fl}$ (n=3) and DARS2$^{IEC\text{-}KO}$ (n=3) mice were analyzed by immunoblot with the indicated antibodies. Each lane represents one mouse. Numbers indicates protein size (kDa), (c) Representative macroscopic image of mice with the indicated genotypes taken at the age of 7 days (n=5), (d) Body weight of *Dars2*$^{fl/fl}$ mice (n=68) and DARS2^{IEC-KO} mice (n=68) at the age of 7 days, (e) Kaplan-Meier survival curve for *Dars2*$^{fl/fl}$ mice (n=56) and DARS2^{IEC-KO} mice (n=57), Nonparametric Mann–Whitney U test was performed for statistical analysis. Asterisks indicate the level of statistical analysis **** $p \leq 0.0001$.

Macroscopically, small intestine and colon from DARS2^{IEC-KO} mice were considerably thicker and shorter compared to their wt littermates (Figure 15).

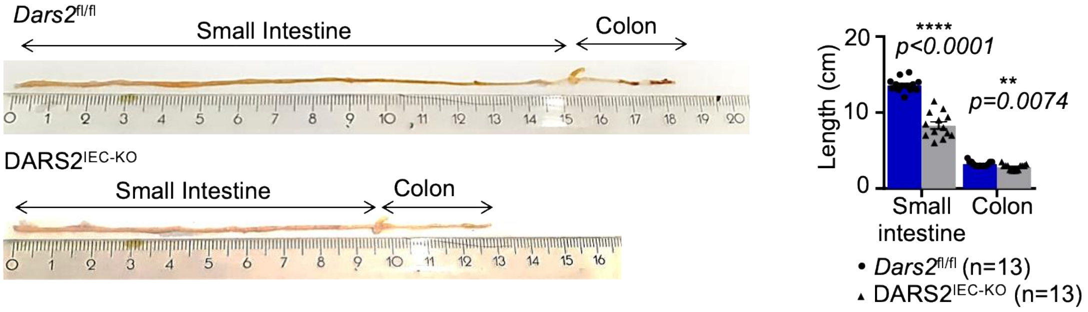

Figure 15. DARS2^{IEC-KO} mice exhibit markedly shorter small intestine and colon.

Representative pictures and quantification of the length of the small intestine and colon in 7-day-old DARS2^{IEC-KO} (n=13) and Dars2$^{fl/fl}$ littermates (n=13).

3.1.2. Loss of DARS2 causes strong mitochondrial dysfunction in the small intestine of DARS2^{IEC-KO} mice.

To assess if OXPHOS was severely impaired upon efficient DARS2 ablation, immunoblot analysis of individual respiratory chain (RC) complexes was performed in total protein primary IEC extracts. Interestingly, DARS2^{IEC-KO} pups revealed strongly reduced expression of fully steady – state levels of CI, CIII, CIV and CV (Figure 16a). As additionally indicated by BN-PAGE analysis on isolated mitochondria from total small intestinal tissue, the levels of all individual RC complexes containing mitochondrially-encoded subunits (CI, CIII, CIV and CV) were acutely decreased (Figure 16b).

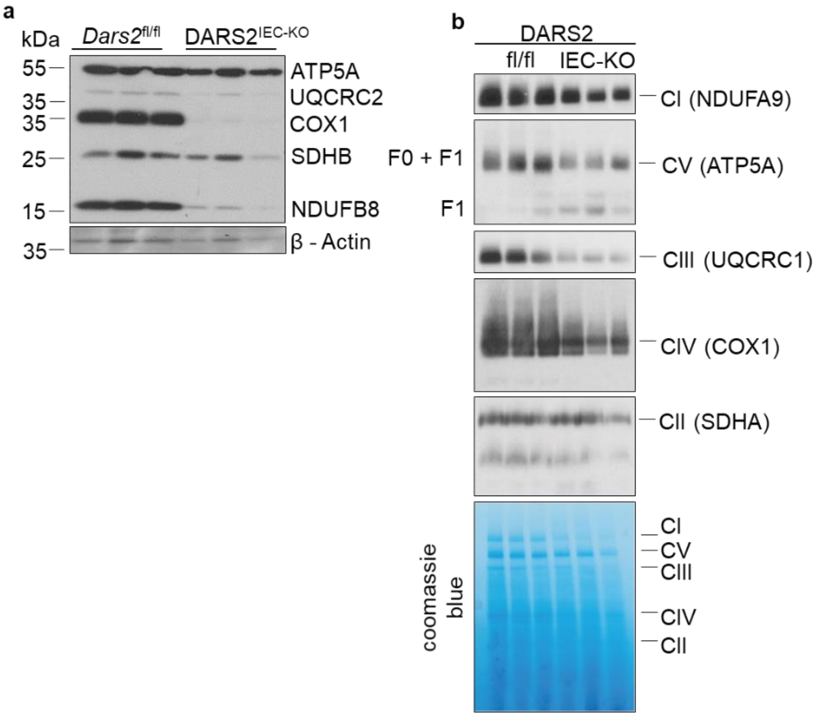

Figure 16. Diminished formation of individual respiratory chain complexes in intestinal mitochondria from DARS2$^{IEC\text{-}KO}$ mice.

(a) Total protein extracts from primary IECs from 7-day-old *Dars2*$^{fl/fl}$ (n=3) and DARS2$^{IEC\text{-}KO}$ (n=3) mice were analyzed by immunoblot with the indicated antibodies. Each lane represents one mouse (b) BN-PAGE analysis of individual respiratory complexes, isolated from the small intestine of 7-day-old *Dars2*$^{fl/fl}$ (fl/fl) and DARS2$^{IEC\text{-}KO}$ (IEC-KO) mice. Each individual lane represents mitochondria isolated from one mouse (n=3 per genotype). Numbers indicates protein size (kDa). Respiratory complexes were visualized by immunoblotting with indicated antibodies. Coomassie blue stains and Complex II levels (anti-SDHA) were used as the loading controls. The experiment depicted in Figure 16b was performed in collaboration with Dr. Karolina Szczepanowska from the lab of Prof. Dr. Aleksandra Trifunovic, CECAD, Cologne.

Consequently, noticeable decline in the formation of OXPHOS supercomplexes was detected in mitochondria from DARS2$^{IEC\text{-}KO}$ mice, including high-molecular-weight respirasome highlighted by CI *in gel* activity (Figure 17). In general, the CIV-containing supercomplexes were predominantly affected. Likewise, the levels of ATP synthase (CV) were also reduced and accompanied by accumulation of free, nuclearly-encoded F1 part of the complex, a frequent manifestation of severe mitochondrial gene expression defects. In contrast, the level of CII that is solely encoded by the nuclear genome remained unchanged (Figure 17). Altogether, those data suggest that DARS2 depletion in the small intestine results in strong mitochondrial gene expression defect (deregulated translation), which leads to preferential loss of mitochondrially encoded respiratory chain complexes, and presumably associates with severe OXPHOS dysfunction.

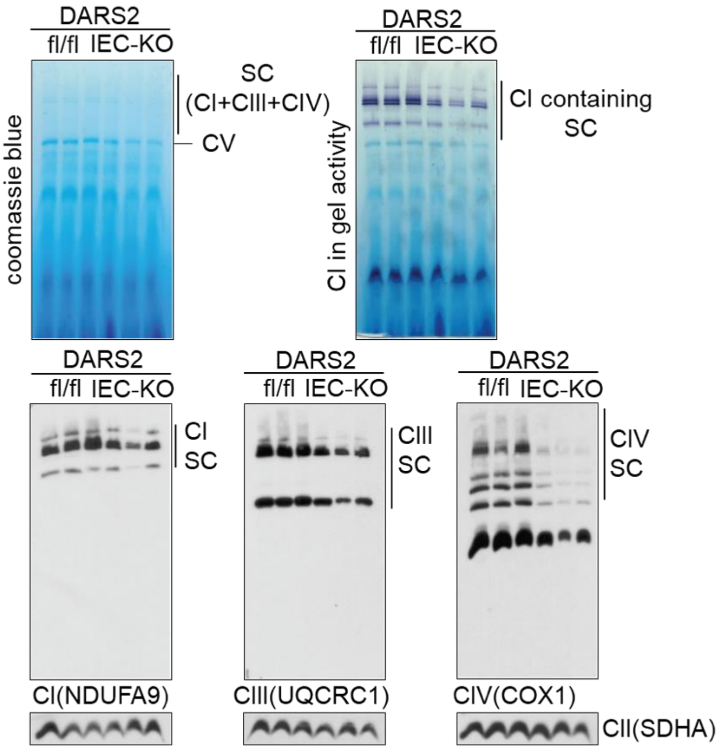

Figure 17. Reduced formation of respiratory supercomplexes in intestinal mitochondria from DARS2^{IEC-KO} mice.

BN-PAGE analysis of OXPHOS supercomplexes, isolated from the small intestine of 7-day-old *Dars2*$^{fl/fl}$ (fl/fl) and DARS2^{IEC-KO} (IEC-KO) mice. Each individual lane represents mitochondria isolated from one mouse (n=3 per genotype). Respiratory complexes were visualized by immunoblotting with indicated antibodies. The activity of supercomplex-associated Complex I was determined with in-gel assay Coomassie blue stains and Complex II levels (anti-SDHA) were used as the loading controls. The experiment depicted in Figure 17 was performed in collaboration with Dr. Karolina Szczepanowska from the lab of Prof. Dr. Aleksandra Trifunovic, CECAD, Cologne.

Further visualization of the RC function was achieved by COX/SDH double-labelling histochemical staining that enables the sequential analysis of the enzymatic activities of cytochrome c oxidase (COX) and succinate dehydrogenase (SDH) *in situ* (Ross 2011). Remarkably, consistent with the diminished respiratory subunit expression, strong COX deficiency was apparent in small intestinal cryosections from 7-day-old DARS2^{IEC-KO} mice. (Figure 18a). IECs with dysfunctional COX activity represented by the intense blue colour derived from the nuclear-encoded SDH, which easily penetrates once COX activity is low or completely absent (Figure 18a). Furthermore, TEM analysis displayed swollen mitochondria with less densely packed and fragmented cristae in SI enterocytes of DARS2^{IEC-KO} mice in sharp contrast to the compact, well-formed mitochondria of their wt littermates, implicating defects in their functionality. Surprisingly, mitochondrial biogenesis was markedly reduced in the small intestine of Moreover, DARS2^{IEC-KO} mice exhibited disrupted brush border microvillus architecture with reduced density and height (Figure 18b). Therefore, DARS2 ablation caused severe mitochondrial deficiency in enterocytes.

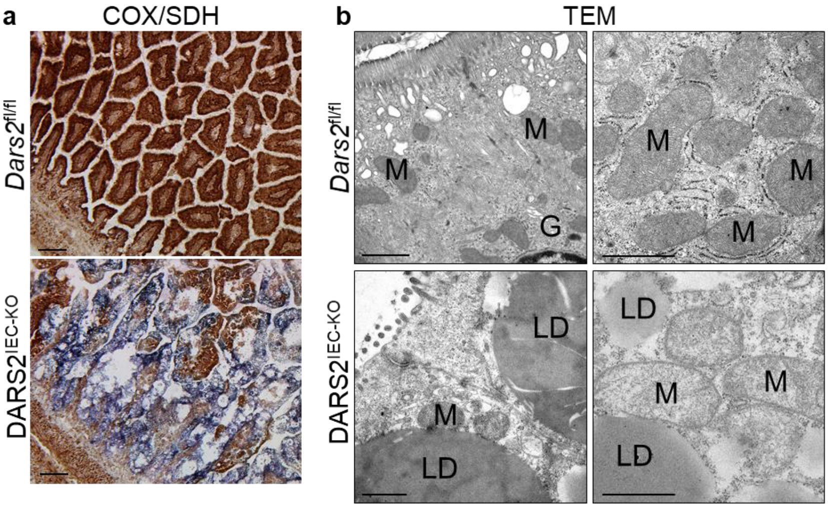

Figure 18. Complete loss of DARS2 induces robust mitochondrial dysfunction in the small intestine of DARS2$^{IEC\text{-}KO}$ mice.

(a) Representative images of SI sections from *Dars2*$^{fl/fl}$ (n=8) and DARS2$^{IEC\text{-}KO}$ (n=8) mice stained with enzyme histochemical staining for cytochrome c oxidase (COX) and succinate dehydrogenase (SDH). Scale bars = 50um, (b) Representative transmission electron micrographs (TEM) of SI sections from 7-day-old *Dars2*$^{fl/fl}$ and DARS2$^{IEC\text{-}KO}$ mice (n=3 per genotype). Scale bars = 1um. M, mitochondria; LD, lipid droplet; G, Golgi

3.1.3. DARS2$^{IEC\text{-}KO}$ mice display severe intestinal pathology accompanied by impaired intestinal epithelial cell proliferation, stemness and differentiation.

Histological examination of Hematoxylin and Eosin (H&E) intestinal sections from the small intestine of 7-day-old DARS2$^{IEC\text{-}KO}$ mice showed perturbed intestinal tissue architecture characterized by shortened and blunted villi, as well as frequent villus bridging and branches formation (Figure 19).

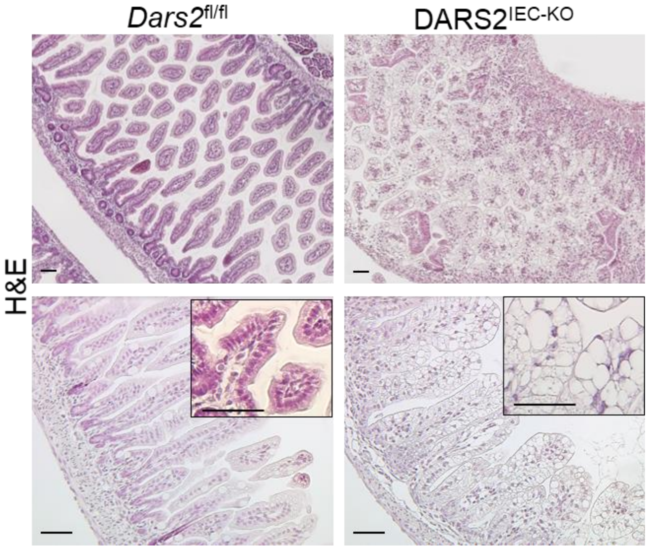

Figure 19. Marked intestinal architectural disorganization in DARS2$^{IEC\text{-}KO}$ mice.

Representative images of H&E stained ileal sections from 7-days-old *Dars2*$^{fl/fl}$ (n=17) and DARS2$^{IEC\text{-}KO}$ (n=19) mice. Scale bars = 50um. The highlighted box constitutes higher magnification inset.

Epithelial DARS2 deficiency leads to decreased cell proliferation in the intestinal crypts, since a significantly reduced number of Ki67+ proliferative cells were found aberrantly scattered along the intestinal tract and not exclusively in transit amplifying (TA) cells (Figure 20a). Furthermore, DARS2$^{IEC\text{-}KO}$ mice displayed notable reduction of Olfm4+ stem cells in crypt stem cells (Figure 20a). Concomitantly, relatively reduced mRNA expression of genes encoding intestinal stem cell–associated factors (*Lgr5, Olfm4*), was revealed by RT-qPCR expression analysis in the small intestine of DARS2$^{IEC\text{-}KO}$ mice, indicating a diminished stem cell compartment (Figure 20b).

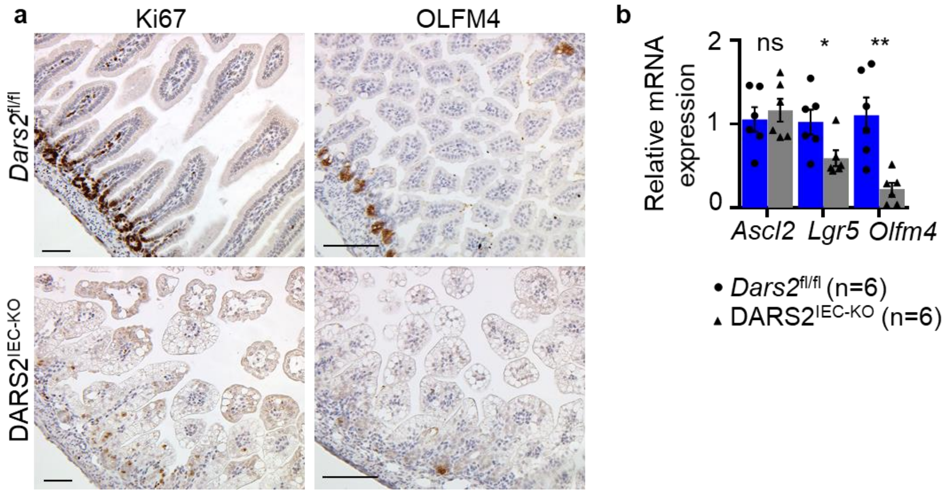

Figure 20. Impairment of proliferation and stemness in the intestinal epithelium of DARS2$^{IEC\text{-}KO}$ mice.

(a) Representative images of SI sections from 7-days-old *Dars2*$^{fl/fl}$ (n=6, n=9) and DARS2$^{IEC\text{-}KO}$ (n=6, n=9) mice immunostained against Ki67 or OLFM4. Scale bars = 50um. Positive staining is depicted in brown. Sections were counterstained with hematoxylin, which stains nuclei in blue, (b) Graph depicting relative mRNA expression of the indicated genes measured by qRT-PCR in the SI from 7-day-old *Dars2*$^{fl/fl}$ (n=6) and DARS2$^{IEC\text{-}KO}$ (n=6) mice normalized to *Tbp*. The graph presents mean ± SEM. Non-parametric Mann–Whitney U test was performed for statistical analysis ** $p \leq 0.01$,* $p \leq 0.05$, ns = not significant. OLFM4, Olfactomedin 4.

Noticeably, granule-filled PCs were highly elevated in the ileal crypt area of DARS2$^{IEC\text{-}KO}$ mice, pinpointed by lysozyme staining (Figure 21a). This observation was coupled with a robust increase in the mRNA expression of anti-microbial peptides specifically produced by PCs, such as defensins (*Defa-rs1, Defa-20*), lysozyme (*Lyz-1, Lyz-2*) and angiogenin 4 (*Ang4*) in the DARS2$^{IEC\text{-}KO}$ mice, as indicated by RT-qPCR and whole genome microarray analysis (Figure 21b, c). Thus, RC deficiency diminished the stem cell compartment and favoured differentiation of PCs, consistent with previous results suggesting that stem cells primarily depend on OXPHOS while PCs are predominantly glycolytic (Rodriguez-Colman, Schewe et al. 2017). In contrast to PCs, other intestinal specialized epithelial lineages, including mucus-producing Goblet cells and mature absorptive enterocytes were found greatly diminished, as suggested by notably reduced Periodic acid-Schiff (PAS) staining against glycosylated mucus – proteins, as well as staining against alkaline phosphatase (ALP), respectively (Figure 22).

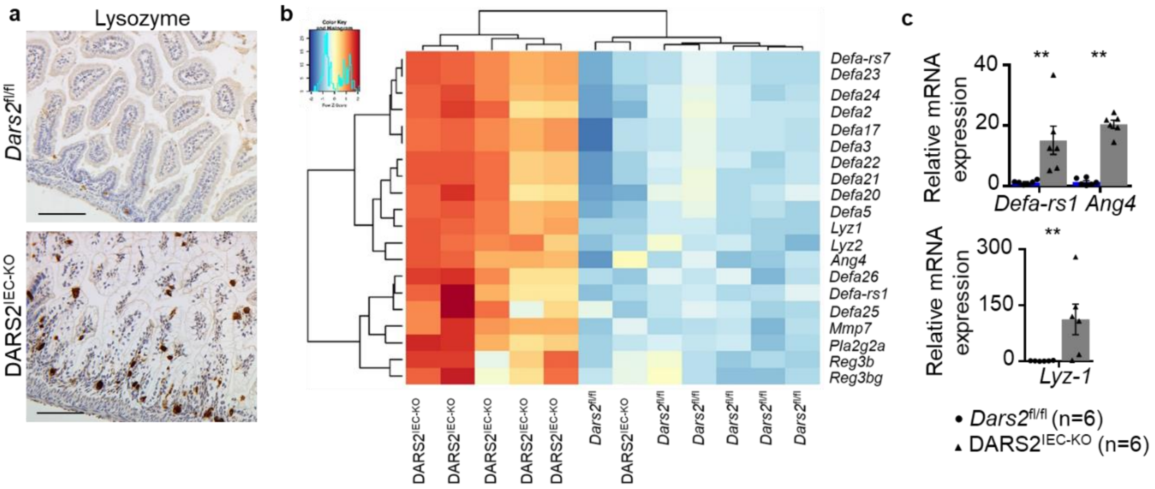

Figure 21. Highly abundant lysozyme-positive Paneth cells in DARS2^{IEC-KO} mice compared to littermate controls.

(a) Representative images of SI sections from 7-days-old *Dars2*$^{fl/fl}$ (n=6) and DARS2^{IEC-KO} (n=6) mice immunostained against Lysozyme. Scale bars = 50um. Positive staining is depicted in brown. Sections were counterstained with hematoxylin, which stains nuclei in blue, (b) Clustered heat map of gene expression data (log2) significantly upregulated or downregulated in DARS2^{IEC-KO} (fold change ≥ 2.5, p-value <0.005) small intestinal tissue. Each column represents one mouse. Each row represents one gene indicated on the right. Z-scores are shown. Color code: **Red**: high expression, **Blue**: low expression, (c) Graph depicting relative mRNA expression of the indicated genes measured by qRT-PCR in the SI from 7-day-old *Dars2*$^{fl/fl}$ (n=6) and DARS2^{IEC-KO} (n=6) mice normalized to *Tbp*. The graphs present mean ± SEM. Non-parametric Mann–Whitney U test was performed for statistical analysis ** p ≤ 0.01. The clustered heat map depicted in Figure 21b has been generated in collaboration with Antonis Papadakis from the group of Prof. Dr. Andreas Beyer, CECAD, Cologne.

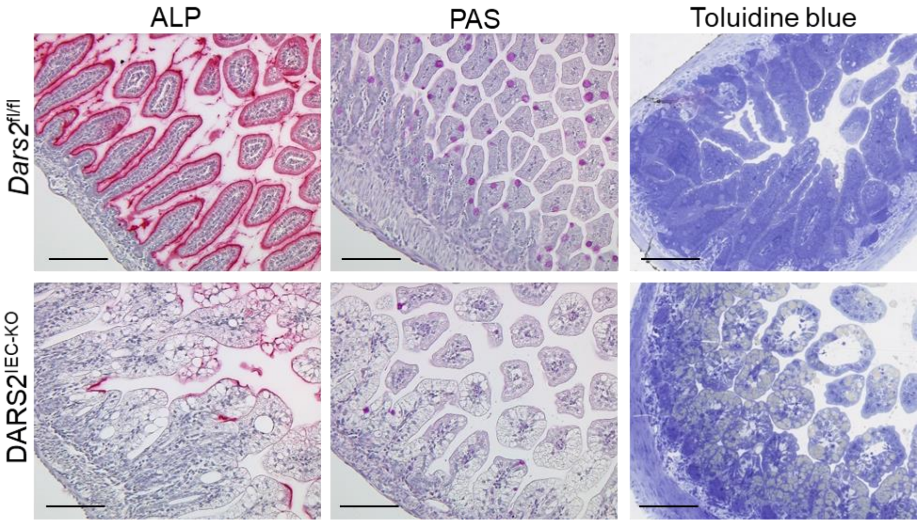

Figure 22. Greatly diminished numbers of differentiated epithelial cells in DARS2^{IEC-KO} mice.

Representative images of SI sections from 7-days-old *Dars2*$^{fl/fl}$ (n=7) and DARS2^{IEC-KO} (n=7) mice stained for alkaline phosphatase (ALP), Periodic acid-Schiff (PAS) and Toloudine blue (TBO). Positive staining is depicted in red, purple and blue respectively. Sections stained with ALP and PAS were counterstained with hematoxylin, which stains nuclei in blue. Scale bars = 50um.

3.1.4. Mild intestinal inflammation and IEC apoptosis in the small intestine of 1-week-old DARS2^{IEC-KO} mice.

Intestinal epithelial - specific DARS2 ablation leads to the development of a mild inflammatory response, characterized by focal recruitment of immune cells in the small intestine of 1-week old DARS2^{IEC-KO} mice. In particular, ileal sections from DARS2^{IEC-KO} mice showed increased number of infiltrating CD45+ immune cells and moderately enhanced amount of macrophages and neutrophils scattered throughout the lamina propria as indicated by positive immunostaining for F4/80 and Gr-1, respectively (Figure 23a). Concomitantly, immune cell infiltration was accompanied by slightly elevated expression of pro inflammatory cytokines and chemokines, including *Tnf*, *Il1b*, *Ccl2 and Il-6* (Figure 23b). Strikingly, only a few apoptotic IECs were detected mainly in the crypts and the TA compartment, as designated by immunostaining for the presence of cleaved activated caspase-3 and 8 positive cells, implying that apoptotic cell death might not be the main driver of this severe pathology (Figure 24).

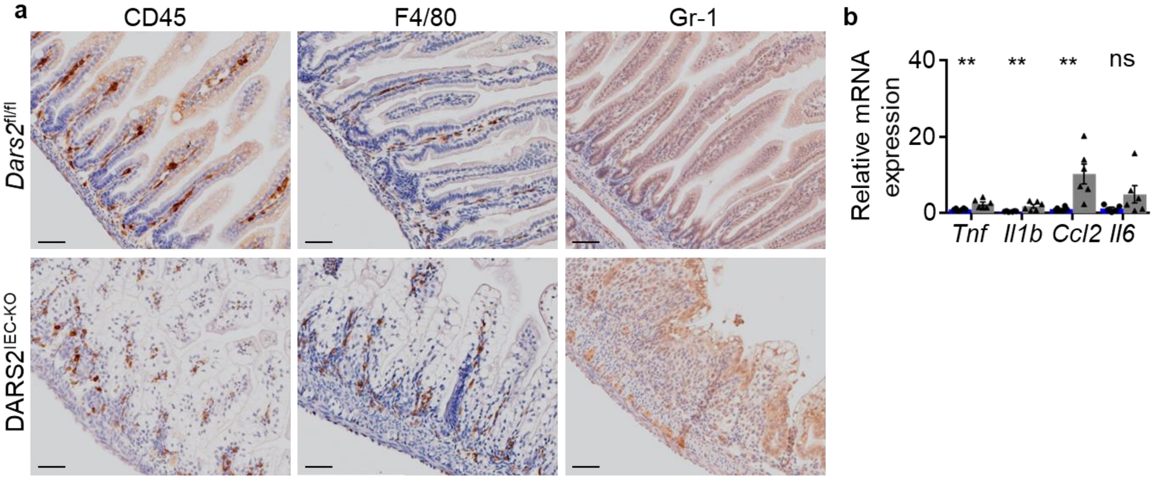

Figure 23. Slightly increased numbers of infiltrating immune cells in the mucosa of DARS2^{IEC-KO} mice.

(a) Representative images of SI sections from 7-days-old *Dars2*$^{fl/fl}$ (n=6) and DARS2^{IEC-KO} (n=6) mice immunostained for CD45, F4-80 and Gr-1 and counterstained with hematoxylin. Scale bars = 50um. Positive staining is depicted in dark brown, (b) Graph depicting relative mRNA expression levels of the inflammatory cytokine and chemokine measured by qRT-PCR in the SI from 7-day-old *Dars2*$^{fl/fl}$ (n=6) and DARS2^{IEC-KO} (n=6) mice normalized to *Tbp*. The graphs present mean ± SEM. Non-parametric Mann–Whitney U test was performed for statistical analysis ** $p \leq 0.01$, ns=not significant

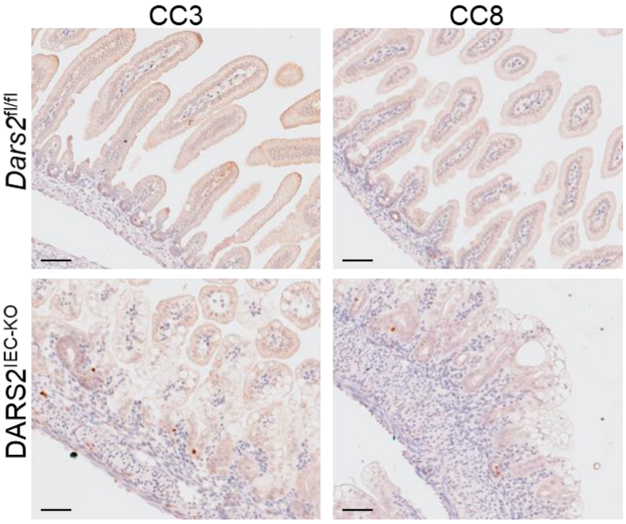

Figure 24. DARS2 deficiency does not sensitize IECs to apoptotic cell death.

Representative images of SI sections from 7-days-old *Dars2*$^{fl/fl}$ (n=10) and DARS2^{IEC-KO} (n=10) mice immunostained for CC3 and CC8 and counterstained with hematoxylin. Positive staining is depicted in dark brown. Scale bars = 50um.

3.1.5. DARS2^{IEC-KO} mice develop severe intestinal pathology with massive lipid accumulation within lipid droplets in the enterocytes and systemic alterations of lipid homeostasis.

Strikingly, a prominent microscopic feature of SI sections from DARS2^{IEC-KO} mice was the presence of extensive vesicular vacuolation within the enterocytes lining the villi. Therefore, we sought to investigate the origin of these pronounced vacuoles. Even though they resemble the characteristic intestinal Goblet cells, the absence of PAS staining, which detects glycoproteins and mucins, as well as the negative TBO staining for polysaccharides, highly excluded this possibility (Figure 22). In fact, positive Oil Red O (ORO) staining revealed that the vacuoles were stuffed with neutral lipids. Increased accumulation of large lipid droplets (LDs) was further confirmed by the presence of perilipin 2 (PLIN2), a protein coating the LDs (Lee, Zhu et al. 2009) (Figure 25). Hence, IECs in DARS2^{IEC-KO} mice contain large cytosolic LDs as opposed to the few tiny LDs found in IECs from *Dars2*$^{fl/fl}$ mice. Enchanced deposition of enormous LDs was also visualized by TEM analysis which revealed that LDs were frequently found in close proximity to existing mitochondria in IECs, hence proposing a potential reciprocal interaction among the two organelles (Benador, Veliova et al. 2018) (Figure18b).

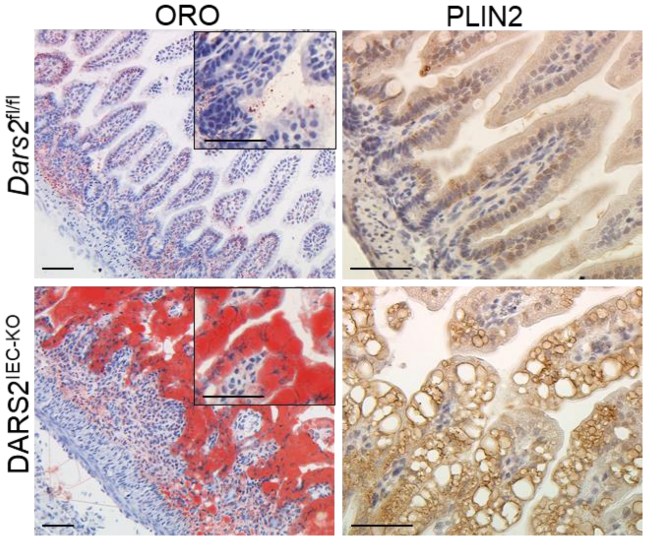

Figure 25. Lipid droplets are highly enriched in the enterocytes of DARS2^{IEC-KO} mice.

Representative images of SI sections from 7-days-old *Dars2*$^{fl/fl}$ and DARS2^{IEC-KO} mice stained with ORO (n=12 per genotype) and immunostained with PLIN2 (n=6 per genotype). Positive staining is presented as red and dark brown, respectively. All sections were counterstained with hematoxylin. The highlighted box constitutes higher magnification inset. Scale bars = 50um.

Next, we shought to investigate further the remarkable lipid-related phenotype of the DARS2^{IEC-KO} mice by performing extensive mass spectrometry (MS) – mediated lipidomic analysis. In line with the augmented intracellular lipid accumulation, we detected dramatically eleveted levels of lipids and particularly of triacylglycerol (TAG) species in the intestine of DARS2^{IEC-KO} pups compared to their *Dars2*$^{fl/fl}$ littermates (Figure 26a). As opposed to the intestine, the livers of DARS2^{IEC-KO} pups displayed a strong reduction of TAG levels in comparison to the control *Dars2*$^{fl/fl}$ mice (Figure 26b).

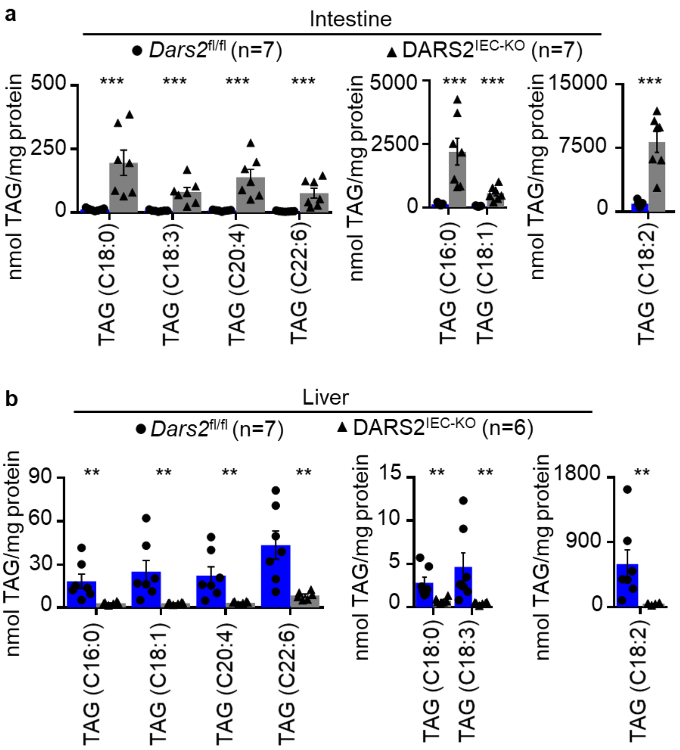

Figure 26. DARS2$^{\text{IEC-KO}}$pups present profoundly increased levels of TAG in the intestine, while markedly lessened TAG levels in the liver compared to control littermates.

(a) Graph depicting the content of triacylglycerol species detected in the SI from 7-day-old *Dars2*$^{\text{fl/fl}}$ (n=7) and DARS2$^{\text{IEC-KO}}$ (n=7) mice normalized by protein content. (b) Graph depicting the content of triacylglycerol species detected in the liver from 7-day-old *Dars2*$^{\text{fl/fl}}$ (n=7) and DARS2$^{\text{IEC-KO}}$ (n=6) mice normalized by protein content. TAGs were measured by Nano-Electrospray Ionization Tandem Mass Spectrometry (Nano-ESI-MS/MS). Results are means ± SEM of 6-7 biological replicates (individual mouse tissue samples). Mann–Whitney U test was performed for statistical analysis *** p ≤ 0,001-0,004, **p≤0,01**.**

To decipher whether lipid alterations are extended to a broader spectrum of lipid classes, certain groups of structurally distinct lipid species were acurately assessed by mass spectrometry (MS) – mediated lipidomic analysis. Levels of Diacylglycerol (DAG), main precursor of TAG and phospholipid biosynthetic process, were greatly elevated in the SI of DARS2$^{\text{IEC-KO}}$ mice (Figure 27a). Moreover, among the glycerophospholipids (GLPs) that constitute predominant components of the cell membranes, only phosphatidylinositol (PI) and phosphatidylglycerol (PG) were found raised in the SI of DARS2$^{\text{IEC-KO}}$ mice, while phosphatidylcholine (PC), phosphatidylethanolamine (PE) and phosphatidylserine (PS) were not changed (Figure 27b). Additionally, the majority of sphingolipids including the bioactive lipids ceramides and sphingomyelins that coordinate numerous cellular functions such as cell proliferation, inflammation and cell death (Taniguchi and Okazaki 2020), were notably enhanced (Figure 27c, d). Lastly, CEs composing parts of the circulating lipoproteins as well as critical components of the LDs together with the TAG species (Gonen and Miller 2020), were mostly lowered whereas total cholesterol remain unaltered in the SI of DARS2$^{\text{IEC-KO}}$ mice (Figure 27e, f).

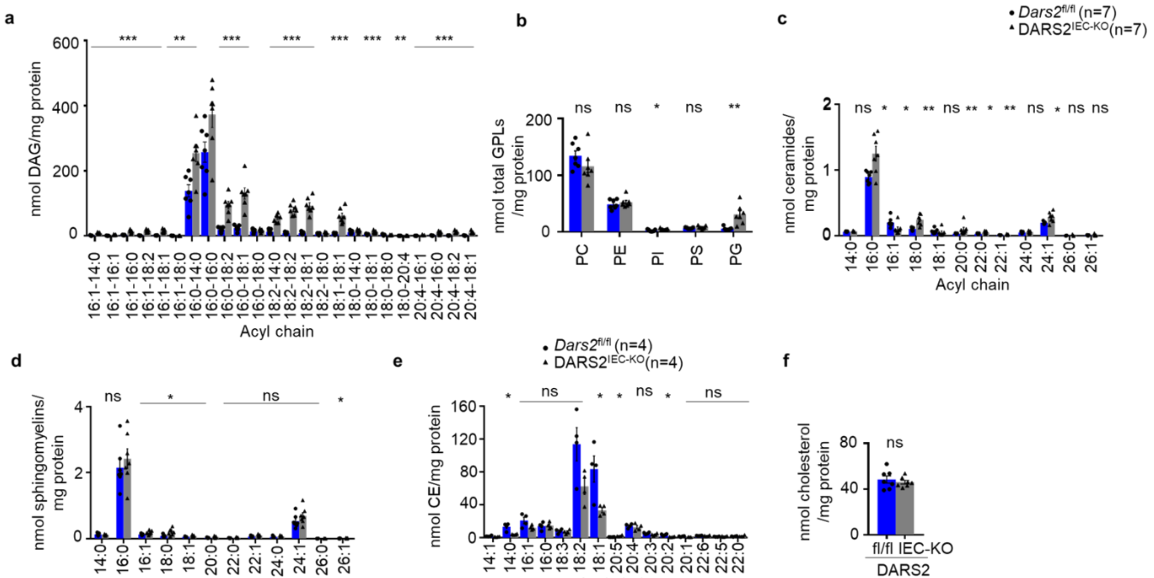

Figure 27. Broad lipid alterations in the intestines of DARS2$^{\text{IEC-KO}}$ mice.

(a-f), Graphs depicting quantification of DAG (a), GPLs (b), ceramides (c), sphingomyelins (d), CEs (e) and total cholesterol levels (f) normalized by protein content in SI tissues from 7-day-old *Dars2*$^{\text{fl/fl}}$ and DARS2$^{\text{IEC-KO}}$ mice, n=7 (DAG, GLPs, ceramides, sphingomyelins, cholesterol), n=4 (CE) mice per genotype. DAGs, CEs and GLPs were measured by Nano-Electrospray Ionization

Tandem Mass Spectrometry (Nano-ESI-MS/MS), whereas ceramides and sphingomyelins were assessed by Liquid Chromatography coupled to Electrospray Ionization Tandem Mass Spectrometry (LC-ESI-MS/MS). Data shown as mean ± SEM of 4-7 biological replicates. Statistical analysis was performed by non-parametric Mann-Whitney U test. *** $p \leq 0.001$-0.004, ** $p \leq 0.01$, * $p \leq 0.05$, ns = not significant. DAG, Diacylglycerol, GPLs, Glycerophospholipids, PC, phosphatidylcholine, PE, phosphatidylethanolamine, PI, phosphatidylinositol, PS, phosphatidylserine, PG, phosphatidylglycerol, CE, cholesterol esters.

To further investigate the profound systemic metabolic changes observed in the DARS2$^{IEC\text{-}KO}$ mice, serum parameters were analyzed. Of note, non-fasted 7-days-old DARS2$^{IEC\text{-}KO}$ mice exhibited severe hypoglycemia, as pointed out by the significantly lower blood glucose levels. In addition, HDL cholesterol levels were highly reduced in DARS2$^{IEC\text{-}KO}$ mice, while low density lipoprotein cholesterol (LDL), total cholesterol and triglycerides were not appreciably affected (Figure 28).

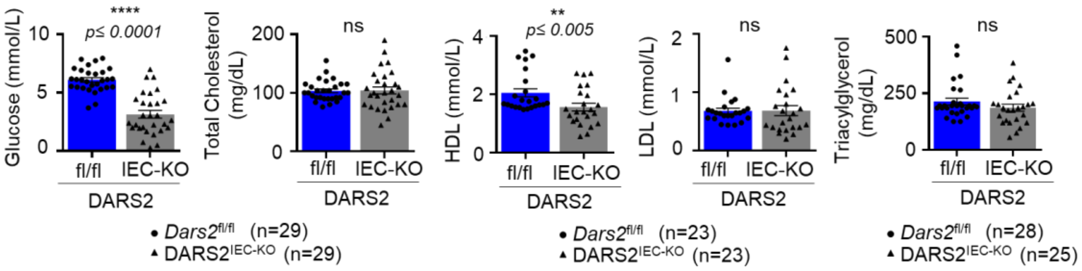

Figure 28. Loss of DARS2 in the IECs greatly lowered blood glucose and HDL cholesterol levels.

Graphs depicting the concentration of glucose, total cholesterol, HDL- and LDL-cholesterol and triacylglycerides in sera from 7-day-old *Dars2*$^{fl/fl}$ and DARS2$^{IEC\text{-}KO}$ mice (n=29 (glucose, total cholesterol) per genotype, n=23 (HDL, LDL) per genotype), triacylglycerides (*Dars2*$^{fl/fl}$ (n=28) and DARS2$^{IEC\text{-}KO}$ (n=25)) assessed by COBAS analyzer. Non parametric Mann–Whitney U test was performed for statistical analysis. Asterisks indicate the level of statistical analysis (**** $p \leq 0.0001$, ** $p \leq 0.01$, ns = not significant).

To gain further insights into the deregulated lipid homeostasis in DARS2$^{IEC\text{-}KO}$ mice, the expression of crucial enzymes involved in de novo lipid biosynthesis, TAG synthesis and catabolism, as well as FAO were determined in the total SI. Remarkably, a marked suppression in the mRNA levels of the lipogenic genes was apparent upon DARS2 deficiency in the SI (Figure 29a). Similarly, the expression of genes implicated into TAG catabolism and FAO was significantly downregulated (Figure 29b, c, d). Collectively, the above-mentioned data indicate that the underlying cause of the dramatic accumulation of lipids in large LDs upon IEC-specific DARS2 deficiency is potentially the impaired transport to the peripheral tissues, such as the liver rather than an activated lipogenic gene expression program.

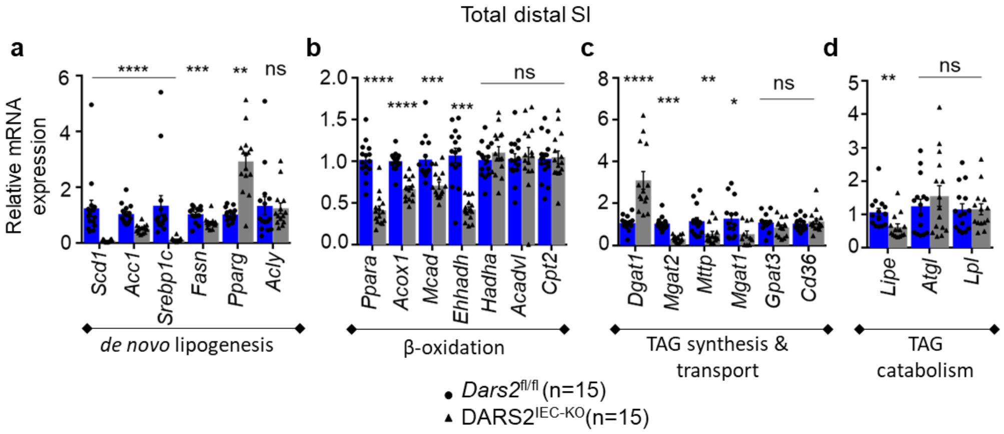

Figure 29. Impaired lipid homeostasis in the intestines of DARS2$^{IEC\text{-}KO}$ mice.

a-d, Graphs depicting the relative mRNA expression of lipid-regulating genes measured by qRT-PCR in the SI of 7-day-old *Dars2*$^{fl/fl}$ (n=15) and DARS2$^{IEC\text{-}KO}$ (n=15) mice normalized to *Hprt1*. Non parametric Mann–Whitney U test was performed for statistical analysis. Asterisks indicate the level of statistical analysis (**** p ≤ 0.0001, *** p ≤ 0,001-0,004, * p ≤ 0.05, ** p ≤ 0.01, ns = not significant).

3.2. Loss of DARS2 leads to the development of a mild phenotype in the colon of 1-week-old DARS2$^{IEC\text{-}KO}$ mice.

To investigate the colon pathology of the DARS2$^{IEC\text{-}KO}$ mice, histological examination of colonic sections from 1-week-old mice was performed. Interestingly, DARS2$^{IEC\text{-}KO}$ mice displayed signs of a mild disease manifestation compared to the small intestine. In particular, DARS2$^{IEC\text{-}KO}$ mice revealed a well-conserved epithelial architecture with relatively intact epithelial barrier without any prominent tissue damage and only a few tiny epithelial erosions (Figure 30). Surprisingly, smaller vacuoles filled with neutral lipids were detected on the tip of the proximal colonic protrusions, resembling a lipid malabsorption phenotype similar to steatorrhoea (Figure 30).

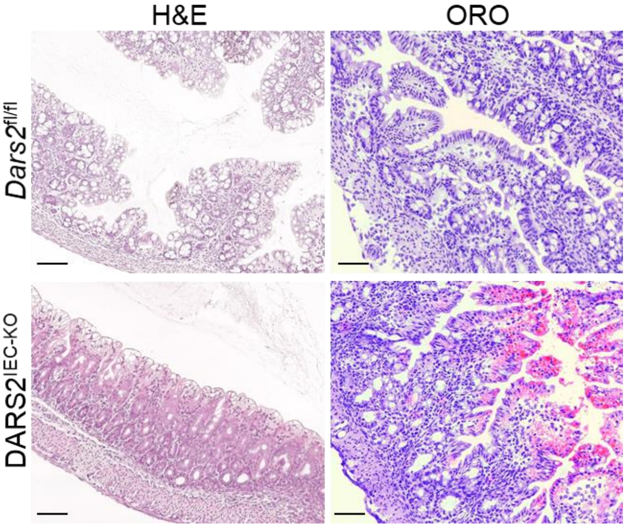

Figure 30. Mild intestinal pathology in the colon of DARS2$^{IEC\text{-}KO}$ mice.

Representative images colonic sections from 7-days-old *Dars2*$^{fl/fl}$ and DARS2$^{IEC\text{-}KO}$ mice stained with H/E (n=16 per genotype) and ORO (n=6 per genotype). Scale bars = 50um.

Furthermore, COX-deficient colonic epithelial cells were observed yet to a lesser extent in contrast to the small intestine (Figure 31a). Electron microscopy of colonic sections confirmed the existence of small stored LDs and further unravelled a profound increase of mitochondrial biogenesis. Interestingly, a mosaic distribution of well-shaped mitochondria with relatively compact cristae and mitochondria with abnormal morphology devoid of cristae was apparent in these colonic sections. Of note, dense and dark spots were frequently observed within mitochondria that highly resembled inclusion bodies as a possible response to mitochondrial cellular injury (Figure 31b).

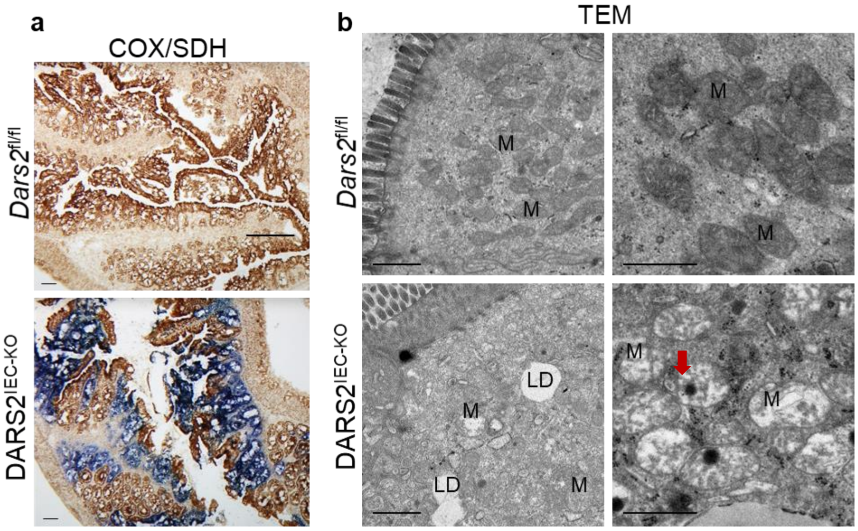

Figure 31. DARS2 deficiency in the colon accompanied by moderate mitochondrial dysfunction.

(a) Representative images of colonic sections from 7-days-old *Dars2*$^{fl/fl}$ (n=6) and DARS2^{IEC-KO} (n=6) mice stained with enzyme histochemical staining for cytochrome c oxidase (COX) and succinate dehydrogenase (SDH). Scale bars = 50um, (b) Representative transmission electron micrographs (TEM) of colonic sections from 7-day-old *Dars2*$^{fl/fl}$ and DARS2^{IEC-KO} mice (n=3 per genotype). Red arrow indicates dense inclusion bodies. Scale bars = 1um. M, mitochondria; LD, lipid droplet

In order to find out whether loss of DARS2 in the colon could have an effect on proliferation, stemness and differentiation, colonic sections were further histologically analyzed. Slightly augmented Ki67 positive staining was present in DARS2^{IEC-KO} colonic crypts, indicating increased numbers of proliferative cells and an ongoing epithelial regeneration (Figure 32a). Following the pattern of small intestine, less differentiated epithelial cell subpopulations, such as Goblet cells and enterocytes, were noticed in the colon of DARS2^{IEC-KO} mice as suggested by staining of PAS and ALP, respectively (Figure 32a). However, no significant changes in the expression of the intestinal epithelial stem cell genes was detected, besides the strong upregulation of *Olfm4*, previously shown to be regulated by NF-κB (Chin, Aerbajinai et al. 2008) (Figure 32b). Furthermore, fairly increased focal immune cell infiltration was present in the colon from DARS2^{IEC-KO} pups, alongside with a tendency towards upregulation of the mRNA levels of the tested chemokines and cytokines (Figure 33a, b). Lastly, IHC against CC3 revealed only a scarce presence of apoptotic IECs in the colon of DARS2^{IEC-KO} mice compared to floxed littermates (Figure 33a). These results suggest that the colon of the DARS2^{IEC-KO} is less severely affected in sharp contrast to the acute small intestinal pathology developed shortly after birth.

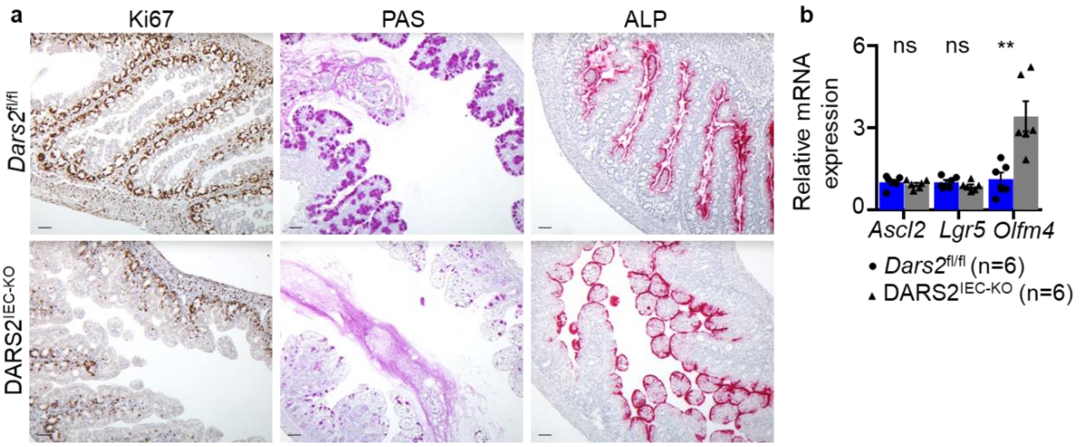

Figure 32. Hyperproliferation and diminished epithelial cell differentiation is readily overt in the colon of DARS2^{IEC-KO} mice.

(a) Representative images of colonic sections from 7-days-old *Dars2*$^{fl/fl}$ (n=6) and DARS2^{IEC-KO} (n=6) mice immunostained for Ki67 and stained for PAS and ALP. All sections were counterstained with hematoxylin. Scale bars = 50um, (b) Graph depicting relative mRNA expression levels of the stem cell related genes measured by qRT-PCR in the total colon from 7-day-old *Dars2*$^{fl/fl}$ (n=6) and DARS2^{IEC-KO} (n=6) mice normalized to *Tbp*. The graphs present mean ± SEM. Non-parametric Mann–Whitney U test was performed for statistical analysis ** $p \leq 0.01$, ns=not significant.

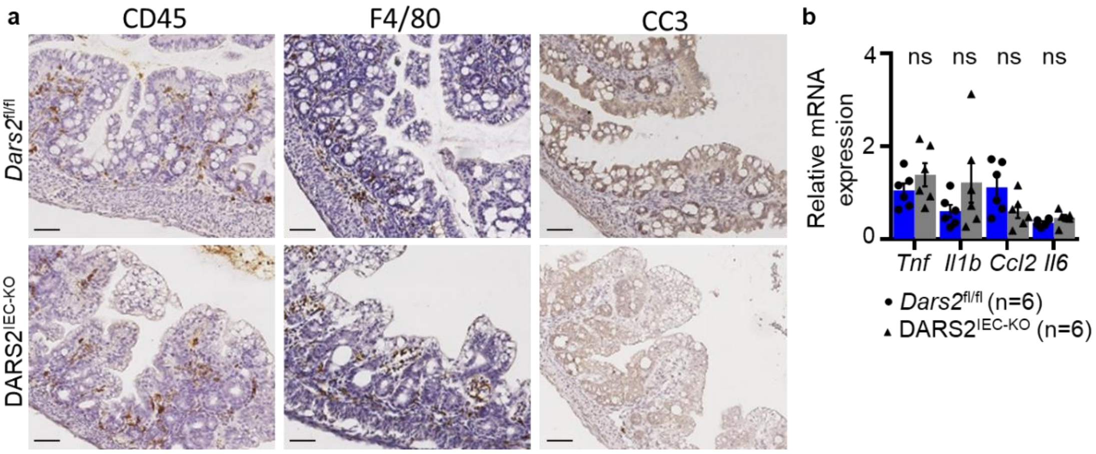

Figure 33. Slightly elevated numbers of infiltrating immune cells in the colonic mucosa of DARS2^{IEC-KO} mice.

(a) Representative images of SI sections from 7-days-old *Dars2*$^{fl/fl}$ (n=6) and DARS2^{IEC-KO} (n=6) mice immunostained for CD45, F4-80 and CC3 and counterstained with hematoxylin. Scale bars = 50um. Positive staining is depicted in dark brown, (b) Graph depicting relative mRNA expression levels of the inflammatory cytokine and chemokine measured by qRT-PCR in the SI from 7-day-old *Dars2*$^{fl/fl}$ (n=6) and DARS2^{IEC-KO} (n=6) mice normalized to *Tbp*. The graphs present mean ± SEM. Non-parametric Mann–Whitney U test was performed for statistical analysis ** $p \leq 0.01$, ns=not significant

3.3. Simultaneous inhibition of apoptosis and necroptosis do not prevent intestinal pathology in the DARS2^{IEC-KO} mice.

As mentioned previously, DARS2^{IEC-KO} mice displayed low numbers of dying epithelial cells that positively stained for CC3, proposing that DARS2 ablation does not sensitize IECs to apoptosis. However, to unequivocally address the role of possible involvement of epithelial cell death in the prominent lipid – related phenotype observed in DARS2^{IEC-KO} mice, we decided to test the effect of simultaneous apoptosis and necroptosis inhibition by generating DARS2^{IEC-KO};CASP8^{IEC-KO} ;*Mlkl* $^{-/-}$ mice.

Caspase-8 induces cell death by initiating the extrinsic apoptotic pathway downstream of death receptors. Active caspase-8 ultimately targets the effector caspases -3 and -7 to induce apoptosis. Despite the fact that caspase-8 is required for extrinsic apoptosis, complete abrogation of FADD-caspase-8-dependent apoptosis through FADD or caspase-8 deletion can induce a caspase-independent cell death initiated by receptor-interacting serine/threonine kinase 3 (RIPK3) and mixed lineage kinase domain-like protein (MLKL), termed necroptosis (Pasparakis and Vandenabeele 2015). We therefore used CASP8^{IEC-KO} *Mlkl* $^{-/-}$ mice to inhibit both FADD-caspase-8-dependent apoptosis and RIPK3-MLKL-dependent necroptosis.

Mice with homozygous deletion of *Dars2* and *Mlkl* upon homozygous or heterozygous deletion of *Casp8* in IECs (Dars2^{IEC-KO};Casp8^{IEC-KO};Mlkl$^{-/-}$ and Dars2^{IEC-KO}; Casp8$^{IEC-KO/WT}$;Mlkl$^{-/-}$, respectively) were closely monitored after birth for the development of a spontaneous macroscopic phenotype. Interestingly, any of the mice born with the abovementioned genotype could not survive beyond the age of four weeks (data not shown), indicating that the premature death of DARS2^{IEC-KO} could not prevented. Therefore, we decided to analyze the pups at the same age as the DARS2^{IEC-KO} mice to test whether the severe pathology could be ameliorated by the concomitant blocking of apoptosis and necroptosis. Both 7-days- old Dars2^{IEC-KO};Casp8^{IEC-KO};Mlkl$^{-/-}$ and Dars2^{IEC-KO};Casp8$^{IEC-KO/WT}$;Mlkl$^{-/-}$ exhibited noticeably reduced body weight almost 50% less than the control littermates and comparable to DARS2^{IEC-KO} mice (Figure 34a). Additionally, the glucose and HDL-cholesterol levels were markedly lower compared to controls, while total cholesterol and LDL remained unchanged matching the serum profile of the DARS2^{IEC-KO} mice (Figure 34b).

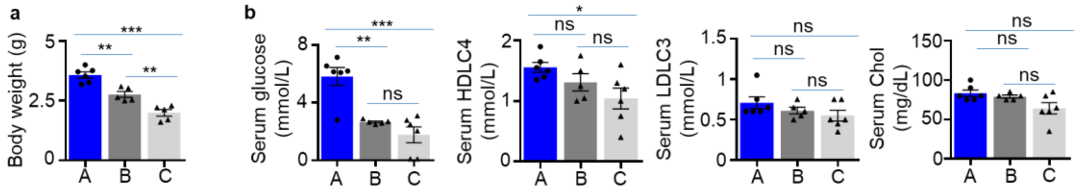

Bar graph	A	B	C
Dars2	fl/fl	fl/fl	fl/fl
VillinCre	wt/wt	tg/wt	tg/wt
Casp8	fl/fl	fl/wt	fl/fl
Mlkl	-/-	-/-	-/-

Figure 34. Simultaneous inhibition of apoptosis and necroptosis cannot prevent cachexia and hypoglycemia in DARS2^{IEC-KO} mice.

Graphs depicting the body weight (a) and the concentration of glucose, total cholesterol, HDL- and LDL-cholesterol assessed by COBAS analyzer in sera from 7-day-old mice with the indicated genotypes, which are clearly illustrated in the blue table, n=6 (A,C) n=5 (B). Non parametric Mann–Whitney U test was performed for statistical analysis. Asterisks indicate the level of statistical analysis (*** p ≤ 0,001-0,004, ** p ≤ 0.01, ns = not significant).

Afterwards, histopathological examination of the 7-days- old Dars2^{IEC-KO};Casp8^{IEC-KO};Mlkl$^{-/-}$ and Dars2^{IEC-KO};Casp8$^{IEC-KO/WT}$;Mlkl$^{-/-}$ revealed extensively disturbed tissue architecture accompanied by massive LD accumulation within enterocytes and barely detected CC3+ cells, as expected. Lastly, IEC proliferation was greatly impaired to the same extent as the DARS2^{IEC-KO} mice, demonstrating that neither intestinal pathology predominantly manifested by widespread LD deposition nor IEC proliferation defect was attenuated in DARS2^{IEC-KO} pups upon concurrent inhibition of apoptosis and necroptosis and further suggesting that cell death does not play a role in the development of the phenotype (Figure 35).

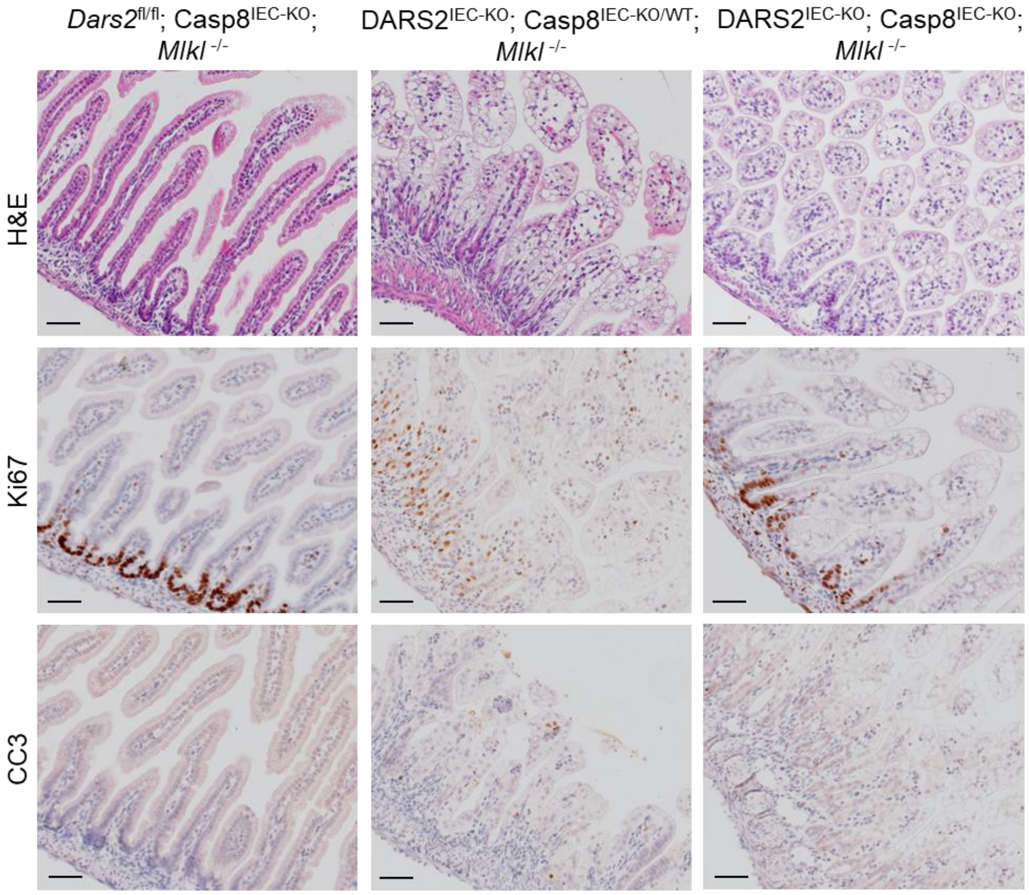

Figure 35. Simultaneous inhibition of apoptosis and necroptosis do not ameliorate the severe intestinal pathology of DARS2^{IEC-KO} mice.

Representative images of SI sections from 7-days-old mice with the indicated genotypes (n=6 mice per genotype) stained for H/E and immunostained for Ki67 and CC3. All sections were counterstained with hematoxylin. Scale bars = 50um.

3.4. Mice with intestinal epithelial cell - specific deletion of SDHA and COX10 develop severe intestinal pathology identical to DARS2^{IEC-KO} mice.

3.4.1. Generation and phenotypic characterization of mice with intestinal epithelial cell specific SDHA ablation.

Next, we sought to investigate whether mitochondrial dysfunction caused by ablation of specific respiratory chain subunits could drive a similar phenotype to that revealed by DARS2 deletion. Therefore, we employed mice lacking the catalytically active complex II subunit SDHA specifically in IECs by crossing mice carrying loxP flanked *Sdha* alleles with *Vil1-Cre* mice (hereafter SDHA^{IEC-KO}). SDHA^{IEC-KO} mice were born at expected Mendelian ratio but developed a postnatal phenotype remarkably resembling to that of DARS2^{IEC-KO} pups. SDHA^{IEC-KO} mice were extremely cachectic, as stated by the significantly reduced body weight in sharp contrast to the control littermates (Figure 36a,

b) and they died prematurely within the first four weeks of life (Figure 36c). Efficient ablation of SDHA was confirmed by both qRT-PCR and immunoblot analysis with a concomitant reduction in the expression of SDHB. Normal respiratory chain subunit abundance is designated by the unaltered levels of CI, CIII and CIV in primary IECs from 7-day-old SDHA$^{\text{IEC-KO}}$ pups (Figure 36d, e). SDHA$^{\text{IEC-KO}}$ mice displayed clear signs of hypoglycemia, whereas HDL and LDL-cholesterol, total cholesterol and triglycerides remained comparable to the *Sdha*$^{\text{fl/fl}}$ littermates (Figure 37a). Additionally, qRT-PCR analysis of the ileal SI from 7-days-old SDHA$^{\text{IEC-KO}}$ mice revealed markedly decreased mRNA expression levels of several apolipoproteins, such as *Apoa4*, *Apoa5*, *Apob*, *Apoc1*, *Apoc3* which constitutes integral components of the intestinal – derived lipoprotein particles facilitating efficient dietary lipid transport. Moreover, *de novo* lipogenesis appears to be suppressed, as suggested by significant downregulation of *Scd1* (Figure 37b).

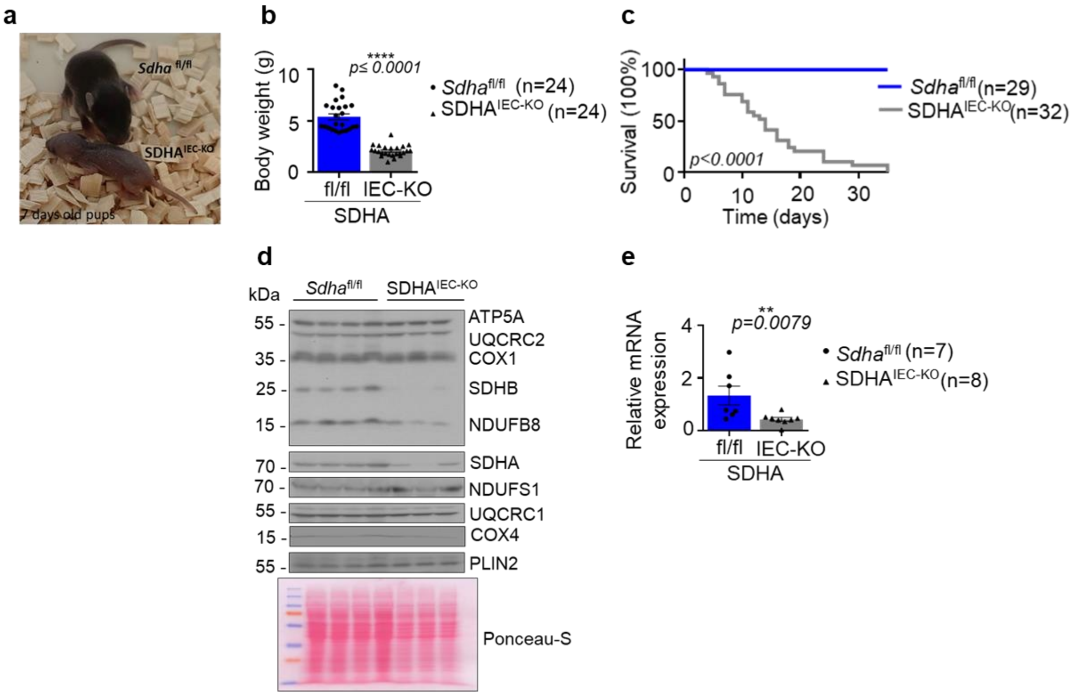

Figure 36. SDHA$^{\text{IEC-KO}}$ mice develop spontaneous phenotype manifested by cachexia and premature death.

(a) Representative macroscopic image of mice with the indicated genotypes taken at the age of 7 days (n=5), (b) Body weight of *Sdha*$^{\text{fl/fl}}$ mice (n=24) and SDHA$^{\text{IEC-KO}}$ mice (n=24) at the age of 7 days, (c) Kaplan-Meier survival curve for *Sdha*$^{\text{fl/fl}}$ mice (n=29) and SDHA$^{\text{IEC-KO}}$ mice (n=32), (d) Total protein extracts from primary IECs from 7-day-old *Sdha*$^{\text{fl/fl}}$ (n=4) and SDHA$^{\text{IEC-KO}}$ (n=3) mice were analyzed by immunoblot with the indicated antibodies. Each lane represents one mouse. Numbers indicates protein size (kDa), (e) Graph depicting relative mRNA expression levels of *Sdha* gene by qRT-PCR in the SI from 7-day-old *Sdha*$^{\text{fl/fl}}$ (n=7) and SDHA$^{\text{IEC-KO}}$ (n=8) mice normalized to *Hprt1*. The graphs present mean ± SEM. Non-parametric Mann–Whitney U test was performed for statistical analysis. Asterisks indicate the level of statistical analysis **** $p \leq 0.0001$, ** $p \leq 0.01$, ns=not significant.

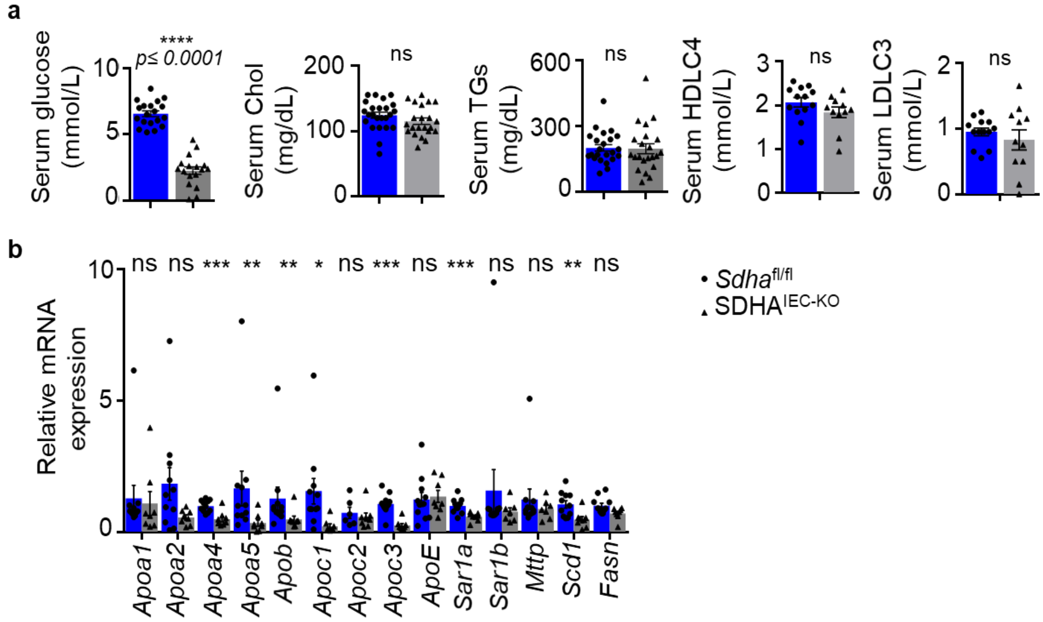

Figure 37. SDHA^{IEC-KO} mice present severe hypoglycemia and altered expression of apolipoproteins in the small intestine.

(a) Graphs depicting the concentration of glucose, total cholesterol, triacylglycerides and HDL- and LDL-cholesterol and in sera from 7-day-old *Sdha*$^{fl/fl}$ (n=19 (glucose), n=22 (total cholesterol), n=23 (triglycerides), n=13 (HDL, LDL) and SDHA^{IEC-KO} mice (n=17 (glucose), n=22 (total cholesterol, triglycerides) n=11 (HDL, LDL) assessed by COBAS analyzer, (b) Graphs depicting the relative mRNA expression of lipid-regulating genes measured by qRT-PCR in the SI of 7-day-old *Sdha*$^{fl/fl}$ (n=11) and SDHA^{IEC-KO} (n=8) mice normalized to *Hprt1*. Non parametric Mann–Whitney U test was performed for statistical analysis. Asterisks indicate the level of statistical analysis **** $p \leq 0.0001$, *** $p \leq 0,001\text{-}0,004$, * $p \leq 0.05$, ** $p \leq 0.01$, ns = not significant.

Histological examination of H&E stained intestinal sections from the small intestine of 7-day-old SDHA^{IEC-KO} mice revealed pronounced tissue alterations exhibiting villus shortening and thickening. In addition, extensive lipid accumulation within large LDs was remarkably prominent within SDHA^{IEC-KO} enterocytes pointed out by ORO and PLIN2 staining, as seen in DARS2^{IEC-KO} mice (Figure 38). Histochemical analyses of complex IV activity showed that the number of COX+ cells in the SDHA^{IEC-KO} sections was indistinguishable from the respective floxed littermates in agreement with the normal levels of the individual CIV respiratory chain subunits (Figure 38). Interestingly, defective IEC proliferation, as proposed by greatly lessened Ki67+ cells and low mRNA expression of Ki67. Moreover, a significantly diminished stem cell compartment was revealed upon the strikingly reduced mRNA expression of genes encoding intestinal stem cell–associated factors (*Lgr5, Olfm4*). Lastly, aberrantly enhanced lysozyme-positive PCs was documented in the SI from SDHA^{IEC-KO} mice comparatively to DARS2^{IEC-KO} (Figure 39a, b).

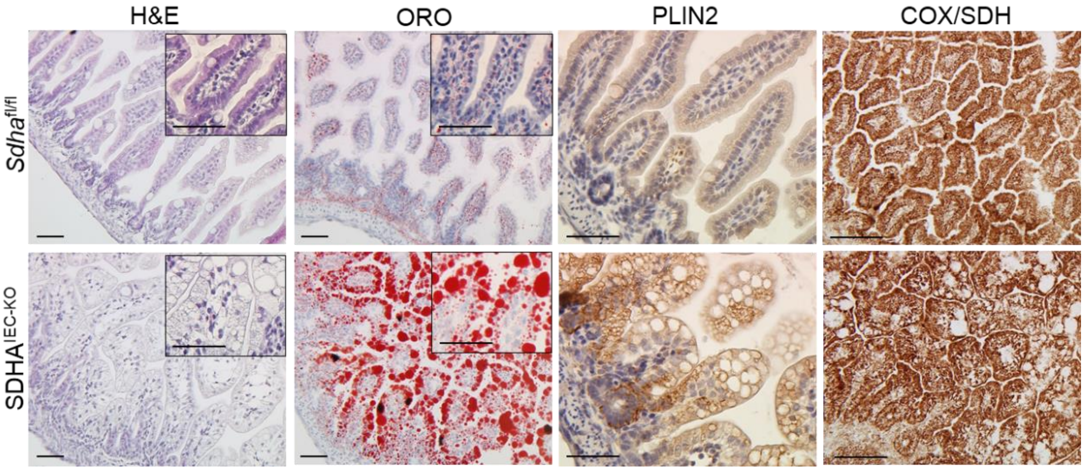

Figure 38. Severe intestinal pathology in SDHA^{IEC-KO} mice denoted by vast LD accumulation within enterocytes.

Representative images of ileal sections from 7-days-old *Sdha*$^{fl/fl}$ and SDHA^{IEC-KO} mice stained with H/E (n=10 per genotype), ORO (n=8 per genotype) and COX/SDH (n=5 per genotype) and immunostained with PLIN2 (n=5 per genotype). Scale bars = 50um. The highlighted box constitutes higher magnification inset.

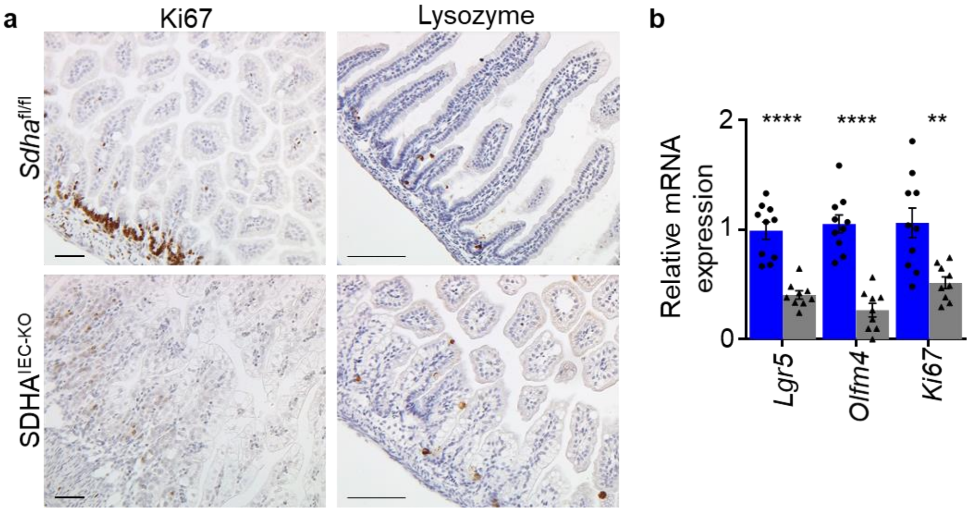

Figure 39. IEC proliferation, stemness and differentiation is considerably affected by the loss of SDHA.

(a) Representative images of ileal sections from 7-days-old *Sdha*$^{fl/fl}$ (n=5) and SDHA^{IEC-KO} (n=5) mice immunostained with Ki67 and Lysozyme and counterstained with hematoxylin. Scale bars = 50um, (b) Graph depicting relative mRNA expression of the indicated genes measured by qRT-PCR in the SI from 7-day-old *Sdha*$^{fl/fl}$ (n=10) and SDHA^{IEC-KO} (n=9) mice normalized to *Hprt1*. The graph presents mean ± SEM. Non-parametric Mann–Whitney U test was performed for statistical analysis. Asterisks indicate the level of statistical analysis **** $p \leq 0.0001$, ** $p \leq 0.01$.

3.4.2. Generation and phenotypic characterization of mice with intestinal epithelial cell specific COX10 ablation.

In parallel with SDHA^{IEC-KO}, we decided to further test our hypothesis by targeting COX10. Therefore, we generated mice devoid of COX10 specifically in IECs by crossing mice carrying loxP flanked *Cox10* alleles with *Vil1-Cre* mice (hereafter COX10$^{\text{IEC-KO}}$). COX10$^{\text{IEC-KO}}$ mice showed an identical early postnatal phenotype manifested by greatly decreased body weight compared to control littermates (Figure 40a, b). COX10$^{\text{IEC-KO}}$ mice failed to thrive and could not survive beyond the age of four weeks (Figure 40c). Markedly decreased mRNA levels of *Cox10* were detected upon qRT-PCR analysis using ileal SI, while immunoblotting revealed loss of complex IV subunits including COX1 and COX4 in IECs from COX10$^{\text{IEC-KO}}$ mice, thus proving proper COX10 deletion (Figure 40d, e). Equally to DARS2$^{\text{IEC-KO}}$ and SDHA$^{\text{IEC-KO}}$ mice, COX10$^{\text{IEC-KO}}$ exhibited noticeable low levels of blood glucose with no apparent changes in the other analyzed serum parametes comprising total cholesterol, triglycerides, as well as HDL- and LDL- cholesterol, whereas only a few apolipoproteins (*Apob*, *Apoc1*, *Apoc3)* were spotted to be slightly downregulated (Figure 41a, b).

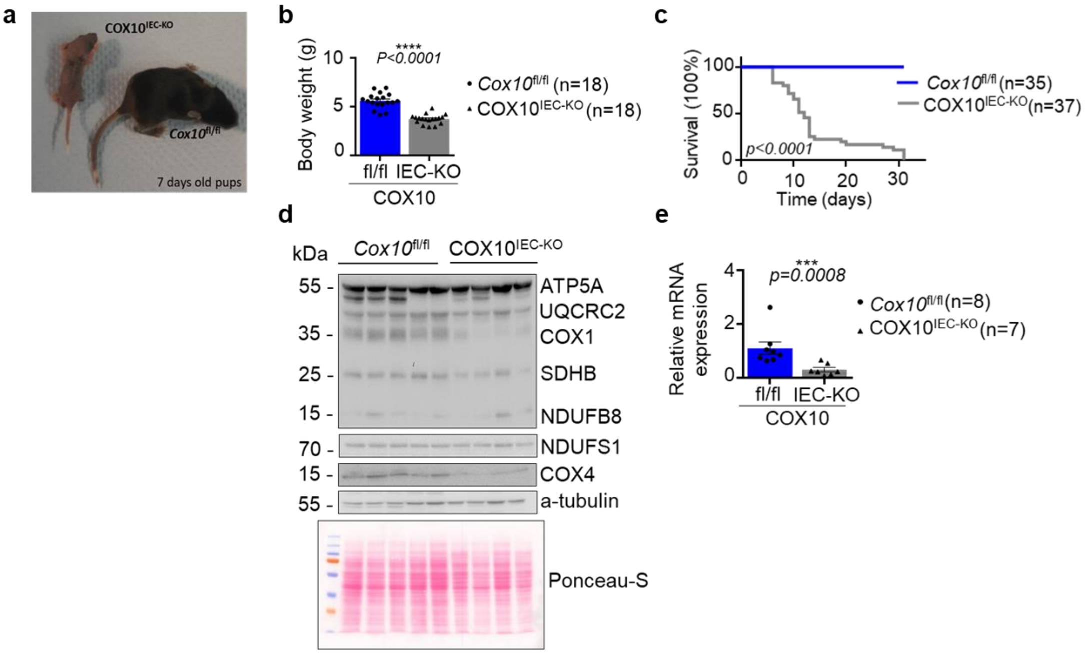

Figure 40. COX10$^{\text{IEC-KO}}$ mice show notably similar phenotype to that revealed by DARS2 and SDHA ablation with cachexia and premature death.

(a) Representative macroscopic image of mice with the indicated genotypes taken at the age of 7 days (n=5), (b) Body weight of *Cox10*$^{\text{fl/fl}}$ mice (n=18) and COX10$^{\text{IEC-KO}}$ mice (n=18) at the age of 7 days, (c) Kaplan-Meier survival curve for *Cox10*$^{\text{fl/fl}}$ mice (n=35) and COX10$^{\text{IEC-KO}}$ mice (n=37), (d) Total protein extracts from primary IECs from 7-day-old *Cox10*$^{\text{fl/fl}}$ (n=5) and COX10$^{\text{IEC-KO}}$ (n=4) mice were analyzed by immunoblot with the indicated antibodies. Each lane represents one mouse. Numbers indicates protein size (kDa), (e) Graph depicting relative mRNA expression levels of *Cox10* gene by qRT-PCR in the SI from 7-day-old *Cox10*$^{\text{fl/fl}}$ (n=8) and COX10$^{\text{IEC-KO}}$ (n=7) mice normalized to *Hprt1*. The graphs present mean ± SEM. Non-parametric Mann–Whitney U test was performed for statistical analysis. Asterisks indicate the level of statistical analysis **** p ≤ 0.0001, *** p ≤ 0,001-0,004.

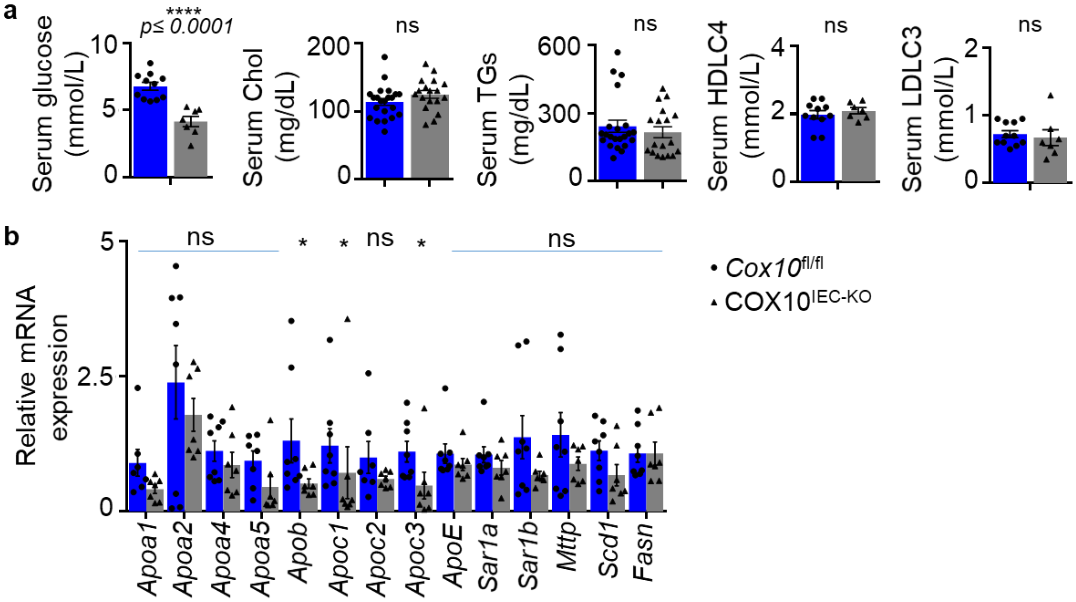

Figure 41. Intestinal specific loss of COX10 leads to severe hypoglycemia and moderately reduced expression of apolipoproteins in the small intestine.

(a) Graphs depicting the concentration of glucose, total cholesterol, triacylglycerides and HDL- and LDL-cholesterol and in sera from 7-day-old *Cox10*$^{fl/fl}$ (n=11 (glucose, HDL, LDL), n=22 (total cholesterol, triglycerides) and COX10^{IEC-KO} mice (n=7 (glucose, HDL, LDL), n=18 (total cholesterol, triglycerides) assessed by COBAS analyzer, (b) Graphs depicting the relative mRNA expression of lipid-regulating genes measured by qRT-PCR in the SI of 7-day-old *Cox10*$^{fl/fl}$ (n=8) and COX10^{IEC-KO} (n=7) mice normalized to *Hprt1*. Non parametric Mann–Whitney U test was performed for statistical analysis. Asterisks indicate the level of statistical analysis **** $p \leq 0.0001$, * $p \leq 0.05$, ns = not significant.

Intestinal-specific COX10 depletion resulted in distorted, blunted villi and extensive architectural abnormalities as pointed by histological examination of H&E stained intestinal sections from the small intestine of 7-day-old COX10^{IEC-KO} mice. Identically to DARS2^{IEC-KO} and SDHA^{IEC-KO} mice, small intestine of COX10^{IEC-KO} mice was utterly stuffed with large LDs positively labelled with ORO and PLIN2 staining (Figure 42). COX/SDH staining unravelled profound COX deficiency coincided with the strongly reduced expression of all complexes containing mitochondrially-encoded subunits (Figure 42). Impaired IEC proliferation and stemness, as well as abundance of Paneth cells was uniformly prominent in the SI from COX10^{IEC-KO} mice in the same manner as the other two conditional knockouts (Figure 43a, b). Therefore, loss of specific subunits of respiratory chain complexes II or IV phenocopied the intestinal pathology induced by DARS deficiency in IECs, showing that the impaired transport and accumulation of lipids within large LDs in enterocytes is the result of strong respiratory chain deficiency.

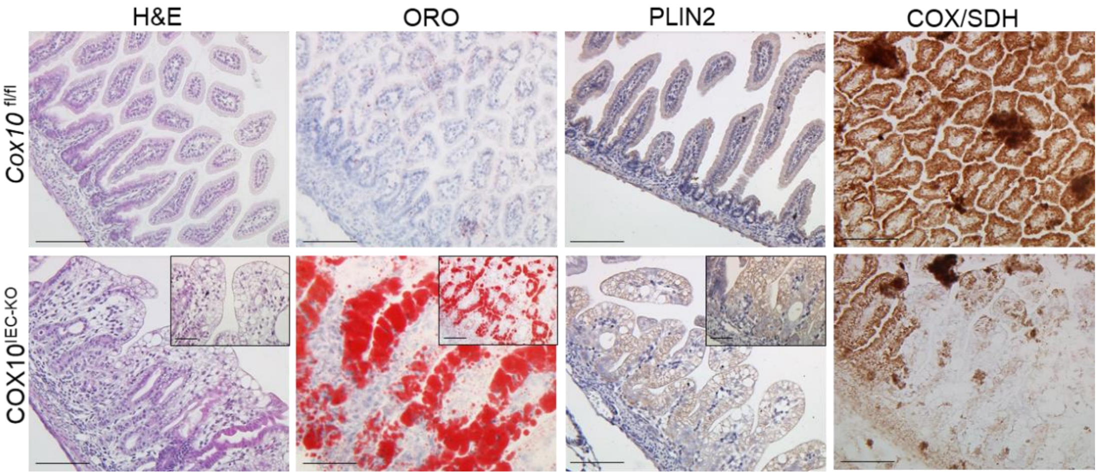

Figure 42. COX10 deficiency drastically altered structural organization of the SI, leading to accumulation of large LDs within enterocytes.

Representative images of ileal sections from 7-days-old *Cox10*$^{fl/fl}$ and COX10$^{IEC\text{-}KO}$ mice stained with H/E (n=8 per genotype), ORO (n=5 per genotype) and COX/SDH (n=5 per genotype) and immunostained with PLIN2 (n=5 per genotype). Scale bars = 50um. The highlighted box constitutes higher magnification inset.

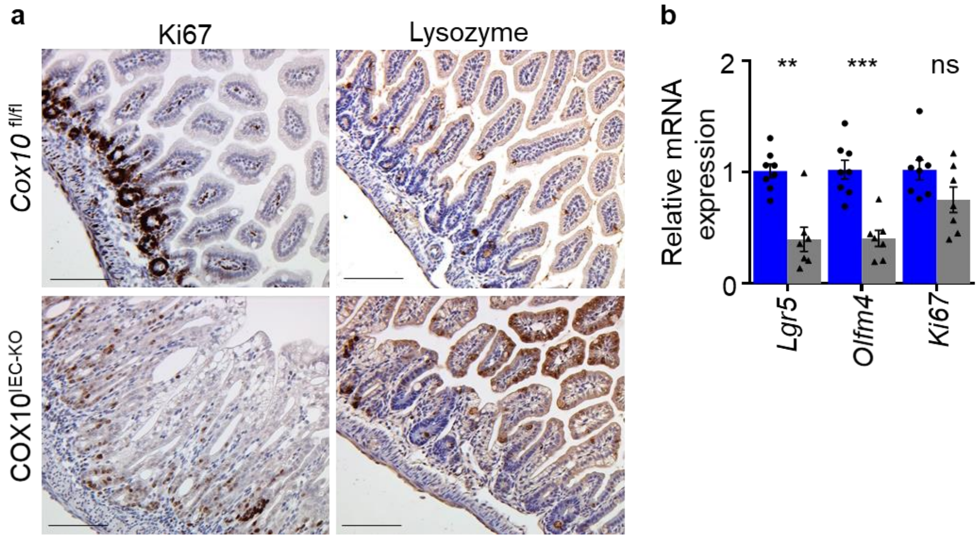

Figure 43. COX10 ablation severely impacts IEC proliferation, stemness and differentiation.

(a) Representative images of ileal sections from 7-days-old *Cox10*$^{fl/fl}$ (n=5) and COX10$^{IEC\text{-}KO}$ (n=5) mice immunostained with Ki67 and Lysozyme and counterstained with hematoxylin. Scale bars = 50um, (b) Graph depicting relative mRNA expression of the indicated genes measured by qRT-PCR in the SI from 7-day-old *Cox10*$^{fl/fl}$ (n=8) and COX10$^{IEC\text{-}KO}$ (n=7) mice normalized to *Hprt1*. The graph presents mean ± SEM. Non-parametric Mann–Whitney U test was performed for statistical analysis. Asterisks indicate the level of statistical analysis *** p ≤ 0,001-0,004, ** p ≤ 0.01, ns = not significant.

3.5. Tamoxifen - inducible ablation of DARS2 in IECs of adult mice results in severe intestinal pathology 7- 8 days upon the last tamoxifen injection

The increased lipid accumulation in IECs from DARS2$^{IEC\text{-}KO}$ pups could be related to the very high fat content of milk or developmental defects caused by ablation of the respective genes during embryonic life (Madison, Dunbar et al. 2002). To assess the consequences of DARS2 ablation in IECs of adult mice with a fully developed gastrointestinal tract, we crossed DARS2 floxed mice with *Villin-CreER*^{T2} transgenics, thus generating *Dars2*$^{fl/fl}$*Villin-CreER*^{T2} (hereafter referred to as DARS2$^{tamIEC\text{-}KO}$). The inducible Cre/loxP estrogen receptor (ER) transgenic system is a widely used for spatial and temporal control of a gene function. The CreERT2 is a fusion protein comprising of Cre recombinase and a mutated form of the estrogen receptor ligand binding domain (ERT2), which binds tamoxifen, an estrogen antagonist with higher affinity that endogenous estrogens. Upon tamoxifen induction, CreERT2 translocates to the nucleus and promotes Cre-mediated recombination (el Marjou, Janssen et al. 2004).

DARS2$^{tamIEC\text{-}KO}$ mice at the age of 8 -12 week old feeding on normal chow diet (NCD) and their control littermates, *Dars2*$^{fl/fl}$ which do not carry the *VillinCreER*^{T2} transgene, were intraperitoneally injected with tamoxifen on five consecutive days (Figure 44a). Tamoxifen administration induced DARS2 ablation in IECs, resulting in rapid weight loss necessitating the sacrifice of DARS2$^{tamIEC\text{-}KO}$ mice due to pre-determined termination criteria 7-8 days after the last injection (Figure 44b). Immunoblot and proteomic analysis of primary IEC protein extracts from the SI of DARS2$^{tamIEC\text{-}KO}$ mice revealed efficient ablation of DARS2 and strong downregulation of respiratory chain subunit expression (Figure 45a, b).

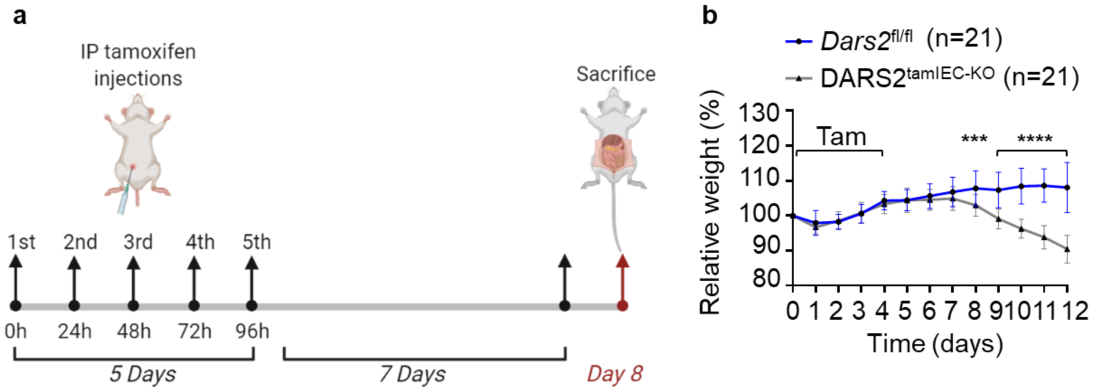

Figure 44. DARS2$^{tamIEC\text{-}KO}$ mice exhibited considerable drop of their body weight 8 days after the last tamoxifen injection.

(a) Schematic depicting the experimental design for inducible DARS2 deletion. Mice received daily intraperitoneal injections of tamoxifen (1mg) for 5 consecutive days and were sacrificed 8 days upon the last injection as indicated. The scheme was created by BioRender. (b) Graph depicting relative body weight change of 8-12 week old *Dars2*$^{fl/fl}$ and DARS2$^{tamIEC\text{-}KO}$ mice after tamoxifen administration. Data are represented as mean ± SEM (n=21 mice per genotype). 2-way ANOVA followed by Bonferroni's multiple comparisons test was applied for statistical analysis. Asterisks indicate the level of statistical analysis **** $p \leq 0.0001$, *** $p \leq 0{,}001\text{-}0{,}004$.

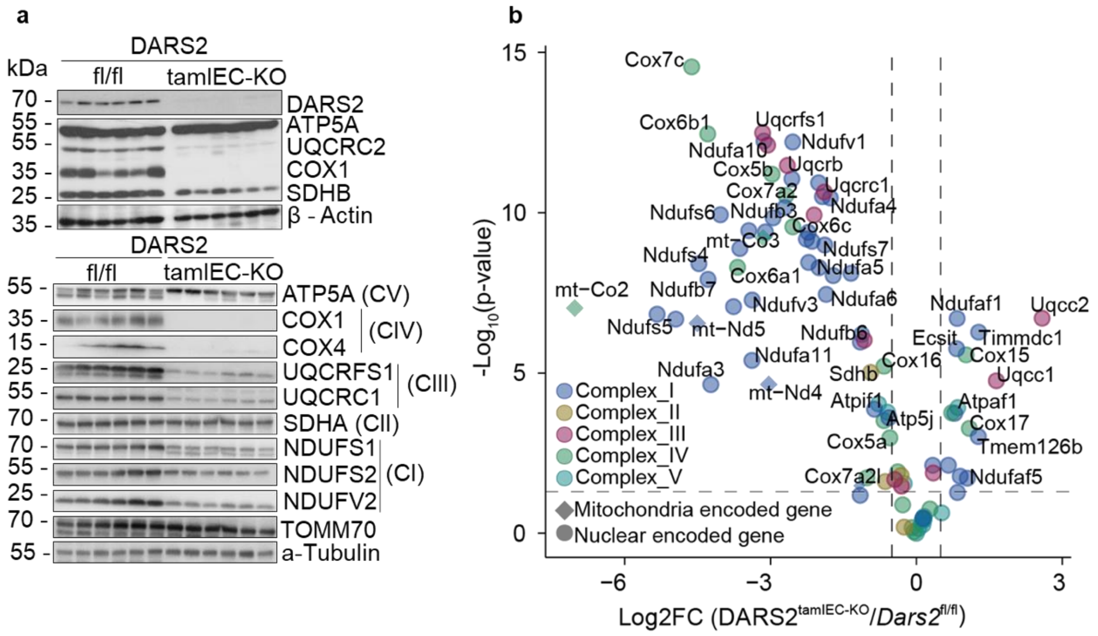

Figure 45. Significant reduction of individual respiratory chain complexes upon inducible DARS2 ablation in IECs of adult mice.

(a) Immunoblot analysis with the indicated antibodies of protein extracts isolated from small intestinal IECs of *Dars2*$^{fl/fl}$ and DARS2$^{tamIEC-KO}$ mice 8 days upon the last tamoxifen injection. Each lane represents one mouse (n=6 mice per genotype), (b) Volcano plot illustrating the protein expression profile of the mitochondria respiratory chain complex proteins detected in proximal IECs isolated from DARS2$^{tamIEC-KO}$ (n=11) compared to *Dars2*$^{fl/fl}$ (n=9) 7 days upon the last tamoxifen injection. The volcano plot depicted in Figure 45b has been generated in collaboration with Christina Schmidt and Theresa Bock from the group of Prof. Dr. Christian Frezza and Prof. Dr. Marcus Krüger, CECAD, Cologne.

Necropsy of the DARS2$^{tamIEC-KO}$ mice revealed a dilated gastrointestinal tract, filled with fluids and frothy content with the proximal SI appearing white, indicating massive accumulation of lipids eight days after the last tamoxifen injection (Figure 46a). Histological analysis of proximal SI sections stained with H/E demonstrated distorted epithelial architecture manifesting by shortening of the villi and extensive erosions (Figure 46b).

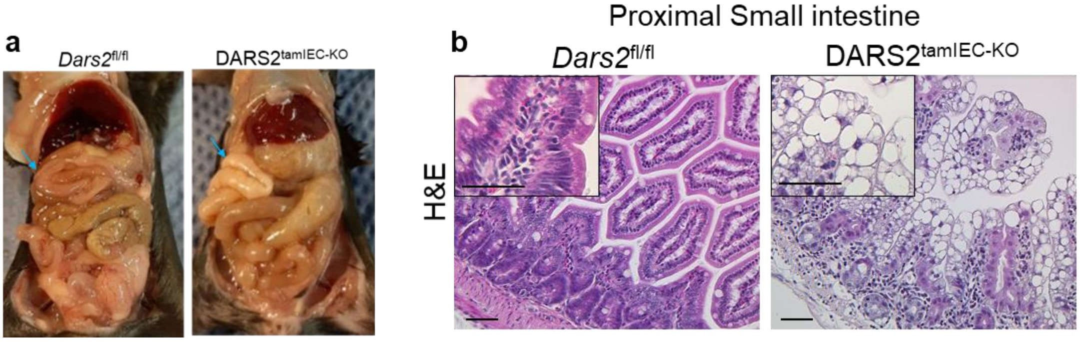

Figure 46. Tamoxifen-inducible ablation of DARS2 in IECs of adult mice results in severe intestinal pathology 8 days upon the last tamoxifen injection.

(a) Representative pictures from necropsy examination of *Dars2*$^{fl/fl}$ (n=4) and DARS2$^{tamIEC-KO}$ (n=4) mice sacrificed 8 days after the last tamoxifen injection. Blue arrows indicate the proximal SI appearing white in DARS2$^{tamIEC-KO}$ mice, (b) Representative images of sections from the proximal small intestine of *Dars2*$^{fl/fl}$ (n=31) and DARS2$^{tamIEC-KO}$ (n=31) mice stained with H&E. Scale bars = 50um.

Deficiency of COX activity has been proven by COX/SDH staining, in accordance to the noticeable decline of the mtDNA-encoded respiratory chain subunits (Figure 47a). In line with this findings, TEM analysis revealed enlargement of abnormal mitochondria with loss of matrix density and dissolution of cristae broadly in the small intestine of DARS2$^{tamIEC-KO}$ mice in sharp contrast to the normal morphology of the mitochondria detected in the *Dars2*$^{fl/fl}$ littermates (Figure 47b, c).

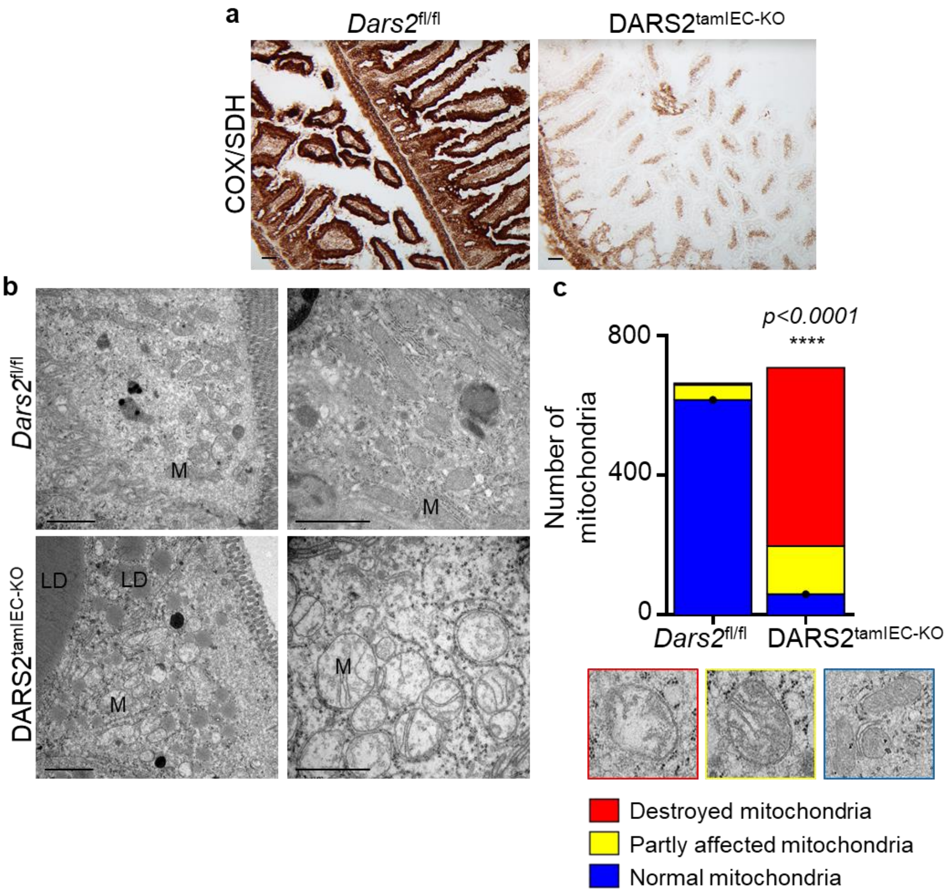

Figure 47. Strong COX deficiency and substantial alterations of the mitochondrial structure in the proximal SI of DARS2$^{tamIEC-KO}$ mice.

(a) Representative images of sections from the proximal small intestine of *Dars2*$^{fl/fl}$ (n=6) and DARS2$^{tamIEC-KO}$ (n=6) mice stained with COX/SDH. Scale bars = 50um, (b) Representative transmission electron micrographs (TEM) of proximal SI sections from *Dars2*$^{fl/fl}$ (n=5) and DARS2$^{tamIEC-KO}$ (n=5) mice. Scale bars = 1µm. M, mitochondria; LD, lipid droplet, (c) Quantification of normal, partly affected and destroyed mitochondria in proximal sections from DARS2$^{tamIEC-KO}$ (n=4) mice (analysis of 707 mitochondria in 80 cells) compared to *Dars2*$^{fl/fl}$ (n=4) mice (analysis of 663 mitochondria in 69 cells). Chi-square test was applied for statistical analysis. Asterisks indicate the level of statistical analysis **** $p \leq 0.0001$. The mitochondrial quantification presented in figure 47c has been performed in collaboration with Dr. Evangelos Kondylis.

Diminished numbers of IEC proliferating cells was prominantly observed upon staining for Ki67, as well as considerably reduced transcript levels of stem cell markers (*Ascl2*, *Lgr5*, *Olfm4*) and decreased amount of OLFM4+ stem cells at the jejenal crypts of DARS2$^{tamIEC-KO}$ mice 8 days upon the last tamoxifen injection (Figure 48a, b). Moreover, an altered differantiation status including reduction of Goblet cells and absorptive enterocytes along with mislocalized PCs with diffuse lysozyme staining was noticed in the DARS2$^{tamIEC-KO}$ mice (Figure 48c). However, the expression of Paneth cell antimicrobials was slightly but not significantly enchanced (Figure 48d).

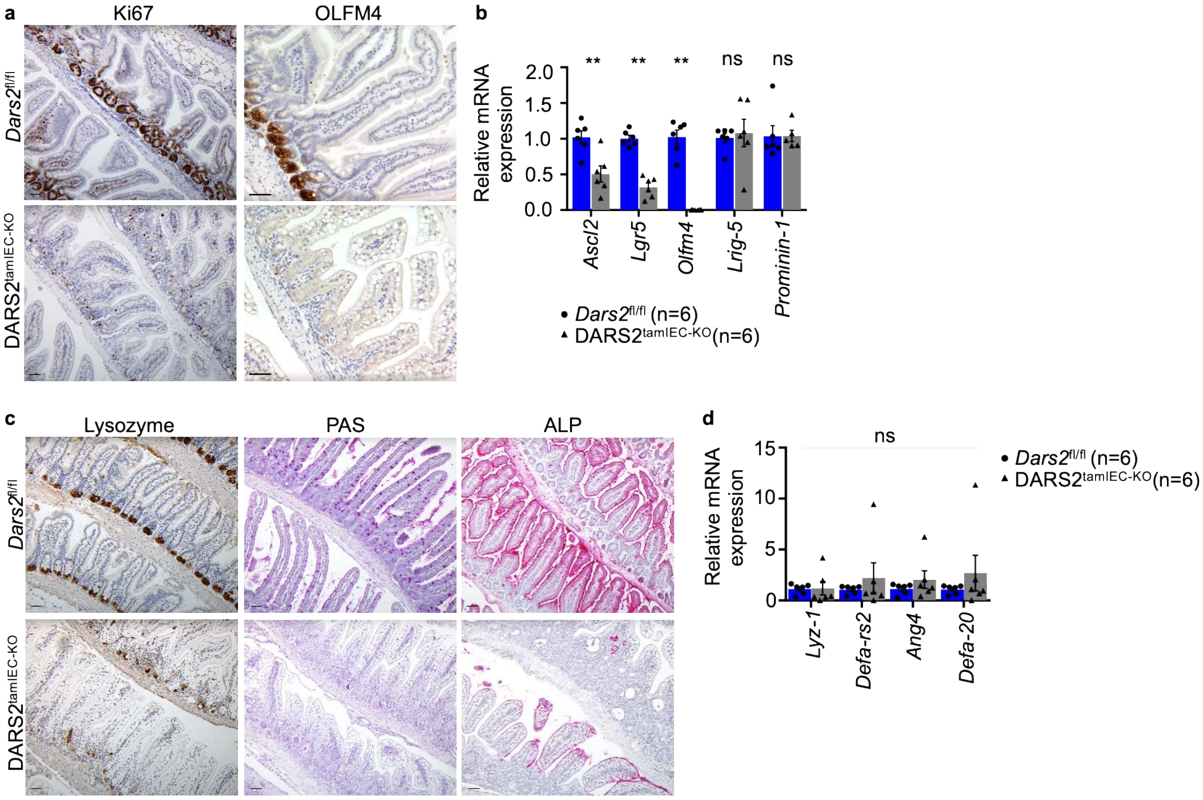

Figure 48. Inducible loss of DARS2 reduces epithelial cell proliferation, stemness and differentiation in the proximal SI.

(a) Representative images of proximal SI sections of *Dars2*$^{fl/fl}$ (n=7) and DARS2$^{tamIEC-KO}$ (n=7) mice immunostained against Ki67 or OLFM4. Scale bars = 50um. Positive staining is depicted in brown, (b) Graph depicting relative mRNA expression of the indicated genes measured by qRT-PCR in the SI from *Dars2*$^{fl/fl}$ (n=6) and DARS2$^{tamIEC-KO}$ (n=6) normalized to *Tbp*, (c) Representative images of proximal SI sections of *Dars2*$^{fl/fl}$ (n=7) and DARS2$^{tamIEC-KO}$ (n=7) mice immunostained against Lysozyme and stained for PAS and ALP, (d) Graph depicting relative mRNA expression of the indicated genes measured by qRT-PCR in the proximal SI from *Dars2*$^{fl/fl}$ (n=6) and DARS2$^{tamIEC-KO}$ (n=6) normalized to *Tbp*. The graph presents mean ± SEM. Non-parametric Mann–Whitney U test was performed for statistical analysis, ns = not significant, Olfactomedin 4.

3.5.1. Inducible DARS2 deletion in IECs of adult mice causes lipid accumulation only in proximal enterocytes and not in the distal in spite of the strong mitochondrial dysfunction.

The appearance of prevalent vacuolization on the H/E - stained proximal sections of DARS2$^{tamIEC-KO}$ alongside the whitish colour of the proximal part of the SI at 8 days upon the last tamoxifen injection was a presage of LD presence. Indeed, proximal enterocytes were eminently filled with large LDs stained positively with ORO and PLIN2, similarly to 7-day-old DARS2^{IEC-KO} mice (Figure 49a). Consistent with the accumulation of large lipid droplets in these cells, lipidomic analysis revealed increased amounts of TAGs in the enterocytes from DARS2^{IEC-KO} mice 7 days upon the last tamoxifen injection (Figure 49b).

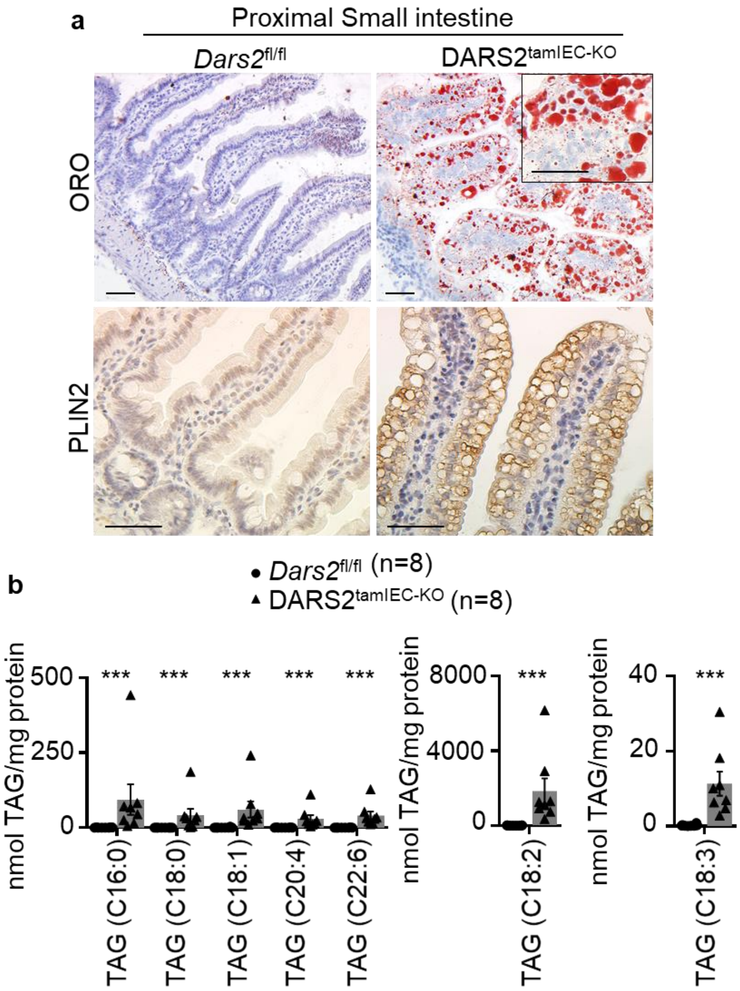

Figure 49. Proximal enterocytes were abundantly filled with massive LDs upon inducible loss of DARS2.

(a) Representative images of proximal SI sections of *Dars2*$^{fl/fl}$ and DARS2$^{tamIEC-KO}$ mice stained for ORO (n=12 mice per genotype) and immunostained against PLIN2 (n=5 mice per genotype). Scale bars = 50um. Sections were counterstained with hematoxylin, (b) Graph depicting TAG content in proximal SI from *Dars2*$^{fl/fl}$ (n=8) and DARS2$^{tamIEC-KO}$ (n=8).The graph presents mean ± SEM. Non-parametric Mann–Whitney U test was performed for statistical analysis, *** $p \leq 0.001$-0.004.

In order to fully recapitulate the intestinal phenotype of the adult mice upon tamoxifen-inducible DARS2 deletion, we subsequently focus our attention to the distal small intestine pathology. Histological examination of the ileum from DARS2$^{tamIEC-KO}$ mice revealed aberrant morphological changes and shortening of the villi, as indicated by H/E staining (Figure 50). Similar to the proximal SI, a prominent reduction of Ki67+ proliferating cells, considerably diminished numbers of Goblet cells and absorptive enterocytes, as well as altered allocation pattern of lysozyme – stained Paneth cells were primarily reported at the ileal sections from DARS2$^{tamIEC-KO}$, hence demonstrating suppression of epithelial cell proliferation and differentiation (Figure 50). However, in spite of the severe respiratory chain deficiency confirmed by COX/SDH staining, epithelial cells of the distal small intestine do not show any signs of lipid droplet formation visualized by the lack of ORO and PLIN2 staining in stark contrast to the fully-filled proximal enterocytes (Figure 51). This exciting observation suggested that LDs exclusively accumulated in those enterocytes that are primarily endowed with the task to absorb and trasport dietary fat. Lastly, immunostaining for CD45+ cells indicated the presence of focal inflammatory infiltrates in the mucosa of both proximal and distal SI, suggesting a mild inflammatory response (Figure 52a, b). Occasionally apparent CC3+ apoptotic cells detected at the proximal and ileal crypts of DARS2$^{tamIEC-KO}$ mice, further validating that DARS2 deficiency does not cause increased death of the enterocytes (Figure 53a, b).

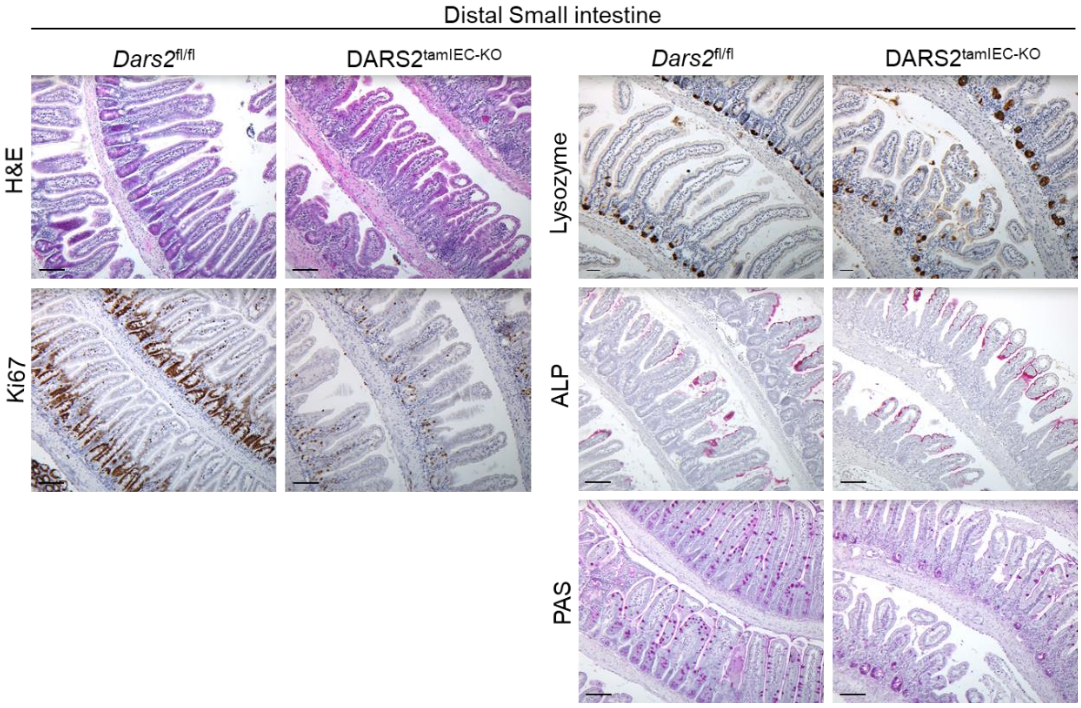

Figure 50. Inducible DARS2 deletion leads to impairment of IEC proliferation and differentiation in the distal SI of adult mice.

Representative images of ileal SI sections from of *Dars2*$^{fl/fl}$ and DARS2$^{tamIEC-KO}$ mice stained for H/E (n=31 per genotype), PAS or ALP (n=7 per genotype) and immunostained against Ki67 or Lysozyme (n=7 per genotype). Scale bars = 50um. Sections were counterstained with hematoxylin, which stains nuclei in blue.

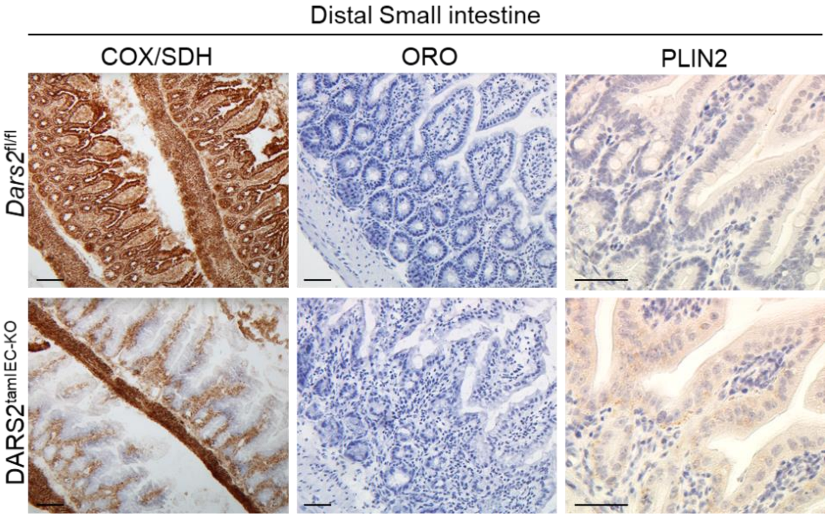

Figure 51. Inducible DARS2 deletion results in strong OXPHOS dysfunction without lipid accumulation in the distal SI of adult mice.

Representative images of ileal SI sections from of *Dars2*$^{fl/fl}$ and DARS2$^{tamIEC-KO}$ mice stained for COX/SDH or ORO (n=12 per genotype) and immunostained against PLIN2 (n=6 per genotype). Scale bars = 50um. Sections were counterstained with hematoxylin, which stains nuclei in blue.

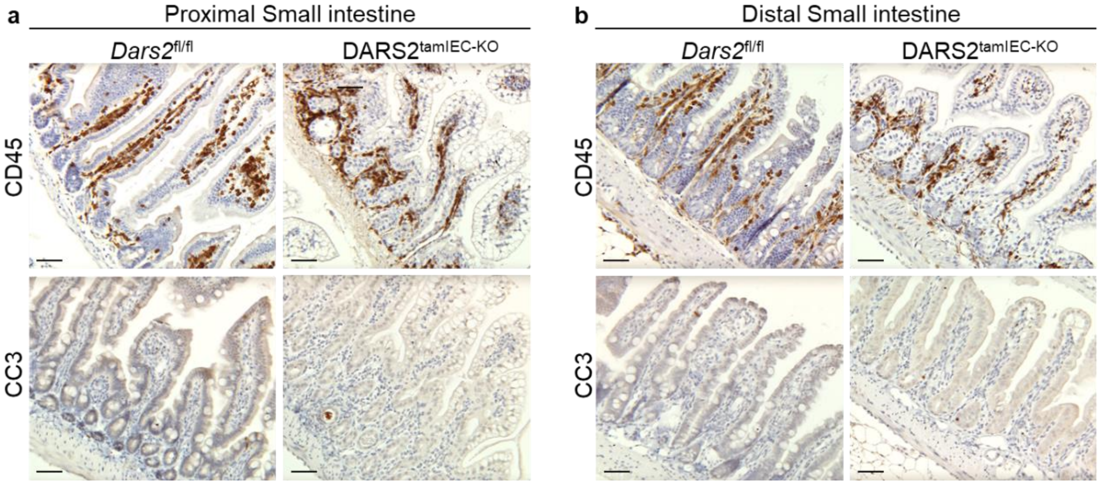

Figure 52. Inducible DARS2 deletion accompanied by increased focal immune cell infiltrates and a few apoptotic CC3+ cells both in the proximal and distal SI of adult mice.

(a, b) Representative images of proximal (a) and ileal (b) SI sections from of *Dars2*$^{fl/fl}$ and DARS2$^{tamIEC-KO}$ mice immunostained against CD45 and CC3 (n=6 per genotype). Scale bars = 50um. Sections were counterstained with hematoxylin, which stains nuclei in blue.

Next, we attempted to assess widespread transcriptome changes mediated by the ablation of DARS2 by performing RNA sequencing (RNA-Seq), which allows unbiased investigation of the gene expression profile. By comparing steady - state levels of transcripts isolated from *Dars2*$^{fl/fl}$ and DARS2$^{tamIEC-KO}$ 7 days upon the last tamoxifen injection, 21166 genes were differentially expressed comprising 10085 upregulated genes and 11081 downregulated genes. RNAseq data were subsequently filtered, selecting exclusively significantly altered transcripts and particularly with Log2fold change (FC) > 0.5 or Log2FC > -0.5 and p adjusted value < 0.05 in order to narrow down our focus of interest. Therefore, 876 genes were highly upregulated, while 1478 genes greatly downregulated. Since the spectrum of importantly altered genes was quite wide, we decided to use the over representation analysis (ORA) to delineate which gene ontology (GO) biological processes are distinctly enriched in our list of genes. Therefore, among the top downregulated GO terms we identified fatty acid metabolic process, cellular lipid catabolic process, lipid oxidation, long-chain fatty acid metabolic process, intestinal lipid absorption and digestion as well as several terms related to nuclear division and chromosome segregation most likely due to impairment in IEC proliferation (Figure 53a). Then, to uniquelly assess the expression levels of genes of particular interest implicated in specific pathways such as fatty acid biosynthesis and oxidation, we generated a volcano plot against a list of manually curated gene signatures obtained from (Gaude and Frezza 2016). Volcano plot representation highlighted that the fatty acid pathways were only slightly downregulated on the mRNA level (Figure 53b). To gain knowledge into possible alterations in the protein landscape of the mice, we decided to perform proteomics on isolated IECs from *Dars2*$^{fl/fl}$ and DARS2$^{tamIEC-KO}$ mice 7 days upon the last tamoxifen injection. In fact, orthogonal approaches confirmed the dysregulation of lipid metabolism in enterocytes from DARS2$^{tamIEC\text{-}KO}$. ORA analysis of the proteomics data revealed “lipid droplet formation” as one of the most upregulated pathways (Figure 54a). Likewise, proteins associated with lipid droplet formation, such as PLIN2 and PLIN4 showed elevated expression in IECs from DARS2$^{tamIEC\text{-}KO}$ mice (Figure 54b).

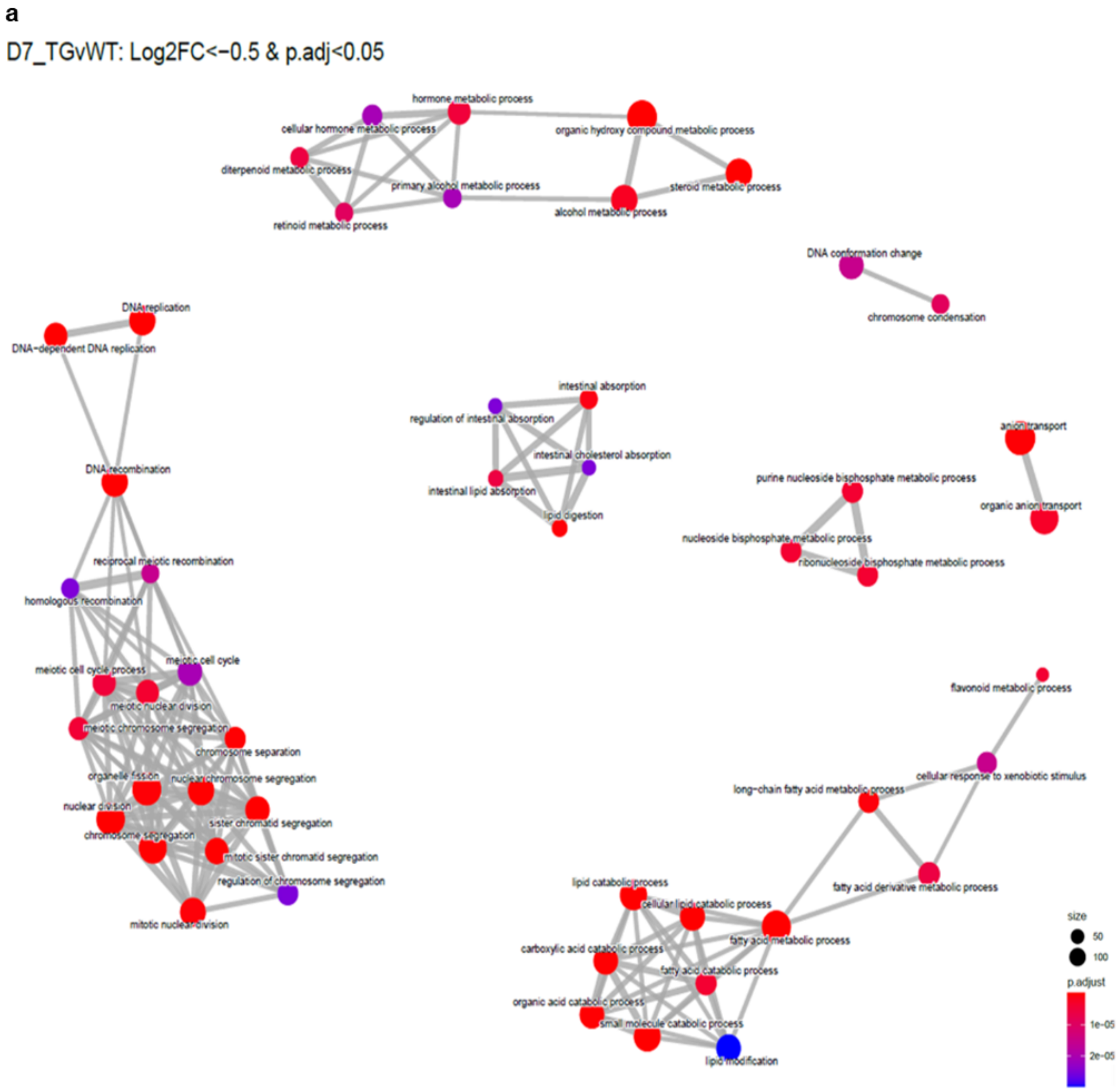

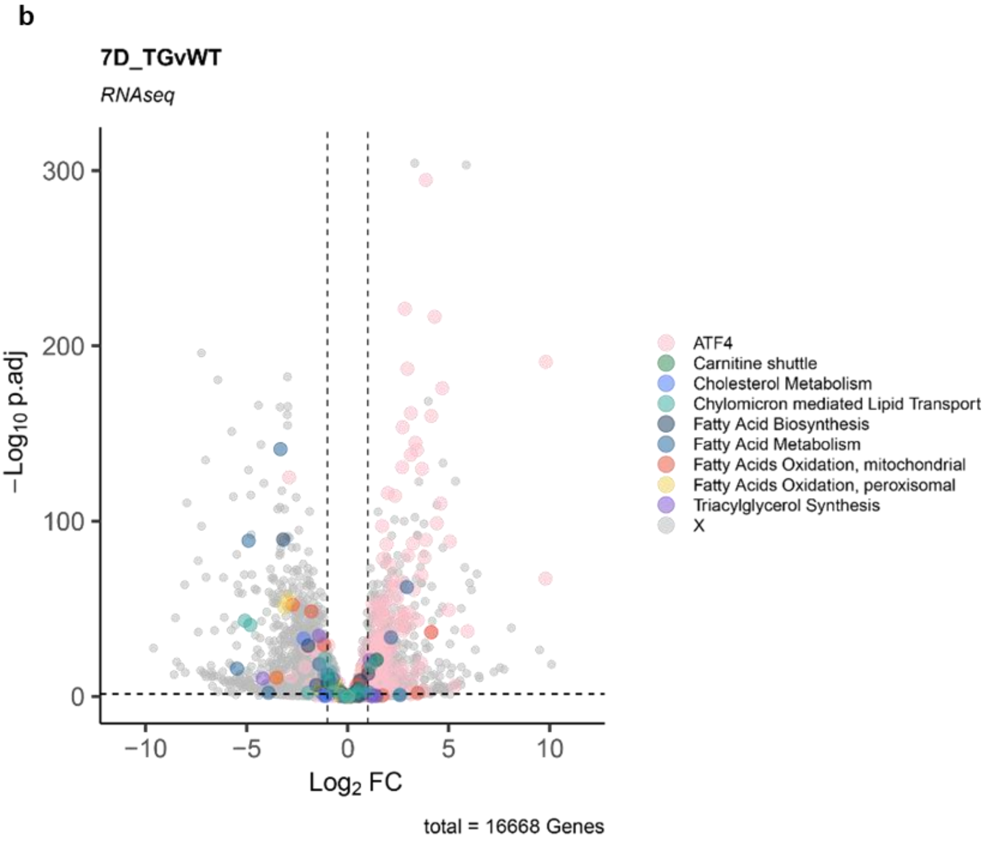

Figure 53. RNAseq analysis of total SI from *Dars2*$^{fl/fl}$ and DARS2$^{tamIEC\text{-}KO}$ suggested suppression of fatty acid biosynthesis and oxidation 7 days upon the last tamoxifen injection.

(a) Emapplot of the ORA results performed on the significantly downregulated (Log2FC>0.5 and p.adj<0.05) transcripts upon inducible DARS2 ablation, (b) Volcano plot representation of mean fold change expression of genes in each key pathway indicated on the right with distinct color code (x axis) vs enrichment P-values (y axis) in DARS2$^{tamIEC\text{-}KO}$ mice compared to *Dars2*$^{fl/fl}$. The emapplot and volcano plot depicted in Figure 53 has been generated in collaboration with Christina Schmidt from the group of Prof. Dr. Christian Frezza.

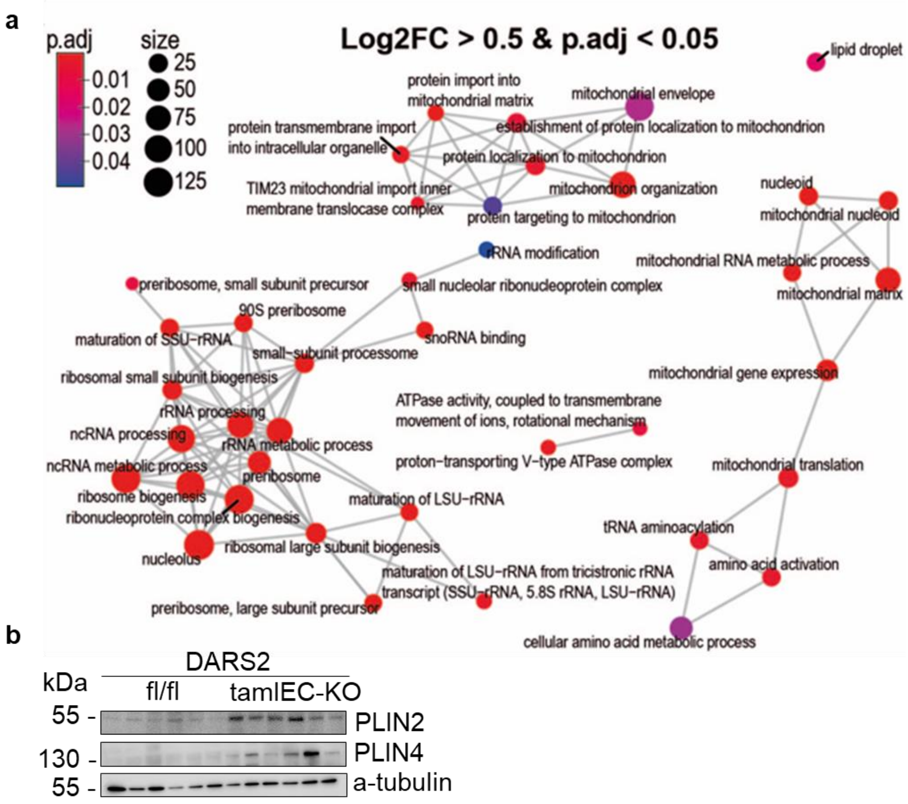

Figure 54. Proteomic analysis of DARS2-deficient enterocytes revealed increased lipid droplet formation.

(a) Emapplot of the ORA results performed on the significantly upregulated (Log2FC>0.5 and p.adj<0.05) protein landscape comparing DARS2$^{tamIEC-KO}$ mice to *Dars2*$^{fl/fl}$. Size of dots corresponds to the number of differentially expressed genes which belong to the enriched gene ontology term, (b) Immunoblot analysis with the indicated antibodies of protein extracts from proximal SI IECs isolated from *Dars2*$^{fl/fl}$ and DARS2$^{tamIEC-KO}$ mice 7 days upon tamoxifen injection. Each lane represents one mouse (n=6 per genotype). The emapplot and volcano plot depicted in Figure 54 has been generated in collaboration with Dr. Christina Schmidt from the group of Prof. Dr. Christian Frezza.

Moreover, further analysis of proteomics data by ORA demonstrated that many lipid metabolism pathways were downregulated in DARS2-deficient IECs (Figure 55). Consistently, volcano plot representation highlighted the reduced expression of several proteins important for lipid biosynthesis including FASN, as well as fatty FABP2, which were also confirmed by immunoblotting together with ACLY and cytoplasmic acetyl-CoA synthetase (AceCS1). In the same volcane plot, PLIN2 is also emphazised as being the most markedly upregulated protein in the IECs from DARS2$^{tamIEC-KO}$ 7 days upon the last tamoxifen injection (Figure 56a, b). Additionally, protein expression of crucial enzymes involved in the fatty acid beta oxidation was examined by immunobloting (Figure 56b). Despite the fact that FAO was identified among the most suppressed pathways by ORA (Figure 55), immunoblot analysis showed that only ACADL was upregulated, whereas ACADS, HADHA, EHHADH, as well as CPT2 were not obviously changed in DARS2-deficient IECs (Figure 56b).

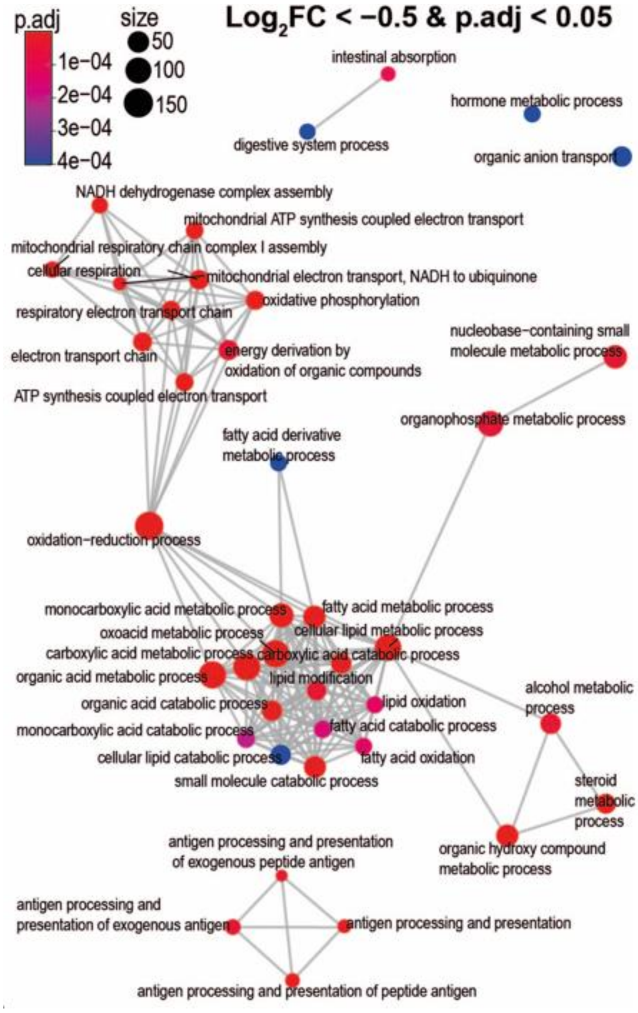

Figure 55. Proteomic analysis of DARS2-deficient enterocytes indicated downregulation of lipid biosynthesis.

Emapplot of the ORA results performed on the significantly downregulated (Log2FC<-0.5 and p.adj<0.05) protein landscape comparing DARS2$^{tamIEC\text{-}KO}$ mice to *Dars2*$^{fl/fl}$. Size of dots corresponds to the number of differentially expressed genes which belong to the enriched gene ontology term. This emapplot has been generated in collaboration with Dr. Christina Schmidt from the group of Prof. Dr. Christian Frezza, CECAD, Cologne.

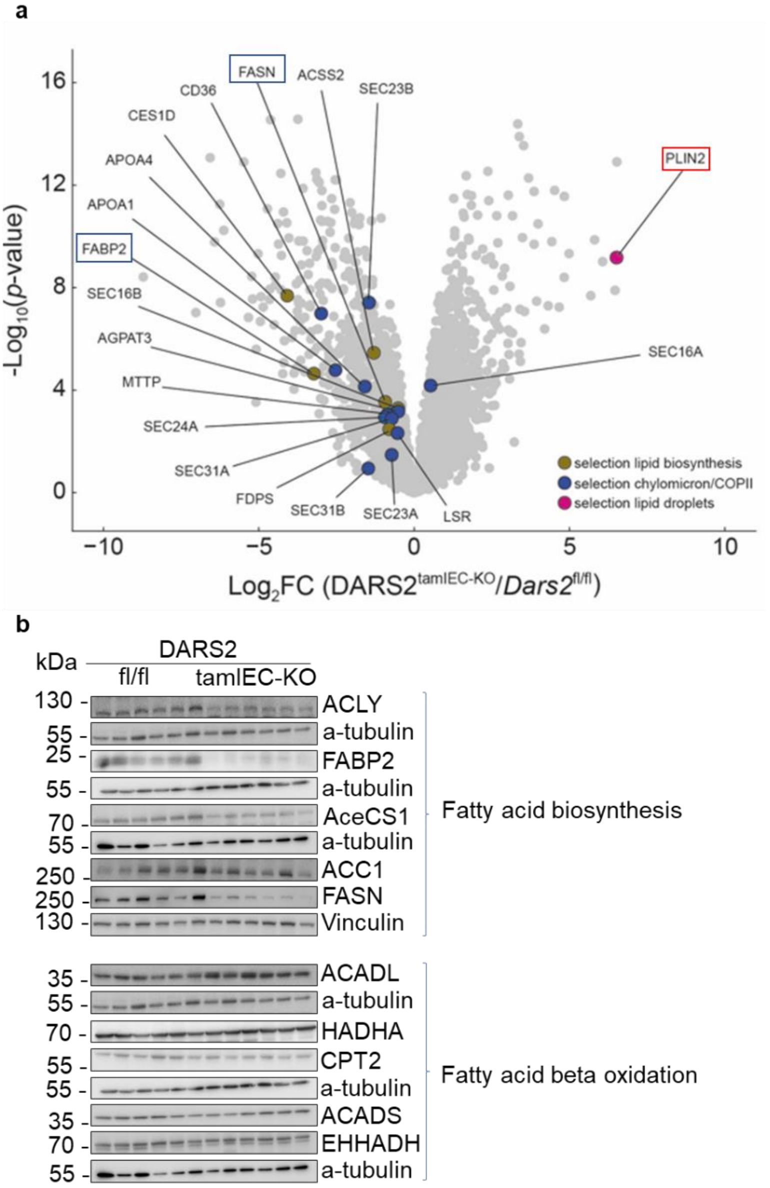

Figure 56. Inducible deletion of DARS2 in the adult mice suppressed the expression levels of major biosynthetic enzymes, whereas but did not significantly alter the expression profile of fatty acid beta oxidation proteins.

(a) Volcano plot presenting the proteome landscape comparing DARS2$^{tamIEC-KO}$ mice to *Dars2*$^{fl/fl}$ highlighting key proteins. FASN, FABP2 and PLIN2 are marked with a box, (b) Immunoblot analysis with the indicated antibodies of protein extracts from proximal SI IECs isolated from *Dars2*$^{fl/fl}$ and DARS2$^{tamIEC-KO}$ mice 7 days upon tamoxifen injection. Each lane represents one mouse (n=6 per genotype). The volcano plot in Figure 56a has been generated in collaboration with Dr. Christina Schmidt from the group of Prof. Dr. Christian Frezza, CECAD, Cologne.

3.5.2. Induction of integrated stress responses and suppression of mitochondrial metabolism upon tamoxifen-inducible DARS2 ablation in IECs of adult mice.

Activation of integrated stress response (ISR) is an adaptive mechanism of eukaryotic cell to cope with a multitude of stress stimuli including amino acid or heme deprivation, ER stress or viral infection. Each of these stress signals is recognized by a set of kinases that induce the phosphorylation of the eukaryotic translation initiation factor 2a (eIF2a). Phosphorylated eIF2a impedes the 5’-cap-dependent mRNA translation and promotes the preferential translation of stress – responsive mRNAs harboring internal ribosome entry sites (IRES) that recruit the 40S ribosomal subunit and mediate cell recovery. Activating transcription factor 4 (ATF4) is considered as one of those mRNAs and constitutes the central transcription factor of the ISR pathway, which subsequently culminates in triggering the expression of pro-survival genes upon dimerization with several partners, such as C/EBP homologous protein (CHOP) (Pakos-Zebrucka, Koryga et al. 2016). Induction of ISR has been recently pointed out in DARS2 deficient hearts and numerous other models of mitochondrial dysfunction (Quirós and Prado 2017, Kaspar, Oertlin et al. 2021).

In compliance with these studies, we witnessed a clear integrated stress response activation (Figure 57a). Augmented ATF4 signature has been already identified in the SI of DARS2$^{tamIEC-KO}$ mice on the transcript level (Figure 53b) and conveyed to the protein level in DARS2-deficient IECs, as indicated by gene set enrichment analysis (GSEA) using the proteomics results. In particular, protein expression profile of 233 ATF4 signature genes was markedly enhanced (Figure 57b). GSEA analysis also displayed the depletion of several OXPHOS signatures (Figure 57a). In line with this result, expression levels of CHOP and phosphorylated eIF2a were detected by immunobloting analysis of DARS2-deficient IECs (Figure 57c).

Previous studies have shown that ATF4 activation boosted serine biosynthesis and one carbon metabolism, which is implicated in nucleotide and amino acid biosynthesis (Bao, Ong et al. 2016). Indeed, the mitochondrial enzymes participating in the folate cycle methylenetetrahydrofolate dehydrogenase (MTHFD2) and serine hydroxyl methyltransferase 2 (SHMT2) were highly upregulated, while the levels of the cytosolic MTHFD1 was significantly decreased (Figure 57c). Lastly, immunoblot analysis revealed slightly increased protein expression of the mitochondrial chaperone HSP60, as well as LON Peptidase 1 (LONP1), protease of the mitochondrial matrix entangling the quality control of the mitochondrial proteostasis and direct target of ATF4 in DARS2-deficient IECs (Figure 57c).

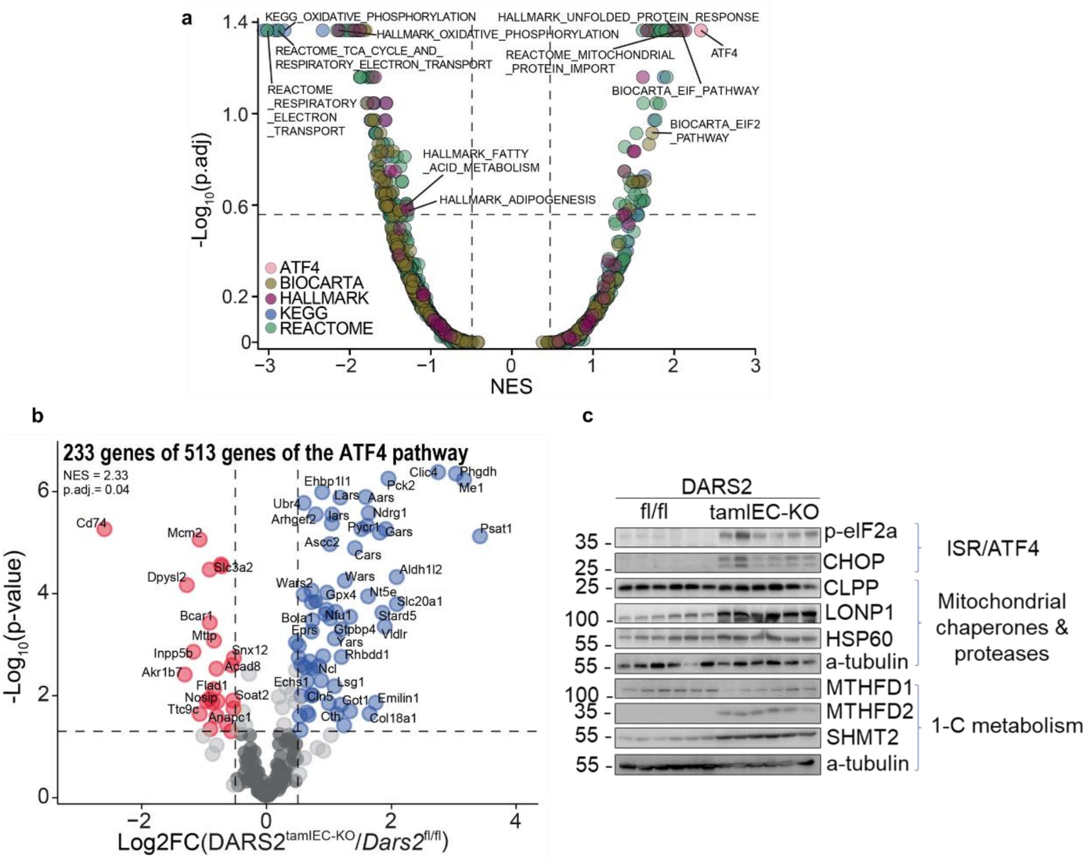

Figure 57. Activation of integrated stress responses upon tamoxifen-inducible DARS2 ablation in IECs of adult mice.

(a) Volcano plot illustrating the profile of the different gene sets (colour coded) after performing GSEA analysis on the pooled signatures comparing DARS2$^{tamIEC-KO}$ (n=11) mice to *Dars2*$^{fl/fl}$ (n=9). Adjusted p-value (p.adj) is the result of the GSEA analysis, (b) Volcano plots illustrating the protein expression profile of ATF4 signature genes of proximal small intestinal IECs from DARS2$^{tamIEC-KO}$ (n=11) mice compared to *Dars2*$^{fl/fl}$ (n=9), (c) Immunoblot analysis of protein extracts from proximal SI IECs from *Dars2*$^{fl/fl}$ and DARS2$^{tamIEC-KO}$ mice 8 days after the last tamoxifen injection with the indicated antibodies. Each lane represents one mouse (n=6 per genotype). The volcano plot in Figure 57a, b has been generated in collaboration with Dr. Christina Schmidt from the group of Prof. Dr. Christian Frezza, CECAD, Cologne.

Afterwards, we sought to portray the metabolic alterations arising from DARS2 deficiency by performing extensive metabolomic analysis using IECs from DARS2$^{tamIEC-KO}$ mice 8 days after the last tamoxifen injection. Metabolomics detected 207 signature metabolites, predominantly involved in TCA cycle, amino acid metabolism, glycolysis and pentose phosphate pathway (PPP), pyrimidine and purine biosynthesis, as well as fatty acid oxidation, to be primarily different between DARS2$^{tamIEC-KO}$ and *Dars2*$^{fl/fl}$ mice (Figure 58). A considerable drop in aspartate, an established marker of mitochondrial function and other TCA cycle intermediates, confirmed the suppression of mitochondrial metabolism in DARS2$^{tamIEC-KO}$ mice (Figure 58). Aspartate shortage prevents nucleotide synthesis, thus causing an accumulation of *de novo* purine synthesis pathway metabolites (Figure 59a). Increased of purine intermediates was in agreement with the higher levels of pentose phosphate pathway (PPP) metabolites (Figure 59b), while the enhanced glycolysis energetically compensated for the strong mitochondrial dysfunction (Figure 59b). Most likely, DARS2-deficient IECs utilized glucose as energy source and boosted their glycolytic capacity for ATP generation. Indeed, the metabolomic analysis revealed that ATP levels and specifically the ATP/ADP ratio, was not substantially reduced in DARS2-deficient enterocytes, arguing against an energy crisis (Figure 59c). Additionally, a total imbalance in the amino acid pool was quite prominent with the majority of the detected amino acids being markedly depleted (Figure 59d). Glutamine, the major nutrient utilized by the intestine and a precursor of purine and pyrimidine biosynthesis (Metzler, Gfeller et al. 2016), was the only highly abundant amino acid in the DARS2-deficient enterocytes, pointing again towards the direction of the augmented purine synthesis. Moreover, TCA cycle intermediates remained largely unaffected apart from a tremendous accumulation of succinate, which was reportedly associated with PHDs and a pseudo-hypoxic condition (Martínez-Reyes and Chandel 2020) (Figure 59e). Lastly, a drastic build-up of long-chain and very long-chain acylcarnitines was particularly observed in DARS2-deficient IECs, implying a potential inhibition of FAO (Figure 58). Consistently, NADH/NAD$^+$ ratio was remarkably raised further supporting this hypothesis (Figure 59c).

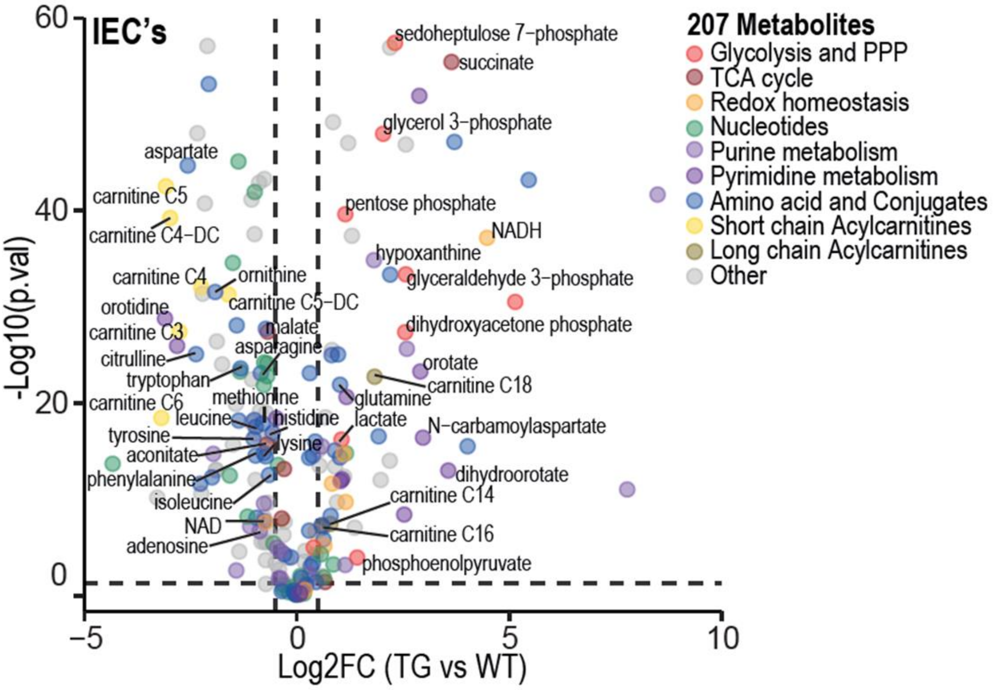

Figure 58. Inducible DARS2 deletion results in suppression of mitochondrial metabolism and broad metabolic abnormalities.

Volcano plot illustrating the differential intracellular metabolite levels comparing IECs from DARS2$^{tamIEC\text{-}KO}$ (n=15) mice to *Dars2*$^{fl/fl}$ (n=9). Each metabolite is clearly labelled with a color code which corresponds to a specific pathway highlighted on the right. The volcano plot in Figure 58 has been generated in collaboration with Dr. Ming Yang and Dr. Christina Schmidt from the group of Prof. Dr. Christian Frezza, CECAD, Cologne.

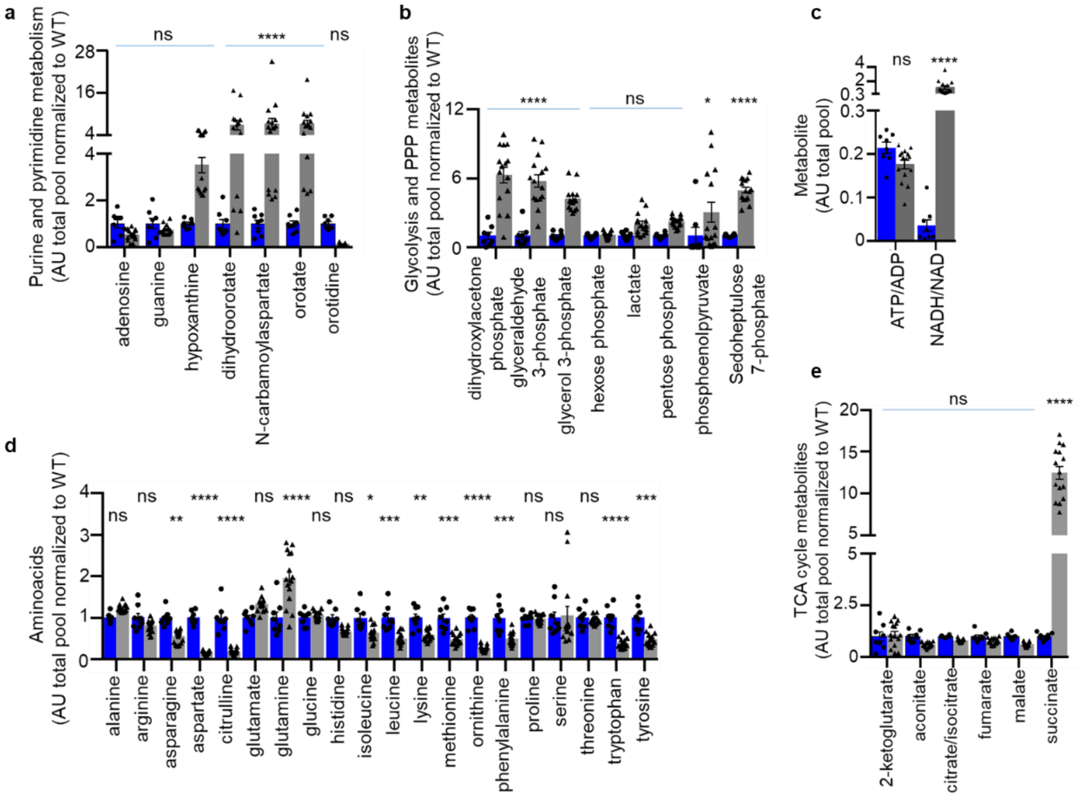

Figure 59. Inducible DARS2 deletion impact numerous metabolic pathways and disturb the ratio of NADH/NAD$^+$.

(a,b) Graphs depicting key metabolites implicated in (a) purine and pyrimidine biosynthesis, (b) glycolysis and PPP metabolism, (c,d,e) graph showing ATP/ADP and NADH/NAD+ ratio (c), amino acids (d) and TCA cycle metabolites (e) from DARS2$^{tamIEC-KO}$ (n=15) mice to *Dars2*$^{fl/fl}$ (n=9). Each data point in the bar graphs is the mean of the replicates of one animal, meaning that each dot represents one animal. Data are normalized for the average of all *Dars2*$^{fl/fl\ mice}$. 2-way ANOVA with Šídák's multiple comparisons test was applied for statistical analysis. Asterisks indicate the level of statistical significance **** p ≤ 0.0001, *** p ≤ 0.001-0.004, ** p ≤ 0.01, * p ≤ 0.05, ns = not significant. The graphs have been produced in collaboration with Dr. Ming Yang and Dr. Christina Schmidt from the group of Prof. Dr. Christian Frezza, CECAD, Cologne.

3.5.3. DARS2 ablation in IECs inhibits the expression of respiratory chain subunits 3 and 5 days after tamoxifen injection and progressively cause lipid accumulation.

3.5.3.1. Phenotypic characterization of adult mice 3 days upon tamoxifen-inducible deletion of DARS2 in IECs.

To obtain insight into the kinetics of lipid accumulation, we initially examined intestinal tissues from DARS2$^{tamIEC-KO}$ mice analysed 3 days after the last tamoxifen injection (Figure 60a). Interestingly, the body weight of DARS2$^{tamIEC-KO}$ mice was indistinguishable from the respective *Dars2*$^{fl/fl}$ controls at the day of sacrifice (Figure 60b). Efficient induction of *Villin*CreER^{T2} recombinase activity and complete deletion of DARS2 in the IECs was already achieved 3 days after the last injection, accompanied by marked reduction of mitochondrially-encoded respiratory subunits (Figure 61a). COX/SDH staining additionally supported noticeable loss of COX activity, while ultrastructural examination of proximal SI unravelled unhealthy, partially damaged mitochondria (Figure 61b, c).

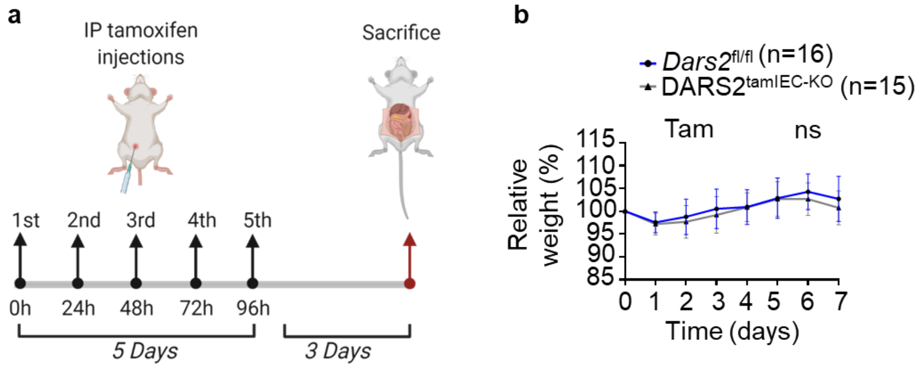

Figure 60. Body weight of DARS2$^{tamIEC-KO}$ mice was not noticeable different from the control *Dars2*$^{fl/fl}$ littermates 3 days after the last tamoxifen injection.

(a) Schematic depicting the experimental design for inducible DARS2 deletion. Mice received daily intraperitoneal injections of tamoxifen (1mg) for 5 consecutive days and were sacrificed 3 days upon the last injection as indicated. The scheme was created by BioRender, (b) Graph depicting relative body weight change of 8-12 week old *Dars2*$^{fl/fl}$ (n=16) and DARS2$^{tamIEC-KO}$ (n=15) mice after tamoxifen administration. Data are represented as mean ± SEM. 2-way ANOVA followed by Bonferroni's multiple comparisons test was applied for statistical analysis. Asterisks indicate the level of statistical analysis, ns=not significant.

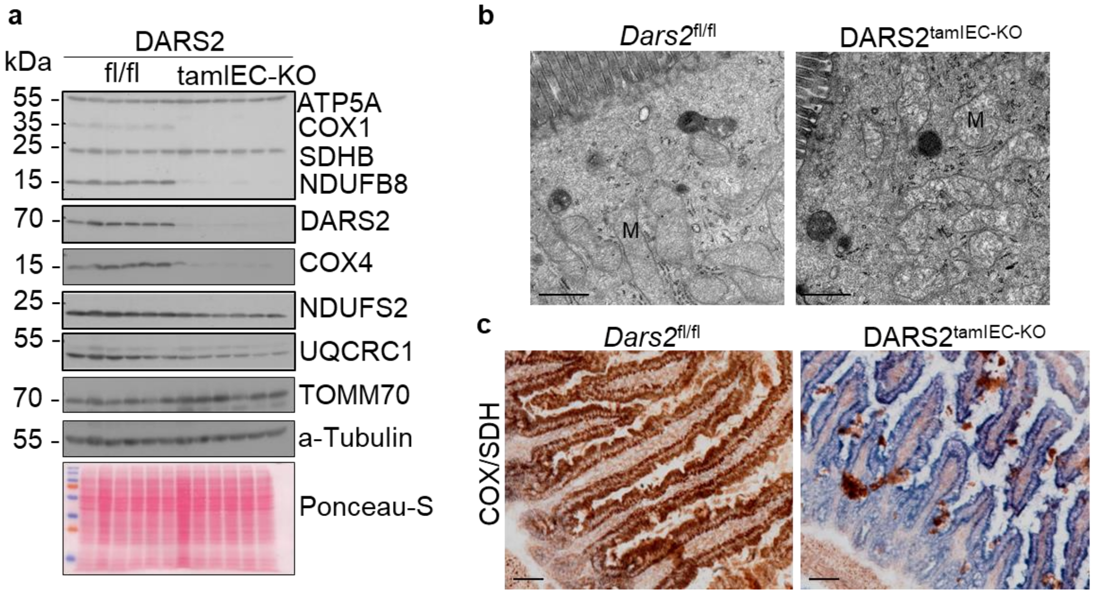

Figure 61. Efficient deletion of DARS2 and considerable decline of respiratory chain complexes already apparent 3 days after the last tamoxifen injection.

(a) Immunoblot analysis with the indicated antibodies of protein extracts isolated from small intestinal IECs of *Dars2*$^{fl/fl}$ and DARS2$^{tamIEC-KO}$ mice 3 days upon the last tamoxifen injection. Each lane represents one mouse (n=6 mice per genotype), (b) Representative transmission electron micrographs (TEM) of proximal SI sections from *Dars2*$^{fl/fl}$ (n=5) and DARS2$^{tamIEC-KO}$ (n=6) mice. Scale bars = 1µm. M, mitochondria, (c) Representative images of sections from the proximal small intestine of *Dars2*$^{fl/fl}$ (n=5) and DARS2$^{tamIEC-KO}$ (n=6) mice stained with COX/SDH. Scale bars = 50um.

Even though no considerable tissue damage was revealed on the proximal SI, strong suppression of IEC proliferation was indicative of DARS2 deletion 3 days upon the last injection, as proposed by immunohistological analysis (Figure 62). Considering the differentiated IEC subpopulations, Goblet cells of the proximal SI of DARS2$^{tamIEC\text{-}KO}$ mice were intensely stained with PAS and did not differ in numbers from them of *Dars2*$^{fl/fl}$ mice. However, they turned out to be smaller in size. On the other hand, moderate defects were visible in granule appearance of PCs stained positively with lysozyme (Figure 62). Of note, lack of ORO and PLIN2 staining in the proximal enterocytes suggested the absence of lipid droplet accumulation at this time point (Figure 63). Histological evaluation of the ileal SI of the same mice presented a milder pathology, manifested by a few areas with aberrantly scattered Ki67+ cells, no signs of LD formation, and a differentiation pattern of the secretory cells similar to the proximal SI (Figure 64).

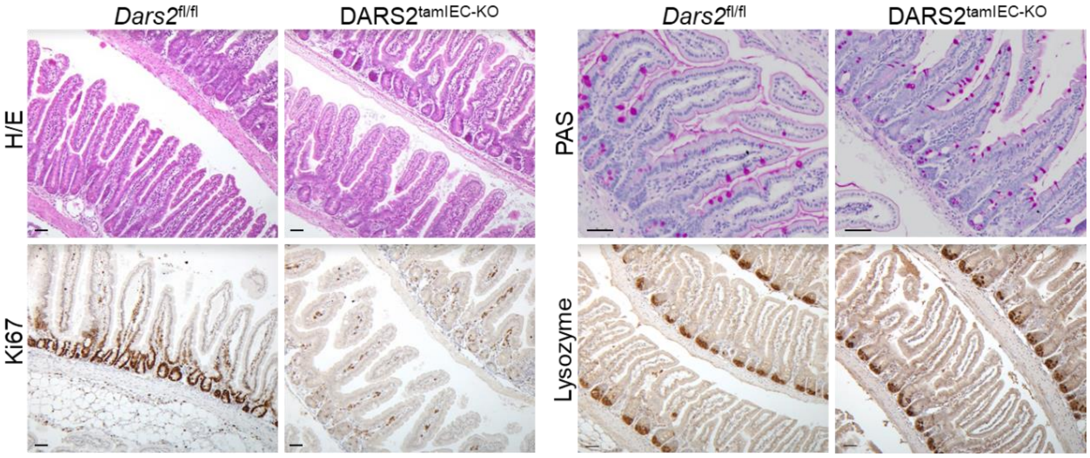

Figure 62. DARS2 deletion in the proximal SI notably reduced IEC proliferation, but moderately affected Goblet and Paneth cells 3 days after the last tamoxifen injection.

Representative images of sections from the proximal small intestine of *Dars2*$^{fl/fl}$ and DARS2$^{tamIEC\text{-}KO}$ mice sacrificed 3 days upon the last tamoxifen injection and stained with H/E (n=6 per genotype), PAS (n=7 per genotype) and immunostained for Ki67 and Lysozyme (n=6 per genotype). Scale bars = 50um.

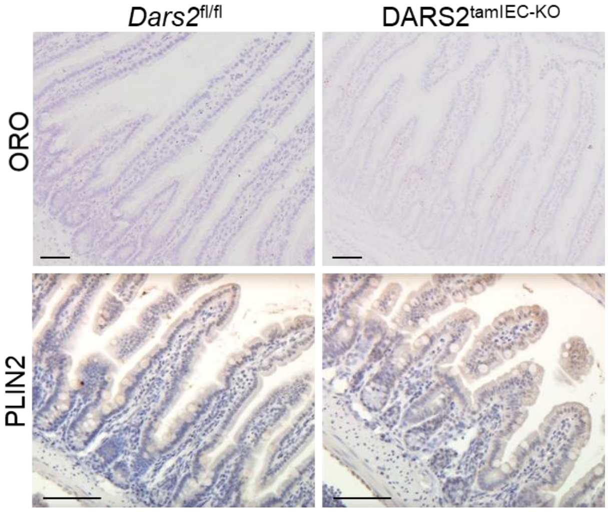

Figure 63. DARS2 deletion in the proximal SI do not cause accumulation of LDs 3 days after the last tamoxifen injection.

Representative images of sections from the proximal small intestine of *Dars2*$^{fl/fl}$ and DARS2$^{tamIEC-KO}$ mice sacrificed 3 days upon the last tamoxifen injection and stained with ORO (n=6 per genotype) and immunostained for PLIN2 (n=6 per genotype). Scale bars = 50um.

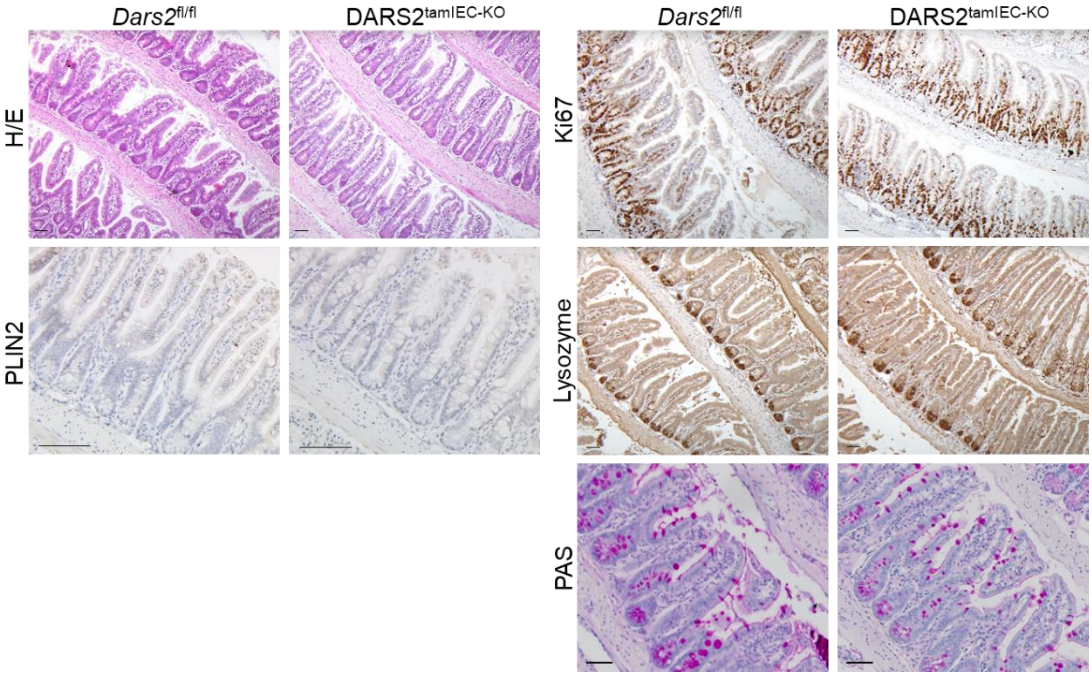

Figure 64. Mild pathology of the ileal SI from DARS2$^{tamIEC-KO}$ at 3 days after the last tamoxifen injection.

Representative images of sections from the distal small intestine of *Dars2*$^{fl/fl}$ and DARS2$^{tamIEC-KO}$ mice sacrificed 3 days upon the last tamoxifen injection and stained with H/E and PAS (n=6 per genotype) and immunostained for PLIN2, Ki67 and lysozyme (n=6 per genotype). Scale bars = 50um.

3.5.3.2. Phenotypic characterization of adult mice 5 days upon tamoxifen-inducible deletion of DARS2 in IECs.

In our attempt to timely resolve how loss of DARS2 in the IECs trigger accumulation of LDs, we continue our study by concentrating on a second time point, 5 days upon the last tamoxifen injection (Figure 65a). DARS2$^{tamIEC-KO}$ mice have lost a considerable portion of their body weight in comparison to the control *Dars2*$^{fl/fl}$ mice at the day of sacrifice (Figure 65b). Immunobloting analysis demonstrated loss of DARS2 and strongly decreased expression of mitochondrially-encoded respiratory subunits in proximal IECs 5 days after tamoxifen, corroborating with morphologically abnormal mitochondrial ultrastructure and severe COX deficiency, as reflected by TEM and COX/SDH staining, respectively (Figure 66a, b, c). Histological examination of proximal SI displayed distorted epithelial architecture pictured by completely diminished proliferating cells, reduced number of Goblet cells and paneth cells filled with irregular granules, weakly stained with lysozyme (Figure 67). Strikingly, the first signs of lipid accumulation in very small LDs within proximal enterocytes are clearly detectable (Figure 68). Finally, the intestinal pathology of the distal SI of DARS2$^{tamIEC-KO}$ mice 5 days upon the last injection was quite comparable to the proximal SI in regards to defective IEC proliferation and differentiation. Expectedly, ileal sections did not accommodate any LDs, as shown by negative ORO and

PLIN2 staining (Figure 69). These results indicated that lipid accumulation occurs gradually after DARS2 ablation in enterocytes of the proximal SI in DARS2$^{tamIEC\text{-}KO}$ mice.

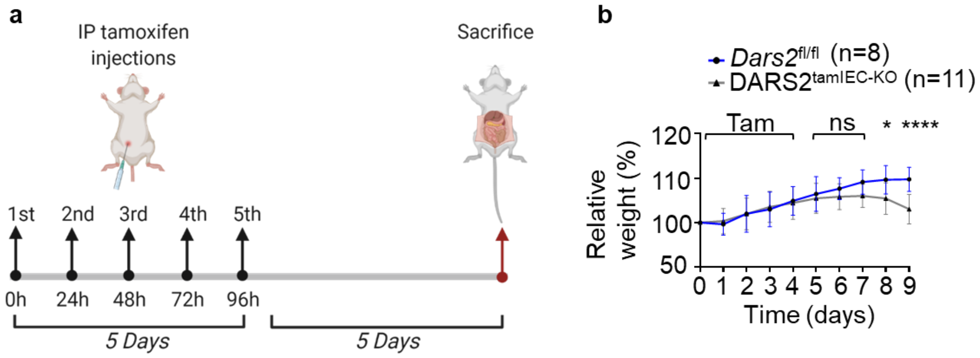

Figure 65. DARS2$^{tamIEC\text{-}KO}$ mice exhibited significant reduction of their body weight compared to the control *Dars2*$^{fl/fl}$ littermates 5 days after the last tamoxifen injection.

(a) Schematic depicting the experimental design for inducible DARS2 deletion. Mice received daily intraperitoneal injections of tamoxifen (1mg) for 5 consecutive days and were sacrificed 5 days upon the last injection as indicated. The scheme was created by BioRender. (b) Graph depicting relative body weight change of 8-12 week old *Dars2*$^{fl/fl}$ (n=8) and DARS2$^{tamIEC\text{-}KO}$ (n=11) mice after tamoxifen administration. Data are represented as mean ± SEM. 2-way ANOVA followed by Bonferroni's multiple comparisons test was applied for statistical analysis. Asterisks indicate the level of statistical analysis, **** $p \leq 0.0001$, * $p \leq 0.05$, ns=not significant.

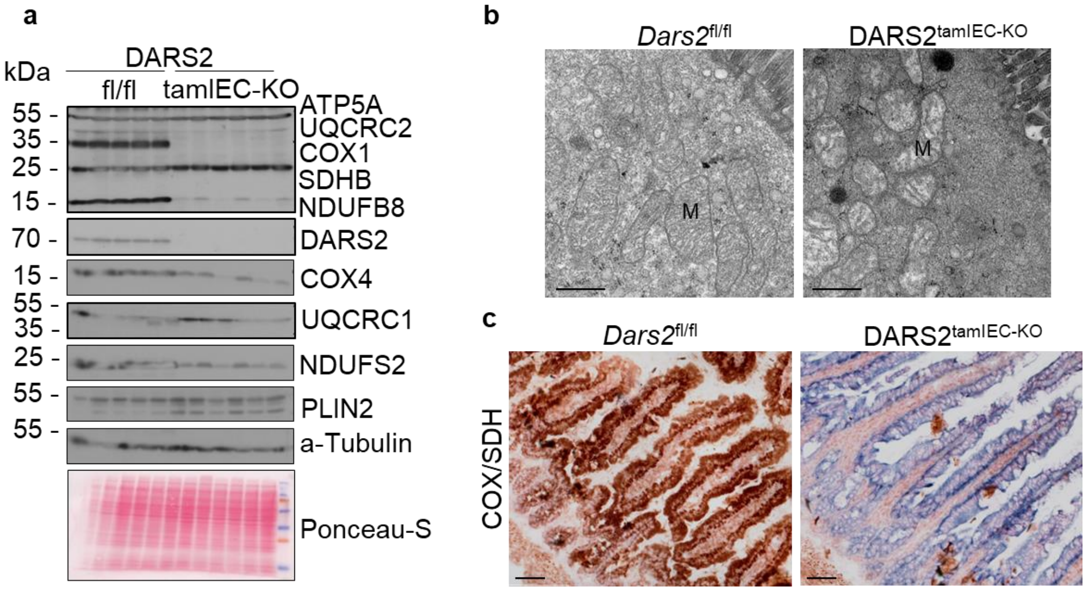

Figure 66. Loss of DARS2 is followed by noticeable decrease of respiratory chain complexes 5 days after the last tamoxifen administration.

(a) Immunoblot analysis with the indicated antibodies of protein extracts isolated from small intestinal IECs of *Dars2*$^{fl/fl}$ (n=5) and DARS2$^{tamIEC\text{-}KO}$ (n=6) mice 5 days upon the last tamoxifen injection. Each lane represents one mouse, b) Representative transmission electron micrographs (TEM) of proximal SI sections from *Dars2*$^{fl/fl}$ (n=5) and DARS2$^{tamIEC\text{-}KO}$ (n=6) mice. Scale bars = 1μm. M, mitochondria, (c) Representative images of sections from the proximal small intestine of *Dars2*$^{fl/fl}$ (n=5) and DARS2$^{tamIEC\text{-}KO}$ (n=5) mice stained with COX/SDH. Scale bars = 50um.

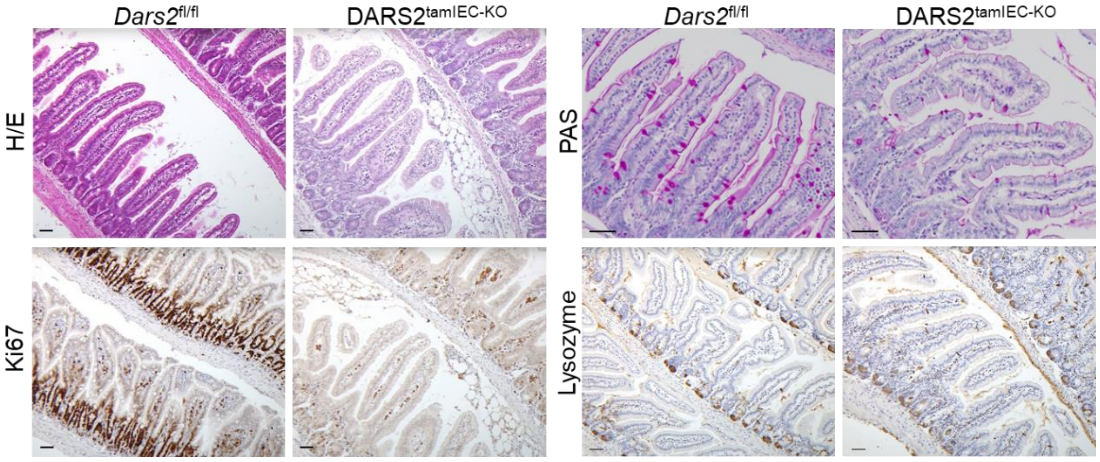

Figure 67. DARS2 deletion in the proximal SI markedly affected IEC proliferation and differentiation 5 days after the last tamoxifen injection.

Representative images of sections from the proximal small intestine of *Dars2*$^{fl/fl}$ and DARS2$^{tamIEC-KO}$ mice sacrificed 5 days upon the last tamoxifen injection and stained with H/E (n=10 per genotype), PAS (n=7 per genotype) and immunostained for Ki67 and Lysozyme (n=6 per genotype). Scale bars = 50um.

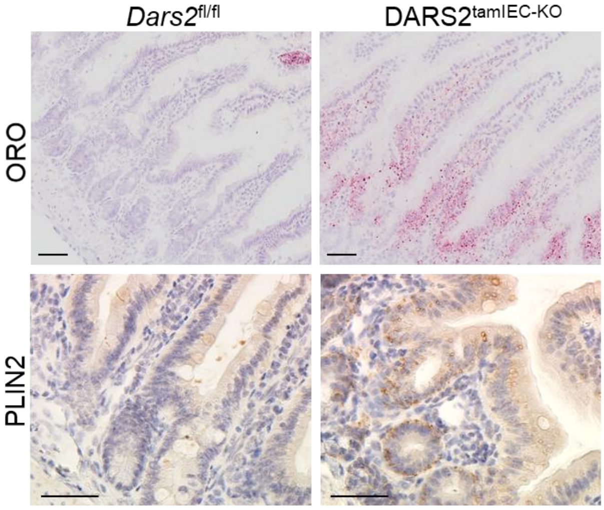

Figure 68. DARS2 deletion in the proximal SI results in mild signs of LD accumulation 5 days after the last tamoxifen injection.

Representative images of sections from the proximal small intestine of *Dars2*$^{fl/fl}$ and DARS2$^{tamIEC-KO}$ mice sacrificed 5 days upon the last tamoxifen injection and stained with ORO (n=6 per genotype) and immunostained for PLIN2 (n=6 per genotype). Scale bars = 50um.

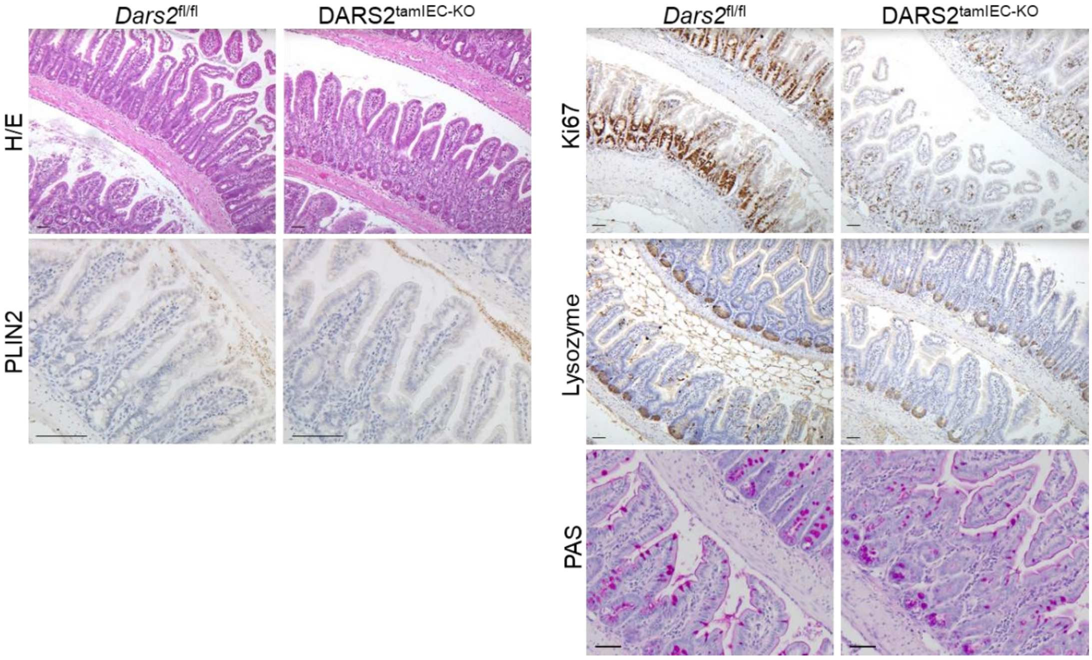

Figure 69. Severe pathology of the ileal SI from DARS2$^{tamIEC-KO}$ at 5 days after the last tamoxifen injection.

Representative images of sections from the distal small intestine of *Dars2*$^{fl/fl}$ and DARS2$^{tamIEC-KO}$ mice sacrificed 5 days upon the last tamoxifen injection and stained with H/E (n=10 per genotype) and PAS (n=6 per genotype) and immunostained for PLIN2, Ki67 and lysozyme (n=6 per genotype). Scale bars = 50um.

3.6. DARS2$^{tamIEC-KO}$ mice fed with fat-free diet (FFD) for 14 days show reduced lipid accumulation in IECs 7 days upon the last tamoxifen injection.

The increased lipid storage within large LDs in enterocytes from the proximal but not the distal SI of DARS2$^{tamIEC-KO}$ mice, together with the overall downregulation of lipid biosynthetic pathways in DARS2-deficient enterocyted, indicated that the accumulating lipids might originate from dietary fat. To assess the contribution of dietary fat in lipid accumulation, we examined whether feeding DARS2$^{tamIEC-KO}$ mice with a fat-free diet (FFD, containing <0.5% of fat), as opposed to normal chow diet (NCD, containing 3.4% fat), could prevent the lipid accumulation phenotype in the enterocytes of DARS2$^{tamIEC-KO}$ mice. Therefore, the group of experimental mice was fed with a mixture of NCD and FFD (1:1) for 4 days to be slowly introduced to the new food. Then, the mice completely switched to FFD and upon 2 days of FFD feeding, they received intraperitoneal injections for 5 consecutive days to induce DARS2 deletion, as have been previously described. DARS2$^{tamIEC-KO}$ mice, sacrificed 7 days after the last tamoxifen injection that have been fed with FFD for 2 weeks, showed less acute weight loss compared to mice on NCD (Figure 70a, b). Tamoxifen administration induced efficient ablation of DARS2 and respiratory chain deficiency, as proposed by the complete loss of COX1 expression along with robust COX deficiency in both proximal and distal SI, 7 days after tamoxifen administration (Figure 71a, b).

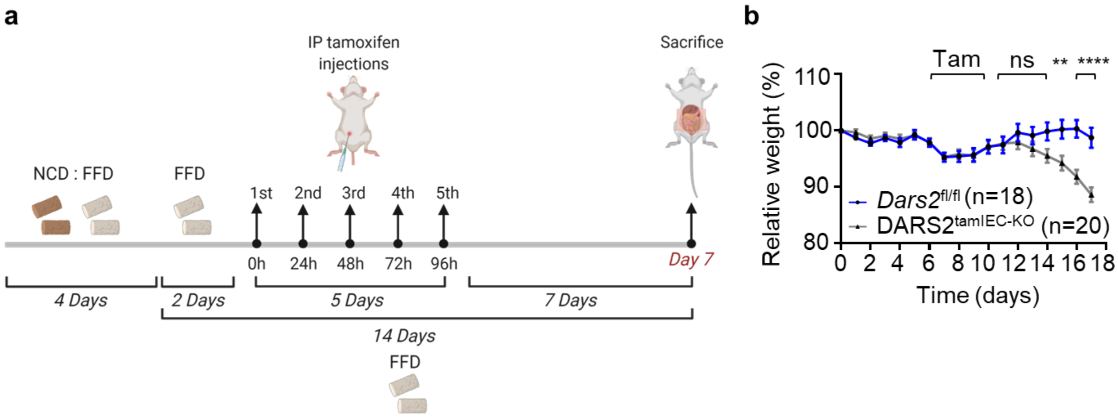

Figure 70. Tamoxifen - inducible ablation of DARS2 in adult mice fed with fat - free diet (FFD) leads to less dramatic weight loss compared to DARS2tamIEC-KO mice under normal chow diet (NCD).

(a) Schematic depicting the experimental design for inducing DARS2 deletion in mice fed with a FFD. 8-12 week old mice were fed with an equal mixture of NCD and FFD for 4 days, which was followed by 14 days FFD feeding and sacrifice 7 days after the last tamoxifen injection. The graph was generated by BioRender, (b) Graph depicting relative body weight change of 8-12 week old *Dars2*$^{fl/fl}$ (n=18) and DARS2$^{tamIEC-KO}$ (n=20) mice after tamoxifen administration. Data are represented as mean ± SEM. 2-way ANOVA followed by Bonferroni's multiple comparisons test was applied for statistical analysis. Asterisks indicate the level of statistical analysis, **** p ≤ 0.0001, ** p ≤ 0.01, ns=not significant, Tam=tamoxifen.

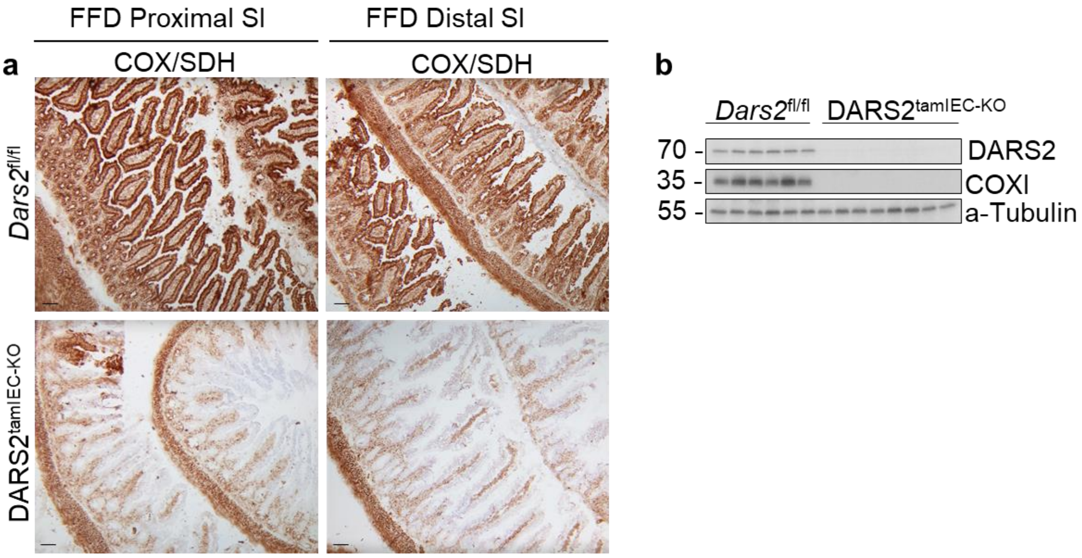

Figure 71. Tamoxifen - inducible ablation of DARS2 in adult mice fed with fat - free diet (FFD) cause strong COX deficiency both in proximal and distal SI at 7 days after the last tamoxifen injection.

(a) Representative images of sections from the proximal and distal small intestine of *Dars2*$^{fl/fl}$ and DARS2$^{tamIEC-KO}$ mice fed with FFD and sacrificed 7 days upon the last tamoxifen injection and stained with COX/SDH (n=6 per genotype). Scale bars = 50um, (b) Immunoblot analysis with the indicated antibodies of protein extracts isolated from small intestinal IECs of FFD – fed *Dars2*$^{fl/fl}$ (n=6) and DARS2$^{tamIEC-KO}$ (n=8) mice 7 days upon the last tamoxifen injection. Each lane represents one mouse.

Histological examination of mice under FFD sacrificed seven days upon the last tamoxifen injection, revealed impaired IEC proliferation both in the proximal and distal SI (Figure 72a, b). Moreover, lowered stem cell gene expression was detected in the proximal SI of FFD-fed mice, which was consistent with our findings on mice feeding on NCD (Figure 72c).

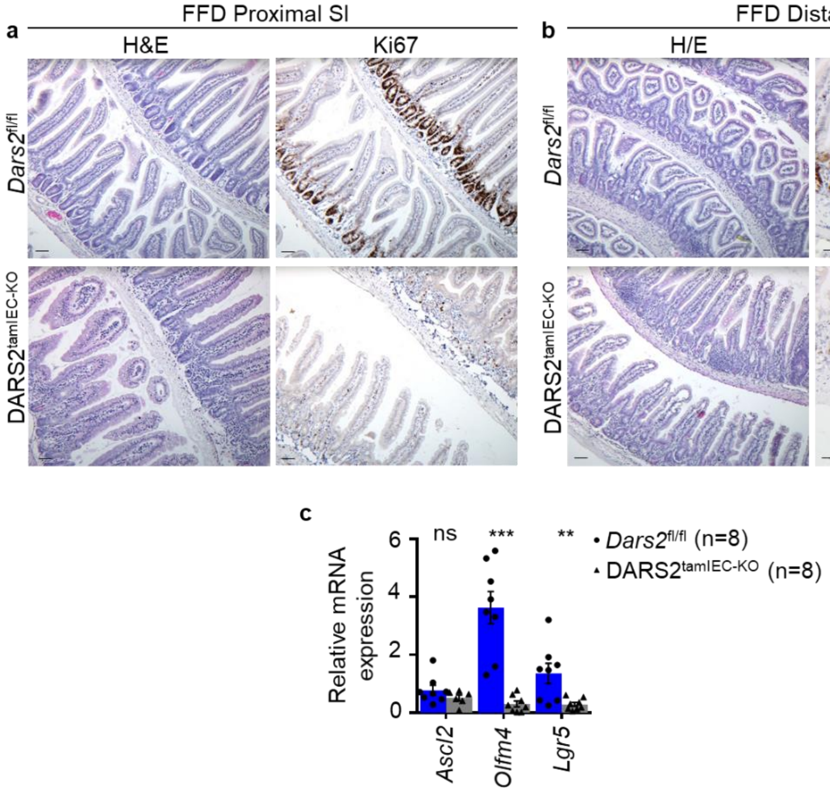

Figure 72. Tamoxifen - inducible ablation of DARS2 in adult mice fed with fat - free diet (FFD) significantly impacts IEC proliferation both in proximal and distal SI at 7 days after the last tamoxifen injection.

(a, b) Representative images of sections from the proximal (a) and distal (b) small intestine of *Dars2*$^{fl/fl}$ and DARS2$^{tamIEC\text{-}KO}$ mice fed with FFD and sacrificed 7 days upon the last tamoxifen injection and stained with H/E (n=32 per genotype) or immunostained with Ki67 (n=6 per genotype). Scale bars = 50um, (c) Graph depicting relative mRNA expression of stem cell genes analyzed by qRT-PCR and normalized to *Tbp* in the SI of *Dars2*$^{fl/fl}$ (n=8) and DARS2$^{tamIEC\text{-}KO}$ (n=8) mice. The graph presents mean ± SEM. Non-parametric Mann-Whitney U test was performed for statistical analysis. Asterisks indicate the level of statistical analysis *** $p \leq 0.001$-0.004, ** $p \leq 0.01$, ns=not significant.

Remarkably, DARS2$^{tamIEC\text{-}KO}$ mice fed with FFD only contained few very small LDs in enterocytes of the proximal SI in sharp contrast to the large LDs observed in mice fed a NCD strongly, hence suggesting that FFD strongly prevented the lipid accumulation (Figure 73). The distal SI of DARS2$^{tamIEC\text{-}KO}$ mice under FFD did not present any signs of LD formation, in the same way as the NCD-fed DARS2$^{tamIEC\text{-}KO}$ mice (Figure 74). These results substantiate that lipids accumulating in DARS2-deficient enterocytes are mostly derived from dietary fat, suggesting that impaired lipid transport could be the underlying cause.

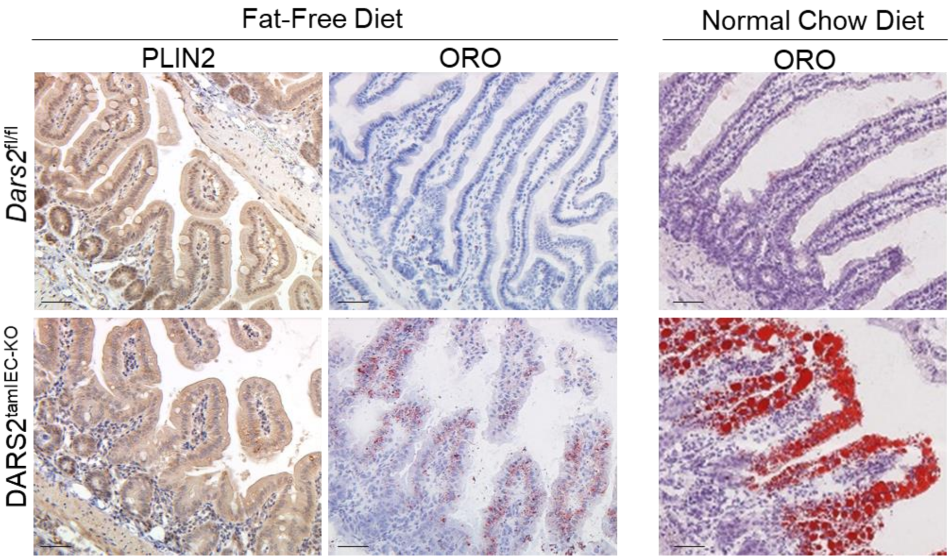

Figure 73. Tamoxifen - inducible ablation of DARS2 in adult mice fed with fat - free diet (FFD) significantly attenuated the massive LD accumulation observed in mice under NCD at 7 days after the last tamoxifen injection.

Representative images of sections from the proximal small intestine of *Dars2*$^{fl/fl}$ and DARS2$^{tamIEC-KO}$ mice fed with FFD and sacrificed 7 days upon the last tamoxifen injection and stained with ORO (n=12 per genotype) or immunostained with PLIN2 (n=7 per genotype). Proximal sections stained with ORO from NCD-fed *Dars2*$^{fl/fl}$ and DARS2$^{tamIEC-KO}$ mice (n=12 per genotype) are depicted for firm comparison. Scale bars = 50um.

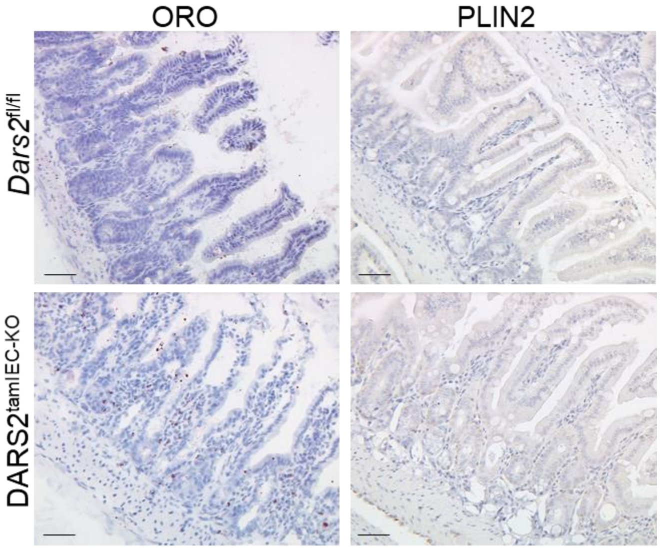

Figure 74. No signs of LD formation in the distal SI from DARS2tamIEC-KO mice fed with fat - free diet (FFD) 7 days after the last tamoxifen injection.

Representative images of sections from the distal small intestine of *Dars2*$^{fl/fl}$ and DARS2$^{tamIEC-KO}$ mice fed with FFD and sacrificed 7 days upon the last tamoxifen injection and stained with ORO (n=7 per genotype) or immunostained with PLIN2 (n=7 per genotype). Scale bars = 50um.

3.7. DARS2 deficiency evoked impaired transport of dietary lipids by enterocytes.

To directly elucidate whether DARS2$^{tamIEC-KO}$ mice cannot properly facilitate transport of dietary lipids from the lumen to the circulation, metabolic tracing experiments were performed in 12-16 week old mice 7 days upon the last tamoxifen injection, when the highest weight drop has been reached (Figure 75a, b, c). DARS2$^{tamIEC-KO}$ mice were subjected to 2 hours fasting with free access to drinking water. Afterwards, the mice received, by oral gavage, a combined lipid-glucose mixture enriched with tracers for TAGs (^{3}H-triolein) and glucose (^{14}C-deoxyglucose, ^{14}C-DOG). Subsequently, radioactivity levels were determined in all organs and plasma (Figure 75a). Oral glucose – fat tolerance test (OGFTT) revealed that ^{3}H-triolein uptake was strongly reduced all metabolically active organs, except the stomach from DARS2$^{tamIEC-KO}$ mice compared to *Dars2*$^{fl/fl}$ littermates (Figure 76a). Due to the fact that IECs are already overloaded with lipids stored within large LDs, they presumably reduce further lipid uptake, thus explaining the significant drop in the uptake of ^{3}H-triolein from duodenum (Figure 76a). However, no considerable difference in ^{3}H-triolein uptake was reported in the jejenum, which is the section of the SI primarily responsible for lipid absorption (Figure 76b), whereas ^{3}H-triolein detection in the plasma was notably lowered, hence highlighting that IECs are capable of absorbing alimentary fats from the lumen, but unable to transport them to the circulation.

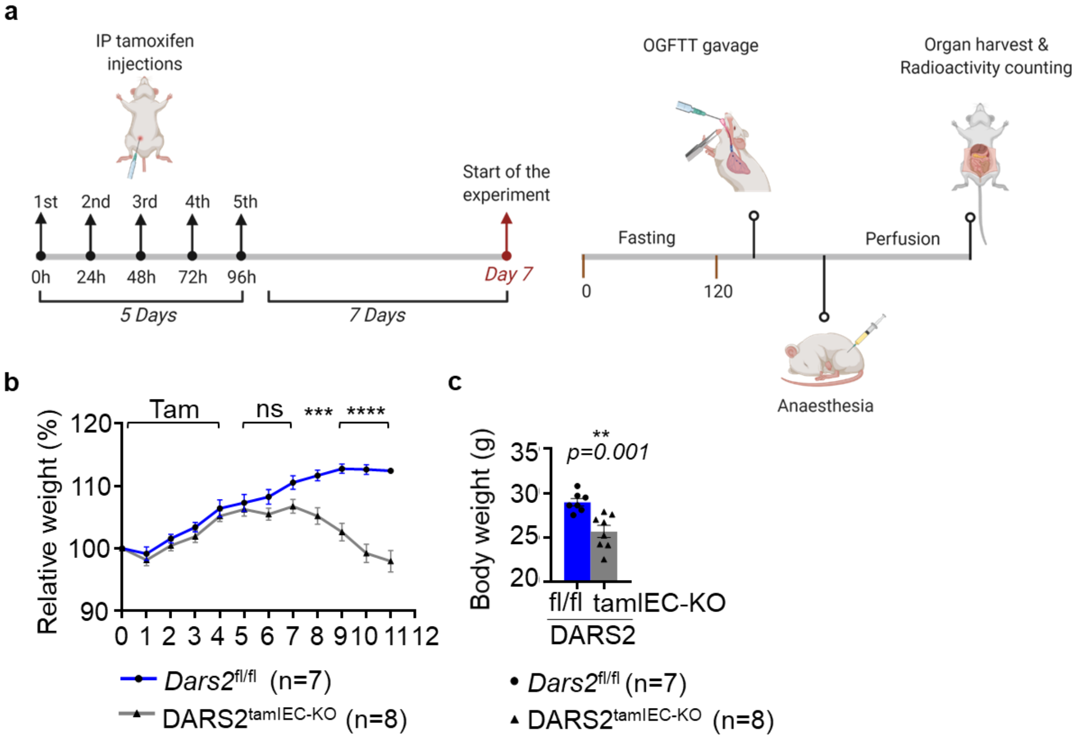

Figure 75. DARS2$^{tamIEC-KO}$ mice were subjected to oral glucose – fat tolerance test (OGFTT) 7 days after the last tamoxifen injection.

(a) Schematic depicting the experimental design of the oral glucose fat tolerance test (OGFTT). On day 7 after the last out of 5 consecutive intraperitoneal tamoxifen injections, mice were fasted for 2 hrs followed by oral gavage with ^{3}H-triolein and ^{14}C-DOG. Tissues were harvested 2 hrs after the oral gavage, (b, c) Relative body weight change over the indicated time period (b) and body weight recorded on the day of sacrifice (c) of *Dars2*$^{fl/fl}$ (n=7) and DARS2$^{tamIEC-KO}$ (n=8) mice subjected to OGFTT. Non-parametric Mann-Witney U test (c) and 2-way ANOVA followed by Bonferroni's multiple comparisons test (b) were applied for statistical analysis. Asterisks indicate the level of statistical analysis; **** p ≤ 0.0001, *** p ≤ 0.001-0.004, ** p≤0.01, ns=not significant.

The OGFTT was performed in collaboration with the group of Prof. Dr. Joerg Heeren, UKE, Hamburg.

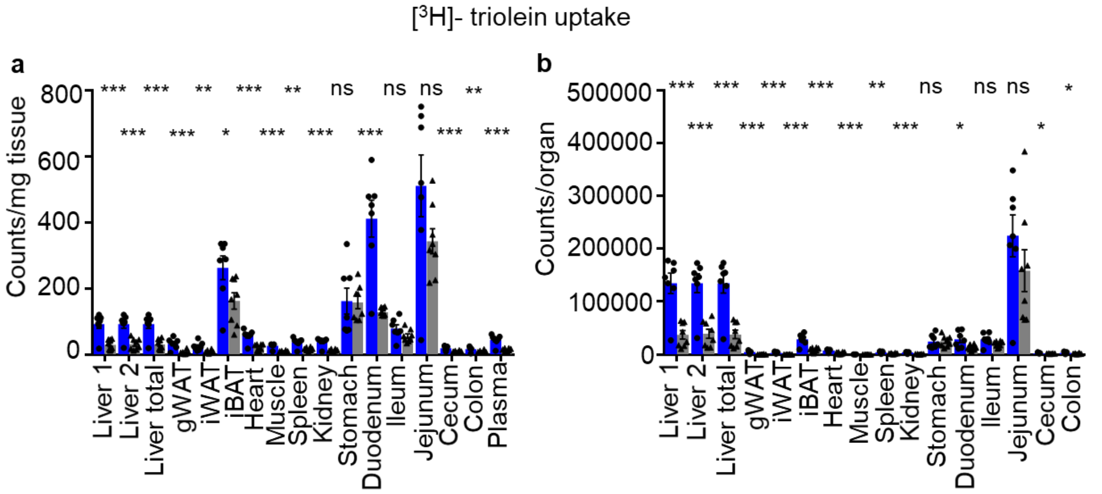

Figure 76. Impaired transport of dietary lipids by enterocytes upon DARS2 deficiency.

(a,b) Graphs depicting counts per mg tissue (a) or counts per organ (b) of ^{3}H-triolein in different organs from *Dars2*$^{fl/fl}$ (n=7) and DARS2$^{tamIEC-KO}$ (n=8) mice determined 120 min after oral gavage. Radioactivity (in dpm) was measured by scintillation counting using a Perkin Elmer Tricarb Scintillation Counter. Data represent mean ± SEM. Unpaired two-tailed Student's t test with no assumption of equal variance was applied for statistical analysis. Asterisks indicate the level of statistical analysis; *** p ≤ 0.001-0.004, ** p ≤ 0.01, * p ≤ 0.05, ns = not significant. The OGFTT was performed in collaboration with the group of Prof. Dr. Joerg Heeren, UKE, Hamburg.

In sharp contrast to ^{3}H-triolein, ^{14}C-DOG uptake was only slightly reduced in some organs (Figure 77a). However, ^{14}C-DOG was normally found in the plasma of DARS2$^{tamIEC-KO}$ mice in comparable levels to *Dars2*$^{fl/fl}$ littermates, whereas its uptake by the liver which the major target organ for glucose absorption, was only marginally decreased, indicating that loss of DARS2 in enterocytes predominantly affects handling of dietary lipids (Figure 77a, b).

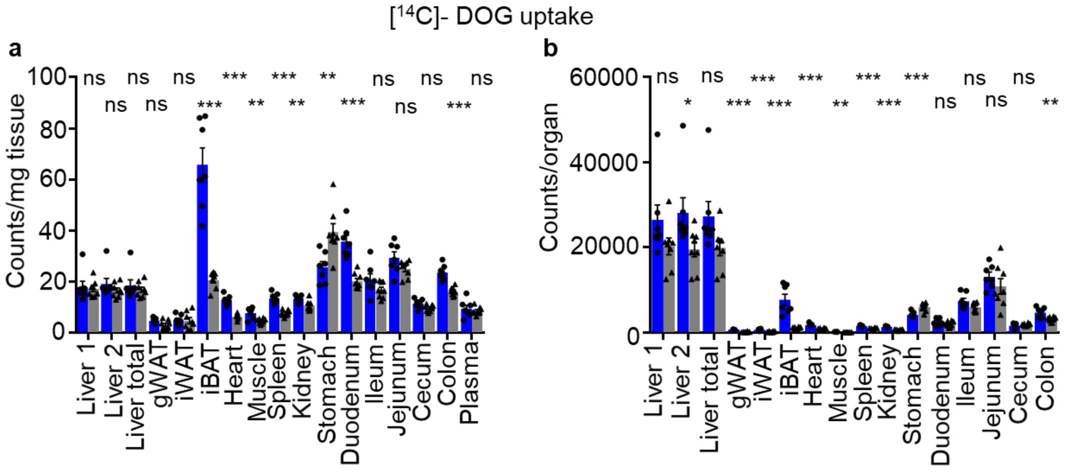

Figure 77. DARS2 deficiency does not significantly affect glucose absorption and transport by the enterocytes.

(a,b) Graphs depicting counts per mg tissue (a) or counts per organ (b) of ^{14}C-DOG in different organs from *Dars2*$^{fl/fl}$ (n=7) and DARS2$^{tamIEC\text{-}KO}$ (n=8) mice determined 120 min after oral gavage. Radioactivity (in dpm) was measured by scintillation counting using a Perkin Elmer Tricarb Scintillation Counter. Data represent mean ± SEM. Unpaired two-tailed Student's t test with no assumption of equal variance was applied for statistical analysis. Asterisks indicate the level of statistical analysis; *** $p \leq 0.001$-0.004, ** $p \leq 0.01$, * $p \leq 0.05$, ns = not significant. The OGFTT was performed in collaboration with the group of Prof. Dr. Joerg Heeren, UKE, Hamburg.

To assess the profile of plasma lipoproteins, plasma was subjected to fast performance liquid chromatography (FPLC) in order to fractionate the distinct lipoprotein classes. Therefore, lipoprotein seperation by FPLC displayed lessened levels of TAG-rich lipoproteins (TRLs), including CMs and very low VLDLs, in DARS2$^{tamIEC\text{-}KO}$ mice compared to *Dars2*$^{fl/fl}$ littermates, whereas HDL and LDL were not affected (Figure 78a). Additionally, the lipoprotein cholesterol profile remained unchanged (Figure 78b). Interestingly, a high peak in the glycerol levels was overt from FPLC, corroborating with the increased amount of plasma glycerol and the slightly enhanced circulating FFA in DARS2$^{tamIEC\text{-}KO}$ mice (Figure 78a, d, e). Notwithstanding, the weight of gonadal and inguinal white adipose tissue (gWAT and iWAT respectively) was notably depleted in DARS2$^{tamIEC\text{-}KO}$ mice 7 days after tamoxifen administration (Figure 78c), when they reached 20% loss of their body weight. The elevated levels of glycerol and FFAs in the blood together with the loss of adipose tissue in DARS2$^{tamIEC\text{-}KO}$ mice suggested that DARS2 deficiency in IECs caused increased intracellular lipolysis of adipose tissue depots, likely as a compensatory response to the impaired supply of dietary lipids by the intestine.

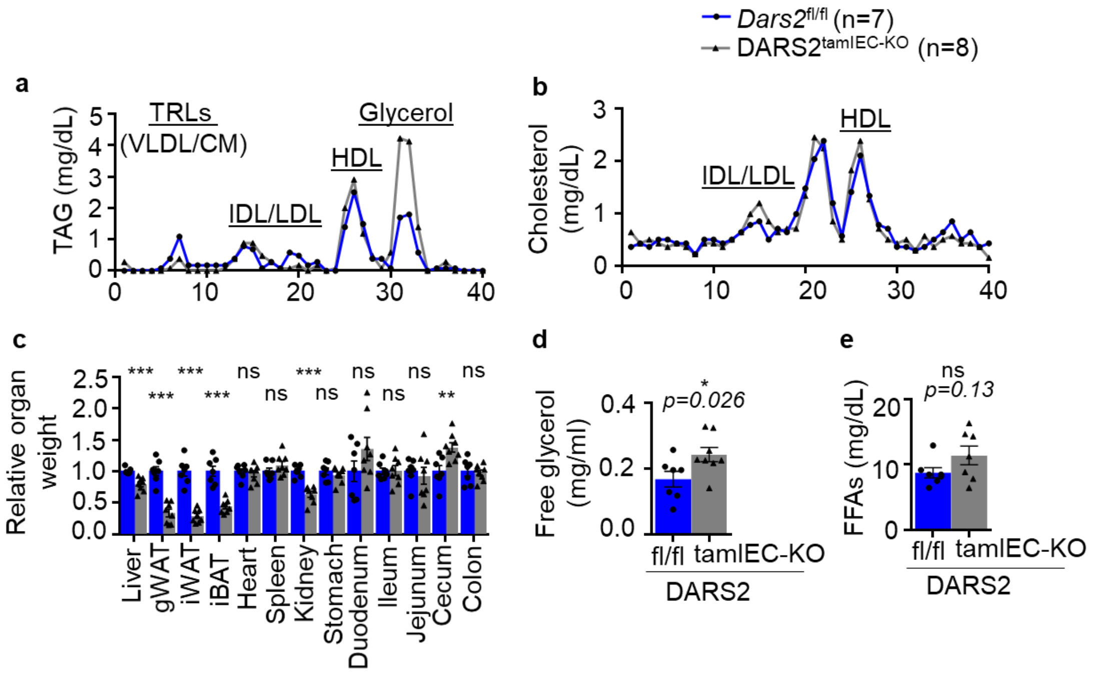

Figure 78. DARS2 deficiency in IECs induces intracellular lipolysis.

(a,b) Graphs depicting TAG (a) and cholesterol (b) FPLC profiles of pooled plasma from fasted *Dars2*$^{fl/fl}$ (n=7) and DARS2$^{tamIEC\text{-}KO}$ (n=8) mice determined 2 hours post - gavage. TLRs, Triclyceride – rich lipoproteins; VLDL, very low – density lipoprotein; CM, chylomicron; IDL/LDL, intermediate & low – density lipoprotein; HDL, high – density lipoprotein, (c) Graph depicting relative organ weight of *Dars2*$^{fl/fl}$ (n=7) and DARS2$^{tamIEC-KO}$ (n=8) mice 7 days after the last tamoxifen injection subjected to OGFTT, (d) Graph depicting free glycerol levels in plasma from *Dars2*$^{fl/fl}$ (n=7) and DARS2$^{tamIEC-KO}$ (n=8), (e) Graph depicting free fatty acid levels in plasma from *Dars2*$^{fl/fl}$ (n=7) and DARS2$^{tamIEC-KO}$ (n=8). Data represent mean ± SEM. Unpaired two-tailed Student's t test with no assumption of equal variance was applied for statistical analysis. Asterisks indicate the level of statistical analysis; *** $p \leq 0.001$-0.004, * $p \leq 0.05$, ns = not significant. The OGFTT and plasma measurements have been performed in collaboration with the group of Prof. Dr. Joerg Heeren, UKE, Hamburg.

Afterwards, we sought to directly determine intestinal transport by performing oral fat tolerance test (OFTT) in 12-16 week old mice 7 days upon the last tamoxifen injection, when they have already lost an important portion of their body weight (Figure 79a, b, c). Following 2 hours fasting, DARS2$^{tamIEC-KO}$ mice were intravenously injected into the tail vein with the LPL inhibitor tyloxapol, which blocks intravascular lipoprotein processing. Then, the mice received by oral gavage a lipid solution traced with radiolabelled triglycerides (^{3}H-triolein) and cholesterol (^{14}C-cholesterol) and blood was subsequently collected from the tail 0, 30, 60 and 120 min upon the oral administration of the emulsion for radioactivity measurement and chylomicron production assessment (Figure 79a). Largely decreased accumulation of ^{3}H-triolein and ^{14}C-cholesterol (Figure 80a, b) together with enzymatically-determined reduced TGs were identified in the plasma of DARS2$^{tamIEC-KO}$ mice, undisputedly indicating severely impaired chylomicron production (Figure 80c). Taken together, metabolic tracing experiments showed that intestinal DARS2 deficiency caused impaired transport of luminal lipids resulting in their accumulation within large LDs in enterocytes.

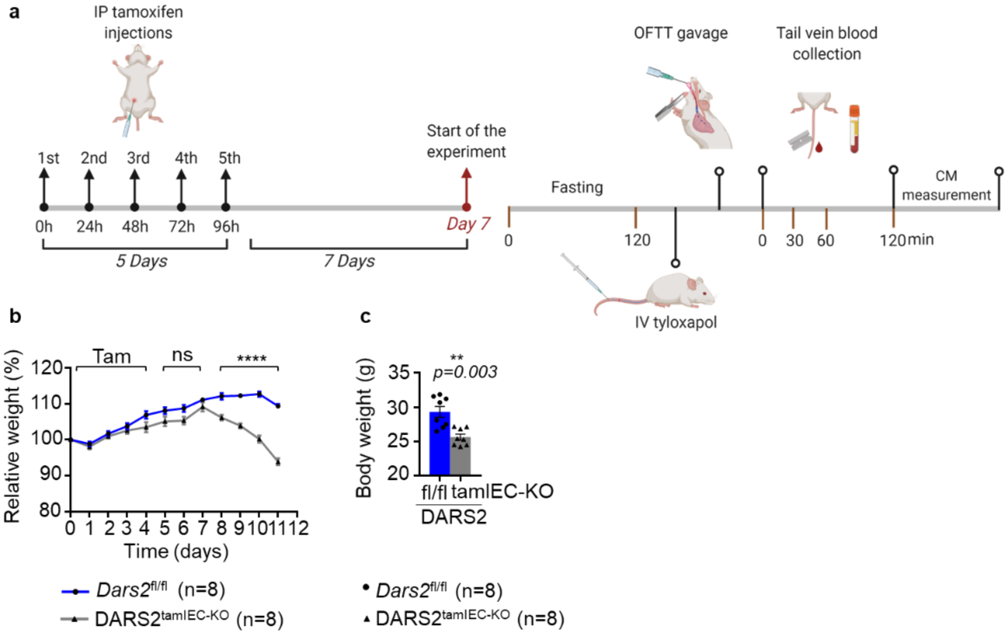

Figure 79. DARS2$^{tamIEC-KO}$ mice were subjected to oral fat tolerance test (OFTT) 7 days after the last tamoxifen injection.

(a) Schematic depicting the experimental design of the oral fat tolerance test (OFTT). On day 7 after the last out of 5 consecutive intraperitoneal tamoxifen injections, mice were fasted for 2 hrs and received an intravenous injection of the lipoprotein lipase inhibitor tyloxapol, followed by oral gavage with a lipid solution containing ^{3}H-triolein and ^{14}C-cholesterol. Afterwards, blood was collected from the tail vein for the indicated time points and CM levels were measured, (b, c) Relative body weight change over the indicated time period (b) and body weight recorded on the day of sacrifice (c) of *Dars2*$^{\mathrm{fl/fl}}$ (n=8) and DARS2$^{\mathrm{tamIEC\text{-}KO}}$ (n=8) mice subjected to OFTT. All graphs show mean ± SEM. Non-parametric Mann-Witney U test (c) and 2-way ANOVA followed by Bonferroni's multiple comparisons test (b) were applied for statistical analysis. Asterisks indicate the level of statistical analysis; **** $p \leq 0.0001$, ** $p \leq 0.01$, ns=not significant.

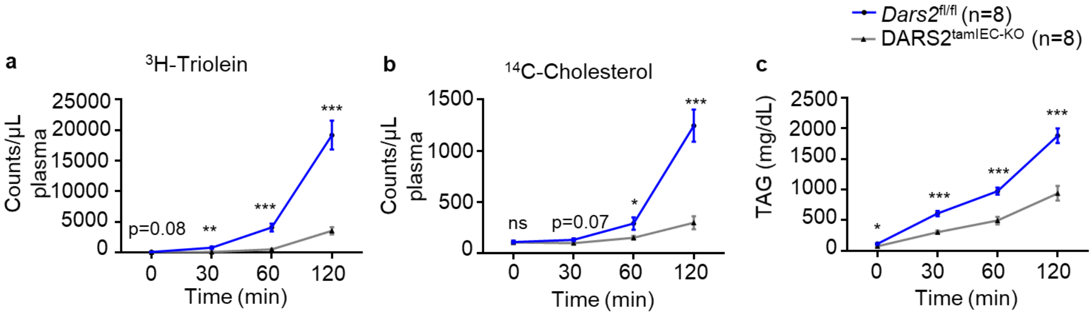

Figure 80. DARS2$^{\mathrm{tamIEC\text{-}KO}}$ mice exhibited greatly impaired CM production 7 days after the last tamoxifen injection.

(a, b, c) Graphs depicting ^{3}H-triolein (a), ^{14}C-cholesterol (b) and TAG content in portal plasma of *Dars2*$^{\mathrm{fl/fl}}$ (n=8) and DARS2$^{\mathrm{tamIEC\text{-}KO}}$ (n=8) mice subjected to OFTT after intravenous tyloxapol injection. Data represent mean ± SEM. Unpaired two-tailed Student's t test with no assumption of equal variance was applied for statistical analysis. Asterisks indicate the level of statistical analysis; *** $p \leq 0.001$-0.004, ** $p \leq 0.01$, * $p \leq 0.05$, ns = not significant. The OFTT measurements have been performed in collaboration with the group of Prof. Dr. Joerg Heeren, UKE, Hamburg.

3.8. DARS2 deficiency causes Golgi disorganization and inhibits chylomicron production in enterocytes

Our results showing that DARS2 deficiency caused impaired transport of luminal lipids resulting in their accumulation within large LDs in enterocytes, suggested that loss of respiratory chain activity may inhibit a step required for the production of chylomicrons. In order to assess the presence of CMs in DARS2-deficient enterocytes, we scrutinized the ultrastructural sections obtained from the proximal SI of DARS2$^{\mathrm{tamIEC\text{-}KO}}$ mice. Interestingly, we noticed that chylomicrons were prominent within extended Golgi cisternae or were secreted across the basolateral surfaces of enterocytes in the proximal SI of *Dars2*$^{\mathrm{fl/fl}}$ control mice (Figure 81). In contrast, an extensive disorganization disorganisation of the secretory pathway in enterocytes of DARS2$^{\mathrm{IEC\text{-}KO}}$ mice, which lacked a Golgi complex containing chylomicrons, was revealed by ultrastructural examination (Figure 81). The cytoplasm of DARS2-deficient enterocytes was instead packed with large LDs, likely a result of LD lateral fusion due to their high density (Figure 81, arrowheads). LDs were also present within the ER lumen of enterocytes in DARS2$^{\mathrm{IEC\text{-}KO}}$ mice (Figure 81, arrows). The striking absence of a Golgi network in DARS2-deficient enterocytes is indicative of impaired ER to Golgi vesicle transport.

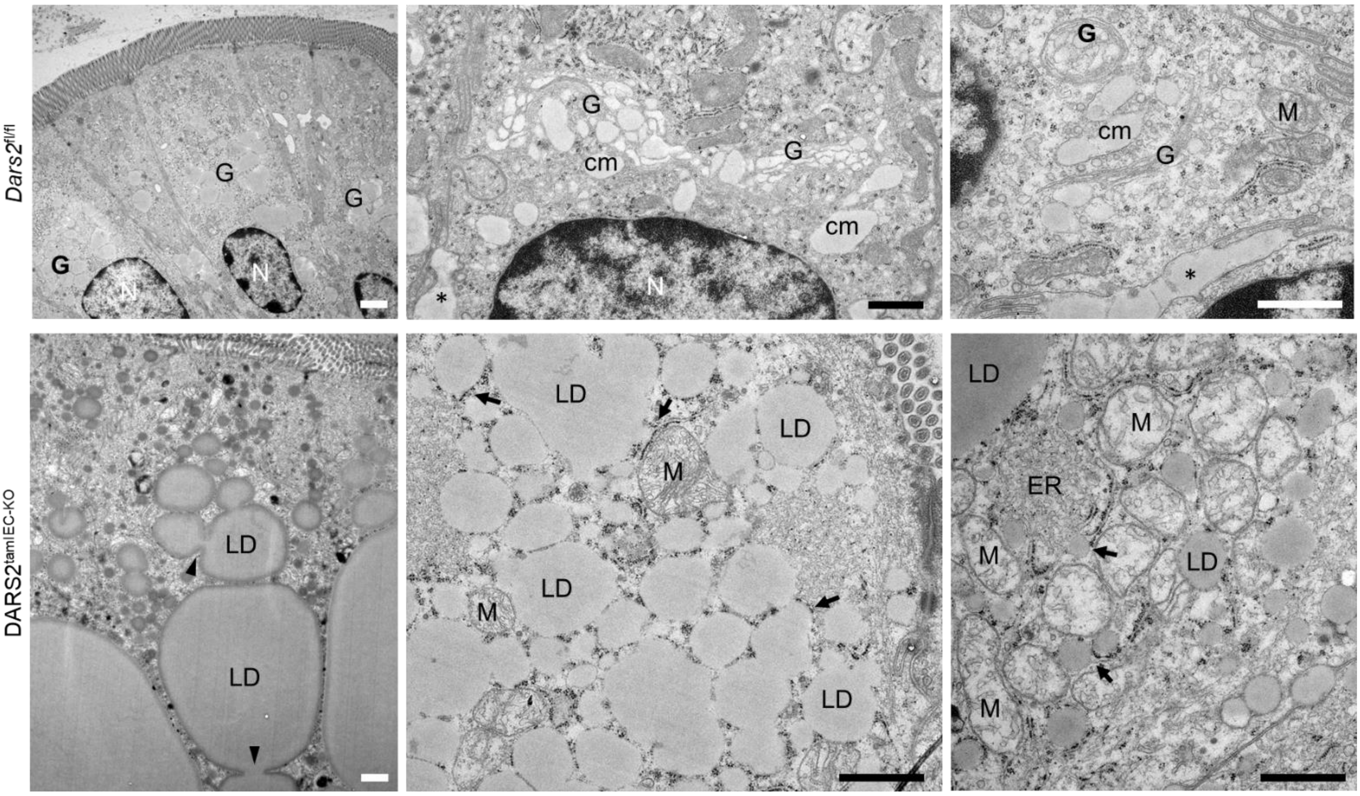

Figure 81. Extensive Golgi disorganization is prominent upon DARS2 deficiency in enterocytes.

Representative EM micrographs from proximal SI sections of Dars2fl/fl (n=4) and DARS2IEC-KO (n=4) mice 7 days after the last tamoxifen injection illustrating the lack of chylomicron-containing Golgi complexes and the appearance of aberrant number of LDs and damaged mitochondria in DARS2-deficient enterocytes. Asterisks indicate chylomicrons secreted in basolateral intercellular space. Arrows point at LDs within the ER lumen in rough and smooth ER neighbouring areas. G, Golgi complex; M, mitochondria; cm, chylomicrons; LD, lipid droplet; ER, endoplasmic reticulum; N, nucleus. Scale bars=1um. The elecron microscopy images were anazyzed in collaboration to Dr. Vangelis Kondylis.

To further assess the integrity of the Golgi and the secretory pathway in enterocytes, we decided to perform immunostaining using a specific trans-Golgi marker, so-called Trans-Golgi network integral membrane protein 1 (TGN38) and E-cadherin, which is indispensable for cell-cell interactions. TGN38 constitutes a transmembrane protein localised in the Golgi (Humphrey, Peters et al. 1993), and E-cadherin is transported through the Golgi to reach the plasma membrane (van Roy and Berx 2008). TGN38 staining revealed a typical compact juxta-nuclear Golgi network in enterocytes from *Dars2*$^{fl/fl}$ mice alongside a predominantly plasma membrane localisation of E-cadherin (Figure 82). In contrast, a pronounced dispersal of TGN38 staining was observed in enterocytes from DARS2$^{tamIEC\text{-}KO}$ mice at 8 days after the last tamoxifen injection, accompanied by a distinct loss of E-cadherin from the plasma membrane (Figure 82). Additionally, E-cadherin was frequently detected in intracellular compartments in DARS2$^{tamIEC\text{-}KO}$ (Figure 82). These results are consistent with an impaired ER-to-Golgi transport in DARS2-deficient enterocytes resulting in the observed disappearance of the Golgi network.

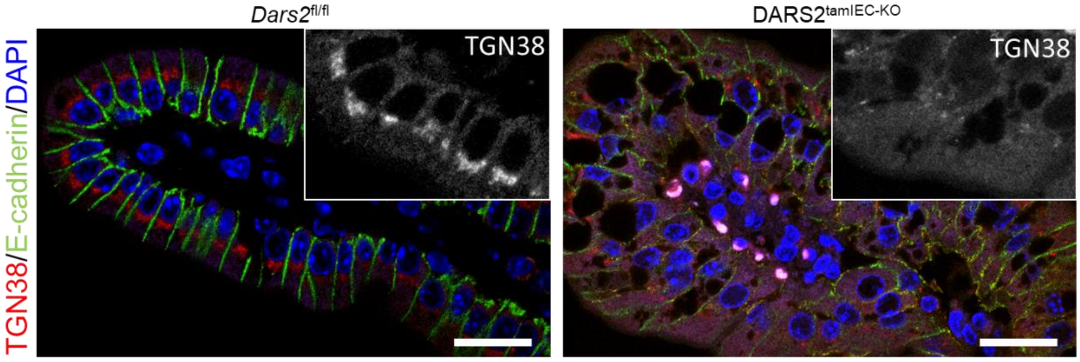

Figure 82. Defective Golgi organization and altered E-cadherin localization upon DARS2 deficiency in enterocytes.

Representative fluorescence microscopy images from the proximal SI of 8-12 week old *Dars2*$^{fl/fl}$ (n=5) and DARS2$^{tamIEC-KO}$ (n=5) mice sacrificed 8 days upon the last tamoxifen injection, immunostained with antibodies against TGN38 (red) and E-cadherin (green). Nuclei stained with DAPI (blue). Scale bars = 50μm.

These results suggest that disruption of the secretory pathway underlies the impaired dietary lipid transport in DARS2-deficient enterocytes by inhibiting the trafficking of PCTVs from the ER to the Golgi and the production of mature chylomicrons. Indeed, KEGG pathway analysis of the RNAseq data revealed that many of the downregulates genes were implicated in the regulation of dietary lipid processing by enterocytes, ER to Golgi transport and CM assembly and maturation in particular (Figure 83). Consistently, the proteomics data demonstrated that several proteins involved in chylomicron production (Neeli, Siddiqi et al. 2007, Giammanco, Cefalu et al. 2015, Ko, Qu et al. 2020), comprising CD36, ApoA4, ApoA1, Mttp and Lsr, as well as COPII vesicle coating proteins (Gillon, Latham et al. 2012), including Sec16, Sec23, Sec24 and Sec31 were downregulated in the DARS2-deficient enterocytes (Figure 84).

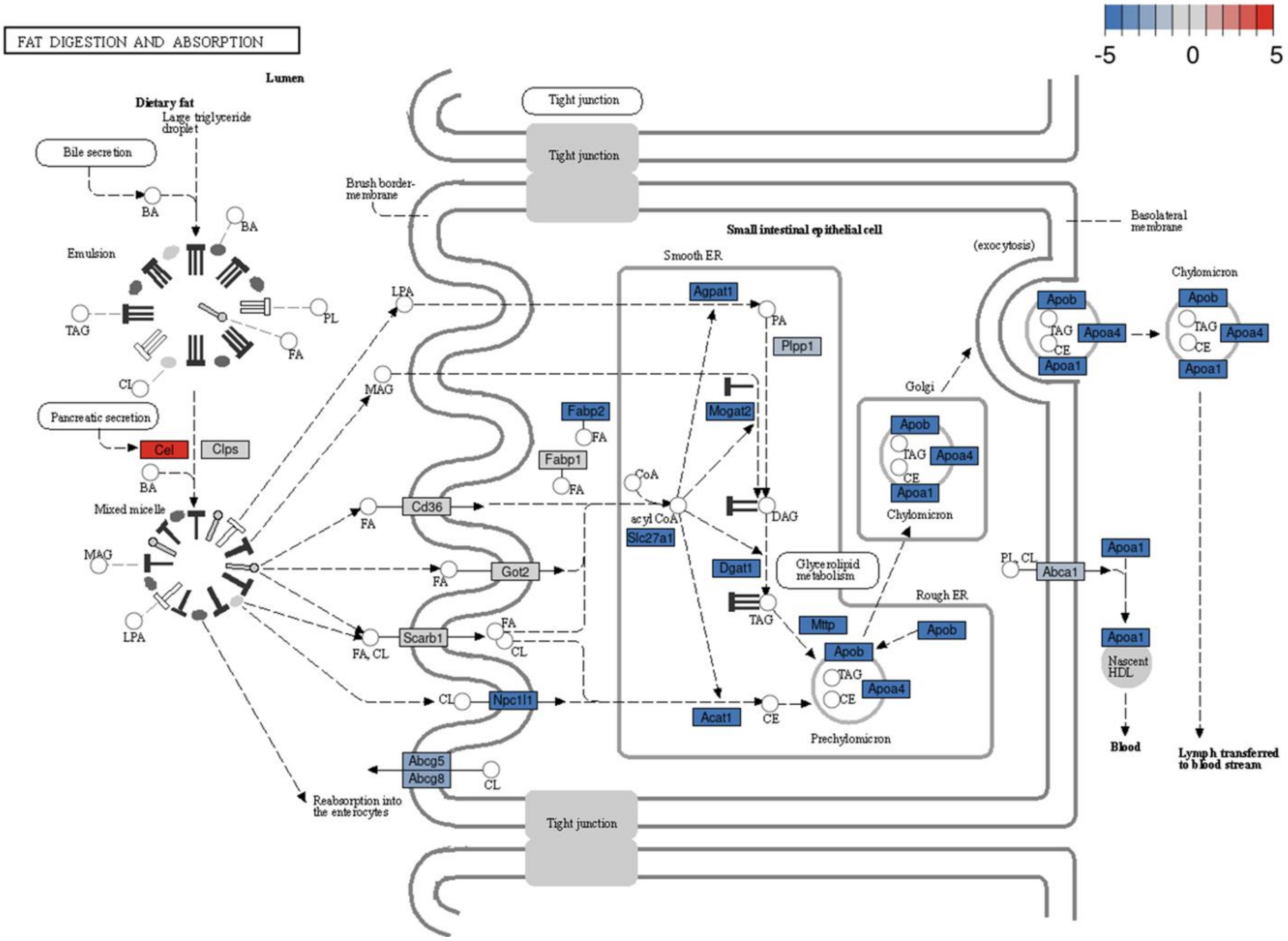

Figure 83. Marked downregulation of genes involved into dietary lipid trasport upon DARS2 ablation in enterocytes.

KEGG pathway visualization of the gene expression on the fat digestion and absorption. The blue colors represent downregulation of the gene, whereas the red corresponds to the upregulated genes. Increased color intensity shades a stronger effect. The generation of this KEGG pathway was perfromed in collaboration with Dr. Ulrike Goebel, University of Cologne.

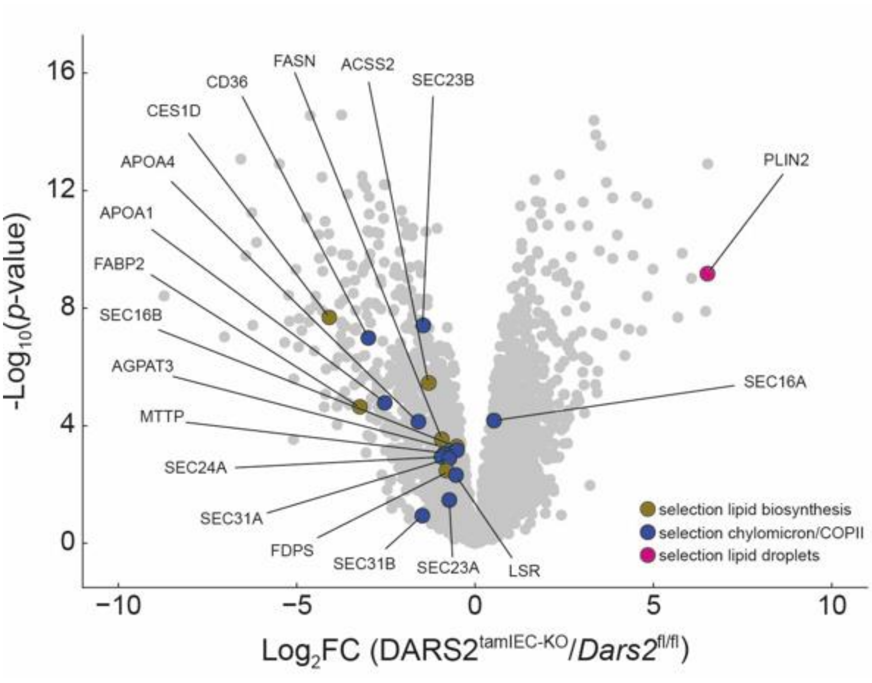

Figure 84. Noticeable suppression of numerous proteins participating in CM production upon DARS2 ablation in enterocytes.

Volcano plot presenting the proteome landscape comparing DARS2$^{tamIEC\text{-}KO}$ mice to *Dars2*$^{fl/fl}$ highlighting key proteins, particularly involved in chylomicron assembly and COPII vesicle production. This volcano plot was perform in collaboration with Dr. Christina Schmidt from the group of Prof. Dr. Christian Frezza.

3.9. Golgi fragmentation gradually occurs and preceeds lipid droplet accumulation upon DARS2 ablation.

In order to temporally dissect the sequence of events culminating in lipid transport defect and fat overloading in DARS2-deficient enterocytes, we focus our attention on earlier time points following inducible DARS2 ablation. Therefore, we performed immunostaining using TGN38 and E-cadherin on proximal sections derived from DARS2$^{tamIEC\text{-}KO}$ mice sacrificed 3 and 5 days upon the last tamoxifen injection. Remarkably, a mild Golgi disorganization was manifested in the proximal enterocytes 3 days after tamoxifen induction. However, E-cadherin staining did not prove any prominent mislocalization at this point (Figure 85). Remarkably, 2 days later Golgi emerges partially fragmented, as indicated by weak and disseminated TGN38 staining alongside with a mildly diffused E-cadherin (Figure 85). Eventually, 8 days upon the last tamoxifen injection, total dispersal of Golgi as well as strongly diminished E-cadherin localization became strongly apparent, ultimately indicating a gradual Golgi fragmentation that follows loss of mitochondrial function (Figure 85).

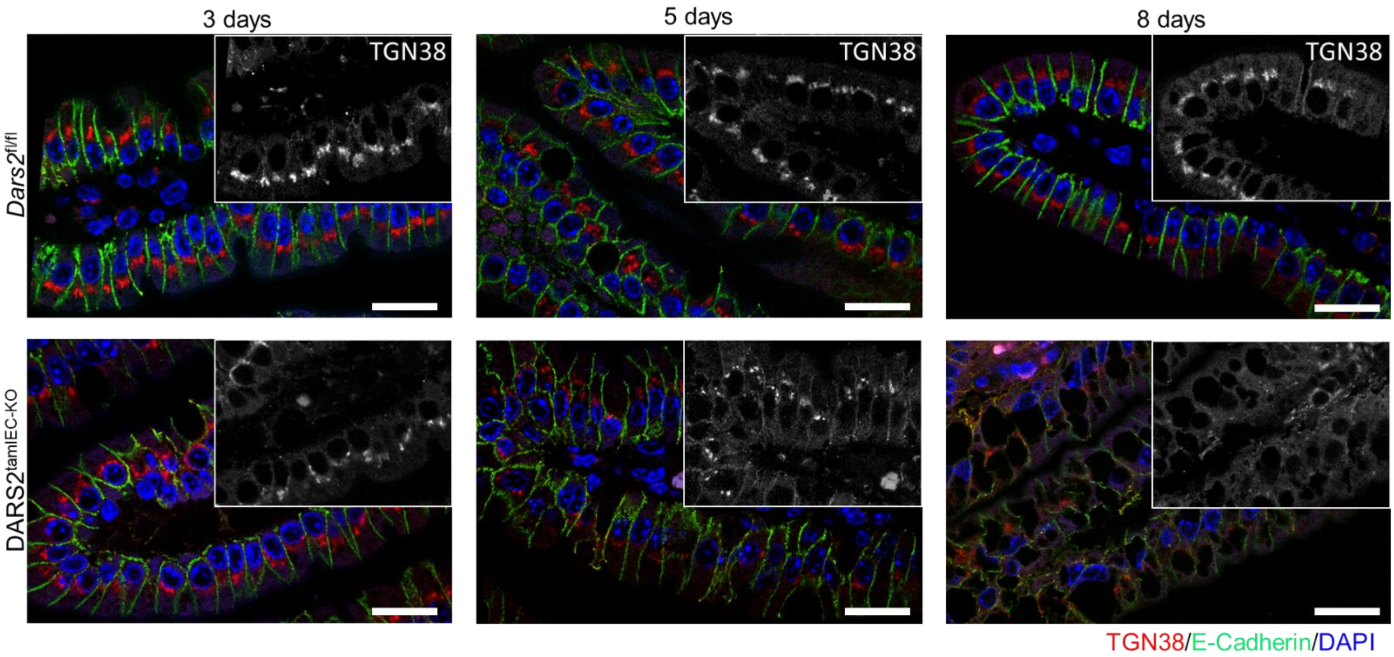

Figure 85. Gradual Golgi fragmentation is reported upon inducible DARS2 depletion in proximal SI.

Representative fluorescence microscopy images from the proximal SI of 8-12 week old *Dars2*$^{fl/fl}$ (n=5) and DARS2$^{tamIEC-KO}$ (n=5) mice sacrificed 3, 5, and 8 days upon the last tamoxifen injection, immunostained with antibodies against TGN38 (red) and E-cadherin (green). Nuclei stained with DAPI (blue). The highlighted box illustrates only TGN38 staining with white. Scale bars = 50µm.

Previously we provided evidence that in spite of the pronounced elimination of IEC proliferation and the strong mitochondrial dysfunction being already apparent 3 days after the last tamoxifen injection, DARS2$^{tamIEC-KO}$ mice did not exhibit any signs of excessive fat deposition in their proximal enterocytes. Interestingly, DARS2$^{tamIEC-KO}$ mice examined 2 days later, displayed an intermediate phenotype manifested by the presence of small LDs along the intestinal villus, thus proposing progressive lipid accumulation initiating around 5 days and peaking at 8 days upon the last tamoxifen injection with DARS2$^{tamIEC-KO}$ mice being massively engorged with fat contained in cytosolic LDs. In order to investigate whether the impairment of Golgi organization precedes or occurs simultaneously with the lipid droplet formation, we immunostained proximal intestinal tissue sections from 3, 5 and 8 days after the last injection against PLIN2 for labelling LDs, TGN38 and E-cadherin. Strikingly, Golgi dispersion was evident in numerous proximal enterocytes that did not contain lipid droplets yet 5 days upon tamoxifen induction, arguing that impairment of the Golgi is not a secondary consequence of lipid droplet formation, but on the contrary it precedes their formation (Figure 86). Afterwards, we questioned whether feeding DARS2$^{tamIEC-KO}$ mice with FFD, which greatly ameliorated the massive LD accumulation observed upon NCD, would have an effect on the Golgi organization. Interestingly, FFD-fed DARS2$^{tamIEC-KO}$ mice exhibited a partially fragmented Golgi to the same extent as the NCD-fed DARS2$^{tamIEC-KO}$ 5 days after the last tamoxifen injection, suggesting that FFD delayed the disruption of the Golgi structure in the proximal enterocytes 7 days upon the last tamoxifen injection (Figure 87). Additionally, we asked if Golgi dispersion was also prominent in distal enterocytes from DARS2$^{tamIEC-KO}$ that do not show any signs of LD overload. Remarkably, triple immunostaining for PLIN2/TGN38/E-cadherin proved that distal enterocytes maintained the Golgi structure and did not display the dramatic impairment of Golgi organisation observed in proximal enterocytes from the same DARS2$^{tamIEC\text{-}KO}$ mice, with the TGN38 staining being only very mildly affected compared to the floxed littermate controls (Figure 88). Lastly, distal enterocytes from FFD-fed DARS2$^{tamIEC\text{-}KO}$ presented mild, almost imperceptible Golgi impairment 7 days after the last tamoxifen injection (Figure 89). Collectively, these findings argue that Golgi disorganisation is not a primary and direct consequence of severe mitochondrial dysfunction generally induced in all enterocytes, but is rather linked to the specific physiology of proximal enterocytes that are primarily responsible of transporting dietary lipids in the form of chylomicrons are therefore under increased demand of extensive and specialized intracellular membrane trafficking.

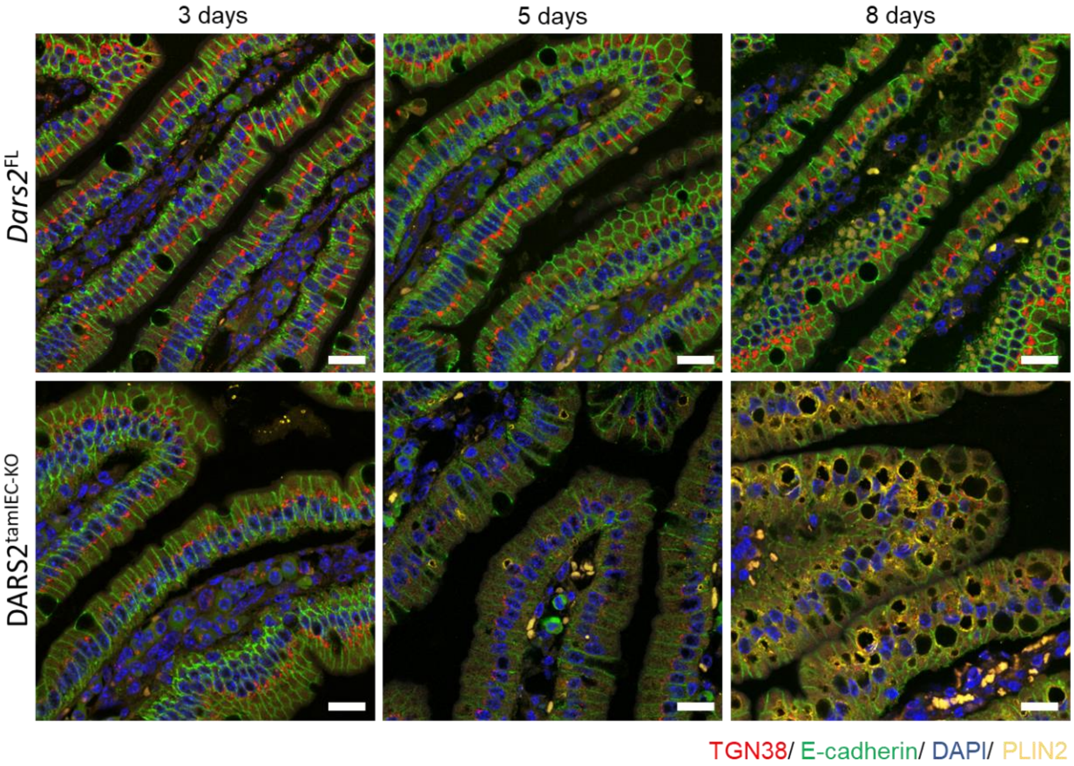

Figure 86. Golgi fragmentation precedes lipid accumulation at the proximal SI upon inducible DARS2 ablation.

Representative fluorescence microscopy images from the proximal SI of 8-12 week old *Dars2*$^{fl/fl}$ (n=5) and DARS2$^{tamIEC\text{-}KO}$ (n=5) mice sacrificed 3, 5, and 8 days upon the last tamoxifen injection, immunostained with antibodies against PLIN2 (yellow), TGN38 (red) and E-cadherin (green). Nuclei stained with DAPI (blue). Scale bars = 50µm.

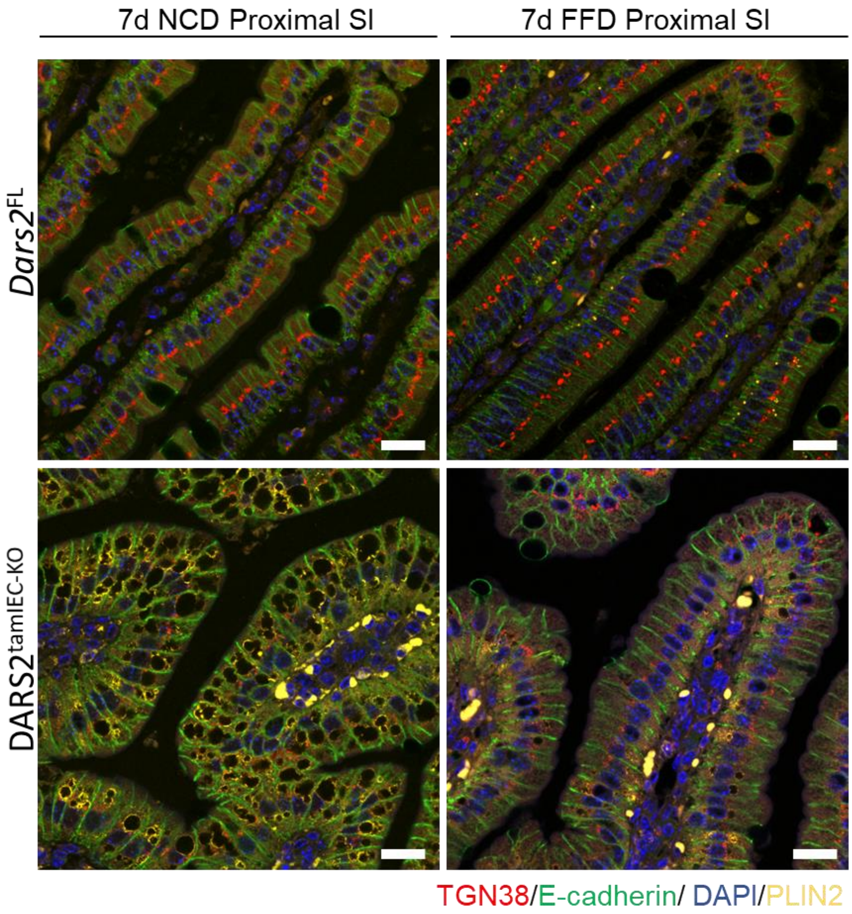

Figure 87. Partial Golgi fragmentation was detected at the proximal SI of DARS2$^{tamIEC-KO}$ mice fed with FFD.

Representative fluorescence microscopy images from the proximal SI of 8-12 week old *Dars2*$^{fl/fl}$ (n=5) and DARS2$^{tamIEC-KO}$ (n=5) mice fed with NCD or FFD and sacrificed 7 days upon the last tamoxifen injection, immunostained with antibodies against PLIN2 (yellow), TGN38 (red) and E-cadherin (green). Nuclei stained with DAPI (blue). Scale bars = 50μm.

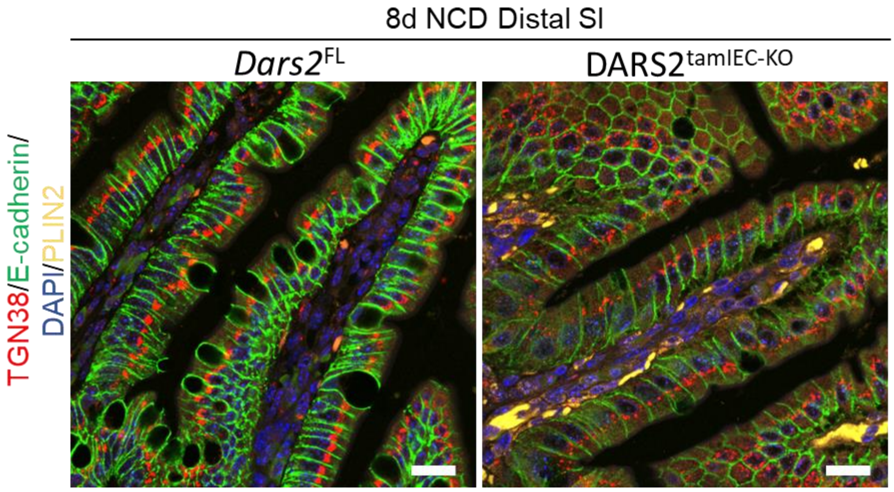

Figure 88. Golgi structure integrity is maintained at the distal SI upon inducible DARS2 ablation.

Representative fluorescence microscopy images from the distal SI of 8-12 week old *Dars2*$^{fl/fl}$ (n=5) and DARS2$^{tamIEC-KO}$ (n=5) mice sacrificed 8 days upon the last tamoxifen injection, immunostained with antibodies against PLIN2 (yellow), TGN38 (red) and E-cadherin (green). Nuclei stained with DAPI (blue). Scale bars = 50µm.

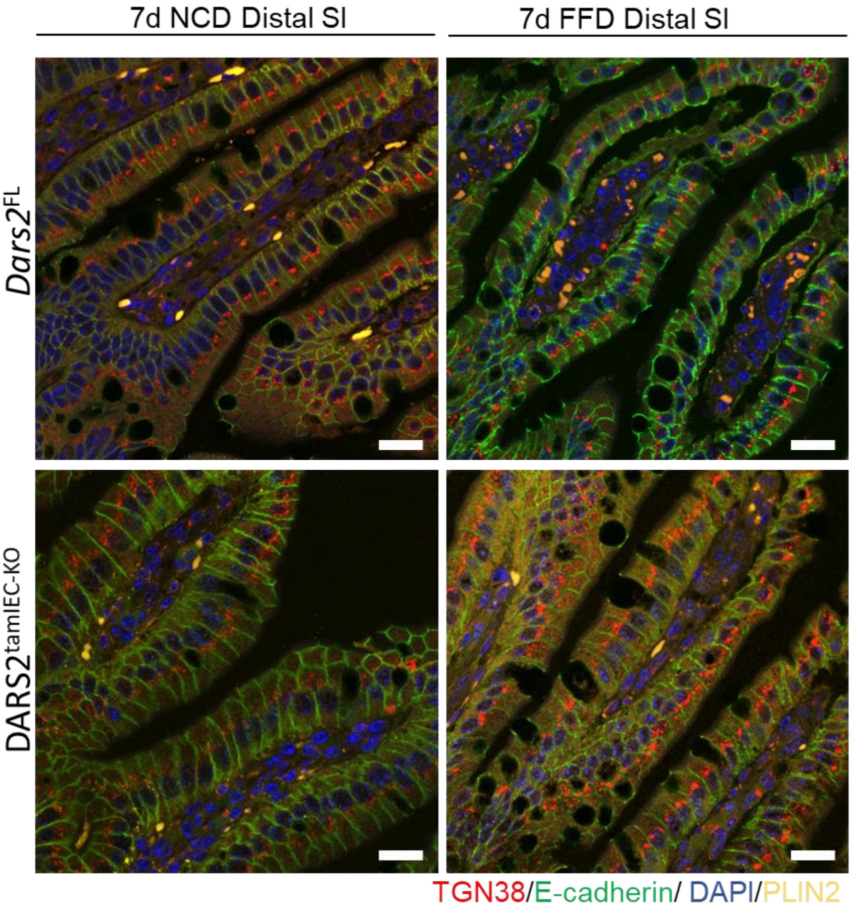

Figure 89. Golgi fragmentation was relatively mild at the distal SI of DARS2$^{\text{tamIEC-KO}}$ mice fed with FFD.

Representative fluorescence microscopy images from the distal SI of 8-12 week old *Dars2*$^{\text{fl/fl}}$ (n=5) and DARS2$^{\text{tamIEC-KO}}$ (n=5) mice fed with NCD or FFD and sacrificed 7 days upon the last tamoxifen injection, immunostained with antibodies against PLIN2 (yellow), TGN38 (red) and E-cadherin (green). Nuclei stained with DAPI (blue). Scale bars = 50µm.

4. Discussion

Mitochondria are critical metabolic and signalling platforms, that are not only implicated in the generation of ATP via OXPHOS, but also coordinate biosynthesis of nucleotides, lipids, amino acids and iron-sulfur clusters, as well as the production of ROS and calcium homeostasis (Eisner, Picard et al. 2018, Spinelli and Haigis 2018).

Mitochondrial diseases, mostly originated from defects in the respiratory chain enzyme complexes, constitute multisystem disorders that affect several organs, thus worsening the quality of life and frequently being related to high morbidity. More than 50% of the patients often present with severe gastrointestinal manifestations including dramatic weight loss and difficulty to put on weight, intense abdominal pain, gut dysmotility and pseudo-obstruction, villous atrophy, diarrhoea and failure to thrive. However, these symptoms are routinely overlooked, as they might be non-specific and some patients end up to be so severely malnourished that they are misdiagnosed with eating disorders, such as anorexia nervosa (Chapman, Hadley et al. 2014, Gorman, Chinnery et al. 2016, Finsterer and Frank 2017). In spite of this rigid clinical manifestation of the widespread gastrointestinal pathologies in patients with mitochondrial diseases, the involvement of mitochondria in the intestinal physiology and particularly in the intestinal lipid homeostasis has not previously experimentally addressed.

This study focuses on deciphering the role of mitochondria in the regulation of dietary lipid processing in intestinal epithelial cells (IECs). To address this question, we decided to induce mitochondrial dysfunction in the IECs, by employing mice with IEC – specific ablation of DARS2, SDHA and COX10, hereafter referred to as DARS2$^{IEC\text{-}KO}$, SDHA$^{IEC\text{-}KO}$ and COX10$^{IEC\text{-}KO}$.

4.1. Ablation of DARS2, SDHA and COX10 induces strong mitochondrial dysfunction.

DARS2$^{IEC\text{-}KO}$ mice exhibited robust mitochondrial dysfunction manifested by markedly reduced levels of all complexes containing mitochondrial – encoded subunits (CI, CIII, CIV and CV), strong CIV deficiency, as well as morphologically damaged mitochondria upon ultrastructural analysis of the intestinal sections at the age of 1-week-old. This observation was in line with previous findings in mouse models with tissue – specific loss of DARS2. In particular, DARS2 ablation in heart and skeletal muscles of 6-week-old mice resulted in prominent respiratory chain deficiency, dramatic suppression of the fully assembled CI, CIII and CIV and significantly diminished substrate-dependent oxygen consumption rate (OCR) (Dogan, Pujol et al. 2014). Similarly, enhanced numbers of COX deficient cells was reported in 15-weeks-old mice lacking DARS2 in the forebrain hippocampal neurons (*Dars2*^{NEKO}) accompanied by reduced enzymatic activities of mitochondrial respiratory chain complexes (MRC) in 28-week-old *Dars2*^{NEKO} mice. Likewise, loss of DARS2 in adult myelin-producing (MPC) cells (*Dars2*^{MYKO}) elicited a strong OXPHOS defect already apparent from 18 weeks of age (Aradjanski, Dogan et al. 2017). Additionally, clear evidence of COX deficiency was observed in 6 to 8-week-old mice with DARS2-specific deletion in Purkinje cells (*Dars2_KO*^{PC}) (Rumyantseva, Motori et al. 2020). Lastly, MRC deficiency was also displayed in bone-marrow-derived macrophages (BMDMs) isolated from mice with DARS2 depletion in myeloid cells (*Dars2*^{MKO}) upon 12 days of culturing (Willenborg, Sanin et al. 2021). Moreover, in DARS2$^{IEC\text{-}KO}$ mice displayed accumulation of the F1 subunit of the F_1F_0-ATP synthase, which is commonly observed in severe MRC defects (Park, Asin-Cayuela et al. 2007, Dogan, Pujol et al. 2014, Aradjanski, Dogan et al. 2017).

Identical to DARS2^{IEC-KO} mice, COX10^{IEC-KO} mice revealed loss of CIV subunits, including COX1 and COX4 in IECs, which coincided with COX-deficiency in enterocytes. This is not surprising as it has been already reported in mouse models lacking COX10 in several tissues. Notably, skeletal muscle specific *COX10* KO mice show greatly lower COX activity at the first month of age in contrast to the control littermates, which progressively aggravated with age. Strongly suppression of the steady-state levels of the fully assembled CIV was observed in muscle mitochondria from 1-, 3- and 6- month old *COX10* KO mice, whereas the other respiratory complexes remained unaltered. Swollen mitochondria with irregular cristae were overt in the ultrastructural sections of *COX10* KO skeletal muscles (Diaz, Thomas et al. 2005). Correspondingly, significantly low COX positive-hepatocytes were detectable in 56-day-old liver specific *COX10* KO mice, while COX subunits, Cox1, Cox5b and Cox6b were completely lost at 56 days with a concomitant increase of the steady-state levels of CI, CII and CV (Diaz, Garcia et al. 2008). In a similar way, markedly decreased COX1 levels and a total 30% reduction of COX activity was described in cerebral cortex and hippocampus of neuron-specific-COX10-deficient mouse at around of 4 months of age (Fukui, Diaz et al. 2007). Mitochondrial dysfunction was visualized in *Cox10*-deficient endothelial cells (ECs), as well as in *Cox10*-silenced primary kidney tubular epithelial cells (TECs), by noticeable decline in the OCR, basal and spare respiratory capacity and production of mitochondrial ATP (Baek, Gomez et al. 2018, Schiffmann, Werthenbach et al. 2020).

Considering the SDHA^{IEC-KO} mice, ablation of SDHA with concomitant reduction in the expression levels of the anchoring subunit SDHB only impacts CII of the ETC, whereas the other respiratory chain subunits remained unaffected. Our findings goes in parallel with the observations made in conditional mouse models lacking SDHA in striated muscles (*Sdha*^{MKO}) and heart and skeletal muscles (*Sdha*^{HKO}) (Hofsetz. 2019, PhD thesis, University of Cologne). Unsurprisingly, loss of SDHA specifically leads to CII isolated deficiency, thus abolishing CII respiration without impacting levels and function of other OXPHOS complexes. CII is one of the two entry points of the electrons (e^-) into the ETC. Therefore, perturbation in the function of CII by interfering with any of the four protein subunits is predicted to affect the input of e^- and disrupt the generation of reducing equivalents from the TCA cycle, ultimately decreasing global respiration and resulting in organismal energy insufficiency. Interestingly, a deleted SDHD subunit of CII in HEK293 cells (HEK293Δ*SDHD*) reduced CI-dependent respiration and markedly repressed basal, reserve and maximal respiratory capacity (Bandara, Drake et al. 2021). Lastly, mitochondrial respiratory chain dysfunction with excessive production of reactive oxygen species was stated in a transgenic mouse model with the V69E mutation in *Sdhc* gene (Ishii, Miyazawa et al. 2011). Consistently, whole – body SDHC knockout mice highly resembled a Leigh-like syndrome, that represents a severe mitochondrial disease with strong ETC deficiency (Al Khazal, Holte et al. 2019).

4.2. DARS2, SDHA and COX10 deficiency results in loss of stemness, impairment of IEC proliferation and differentiation.

In our constitutive models of robust mitochondrial dysfunction, IEC – specific knockout of DARS2, SDHA and COX10 caused identical phenotypes manifested by shortening of the intestinal length, strongly suppressed epithelial proliferation and diminished stem cell compartment. Impaired proliferative response was denoted by lessened expression of Ki67, a typical marker of proliferation, in the TA area. Additionally, loss of stemness was indicated by highly reduced mRNA expression levels of actively cycling intestinal stem cell (ISC)-related genes including *Olfm4* and *Lgr5* (Dehmer, Garrison et al. 2011), as well as by the lack of OLFM4+ cells at the bottom of the intestinal crypts. ISCs divide regularly to give rise to the cells populating the transient amplifying zone, as well as to self-renew in order to maintain the stem cell pool. Consequently, inhibition of proliferation is expected to deprive the intestinal epithelium from stem cells. Similarly, in the early postnatal stage, epithelial cell proliferation is essential for the intestinal growth, hence lack of IEC proliferation will directly impede the proper development of the tissue, thus resulting in blunted intestines in these mice compared to healthy littermates.

The connection between ETC and cell proliferation is clearly indicated in the literature. Interestingly, metformin-mediated inhibition of CI blocked proliferation of prostate cancer cell lines via enhancing reductive glutamine anaplerosis of the TCA cycle (Fendt, Bell et al. 2013). Similarly, attenuated proliferation was observed in HCT-116 *p53*$^{-/-}$ colon cancer cells upon treatment with metformin under low glucose levels (Wheaton, Weinberg et al. 2014). In line with the pharmacological targeting of CI, blockade of CIII by antimycin A halted the proliferation of human lung cancer A549 cells (Han, Kim et al. 2008). Noteworthy, ETC defects resulting in impaired aspartate biosynthesis, which was inverted upon pyruvate supplementation in a cytosolic aspartate aminotransferase (GOT1) – dependent manner (Birsoy, Wang et al. 2015).

Consistent to our observations, IEC-specific ablation of mitochondrial heat shock protein 60 (HSP60) triggered CHOP - independent UPR^{mt} activation, resulting in defective mitochondrial respiration accompanied by considerably impaired IEC proliferation (Berger, Rath et al. 2016). Additionally, IEC-specific overexpression of CHOP (*Chop*$^{IEC\ Tg/Tg}$ mice) highly diminished proliferative colonic IECs, ultimately impacting the regeneration capacity in response to mucosal injury (Waldschmitt, Berger et al. 2014).

Additionally, it has been suggested that proper mitochondrial function and structure is required for maintaining the self-renewal capacity of quiescent stem cell pool. Exhaustion of neural stem cells (NSCs) was mainly driven by ROS- mediated signaling, while hematopoietic cells (HSCs) devoid of mitochondrial complex III subunit Rieske iron-sulfur protein (RISP) exhibited defective respiration and impaired self-renewal capacity (Khacho, Clark et al. 2016, Ansó, Weinberg et al. 2017). In line with loss of stemness of ISCs observed in our conditional knockouts, Berger et al. (2016) demonstrated that mice lacking HSP60 in the IECs promotes abrogation of intestinal stem cells (Berger, Rath et al. 2016). Likewise, loss of HSP60 specifically in intestinal stem cells (ISCs) drives notable disturbance of mitochondria functionality that severely impacts ISC niche and expression of *Lgr5* in the intestinal crypts (Khaloian and Rath 2020). Failure of the Lgr5^{+} CBCs renewal was also prominent upon IEC-specific deletion of the transcription factor YingYang 1 (Yy1), which was shown to affect mitochondrial structural integrity by regulating genes encoding CI subunits (Perekatt, Valdez et al. 2014). Similarly, ablation of TFAM in the adult epithelium notably suppressed the mRNA expression levels of crypt-base columnar stem cells, including *Lgr5*, *Olfm4*, *Smoc2*, *Lrig1* and *Tert*. Further studies using organoid cultures revealed that crypts were initially developed upon the inducible deletion of TFAM but failed to grow after six days, subsequently leading to collapse (Srivillibhuthur, Warder et al. 2018). In a similar fashion, enteroids from mice with IEC-specific loss of *Phb1* displayed impaired budding upon seven days in the culture (Jackson, Panopoulos et al. 2020).

Tamoxifen-inducible ablation of DARS2 in adult IECs highly compromised terminally differentiated IEC subpopulations, as indicated by the significantly diminished number of enterocytes and Goblet cells. Similarly, an abnormal differentiation of the enterocyte lineage has been described in mice with intestinal – specific ablation of TFAM (Srivillibhuthur, Warder et al. 2018) and PHB1 (Jackson, Panopoulos et al. 2020). In addition, clear disturbances in the Paneth cell phenotype were detected in DARS2$^{tamIEC-KO}$ mice. These mice contained many crypts that were completely deprived of Paneth cells and others with mislocalized or frequently diffused lysozyme expression in accordance with the aberrant, degranulated Paneth cells of the mice with ISC-specific deletion of *Hsp60*, as well as IEC-specific loss of *Phb1* (Jackson, Panopoulos et al. 2020, Khaloian and Rath 2020).

4.3. Intestinal-specific deletion of DARS2, SDHA and COX10 results in massive accumulation of lipid droplets (LDs) within the enterocytes.

One of the most striking manifestations of the phenotype in our constitutive mouse models was the extensive vesicular vacuolization of enterocytes. Aberrant vacuolization in intestinal enterocytes has been previously connected to a distortion in the fusion of lysosomes with late endosomes in patients suffering from mucolipidosis type IV (MLIV) due to mutations in a *Trpml1* gene that encodes mucolipin 1 or Lysosomal Storage Disorders (LSDs). In particular, mice deficient in both mucolipin 1 and 3 (*Trpml3*-/-; *Trpml1*-/-) exhibited huge pathological vacuoles within neonatal intestines that were either empty or filled with material largely undigested (Remis, Wiwatpanit et al. 2014). Despite the reduced body weight and failure to thrive, these mice were completely viable and able to overcome the vacuolization upon reaching the weaning age, contrastingly to our mice severe wasting phenotype. Likewise, mice lacking RAB7 GTPase that regulates active endocytosis in the neonatal intestine, in the IECs revealed abnormal vacuoles and defective endocytic nutrient absorption during suckling, without affecting their survival (Takimoto 2021). Interestingly, the prominent vacuoles within the DARS2-, COX10- or SDHA-deficient enterocytes were not loaded with mucins or, but were widely engorged with LDs. Presence of LDs was further validated by markedly elevated levels of TAGs in the intestinal tissue. Moreover, ultrastructural visualization of intestinal sections demonstrated numerous rounded LDs with a phospholipid monolayer, containing homogenous fat content in both the constitutive DARS2^{IEC-KO} and tamoxifen-inducible DARS2$^{tamIEC-KO}$ mice.

Mitochondria are central hubs in the regulation of lipid homeostasis by controlling lipid storage, and metabolism in different organs. Free fatty acid (FFAs) overload can be detrimental for a non-adipose tissue and have to be restrained within triglyceride pools and further packaged into lipid droplets (LDs) to prevent lipotoxicity. Intimate contact between LDs and highly - fused mitochondria allows the channeling of FFAs derived from LD lipolysis via cytoplasmic lipases to mitochondria to be utilized for fatty acid beta oxidation under conditions of nutrient deprivation (Rambold, Cohen et al. 2015, Jarc and Petan 2019). It has been extensively reported in the literature that LD generation can be prompted in response to cellular stress. A multivesicular phenotype of preadipocytes, characterized by elevated LD accumulation, provoked by blocked FAO and enhanced conversion of glucose into TAGs, as a consequence of inhibitor – mediated impaired ETC (Vankoningsloo, Piens et al. 2005). Another study has shown that hypoxic cardiomyocytes displayed augmented intracellular LDs as a direct consequence of HIF-1a induced FAO inhibition (Belanger, Luo et al. 2007). Correspondingly, mice subjected to hypoxic or hyperoxic stimuli or mitochondrial dysfunction induced by mtDNA depletion *in vitro* greatly triggered the biogenesis of LDs with a concomitant aberrant mitochondrial morphology (Lee, Zhang et al. 2013). Decline of FAO in epithelial cells was also the cause of increased

LD deposition mediated by LPS – driven mtROS increase, which was alleviated upon MitoQ treatment (Fock, Bachteeva et al. 2018). Accumulation of LDs has been reported in myosteatosis upon injury of the skeletal muscles, which was attributed to inability of mitochondria to perform FAO and not due to enhanced *de novo* fatty acid synthesis (Gumucio, Qasawa et al. 2019).

By interpreting the data obtained from metabolomics analysis, it can be drawn that FAO might be suppressed in the IECs. In theory, lack of OXPHOS should halt the FAO as the ETC cannot accept energy equivalents from FAO anymore. Thus, the redox cycling of the CoQ pool won't be completed due to the limited presence of CIII. Additionally, NAD+ that required for FAO progression cannot be recycled by CI. In fact, overabundance of LCAC and VLCAC together with the significantly elevated NADH/NAD$^+$ ratio suggests a potential inhibitory effect on FAO. However, we strongly believe that this is not the preeminent reason for the massive lipid accumulation in our experimental mouse models. Increased lipid storage was exclusively observed in the proximal enterocytes of the tamoxifen-inducible DARS2$^{tamIEC-KO}$ mice, which is the crucial site for dietary macronutrient absorption and secretion, and not in the distal section that mainly facilitates bile acid and vitamin uptake, despite similar level of OXPHOS dysfunction (Nassir, Wilson et al. 2007, Lema, Araújo et al. 2020). The fact that only proximal enterocytes deficient for DARS2 were overloaded with LDs and not the distal implies that the striking build-up of LDs is not induced by impaired lipid catabolism and utilization, but is rather the outcome of blocked intestinal lipid transport. In compliance with this finding, restriction to endogenously produced fats upon feeding the mice with FFD strongly suppressed the presence of LDs within enterocytes, hence further confirming their dietary origin. Noteworthy, according to a recent publication, intestinal ATGL and CGI-58 are responsible for the catabolism of basolaterally - derived lipids and not the alimentary ones. Mice with double deletion of *Atgl* and *Cgi-58* (iDKO) specifically in the IECs do not exhibit impaired apical lipid absorption and CM synthesis. iDKO mice present enhanced intracellular CLD accumulation only two hours upon administration of the oral lipid load, but not in the early phase of dietary lipid absorption. Additionally, low-fat feeding is not sufficient to diminish the CLD presence, postulating a basolateral origin of those lipids and supporting that lipids taken up by the basolateral site of the enterocytes were predominantly served for supplying FAO and were not appreciably contributed to the assembly of CMs (Korbelius, Vujic et al. 2019).

The significant suppression in the expression of several enzymes implicated in lipid *de novo* biosynthesis together with the noticeable reduction of the TAG species identified in the liver of DARS2^{IEC-KO} pups points towards the direction of defective transport of lipids to the peripheral tissues, instead of augmented fat synthesis. However, alterations in the lipid metabolism, comprising of increased lipogenesis or hindered FAO is not the primary driving force of LD accumulation in our models of mitochondrial dysfunction. Instead, we favor the hypothesis and provide substantial evidence that accumulating lipids originate from dietary fat and impairment in their transport from the lumen to the circulation, underlying the extensive LD accumulation detected in the enterocytes lacking DARS2, SDHA and COX10.

As we have already extensively described, dietary lipids are taken up by enterocytes in the proximal small intestine where they are re-esterified into TAGs, CEs and PLs. The majority of these lipids are then packaged into pre-chylomicrons with ApoB-48 within the ER, from which they are transported via the PCTV to the Golgi for maturation Mature CMs are then released at the basolateral side by exocytosis and transported by the lymphatic system. Enterocytes also temporarily store excess dietary TGs in cytosolic LDs, which are then mobilised for release in the form of chylomicrons to ensure a stable supply of lipids between meals (Ko, Qu et al. 2020). Previous *in vivo* studies from numerous genetic models clearly demonstrated that interfering with any of these pivotal steps or luminal and basolateral factors that control enterocyte mobilization of CLDs might exert an impact on TAG storage and CM trafficking. In particular, intestinal - specific ablation of proteins that are associated with LDs, including ATGL, CGI-58, CIDEB results in excessive TAG storage in enterocyte CLDs, while secretion rate of TAG was markedly decreased upon *Cgi58* or *Cideb* deficiency in IECs (Haemmerle, Lass et al. 2006, Lass, Zimmermann et al. 2006, Zhang, Wang et al. 2014). Vast vacuolization of the enterocytes constitutes a main feature of Apolipoprotein B and Microsomal triglyceride transfer protein (MTP) deficiency, leading in profound intracellular lipid accumulation within the small intestine (Hussain, Rava et al. 2012, Levy, Beaulieu et al. 2021). Mice with intestinal – specific deletion of *Apob* or *Mttp* revealed lower secretion of CMs and failure to thrive (Kim and Young 1998, Raabe, Flynn et al. 1998). Consistent with the above - mentioned studies, our metabolic tracing experiments unravelled strongly suppressed liver uptake of [^{3}H]-triolein, the radioactive tracer for fatty acids, as well as remarkably reduced accumulation of [^{3}H]-triolein in the bloodstream upon tyloxapol administration, which impedes processing of the TLR core by LPL and intravascular lipolysis. These data provide experimental evidence that transport of dietary lipids to the periphery in the form of CMs is hampered to a great extent.

Our data undoubtedly indicate that the massive accumulation of lipids in large lipid droplets in enterocytes is not a secondary consequence of cell death, inhibition of IEC proliferation, ER stress induction or a general enterocyte malfunction, that additionally corroborate with our hypothesis of defective intestinal dietary lipid transport to the circulation. In particular, we found out that DARS2 deficiency did not trigger increased cell death in the IECs, as indicated by both constitutive DARS2$^{\text{IEC-KO}}$ and tamoxifen-inducible DARS2$^{\text{tamIEC-KO}}$ mice, as well as DARS2$^{\text{IEC-KO}}$ CASP8$^{\text{IEC-KO}}$ *Mlkl*$^{-/-}$ mice that could not ameliorate the robust lipid – related intestinal pathology. Moreover, lipid accumulation has never been reported in any of the mouse models with inactivation of key components of the IKK/NF-κB signalling pathway, which sensitized IECs to different types of cell death including apoptosis, necroptosis and pyroptosis and caused intestinal inflammation (Welz, Wullaert et al. 2011, Dannappel, Vlantis et al. 2014), (Vlantis, Polykratis et al. 2016, Vlantis, Wullaert et al. 2016, Schwarzer, Jiao et al. 2020). Afterwards, we asked whether the strong suppression of IEC proliferation can be considered as the underlying cause of LD accumulation. It has been previously demonstrated that tamoxifen-inducible deletion of transcription factor *Tcf4* that interacts with β-catenin in the IECs, results in complete loss of IEC proliferation and subsequently death of the mice on day 9 upon induction (van Es, Haegebarth et al. 2012). Similarly, mice with intestinal-specific ablation of the transcription factor Krüppel-like factor 5 (KLF5) displayed distorted villus structure, significantly diminished Ki67+ proliferative cells compared to control littermates and the majority of them could not survive beyond 2 days after birth, whereas histological examination of the few surviving mice also revealed impaired IEC proliferation at 8 weeks of age (McConnell, Kim et al. 2011). Likewise, mice with intestinal-specific deficiency of *Arhgef7*, which encodes a Rho guanine nucleotide exchange factor (RhoGEFs) named as βPix, presented blunted villi and markedly reduced IEC proliferation (Cheng, Larabee et al. 2021). Noteworthy, none of these mice has shown any signs of LD overload in spite of the dramatic phenotype and strong inhibition of IEC proliferation.

In addition, a strong signature of ISR has been pinpointed in DARS2-deficient enterocytes both at transcriptional and translational level, which is broadly viewed upon mitochondrial dysfunction (Bao, Ong et al. 2016, Quirós and Prado 2017, Kaspar, Oertlin et al. 2021). It has been recently demonstrated that ISR activation upon mitochondrial dysfunction and ATF4 activation is dependent on the OMA1-DELE1-HRI pathway (Guo and Aviles 2020). However, ER and mitochondria are tightly interact with each other, thus it might be possible that other branches of ER stress, such as XBP1, GRP78 and ATF6 are also activated. Notwithstanding, none of the mouse models lacking critical components regulating ISR and ER stress responses in the intestinal epithelium, entailing XBP1, ATF4, p-eIF2a, CHOP, GRP78, has displayed evidence of LD accumulation or defective lipid processing and transport in enterocytes (Kaser, Lee et al. 2008), (Cao, Wang et al. 2014, van Lidth de Jeude, Meijer et al. 2017, Liu, Li et al. 2018, Hu, Deng et al. 2019).

Furthermore, our findings argue against a general enterocyte malfunction culpable of the LD accumulation and blocked lipid secretion. The packaging of TAGs within LDs implying proper absorption of hydrolyzed monomers (MAG, LPL, cholesterol and FFA) from the lumen and re-esterification into complex lipids (TAG, PL, CE). Additionally, glucose uptake was not notably impaired, as indicated by the almost equal counts of [^{14}C]-DOG detected in the circulation and liver. Therefore, we provide compelling evidence that mitochondrial dysfunction impedes dietary lipid transport in the proximal small intestine, disputing the notion of an indirect effect of general enterocyte collapse incapacitating all nutrient processing by the intestine.

Of note, it becomes evident that feeding the mice with FFD was capable of immensely preventing the massive LD deposition within proximal enterocytes and prolonging the survival of the mice for two days. However, DARS2$^{\text{tamIEC-KO}}$ mice on FFD exhibited pronounced weight loss upon DARS2 ablation, necessitated their culling according to the animal experiment protocol. This observation suggests that LD accumulation exacerbates the phenotype. Therefore, suppression of IEC proliferation and loss of self-renewal capacity of the intestinal epithelium together with the LD overload, appear to be a plausible trigger of weight loss and subsequent death of the mice.

4.4. Intestinal-specific DARS2 deficiency leads to Golgi disorganization and inhibition of chylomicron production in proximal enterocytes.

Ultrastructural morphology of jejunum enterocytes and the process of dietary fat absorption upon gavage with oil bolus has been clearly demonstrated in the literature. Under physiological conditions, pre-CMs can be identified within the lumen of ER, Golgi apparatus, Golgi-derived secretory vesicles for transport to the basolateral side or in the intracellular space among adjacent IECs. CLDs are also temporarily present within enterocytes (D'Aquila, Hung et al. 2016, Hung, Carreiro et al. 2017). Our data demonstrated that DARS2-deficient enterocytes are fully engorged with very large LDs, often trapped within ER lumen and lack ultrastructural signs of CM assembly and release. Similar observations have been previously reported, implicating the indispensable role of proteins whose ablation affected different steps of the ER-to-Golgi transport. Examination of duodenum isolated from 2-week-old mice lacking *ApoB* specifically in the intestine (Young, Cham et al. 1995) revealed a total absence of CM particles within Golgi cisternae and an overload of large LDs, instead (Young, Cham et al. 1995). Similarly, ablation of *Mttp* in the intestine resulted in loss of nascent CMs packed in secretory vesicles and dramatic reduction of mature CM secretion (Xie, Newberry et al. 2006). Additionally, SAR1B KO (*Sar1b*$^{\text{del/+}}$) and mutated (*Sar1b*$^{\text{mut/+}}$) mice exhibited reduced levels of ApoB and MTP, enhanced lipid deposition within proximal enterocytes and failed to secrete CM in the circulation, leading to prominent fat malabsorption (Auclair, Sané et al. 2021). Mice with intestinal-specific loss of the trans-Golgi protein, ARFRP1 cannot facilitate proper CM lipidation within the Golgi and significantly less mature CMs were observed to be liberated from the Golgi (Jaschke, Chung et al. 2012). Another mouse model deficient in DENND5B, which is involved in the vesicular transport, displayed fat accumulation within the enterocytes, lessened ApoB release in the lacteals, whereas ultrastructural analysis revealed impaired CM secretion due to failure of the Golgi-derived secretory vesicles to reach the plasma membrane (Gordon, Neufeld et al. 2019). Lastly, deletion of the Golgi reassembly – stacking protein, GRASP55 caused large LDs and marked suppression in the number of CMs identified in the jejenal epithelial cells after oil gavage (Kim, Kim et al. 2020).

According to our IF experiments, complete dispersal of TGN38 suggests a major disruption of the Golgi disorganization in the proximal DARS2-deficient enterocytes eight days upon the last tamoxifen injection accompanied with a massive accumulation of LDs. Moreover, the noticeable decline in the localization of E-cadherin on the plasma membrane and its enhanced diffused cytoplasmic levels, implying a compromised membrane trafficking along the entire secretory pathway in this particular section of the intestine. However, our data obtained five days after the last tamoxifen injection, when strong mitochondrial dysfunction and first signs of small LDs are already apparent, shown weak and scattered TGN38 staining indicative of Golgi fragmentation in the proximal enterocytes. Strikingly, Golgi fragmentation was evident also in enterocytes that were not loaded with LDs yet, arguing that impairment of the Golgi is not a secondary consequence of LD formation, but on the contrary it precedes the generation of LDs. Of note, Golgi disorganization was mildly impaired in distal enterocytes of the same mice, that also lack DARS2 and present robust ETC deficiency, inferring that defects in Golgi architecture are associated with the specific physiology of proximal enterocytes to perform absorption, processing, packaging and export of dietary lipids in the form of CMs, hence requiring extensive and specialized intracellular membrane trafficking. Therefore, impairment of CM transport is presumably the primary defect in the proximal enterocytes, that subsequently results in a more general secretory pathway distortion as a secondary effect by interfering with intracellular membrane transport, which is essential for sustaining the Golgi network organization.

The secretory pathway in enterocytes consists of distinct, energy-demanding processes, including the assembly, transport and fusion of PCTVs with the *cis*-Golgi membrane, as well as trafficking of Golgi-derived vesicles to the plasma membrane for subsequent release in the lymphatics. In particular, disengagement of FAPB1 protein from a multiprotein complex in order to bind to ER and initiate the budding of PCTV, depends on phosphorylation of Sar1B GTPase by protein kinase C zeta (PKCζ) in a process that requires ATP (Siddiqi, Gorelick et al. 2003, Siddiqi and Mansbach 2012) Therefore, we speculated that energy depletion expected upon OXPHOS disruption might be responsible for the impaired CM secretion. However, our metabolomic analysis revealed that the ratio of ATP/ADP was not substantially reduced in DARS2-deficient enterocytes, most likely due to the enhanced glycolysis to compensate for the energy deficit. Consistently, a totally disturbed Golgi organization in distal enterocytes almost indentical to the proximal phenotype of the same mice 8 days after tamoxifen induction was not evident. Based on these results, it is unlikely that the impaired ER-to-Golgi transport is directly caused by exhaustion of the enterocytes attributable to energy crisis, since distal enterocytes are also deficient in DARS2 and show robust OXPHOS shutdown. Collectivelly, these observations additionally confirmed that the Golgi defect is only induced in enterocytes specializing in lipid transport, suggesting that it is coupled to an impairment in dietary lipid processing and transport in the form of chylomicrons.

4.5. Concluding remarks

Taken together, our results revealed an essential role of mitochondria in regulating dietary lipid processing by enterocytes. We provide evidence that mitochondrial dysfunction inhibited chylomicron formation, thus causing impaired transport of dietary lipids to peripheral tissues, resulting in their accumulation and storage within large LDs in enterocytes. Golgi disorganisation and impaired chylomicron production in DARS2-deficient enterocytes was resembling the phenotype of patients suffering from chylomicron retention disease. This disease is caused by mutations in the GTPase SAR1B, which controls budding of PCTVs from the ER for transport to the Golgi, thus resulting in LD accumulation within human enterocytes and impeding the CM release, proposing that mitochondrial dysfunction could cause the pathology by interfering with PCTV generation or transport. Importantly, the phenotype caused by enterocyte-specific mitochondrial deficiency in mice is reminiscent of the disease manifestations in some mitochondrial disease patients, who present with intestinal complications associated with a severe inability to gain weight and failure to thrive (Chinnery and Turnbull 1997, Chapman, Hadley et al. 2014). In fact, gastrointestinal problems are one of the most common disease manifestations in mitochondrial patients but are often overlooked as non-specific (abdominal pain, vomiting and weight loss) (Chinnery and Turnbull 1997), with some patients so severely malnourished that they are misdiagnosed as anorexia nervosa (Kim, Lee et al. 2009, Chapman, Hadley et al. 2014). Although the precise mechanism remains to be fully elucidated, our findings suggest that disruption of the secretory pathway and ER-to-Golgi vesicle trafficking causes impaired chylomicron production in enterocytes with mitochondrial deficiency. Therefore, our results suggest that the intestinal and nutritional defects in patients with mitochondrial disease could be at least in part caused by impaired dietary lipid transport by enterocytes and warrants future investigation to determine whether a similar mechanism plays a role.

5. References

Acin-Perez, R. and J. A. Enriquez (2014). "The function of the respiratory supercomplexes: The plasticity model." Biochimica et Biophysica Acta (BBA) - Bioenergetics **1837**(4): 444-450.

Advani, R. J., B. Yang, R. Prekeris, K. C. Lee, J. Klumperman and R. H. Scheller (1999). "VAMP-7 mediates vesicular transport from endosomes to lysosomes." J Cell Biol **146**(4): 765-776.

Akram, M. (2014). "Citric acid cycle and role of its intermediates in metabolism." Cell Biochem Biophys **68**(3): 475-478.

Al Khazal, F., M. N. Holte, B. Bolon, T. A. White, N. LeBrasseur and L. J. Maher, 3rd (2019). "A conditional mouse model of complex II deficiency manifesting as Leigh-like syndrome." Faseb j **33**(12): 13189-13201.

Ali, A., H. Tan and G. E. Kaiko (2020). "Role of the Intestinal Epithelium and Its Interaction With the Microbiota in Food Allergy." Frontiers in Immunology **11**.

Altmann, S. W., H. R. Davis, L.-j. Zhu, X. Yao, L. M. Hoos, G. Tetzloff, S. P. N. Iyer, M. Maguire, A. Golovko, M. Zeng, L. Wang, N. Murgolo and M. P. Graziano (2004). "Niemann-Pick C1 Like 1 Protein Is Critical for Intestinal Cholesterol Absorption." Science **303**(5661): 1201-1204.

Amunts, A., A. Brown, J. Toots, S. H. W. Scheres and V. Ramakrishnan (2015). "Ribosome. The structure of the human mitochondrial ribosome." Science **348**(6230): 95-98.

Ansó, E., S. E. Weinberg, L. P. Diebold, B. J. Thompson and S. Malinge (2017). "The mitochondrial respiratory chain is essential for haematopoietic stem cell function." **19**(6): 614-625.

Antonicka, H., S. C. Leary, G.-H. Guercin, J. N. Agar, R. Horvath, N. G. Kennaway, C. O. Harding, M. Jaksch and E. A. Shoubridge (2003). "Mutations in COX10 result in a defect in mitochondrial heme A biosynthesis and account for multiple, early-onset clinical phenotypes associated with isolated COX deficiency." Human Molecular Genetics **12**(20): 2693-2702.

Antonicka, H., S. C. Leary, G. H. Guercin, J. N. Agar, R. Horvath, N. G. Kennaway, C. O. Harding, M. Jaksch and E. A. Shoubridge (2003). "Mutations in COX10 result in a defect in mitochondrial heme A biosynthesis and account for multiple, early-onset clinical phenotypes associated with isolated COX deficiency." Hum Mol Genet **12**(20): 2693-2702.

Aradjanski, M., S. A. Dogan, S. Lotter, S. Wang, S. Hermans, R. Wibom, E. Rugarli and A. Trifunovic (2017). "DARS2 protects against neuroinflammation and apoptotic neuronal loss, but is dispensable for myelin producing cells." Hum Mol Genet **26**(21): 4181-4189.

Auclair, N., A. T. Sané, L. Ahmarani, N. Patey, J.-F. Beaulieu, N. Peretti, S. Spahis and E. Levy (2021). "Sar1b mutant mice recapitulate gastrointestinal abnormalities associated with chylomicron retention disease." Journal of Lipid Research **62**: 100085.

Baek, J. H., I. G. Gomez, Y. Wada, A. Roach, D. Mahad and J. S. Duffield (2018). "Deletion of the Mitochondrial Complex-IV Cofactor Heme A:Farnesyltransferase Causes Focal Segmental Glomerulosclerosis and Interferon Response." Am J Pathol **188**(12): 2745-2762.

Bandara, A. B., J. C. Drake and D. A. Brown (2021). "Complex II subunit SDHD is critical for cell growth and metabolism, which can be partially restored with a synthetic ubiquinone analog." BMC Molecular and Cell Biology **22**(1): 35.

Bao, X. R., S. E. Ong, O. Goldberger, J. Peng, R. Sharma, D. A. Thompson, S. B. Vafai, A. G. Cox, E. Marutani, F. Ichinose, W. Goessling, A. Regev, S. A. Carr, C. B. Clish and V. K. Mootha (2016). "Mitochondrial dysfunction remodels one-carbon metabolism in human cells." **5**.

Bär, F., W. Bochmann, A. Widok, K. von Medem, R. Pagel, M. Hirose, X. Yu, K. Kalies, P. König, R. Böhm, T. Herdegen, A. T. Reinicke, J. Büning, H. Lehnert, K. Fellermann, S. Ibrahim and C. Sina (2013). "Mitochondrial Gene Polymorphisms That Protect Mice From Colitis." Gastroenterology **145**(5): 1055-1063.e1053.

Barker, N. (2014). "Adult intestinal stem cells: critical drivers of epithelial homeostasis and regeneration." Nature Reviews Molecular Cell Biology **15**(1): 19-33.

Barker, N., J. H. van Es, J. Kuipers, P. Kujala, M. van den Born, M. Cozijnsen, A. Haegebarth, J. Korving, H. Begthel, P. J. Peters and H. Clevers (2007). "Identification of stem cells in small intestine and colon by marker gene Lgr5." Nature **449**(7165): 1003-1007.

Beilstein, F., V. Carrière, A. Leturque and S. Demignot (2016). "Characteristics and functions of lipid droplets and associated proteins in enterocytes." Experimental Cell Research **340**(2): 172-179.

Belanger, A. J., Z. Luo, K. A. Vincent, G. Y. Akita, S. H. Cheng, R. J. Gregory and C. Jiang (2007). "Hypoxia-inducible factor 1 mediates hypoxia-induced cardiomyocyte lipid accumulation by reducing the DNA binding activity of peroxisome proliferator-activated receptor alpha/retinoid X receptor." Biochem Biophys Res Commun **364**(3): 567-572.

Ben-Aicha, S., L. Badimon and G. Vilahur (2020). "Advances in HDL: Much More than Lipid Transporters." Int J Mol Sci **21**(3).

Ben Ameur, S., H. Aloulou, N. Jlidi, F. Kamoun, I. Chabchoub, M. Di Filippo, L. Sfaihi and M. Hachicha (2016). "Chylomicron retention disease: A rare cause of chronic diarrhea." Archives de Pédiatrie **23**(7): 735-737.

Benador, I. Y., M. Veliova, K. Mahdaviani, A. Petcherski, J. D. Wikstrom, E. A. Assali, R. Acín-Pérez, M. Shum, M. F. Oliveira, S. Cinti, C. Sztalryd, W. D. Barshop, J. A. Wohlschlegel, B. E. Corkey, M. Liesa and O. S. Shirihai (2018). "Mitochondria Bound to Lipid Droplets Have Unique Bioenergetics, Composition, and Dynamics that Support Lipid Droplet Expansion." Cell Metab **27**(4): 869-885.e866.

Berger, E., E. Rath, D. Yuan, N. Waldschmitt, S. Khaloian, M. Allgäuer, O. Staszewski, E. M. Lobner, T. Schöttl, P. Giesbertz, O. I. Coleman, M. Prinz, A. Weber, M. Gerhard, M. Klingenspor, K. P. Janssen, M. Heikenwalder and D. Haller (2016). "Mitochondrial function controls intestinal epithelial stemness and proliferation." Nat Commun **7**: 13171.

Bernier-Latmani, J., C. Cisarovsky, C. S. Demir, M. Bruand, M. Jaquet, S. Davanture, S. Ragusa, S. Siegert, O. Dormond, R. Benedito, F. Radtke, S. A. Luther and T. V. Petrova (2015). "DLL4 promotes continuous adult intestinal lacteal regeneration and dietary fat transport." J Clin Invest **125**(12): 4572-4586.

Beumer, J. and H. Clevers (2021). "Cell fate specification and differentiation in the adult mammalian intestine." Nature Reviews Molecular Cell Biology **22**(1): 39-53.

Bietrix, F., D. Yan, M. Nauze, C. Rolland, J. Bertrand-Michel, C. Coméra, S. Schaak, R. Barbaras, A. K. Groen, B. Perret, F. Tercé and X. Collet (2006). "Accelerated lipid absorption in mice overexpressing intestinal SR-BI." J Biol Chem **281**(11): 7214-7219.

Birsoy, K., T. Wang, W. W. Chen, E. Freinkman, M. Abu-Remaileh and D. M. Sabatini (2015). "An Essential Role of the Mitochondrial Electron Transport Chain in Cell Proliferation Is to Enable Aspartate Synthesis." Cell **162**(3): 540-551.

Blackburn, C., B. Guan, J. Brown, C. Cullis, S. M. Condon, T. J. Jenkins, S. Peluso, Y. Ye, R. E. Gimeno, S. Punreddy, Y. Sun, H. Wu, B. Hubbard, V. Kaushik, P. Tummino, P. Sanchetti, D. Yu Sun, T. Daniels, E. Tozzo, S. K. Balani and P. Raman (2006). "Identification and characterization of 4-aryl-3,4-dihydropyrimidin-2(1H)-ones as inhibitors of the fatty acid transporter FATP4." Bioorg Med Chem Lett **16**(13): 3504-3509.

Blighe, K., S. Rana and M. Lewis (2021). "EnhancedVolcano: Publication-ready volcano plots with enhanced colouring and labeling." R package version 1.10.0.

Boncompain, G. and F. Perez (2013). "The many routes of Golgi-dependent trafficking." Histochem Cell Biol **140**(3): 251-260.

Bond, P. (2017). "Phosphatidic acid: biosynthesis, pharmacokinetics, mechanisms of action and effect on strength and body composition in resistance-trained individuals." Nutrition & Metabolism **14**(1): 12.

Borisova, M. A., K. M. Achasova, K. N. Morozova, E. N. Andreyeva, E. A. Litvinova, A. A. Ogienko, M. V. Morozova, M. B. Berkaeva, E. Kiseleva and E. N. Kozhevnikova (2020). "Mucin-2 knockout is a model of intercellular junction defects, mitochondrial damage and ATP depletion in the intestinal epithelium." Scientific Reports **10**(1): 21135.

Burgener, A.-V., G. R. Bantug, B. J. Meyer, R. Higgins, A. Ghosh, O. Bignucolo, E. H. Ma, J. Loeliger, G. Unterstab, M. Geigges, R. Steiner, M. Enamorado, R. Ivanek, D. Hunziker, A. Schmidt, B. Müller-Durovic, J. Grählert, R. Epple, S. Dimeloe, J. Lötscher, U. Sauder, M. Ebnöther, B. Burger, I. Heijnen, S. Martínez-Cano, N. Cantoni, R. Brücker, C. R. Kahlert, D.

Sancho, R. G. Jones, A. Navarini, M. Recher and C. Hess (2019). "SDHA gain-of-function engages inflammatory mitochondrial retrograde signaling via KEAP1–Nrf2." Nature Immunology **20**(10): 1311-1321.

Cao, S. S., M. Wang, J. C. Harrington, B. M. Chuang, L. Eckmann and R. J. Kaufman (2014). "Phosphorylation of eIF2α is dispensable for differentiation but required at a posttranscriptional level for paneth cell function and intestinal homeostasis in mice." Inflamm Bowel Dis **20**(4): 712-722.

Chapman, T. P., G. Hadley, C. Fratter, S. N. Cullen, B. E. Bax, M. D. Bain, R. A. Sapsford, J. Poulton and S. P. Travis (2014). "Unexplained gastrointestinal symptoms: Think mitochondrial disease." Digestive and Liver Disease **46**(1): 1-8.

Chapman, T. P., G. Hadley, C. Fratter, S. N. Cullen, B. E. Bax, M. D. Bain, R. A. Sapsford, J. Poulton and S. P. Travis (2014). "Unexplained gastrointestinal symptoms: think mitochondrial disease." Dig Liver Dis **46**(1): 1-8.

Charcosset, M., A. Sassolas, N. Peretti, C. C. Roy, C. Deslandres, D. Sinnett, E. Levy and A. Lachaux (2008). "Anderson or chylomicron retention disease: molecular impact of five mutations in the SAR1B gene on the structure and the functionality of Sar1b protein." Mol Genet Metab **93**(1): 74-84.

Chavez-Jauregui, R. N., R. D. Mattes and E. J. Parks (2010). "Dynamics of fat absorption and effect of sham feeding on postprandial lipema." Gastroenterology **139**(5): 1538-1548.

Cheng, H. M., K. K. Mah and K. Seluakumaran (2020). Fat Digestion: Bile Salt, Emulsification, Micelles, Lipases, Chylomicrons. Defining Physiology: Principles, Themes, Concepts. Volume 2: Neurophysiology and Gastrointestinal Systems. Cham, Springer International Publishing**:** 63-65.

Cheng, K., S. M. Larabee, M. Tolaymat, M. Hanscom, A. C. Shang, A. Schledwitz, S. Hu, C. B. Drachenberg, M. Zhan, A. Chahdi and J. P. Raufman (2021). "Targeted intestinal deletion of Rho guanine nucleotide exchange factor 7, βPIX, impairs enterocyte proliferation, villus maturation, and mucosal defenses in mice." Am J Physiol Gastrointest Liver Physiol **320**(4): G627-g643.

Chin, K. L., W. Aerbajinai, J. Zhu, L. Drew, L. Chen, W. Liu and G. P. Rodgers (2008). "The regulation of OLFM4 expression in myeloid precursor cells relies on NF-kappaB transcription factor." Br J Haematol **143**(3): 421-432.

Chinnery, P. F. and D. M. Turnbull (1997). "Mitochondrial medicine." QJM **90**(11): 657-667.

Chitraju, C., T. C. Walther and R. V. Farese (2019). "The triglyceride synthesis enzymes DGAT1 and DGAT2 have distinct and overlapping functions in adipocytes." Journal of Lipid Research **60**(6): 1112-1120.

Cho, Y. M., S. Kwon, Y. K. Pak, H. W. Seol, Y. M. Choi, D. J. Park, K. S. Park and H.-K. Lee (2006). "Dynamic changes in mitochondrial biogenesis and antioxidant enzymes during the spontaneous differentiation of human embryonic stem cells." Biochemical and biophysical research communications **348 4**: 1472-1478.

Chon, S. H., J. D. Douglass, Y. X. Zhou, N. Malik, J. L. Dixon, A. Brinker, L. Quadro and J. Storch (2012). "Over-expression of monoacylglycerol lipase (MGL) in small intestine alters endocannabinoid levels and whole body energy balance, resulting in obesity." PLoS One **7**(8): e43962.

Cifarelli, V. and N. A. Abumrad (2018). "Intestinal CD36 and Other Key Proteins of Lipid Utilization: Role in Absorption and Gut Homeostasis." Compr Physiol **8**(2): 493-507.

Cifarelli, V. and A. Eichmann (2019). "The Intestinal Lymphatic System: Functions and Metabolic Implications." Cellular and Molecular Gastroenterology and Hepatology **7**(3): 503-513.

Clevers, H. (2013). "The Intestinal Crypt, A Prototype Stem Cell Compartment." Cell **154**(2): 274-284.

Coenen, M. J. H., L. P. van den Heuvel, C. Ugalde, M. Ten Brinke, L. G. J. Nijtmans, F. J. M. Trijbels, S. Beblo, E. M. Maier, A. C. Muntau and J. A. M. Smeitink (2004). "Cytochrome c oxidase biogenesis in a patient with a mutation in COX10 gene." Annals of neurology **56**(4): 560-564.

Collins, T. J., M. J. Berridge, P. Lipp and M. D. Bootman (2002). "Mitochondria are morphologically and functionally heterogeneous within cells." Embo j **21**(7): 1616-1627.

Cosentino, K. and A. J. García-Sáez (2017). "Bax and Bak Pores: Are We Closing the Circle?" Trends Cell Biol **27**(4): 266-275.

Cox, J. and M. Mann (2008). "MaxQuant enables high peptide identification rates, individualized p.p.b.-range mass accuracies and proteome-wide protein quantification." Nat Biotechnol **26**(12): 1367-1372.

Cox, J., N. Neuhauser, A. Michalski, R. A. Scheltema, J. V. Olsen and M. Mann (2011). "Andromeda: a peptide search engine integrated into the MaxQuant environment." J Proteome Res **10**(4): 1794-1805.

Cunningham, K. E., G. Vincent, C. P. Sodhi, E. A. Novak, S. Ranganathan, C. E. Egan, D. B. Stolz, M. B. Rogers, B. Firek, M. J. Morowitz, G. K. Gittes, B. S. Zuckerbraun, D. J. Hackam and K. P. Mollen (2016). "Peroxisome Proliferator-activated Receptor-γ Coactivator 1-α (PGC1α) Protects against Experimental Murine Colitis." J Biol Chem **291**(19): 10184-10200.

D'Aquila, T., Y.-H. Hung, A. Carreiro and K. K. Buhman (2016). "Recent discoveries on absorption of dietary fat: Presence, synthesis, and metabolism of cytoplasmic lipid droplets within enterocytes." Biochimica et Biophysica Acta (BBA) - Molecular and Cell Biology of Lipids **1861**(8, Part A): 730-747.

D'Souza, A. R. and M. Minczuk (2018). "Mitochondrial transcription and translation: overview." Essays Biochem **62**(3): 309-320.

Dallinga-Thie, G. M., R. Franssen, H. L. Mooij, M. E. Visser, H. C. Hassing, F. Peelman, J. J. P. Kastelein, M. Péterfy and M. Nieuwdorp (2010). "The metabolism of triglyceride-rich lipoproteins revisited: new players, new insight." Atherosclerosis **211**(1): 1-8.

Dannappel, M., K. Vlantis, S. Kumari, A. Polykratis, C. Kim, L. Wachsmuth, C. Eftychi, J. Lin, T. Corona, N. Hermance, M. Zelic, P. Kirsch, M. Basic, A. Bleich, M. Kelliher and M. Pasparakis (2014). "RIPK1 maintains epithelial homeostasis by inhibiting apoptosis and necroptosis." Nature **513**(7516): 90-94.

Dash, S., C. Xiao, C. Morgantini, P. W. Connelly, B. W. Patterson and G. F. Lewis (2014). "Glucagon-like peptide-2 regulates release of chylomicrons from the intestine." Gastroenterology **147**(6): 1275-1284.e1274.

Dash, S., C. Xiao, C. Morgantini and G. F. Lewis (2015). "New Insights into the Regulation of Chylomicron Production." Annu Rev Nutr **35**: 265-294.

Dashdorj, A., K. R. Jyothi, S. Lim, A. Jo, M. N. Nguyen, J. Ha, K. S. Yoon, H. J. Kim, J. H. Park, M. P. Murphy and S. S. Kim (2013). "Mitochondria-targeted antioxidant MitoQ ameliorates experimental mouse colitis by suppressing NLRP3 inflammasome-mediated inflammatory cytokines." BMC Med **11**: 178.

Davis, R. B., D. O. Kechele, E. S. Blakeney, J. B. Pawlak and K. M. Caron (2017). "Lymphatic deletion of calcitonin receptor-like receptor exacerbates intestinal inflammation." JCI Insight **2**(6): e92465.

Dehmer, J. J., A. P. Garrison, K. E. Speck, C. M. Dekaney, L. Van Landeghem, X. Sun, S. J. Henning and M. A. Helmrath (2011). "Expansion of intestinal epithelial stem cells during murine development." PLoS One **6**(11): e27070.

Delgado, M. E., T. Grabinger and T. Brunner (2016). "Cell death at the intestinal epithelial front line." Febs j **283**(14): 2701-2719.

Desomer, L., M. De Vos and D. De Looze (2015). "Fat accumulation in enterocytes: a key to the diagnosis of abetalipoproteinemia or homozygous hypobetalipoproteinemia." Endoscopy **47 Suppl 1 UCTN**: E223-224.

DeVita, R. J. and S. Pinto (2013). "Current status of the research and development of diacylglycerol O-acyltransferase 1 (DGAT1) inhibitors." J Med Chem **56**(24): 9820-9825.

Di Filippo, M., S. Collardeau Frachon, A. Janin, S. Rajan, O. Marmontel, C. Decourt, A. Rubio, S. Nony, S. Dumont, C. Cuerq, S. Charrière, P. Moulin, A. Lachaux, M. M. Hussain, D. Bozon and

N. Peretti (2019). "Normal serum ApoB48 and red cells vitamin E concentrations after supplementation in a novel compound heterozygous case of abetalipoproteinemia." Atherosclerosis **284**: 75-82.

Diaz, F. (2010). "Cytochrome c oxidase deficiency: Patients and animal models." Biochimica et Biophysica Acta (BBA) - Molecular Basis of Disease **1802**(1): 100-110.

Diaz, F., H. Fukui, S. Garcia and C. T. Moraes (2006). "Cytochrome c oxidase is required for the assembly/stability of respiratory complex I in mouse fibroblasts." Molecular and cellular biology **26**(13): 4872-4881.

Diaz, F., S. Garcia, D. Hernandez, A. Regev, A. Rebelo, J. Oca-Cossio and C. T. Moraes (2008). "Pathophysiology and fate of hepatocytes in a mouse model of mitochondrial hepatopathies." Gut **57**(2): 232-242.

Diaz, F., S. Garcia, K. R. Padgett and C. T. Moraes (2012). "A defect in the mitochondrial complex III, but not complex IV, triggers early ROS-dependent damage in defined brain regions." Human Molecular Genetics **21**(23): 5066-5077.

Diaz, F., C. K. Thomas, S. Garcia, D. Hernandez and C. T. Moraes (2005). "Mice lacking COX10 in skeletal muscle recapitulate the phenotype of progressive mitochondrial myopathies associated with cytochrome c oxidase deficiency." Hum Mol Genet **14**(18): 2737-2748.

DiMauro, S. and E. A. Schon (2008). "Mitochondrial disorders in the nervous system." Annu Rev Neurosci **31**: 91-123.

Diodato, D. and D. Ghezzi (2014). "The Mitochondrial Aminoacyl tRNA Synthetases: Genes and Syndromes." **2014**: 787956.

Dixon, J. B. (2010). "Mechanisms of chylomicron uptake into lacteals." Ann N Y Acad Sci **1207 Suppl 1**(Suppl 1): E52-57.

Dogan, S. A., C. Pujol, P. Maiti, A. Kukat, S. Wang, S. Hermans, K. Senft, R. Wibom, E. I. Rugarli and A. Trifunovic (2014). "Tissue-specific loss of DARS2 activates stress responses independently of respiratory chain deficiency in the heart." Cell Metab **19**(3): 458-469.

Douglass, J. D., Y. X. Zhou, A. Wu, J. A. Zadroga, A. M. Gajda, A. I. Lackey, W. Lang, K. M. Chevalier, S. W. Sutton, S. P. Zhang, C. M. Flores, M. A. Connelly and J. Storch (2015). "Global deletion of MGL in mice delays lipid absorption and alters energy homeostasis and diet-induced obesity." J Lipid Res **56**(6): 1153-1171.

Du, H., M. Heur, M. Duanmu, G. A. Grabowski, D. Y. Hui, D. P. Witte and J. Mishra (2001). "Lysosomal acid lipase-deficient mice: depletion of white and brown fat, severe hepatosplenomegaly, and shortened life span." J Lipid Res **42**(4): 489-500.

Eisner, V., M. Picard and G. Hajnóczky (2018). "Mitochondrial dynamics in adaptive and maladaptive cellular stress responses." Nature Cell Biology **20**(7): 755-765.

el Marjou, F., K. P. Janssen, B. H. Chang, M. Li, V. Hindie, L. Chan, D. Louvard, P. Chambon, D. Metzger and S. Robine (2004). "Tissue-specific and inducible Cre-mediated recombination in the gut epithelium." Genesis **39**(3): 186-193.

Ellenrieder, L., M. P. Dieterle, K. N. Doan, C. U. Mårtensson, A. Floerchinger, M. L. Campo, N. Pfanner and T. Becker (2019). "Dual Role of Mitochondrial Porin in Metabolite Transport across the Outer Membrane and Protein Transfer to the Inner Membrane." Mol Cell **73**(5): 1056-1065.e1057.

Falkenberg, M. (2018). "Mitochondrial DNA replication in mammalian cells: overview of the pathway." Essays in biochemistry **62**(3): 287-296.

Farr, S., J. Taher and K. Adeli (2016). "Central nervous system regulation of intestinal lipid and lipoprotein metabolism." Curr Opin Lipidol **27**(1): 1-7.

Fedor, J. G. and J. Hirst (2018). "Mitochondrial Supercomplexes Do Not Enhance Catalysis by Quinone Channeling." Cell Metab **28**(3): 525-531.e524.

Fendt, S.-M., E. L. Bell, M. A. Keibler, S. M. Davidson, G. J. Wirth, B. Fiske, J. R. Mayers, M. Schwab, G. Bellinger, A. Csibi, A. Patnaik, M. J. Blouin, L. C. Cantley, L. Guarente, J. Blenis, M. N. Pollak, A. F. Olumi, M. G. Vander Heiden and G. Stephanopoulos (2013). "Metformin Decreases Glucose Oxidation and Increases the Dependency of Prostate Cancer Cells on Reductive Glutamine Metabolism." Cancer Research **73**(14): 4429-4438.

Ferrari, A., S. Del'Olio and A. Barrientos (2021). "The Diseased Mitoribosome." **595**(8): 1025-1061.

Ferreira, H., R. N. Ramos, C. F. Quan, S. R. Ferreiro, V. C. Ruiz, J. Juampérez Goñi, J. Quintero Bernabeu, O. Segarra Cantón and M. Álvarez Beltran (2018). "Chylomicron Retention Disease: a Description of a New Mutation in a Very Rare Disease." Pediatr Gastroenterol Hepatol Nutr **21**(2): 134-140.

Finsterer, J. and M. Frank (2017). "Gastrointestinal manifestations of mitochondrial disorders: a systematic review." Therapeutic advances in gastroenterology **10**(1): 142-154.

Finsterer, J. and S. Zarrouk-Mahjoub (2017). "Phenotypic spectrum of DARS2 mutations." J Neurol Sci **376**: 117-118.

Fock, E. M., V. T. Bachteeva, E. A. Lavrova and R. G. Parnova (2018). "Mitochondrial-Targeted Antioxidant MitoQ Prevents E. coli Lipopolysaccharide-Induced Accumulation of Triacylglycerol and Lipid Droplets Biogenesis in Epithelial Cells." Journal of Lipids **2018**.

Fontanesi, F., I. C. Soto, D. Horn and A. Barrientos (2006). "Assembly of mitochondrial cytochrome c-oxidase, a complicated and highly regulated cellular process." Am J Physiol Cell Physiol **291**(6): C1129-1147.

Frank, D. N., E. S. Bales, J. Monks, M. J. Jackman, P. S. MacLean, D. Ir, C. E. Robertson, D. J. Orlicky and J. L. McManaman (2015). "Perilipin-2 Modulates Lipid Absorption and Microbiome Responses in the Mouse Intestine." PLoS One **10**(7): e0131944.

Freyre, C. A. C., P. C. Rauher, C. S. Ejsing and R. W. Klemm (2019). "MIGA2 Links Mitochondria, the ER, and Lipid Droplets and Promotes De Novo Lipogenesis in Adipocytes." Mol Cell **76**(5): 811-825.e814.

Fujiwara, H., K. Seike, M. D. Brooks, A. V. Mathew, I. Kovalenko, A. Pal, H.-J. Lee, D. Peltier, S. Kim, C. Liu, K. Oravecz-Wilson, L. Li, Y. Sun, J. Byun, Y. Maeda, M. S. Wicha, T. L. Saunders, A. Rehemtulla, C. A. Lyssiotis, S. Pennathur and P. Reddy (2021). "Mitochondrial complex II in intestinal epithelial cells regulates T cell-mediated immunopathology." Nature Immunology **22**(11): 1440-1451.

Fukui, H., F. Diaz, S. Garcia and C. T. Moraes (2007). "Cytochrome <i>c</i> oxidase deficiency in neurons decreases both oxidative stress and amyloid formation in a mouse model of Alzheimer's disease." Proceedings of the National Academy of Sciences **104**(35): 14163-14168.

Fünfschilling, U., L. M. Supplie, D. Mahad, S. Boretius, A. S. Saab, J. Edgar, B. G. Brinkmann, C. M. Kassmann, I. D. Tzvetanova, W. Möbius, F. Diaz, D. Meijer, U. Suter, B. Hamprecht, M. W. Sereda, C. T. Moraes, J. Frahm, S. Goebbels and K. A. Nave (2012). "Glycolytic oligodendrocytes maintain myelin and long-term axonal integrity." Nature **485**(7399): 517-521.

Galluzzi, L., O. Kepp and G. Kroemer (2012). "Mitochondria: master regulators of danger signalling." Nat Rev Mol Cell Biol **13**(12): 780-788.

Gao, Y., D. W. Nelson, T. Banh, M. I. Yen and C. E. Yen (2013). "Intestine-specific expression of MOGAT2 partially restores metabolic efficiency in Mogat2-deficient mice." J Lipid Res **54**(6): 1644-1652.

Gaude, E., F. Chignola, D. Spiliotopoulos, A. Spitaleri, M. Ghitti, J. M. Garcia-Manteiga, S. Mari and G. Musco (2013). "muma, An R Package for Metabolomics Univariate and Multivariate Statistical Analysis." Current Metabolomics **1**(2): 180-189.

Gaude, E. and C. Frezza (2016). "Tissue-specific and convergent metabolic transformation of cancer correlates with metastatic potential and patient survival." Nature Communications **7**(1): 13041.

Gehart, H. and H. Clevers (2019). "Tales from the crypt: new insights into intestinal stem cells." **16**(1): 19-34.

Giacomello, M., A. Pyakurel, C. Glytsou and L. Scorrano (2020). "The cell biology of mitochondrial membrane dynamics." **21**(4): 204-224.

Giacomello, M., A. Pyakurel, C. Glytsou and L. Scorrano (2020). "The cell biology of mitochondrial membrane dynamics." Nature Reviews Molecular Cell Biology **21**(4): 204-224.

Giammanco, A., A. B. Cefalu, D. Noto and M. R. Averna (2015). "The pathophysiology of intestinal lipoprotein production." Front Physiol **6**: 61.

Gilkerson, R. W., J. M. Selker and R. A. Capaldi (2003). "The cristal membrane of mitochondria is the principal site of oxidative phosphorylation." FEBS Lett **546**(2-3): 355-358.

Gillespie, M. N., V. Pastukh and M. V. Ruchko (2009). "Oxidative DNA modifications in hypoxic signaling." Ann N Y Acad Sci **1177**: 140-150.

Gillon, A. D., C. F. Latham and E. A. Miller (2012). "Vesicle-mediated ER export of proteins and lipids." Biochim Biophys Acta **1821**(8): 1040-1049.

Gonen, A. and Y. I. Miller (2020). "From Inert Storage to Biological Activity—In Search of Identity for Oxidized Cholesteryl Esters." Frontiers in Endocrinology **11**.

Gordon, S. M., E. B. Neufeld, Z. Yang, M. Pryor, L. A. Freeman, X. Fan, I. J. Kullo, L. G. Biesecker and A. T. Remaley (2019). "DENND5B Regulates Intestinal Triglyceride Absorption and Body Mass." Scientific Reports **9**(1): 3597.

Gorman, G. S., P. F. Chinnery, S. DiMauro, M. Hirano, Y. Koga, R. McFarland, A. Suomalainen, D. R. Thorburn, M. Zeviani and D. M. Turnbull (2016). "Mitochondrial diseases." Nature Reviews Disease Primers **2**(1): 16080.

Greber, B. J. and N. Ban (2016). "Structure and Function of the Mitochondrial Ribosome." Annual Review of Biochemistry **85**(1): 103-132.

Gribble, F. M. and F. Reimann (2019). "Function and mechanisms of enteroendocrine cells and gut hormones in metabolism." Nature Reviews Endocrinology **15**(4): 226-237.

Gumucio, J. P., A. H. Qasawa, P. J. Ferrara, A. N. Malik, K. Funai, B. McDonagh and C. L. Mendias (2019). "Reduced mitochondrial lipid oxidation leads to fat accumulation in myosteatosis." Faseb j **33**(7): 7863-7881.

Guo, R., S. Zong, M. Wu, J. Gu and M. Yang (2017). "Architecture of Human Mitochondrial Respiratory Megacomplex I(2)III(2)IV(2)." Cell **170**(6): 1247-1257.e1212.

Guo, X. and G. Aviles (2020). "Mitochondrial stress is relayed to the cytosol by an OMA1-DELE1-HRI pathway." **579**(7799): 427-432.

Gustafsson, C. M., M. Falkenberg and N. G. Larsson (2016). "Maintenance and Expression of Mammalian Mitochondrial DNA." Annu Rev Biochem **85**: 133-160.

Hackenbrock, C. R., B. Chazotte and S. S. Gupte (1986). "The random collision model and a critical assessment of diffusion and collision in mitochondrial electron transport." J Bioenerg Biomembr **18**(5): 331-368.

Haemmerle, G., A. Lass, R. Zimmermann, G. Gorkiewicz, C. Meyer, J. Rozman, G. Heldmaier, R. Maier, C. Theussl, S. Eder, D. Kratky, E. F. Wagner, M. Klingenspor, G. Hoefler and R. Zechner (2006). "Defective lipolysis and altered energy metabolism in mice lacking adipose triglyceride lipase." Science **312**(5774): 734-737.

Han, J., S. H. Back, J. Hur, Y. H. Lin, R. Gildersleeve, J. Shan, C. L. Yuan, D. Krokowski, S. Wang, M. Hatzoglou, M. S. Kilberg, M. A. Sartor and R. J. Kaufman (2013). "ER-stress-induced transcriptional regulation increases protein synthesis leading to cell death." Nat Cell Biol **15**(5): 481-490.

Han, J., C. Yu, R. F. Souza and A. L. Theiss (2014). "Prohibitin 1 modulates mitochondrial function of Stat3." Cellular signalling **26**(10): 2086-2095.

Han, Y. H., S. H. Kim, S. Z. Kim and W. H. Park (2008). "Antimycin A as a mitochondrial electron transport inhibitor prevents the growth of human lung cancer A549 cells." Oncol Rep **20**(3): 689-693.

Harris, C. A., J. T. Haas, R. S. Streeper, S. J. Stone, M. Kumari, K. Yang, X. Han, N. Brownell, R. W. Gross, R. Zechner and J. R. V. Farese (2011). "DGAT enzymes are required for triacylglycerol synthesis and lipid droplets in adipocytes[S]." Journal of Lipid Research **52**(4): 657-667.

Hashidate-Yoshida, T., T. Harayama, D. Hishikawa, R. Morimoto, F. Hamano, S. M. Tokuoka, M. Eto, M. Tamura-Nakano, R. Yanobu-Takanashi, Y. Mukumoto, H. Kiyonari, T. Okamura, Y. Kita, H. Shindou and T. Shimizu (2015). "Fatty acid remodeling by LPCAT3 enriches arachidonate in phospholipid membranes and regulates triglyceride transport." Elife **4**.

Heller, S., H. M. Penrose, C. Cable, D. Biswas, H. Nakhoul, M. Baddoo, E. Flemington, S. E. Crawford and S. D. Savkovic (2017). "Reduced mitochondrial activity in colonocytes facilitates AMPKα2-dependent inflammation." Faseb j **31**(5): 2013-2025.

Hillen, H. S., Y. I. Morozov, A. Sarfallah, D. Temiakov and P. Cramer (2017). "Structural Basis of Mitochondrial Transcription Initiation." Cell **171**(5): 1072-1081.e1010.

Ho, G. T., R. E. Aird, B. Liu, R. K. Boyapati, N. A. Kennedy, D. A. Dorward, C. L. Noble, T. Shimizu, R. N. Carter, E. T. S. Chew, N. M. Morton, A. G. Rossi, R. B. Sartor, J. P. Iredale and J. Satsangi (2018). "MDR1 deficiency impairs mitochondrial homeostasis and promotes intestinal inflammation." Mucosal Immunology **11**(1): 120-130.

Hofsetz, E., A. Trifunovic and T. Langer (2019). The Role of SDHA in the Tissue-specific Regulation of Metabolism and Proteomic Approaches to Identify Novel ClpXP Substrates, Universitäts- und Stadtbibliothek Köln.

Hooper, A. J., K. Robertson, P. H. Barrett, K. G. Parhofer, F. M. van Bockxmeer and J. R. Burnett (2007). "Postprandial lipoprotein metabolism in familial hypobetalipoproteinemia." J Clin Endocrinol Metab **92**(4): 1474-1478.

Horváth, R., A. Abicht, E. Holinski-Feder, A. Laner, K. Gempel, H. Prokisch, H. Lochmüller, T. Klopstock and M. Jaksch (2006). "Leigh syndrome caused by mutations in the flavoprotein (Fp) subunit of succinate dehydrogenase (SDHA)." Journal of neurology, neurosurgery, and psychiatry **77**(1): 74-76.

Houten, S. M. and R. J. Wanders (2010). "A general introduction to the biochemistry of mitochondrial fatty acid β-oxidation." J Inherit Metab Dis **33**(5): 469-477.

Hsieh, J., C. Longuet, C. L. Baker, B. Qin, L. M. Federico, D. J. Drucker and K. Adeli (2010). "The glucagon-like peptide 1 receptor is essential for postprandial lipoprotein synthesis and secretion in hamsters and mice." Diabetologia **53**(3): 552-561.

Hsieh, J., K. E. Trajcevski, S. L. Farr, C. L. Baker, E. J. Lake, J. Taher, J. Iqbal, M. M. Hussain and K. Adeli (2015). "Glucagon-Like Peptide 2 (GLP-2) Stimulates Postprandial Chylomicron Production and Postabsorptive Release of Intestinal Triglyceride Storage Pools via Induction of Nitric Oxide Signaling in Male Hamsters and Mice." Endocrinology **156**(10): 3538-3547.

Hsieh, S. Y., T. C. Shih, C. Y. Yeh, C. J. Lin, Y. Y. Chou and Y. S. Lee (2006). "Comparative proteomic studies on the pathogenesis of human ulcerative colitis." Proteomics **6**(19): 5322-5331.

Hu, X., J. Deng, T. Yu, S. Chen, Y. Ge, Z. Zhou, Y. Guo, H. Ying, Q. Zhai, Y. Chen, F. Yuan, Y. Niu, W. Shu, H. Chen, C. Ma, Z. Liu and F. Guo (2019). "ATF4 Deficiency Promotes Intestinal Inflammation in Mice by Reducing Uptake of Glutamine and Expression of Antimicrobial Peptides." Gastroenterology **156**(4): 1098-1111.

Humphrey, J. S., P. J. Peters, L. C. Yuan and J. S. Bonifacino (1993). "Localization of TGN38 to the trans-Golgi network: involvement of a cytoplasmic tyrosine-containing sequence." J Cell Biol **120**(5): 1123-1135.

Hung, Y.-H., A. L. Carreiro and K. K. Buhman (2017). "Dgat1 and Dgat2 regulate enterocyte triacylglycerol distribution and alter proteins associated with cytoplasmic lipid droplets in response to dietary fat." Biochimica et Biophysica Acta (BBA) - Molecular and Cell Biology of Lipids **1862**(6): 600-614.

Hung, Y. H., A. L. Carreiro and K. K. Buhman (2017). "Dgat1 and Dgat2 regulate enterocyte triacylglycerol distribution and alter proteins associated with cytoplasmic lipid droplets in response to dietary fat." Biochim Biophys Acta Mol Cell Biol Lipids **1862**(6): 600-614.

Hussain, M. M., P. Rava, M. Walsh, M. Rana and J. Iqbal (2012). "Multiple functions of microsomal triglyceride transfer protein." Nutrition & Metabolism **9**(1): 14.

Hussain, M. M., P. Rava, M. Walsh, M. Rana and J. Iqbal (2012). "Multiple functions of microsomal triglyceride transfer protein." Nutr Metab (Lond) **9**: 14.

Igarashi, M. and L. Guarente (2016). "mTORC1 and SIRT1 Cooperate to Foster Expansion of Gut Adult Stem Cells during Calorie Restriction." Cell **166**(2): 436-450.

Indriolo, A., S. Greco, P. Ravelli and S. Fagiuoli (2011). "What can we learn about biofilm/host interactions from the study of inflammatory bowel disease." J Clin Periodontol **38 Suppl 11**: 36-43.

Iqbal, J., M. Boutjdir, L. L. Rudel and M. M. Hussain (2014). "Intestine-specific MTP and global ACAT2 deficiency lowers acute cholesterol absorption with chylomicrons and HDLs." J Lipid Res **55**(11): 2261-2275.

Iqbal, J. and M. M. Hussain (2009). "Intestinal lipid absorption." Am J Physiol Endocrinol Metab **296**(6): E1183-1194.

Ishii, T., M. Miyazawa, A. Onodera, K. Yasuda, N. Kawabe, M. Kirinashizawa, S. Yoshimura, N. Maruyama, P. S. Hartman and N. Ishii (2011). "Mitochondrial reactive oxygen species generation by the SDHC V69E mutation causes low birth weight and neonatal growth retardation." Mitochondrion **11**(1): 155-165.

Jackson, D. N., M. Panopoulos, W. L. Neumann, K. Turner, B. L. Cantarel, L. Thompson-Snipes and T. Dassopoulos (2020). "Mitochondrial dysfunction during loss of prohibitin 1 triggers Paneth cell defects and ileitis." **69**(11): 1928-1938.

Jain-Ghai, S., J. M. Cameron, A. Al Maawali, S. Blaser, N. MacKay, B. Robinson and J. Raiman (2013). "Complex II deficiency--a case report and review of the literature." Am J Med Genet A **161a**(2): 285-294.

Jarc, E. and T. Petan (2019). "Lipid Droplets and the Management of Cellular Stress." Yale J Biol Med **92**(3): 435-452.

Jaschke, A., B. Chung, D. Hesse, R. Kluge, C. Zahn, M. Moser, K. J. Petzke, R. Brigelius-Flohé, D. Puchkov, H. Koepsell, J. Heeren, H. G. Joost and A. Schürmann (2012). "The GTPase ARFRP1 controls the lipidation of chylomicrons in the Golgi of the intestinal epithelium." Hum Mol Genet **21**(14): 3128-3142.

Javadov, S., S. Jang, X. R. Chapa-Dubocq, Z. Khuchua and A. K. Camara (2021). "Mitochondrial respiratory supercomplexes in mammalian cells: structural versus functional role." J Mol Med (Berl) **99**(1): 57-73.

Jeppesen, P. B., M. Pertkiewicz, B. Messing, K. Iyer, D. L. Seidner, J. O'Keefe S, A. Forbes, H. Heinze and B. Joelsson (2012). "Teduglutide reduces need for parenteral support among patients with short bowel syndrome with intestinal failure." Gastroenterology **143**(6): 1473-1481.e1473.

Jia, L., J. L. Betters and L. Yu (2011). "Niemann-pick C1-like 1 (NPC1L1) protein in intestinal and hepatic cholesterol transport." Annu Rev Physiol **73**: 239-259.

Jonckheere, A. I., J. A. Smeitink and R. J. Rodenburg (2012). "Mitochondrial ATP synthase: architecture, function and pathology." J Inherit Metab Dis **35**(2): 211-225.

Jones, B., E. L. Jones, S. A. Bonney, H. N. Patel, A. R. Mensenkamp, S. Eichenbaum-Voline, M. Rudling, U. Myrdal, G. Annesi, S. Naik, N. Meadows, A. Quattrone, S. A. Islam, R. P. Naoumova, B. Angelin, R. Infante, E. Levy, C. C. Roy, P. S. Freemont, J. Scott and C. C. Shoulders (2003). "Mutations in a Sar1 GTPase of COPII vesicles are associated with lipid absorption disorders." Nature Genetics **34**(1): 29-31.

Julve, J., J. M. Martín-Campos, J. C. Escolà-Gil and F. Blanco-Vaca (2016). "Chylomicrons: Advances in biology, pathology, laboratory testing, and therapeutics." Clin Chim Acta **455**: 134-148.

Kanki, T., H. Nakayama, N. Sasaki, K. Takio, T. I. Alam, N. Hamasaki and D. Kang (2004). "Mitochondrial nucleoid and transcription factor A." Ann N Y Acad Sci **1011**: 61-68.

Karmakar, S., L. Deng, X. C. He and L. Li (2020). "Intestinal epithelial regeneration: active versus reserve stem cells and plasticity mechanisms." Am J Physiol Gastrointest Liver Physiol **318**(4): G796-g802.

Kaser, A., A. H. Lee, A. Franke, J. N. Glickman, S. Zeissig, H. Tilg, E. E. Nieuwenhuis, D. E. Higgins, S. Schreiber, L. H. Glimcher and R. S. Blumberg (2008). "XBP1 links ER stress to intestinal inflammation and confers genetic risk for human inflammatory bowel disease." Cell **134**(5): 743-756.

Kaspar, S., C. Oertlin and K. Szczepanowska (2021). "Adaptation to mitochondrial stress requires CHOP-directed tuning of ISR." **7**(22).

Khacho, M., A. Clark, Devon S. Svoboda, J. Azzi, Jason G. MacLaurin, C. Meghaizel, H. Sesaki, Diane C. Lagace, M. Germain, M.-E. Harper, David S. Park and Ruth S. Slack (2016).

"Mitochondrial Dynamics Impacts Stem Cell Identity and Fate Decisions by Regulating a Nuclear Transcriptional Program." Cell Stem Cell **19**(2): 232-247.

Khalifeh-Soltani, A., D. Gupta, A. Ha, J. Iqbal, M. Hussain, M. J. Podolsky and K. Atabai (2016). "Mfge8 regulates enterocyte lipid storage by promoting enterocyte triglyceride hydrolase activity." JCI Insight **1**(18): e87418.

Khaloian, S. and E. Rath (2020). "Mitochondrial impairment drives intestinal stem cell transition into dysfunctional Paneth cells predicting Crohn's disease recurrence." **69**(11): 1939-1951.

Khatun, I., R. W. Clark, N. B. Vera, K. Kou, D. M. Erion, T. Coskran, W. F. Bobrowski, C. Okerberg and B. Goodwin (2016). "Characterization of a Novel Intestinal Glycerol-3-phosphate Acyltransferase Pathway and Its Role in Lipid Homeostasis*." Journal of Biological Chemistry **291**(6): 2602-2615.

Khor, B., A. Gardet and R. J. Xavier (2011). "Genetics and pathogenesis of inflammatory bowel disease." Nature **474**: 307.

Kim, E. and S. G. Young (1998). "Genetically modified mice for the study of apolipoprotein B." J Lipid Res **39**(4): 703-723.

Kim, J., H. Kim, S. H. Noh, D. G. Jang, S.-Y. Park, D. Min, H. Kim, H.-S. Kweon, H. Kim, S. Aum, S. Seo, C. S. Choi, H. Kim, J. W. Kim, S. J. Moon, H. Y. Gee and M. G. Lee (2020). "Grasp55−/− mice display impaired fat absorption and resistance to high-fat diet-induced obesity." Nature Communications **11**(1): 1418.

Kim, J. T., Y. J. Lee, Y. M. Lee, H. C. Kang, J. S. Lee and H. D. Kim (2009). "Clinical characteristics of patients with non-specific and non-categorized mitochondrial diseases." Acta Paediatr **98**(11): 1825-1829.

Klucnika, A. and H. Ma (2019). "A battle for transmission: the cooperative and selfish animal mitochondrial genomes." Open Biol **9**(3): 180267.

Ko, C.-W., J. Qu, D. D. Black and P. Tso (2020). "Regulation of intestinal lipid metabolism: current concepts and relevance to disease." Nature Reviews Gastroenterology & Hepatology **17**(3): 169-183.

Ko, C. W., J. Qu, D. D. Black and P. Tso (2020). "Regulation of intestinal lipid metabolism: current concepts and relevance to disease." Nat Rev Gastroenterol Hepatol **17**(3): 169-183.

Kohan, A. B., F. Wang, C. M. Lo, M. Liu and P. Tso (2015). "ApoA-IV: current and emerging roles in intestinal lipid metabolism, glucose homeostasis, and satiety." Am J Physiol Gastrointest Liver Physiol **308**(6): G472-481.

Kondo, H., Y. Minegishi, Y. Komine, T. Mori, I. Matsumoto, K. Abe, I. Tokimitsu, T. Hase and T. Murase (2006). "Differential regulation of intestinal lipid metabolism-related genes in obesity-resistant A/J vs. obesity-prone C57BL/6J mice." Am J Physiol Endocrinol Metab **291**(5): E1092-1099.

Korbelius, M., N. Vujic, V. Sachdev, S. Obrowsky, S. Rainer, B. Gottschalk, W. F. Graier and D. Kratky (2019). "ATGL/CGI-58-Dependent Hydrolysis of a Lipid Storage Pool in Murine Enterocytes." Cell Rep **28**(7): 1923-1934.e1924.

Kühlbrandt, W. (2015). "Structure and function of mitochondrial membrane protein complexes." BMC Biology **13**(1): 89.

Kumar, V., J. E. Bouameur, J. Bar, R. H. Rice, H. T. Hornig-Do, D. R. Roop, N. Schwarz, S. Brodesser, S. Thiering, R. E. Leube, R. J. Wiesner, P. Vijayaraj, C. B. Brazel, S. Heller, H. Binder, H. Loffler-Wirth, P. Seibel and T. M. Magin (2015). "A keratin scaffold regulates epidermal barrier formation, mitochondrial lipid composition, and activity." J Cell Biol **211**(5): 1057-1075.

Kurahashi, T., T. Konno, N. Otsuki, M. Kwon, S. Tsunoda, J. Ito and J. Fujii (2012). "A malfunction in triglyceride transfer from the intracellular lipid pool to apoB in enterocytes of SOD1-deficient mice." FEBS Lett **586**(24): 4289-4295.

Kurland, C. G. and S. G. Andersson (2000). "Origin and evolution of the mitochondrial proteome." Microbiology and molecular biology reviews : MMBR **64**(4): 786-820.

Lagakos, W. S., A. M. Gajda, L. Agellon, B. Binas, V. Choi, B. Mandap, T. Russnak, Y. X. Zhou and J. Storch (2011). "Different functions of intestinal and liver-type fatty acid-binding proteins in intestine and in whole body energy homeostasis." Am J Physiol Gastrointest Liver Physiol **300**(5): G803-814.

Lambert, J. E. and E. J. Parks (2012). "Postprandial metabolism of meal triglyceride in humans." Biochim Biophys Acta **1821**(5): 721-726.

Lass, A., R. Zimmermann, G. Haemmerle, M. Riederer, G. Schoiswohl, M. Schweiger, P. Kienesberger, J. G. Strauss, G. Gorkiewicz and R. Zechner (2006). "Adipose triglyceride lipase-mediated lipolysis of cellular fat stores is activated by CGI-58 and defective in Chanarin-Dorfman Syndrome." Cell Metab **3**(5): 309-319.

Le May, C., S. Kourimate, C. Langhi, M. Chétiveaux, A. Jarry, C. Comera, X. Collet, F. Kuipers, M. Krempf, B. Cariou and P. Costet (2009). "Proprotein convertase subtilisin kexin type 9 null mice are protected from postprandial triglyceridemia." Arterioscler Thromb Vasc Biol **29**(5): 684-690.

Lee, B., A. M. Fast, J. Zhu, J.-X. Cheng and K. K. Buhman (2010). "Intestine-specific expression of acyl CoA:diacylglycerol acyltransferase 1 reverses resistance to diet-induced hepatic steatosis and obesity in Dgat1-/- mice." Journal of lipid research **51**(7): 1770-1780.

Lee, B., J. Zhu, N. E. Wolins, J.-X. Cheng and K. K. Buhman (2009). "Differential association of adipophilin and TIP47 proteins with cytoplasmic lipid droplets in mouse enterocytes during dietary fat absorption." Biochimica et biophysica acta **1791**(12): 1173-1180.

Lee, B., J. Zhu, N. E. Wolins, J. X. Cheng and K. K. Buhman (2009). "Differential association of adipophilin and TIP47 proteins with cytoplasmic lipid droplets in mouse enterocytes during dietary fat absorption." Biochim Biophys Acta **1791**(12): 1173-1180.

Lee, I. and M. Hüttemann (2014). "Energy crisis: the role of oxidative phosphorylation in acute inflammation and sepsis." Biochim Biophys Acta **1842**(9): 1579-1586.

Lee, J. and N. D. Ridgway (2020). "Substrate channeling in the glycerol-3-phosphate pathway regulates the synthesis, storage and secretion of glycerolipids." Biochimica et Biophysica Acta (BBA) - Molecular and Cell Biology of Lipids **1865**(1): 158438.

Lee, S.-J., J. Zhang, A. M. K. Choi and H. P. Kim (2013). "Mitochondrial Dysfunction Induces Formation of Lipid Droplets as a Generalized Response to Stress." Oxidative Medicine and Cellular Longevity **2013**: 327167.

Lema, I., J. R. Araújo, N. Rolhion and S. Demignot (2020). "Jejunum: The understudied meeting place of dietary lipids and the microbiota." Biochimie **178**: 124-136.

Levic, D. S., J. R. Minkel, W. D. Wang, W. M. Rybski, D. B. Melville and E. W. Knapik (2015). "Animal model of Sar1b deficiency presents lipid absorption deficits similar to Anderson disease." J Mol Med (Berl) **93**(2): 165-176.

Levy, E. (2015). "Insights from human congenital disorders of intestinal lipid metabolism." Journal of Lipid Research **56**(5): 945-962.

Levy, E., J. F. Beaulieu and S. Spahis (2021). "From Congenital Disorders of Fat Malabsorption to Understanding Intra-Enterocyte Mechanisms Behind Chylomicron Assembly and Secretion." Frontiers in Physiology **12**.

Levy, E., E. Harmel, M. Laville, R. Sanchez, L. Emonnot, D. Sinnett, E. Ziv, E. Delvin, P. Couture, V. Marcil and A. T. Sane (2011). "Expression of Sar1b enhances chylomicron assembly and key components of the coat protein complex II system driving vesicle budding." Arterioscler Thromb Vasc Biol **31**(11): 2692-2699.

Levy, E., P. Poinsot and S. Spahis (2019). "Chylomicron retention disease: genetics, biochemistry, and clinical spectrum." Curr Opin Lipidol **30**(2): 134-139.

Levy, E., S. Spahis, C. Garofalo, V. Marcil, A. Montoudis, D. Sinnet, R. Sanchez, N. Peretti, J. F. Beaulieu and A. Sane (2014). "Sar1b transgenic male mice are more susceptible to high-fat diet-induced obesity, insulin insensitivity and intestinal chylomicron overproduction." J Nutr Biochem **25**(5): 540-548.

Li, D., C. N. Rodia, Z. K. Johnson, M. Bae, A. Muter, A. E. Heussinger, N. Tambini, A. M. Longo, H. Dong, J. Y. Lee and A. B. Kohan (2019). "Intestinal basolateral lipid substrate transport is linked to chylomicron secretion and is regulated by apoC-III." J Lipid Res **60**(9): 1503-1515.

Li, S.-T., D. Huang, S. Shen, Y. Cai, S. Xing, G. Wu, Z. Jiang, Y. Hao, M. Yuan, N. Wang, L. Zhu, R. Yan, D. Yang, L. Wang, Z. Liu, X. Hu, R. Zhou, K. Qu, A. Li, X. Duan, H. Zhang and P. Gao (2020). "Myc-mediated SDHA acetylation triggers epigenetic regulation of gene expression and tumorigenesis." Nature Metabolism **2**(3): 256-269.

Liao, D.-H., J.-B. Zhao and H. Gregersen (2009). "Gastrointestinal tract modelling in health and disease." World journal of gastroenterology **15**(2): 169-176.

Lightowlers, R. N., P. F. Chinnery, D. M. Turnbull and N. Howell (1997). "Mammalian mitochondrial genetics: heredity, heteroplasmy and disease." Trends Genet **13**(11): 450-455.

Liu, R., X. Li, Z. Huang, D. Zhao, B. S. Ganesh, G. Lai, W. M. Pandak, P. B. Hylemon, J. S. Bajaj, A. J. Sanyal and H. Zhou (2018). "C/EBP homologous protein-induced loss of intestinal epithelial stemness contributes to bile duct ligation-induced cholestatic liver injury in mice." **67**(4): 1441-1457.

Lynes, M., S. Narisawa, J. L. Millán and E. P. Widmaier (2011). "Interactions between CD36 and global intestinal alkaline phosphatase in mouse small intestine and effects of high-fat diet." Am J Physiol Regul Integr Comp Physiol **301**(6): R1738-1747.

Madison, B. B., L. Dunbar, X. T. Qiao, K. Braunstein, E. Braunstein and D. L. Gumucio (2002). "Cis elements of the villin gene control expression in restricted domains of the vertical (crypt) and horizontal (duodenum, cecum) axes of the intestine." J Biol Chem **277**(36): 33275-33283.

Mai, N., Z. M. Chrzanowska-Lightowlers and R. N. Lightowlers (2017). "The process of mammalian mitochondrial protein synthesis." Cell Tissue Res **367**(1): 5-20.

Mannella, C. A. (2020). "Consequences of Folding the Mitochondrial Inner Membrane." Frontiers in Physiology **11**.

Mansbach, C. M., 2nd and F. Gorelick (2007). "Development and physiological regulation of intestinal lipid absorption. II. Dietary lipid absorption, complex lipid synthesis, and the intracellular packaging and secretion of chylomicrons." Am J Physiol Gastrointest Liver Physiol **293**(4): G645-650.

Mansbach, C. M., 2nd and S. Siddiqi (2016). "Control of chylomicron export from the intestine." Am J Physiol Gastrointest Liver Physiol **310**(9): G659-668.

Mansbach, C. M. and S. A. Siddiqi (2010). "The Biogenesis of Chylomicrons." Annual Review of Physiology **72**(1): 315-333.

Mansbach, C. M. and S. A. Siddiqi (2010). "The biogenesis of chylomicrons." Annu Rev Physiol **72**: 315-333.

Mardones, P., V. Quiñones, L. Amigo, M. Moreno, J. F. Miquel, M. Schwarz, H. E. Miettinen, B. Trigatti, M. Krieger, S. VanPatten, D. E. Cohen and A. Rigotti (2001). "Hepatic cholesterol and bile acid metabolism and intestinal cholesterol absorption in scavenger receptor class B type I-deficient mice." J Lipid Res **42**(2): 170-180.

Martinez-Guryn, K., N. Hubert, K. Frazier, S. Urlass, M. W. Musch, P. Ojeda, J. F. Pierre, J. Miyoshi, T. J. Sontag, C. M. Cham, C. A. Reardon, V. Leone and E. B. Chang (2018). "Small Intestine Microbiota Regulate Host Digestive and Absorptive Adaptive Responses to Dietary Lipids." Cell Host Microbe **23**(4): 458-469.e455.

Martínez-Reyes, I. and N. S. Chandel (2020). "Mitochondrial TCA cycle metabolites control physiology and disease." Nature Communications **11**(1): 102.

Masuda, D. and S. Yamashita (2017). "Postprandial Hyperlipidemia and Remnant Lipoproteins." J Atheroscler Thromb **24**(2): 95-109.

McCaughey, J. and D. J. Stephens (2018). "COPII-dependent ER export in animal cells: adaptation and control for diverse cargo." **150**(2): 119-131.

McCaughey, J. and D. J. Stephens (2019). "ER-to-Golgi Transport: A Sizeable Problem." Trends in Cell Biology **29**(12): 940-953.

McConnell, B. B., S. S. Kim, K. Yu, A. M. Ghaleb, N. Takeda, I. Manabe, A. Nusrat, R. Nagai and V. W. Yang (2011). "Krüppel-like factor 5 is important for maintenance of crypt architecture and barrier function in mouse intestine." Gastroenterology **141**(4): 1302-1313, 1313.e1301-1306.

Meier, J. J., A. Gethmann, O. Götze, B. Gallwitz, J. J. Holst, W. E. Schmidt and M. A. Nauck (2006). "Glucagon-like peptide 1 abolishes the postprandial rise in triglyceride concentrations and lowers levels of non-esterified fatty acids in humans." Diabetologia **49**(3): 452-458.

Mera, Y., N. Odani, T. Kawai, T. Hata, M. Suzuki, A. Hagiwara, T. Katsushima and M. Kakutani (2011). "Pharmacological characterization of diethyl-2-({3-dimethylcarbamoyl-4-[(4'-trifluoromethylbiphenyl-2-carbonyl)amino]phenyl}acetyloxymethyl)-2-phenylmalonate (JTT-130), an intestine-specific inhibitor of microsomal triglyceride transfer protein." J Pharmacol Exp Ther **336**(2): 321-327.

Metzler, B., P. Gfeller and E. Guinet (2016). "Restricting Glutamine or Glutamine-Dependent Purine and Pyrimidine Syntheses Promotes Human T Cells with High FOXP3 Expression and Regulatory Properties." The Journal of Immunology **196**(9): 3618-3630.

Milenkovic, D., J. N. Blaza, N.-G. Larsson and J. Hirst (2017). "The Enigma of the Respiratory Chain Supercomplex." Cell Metabolism **25**(4): 765-776.

Mitchell, P. (1961). "Coupling of Phosphorylation to Electron and Hydrogen Transfer by a Chemi-Osmotic type of Mechanism." Nature **191**(4784): 144-148.

Mogi, T., K. Saiki and Y. Anraku (1994). "Biosynthesis and functional role of haem O and haem A." Mol Microbiol **14**(3): 391-398.

Moreno, C. and R. M. Santos (2020). "Succinate Dehydrogenase and Ribonucleic Acid Networks in Cancer and Other Diseases." **12**(11).

Morgan, S., S. Falcon and R. Gentleman (2021). "GSEABase: Gene set enrichment data structures and methods." R package version 1.54.0.

Mourier, A., E. Motori, T. Brandt, M. Lagouge, I. Atanassov, A. Galinier, G. Rappl, S. Brodesser, K. Hultenby, C. Dieterich and N. G. Larsson (2015). "Mitofusin 2 is required to maintain mitochondrial coenzyme Q levels." J Cell Biol **208**(4): 429-442.

Mowat, A. M. and W. W. Agace (2014). "Regional specialization within the intestinal immune system." Nature Reviews Immunology **14**(10): 667-685.

Na, U., W. Yu, J. Cox, Daniel K. Bricker, K. Brockmann, J. Rutter, Carl S. Thummel and Dennis R. Winge (2014). "The LYR Factors SDHAF1 and SDHAF3 Mediate Maturation of the Iron-Sulfur Subunit of Succinate Dehydrogenase." Cell Metabolism **20**(2): 253-266.

Nagao, A., T. Suzuki, T. Katoh, Y. Sakaguchi and T. Suzuki (2009). "Biogenesis of glutaminyl-mt tRNAGln in human mitochondria." Proc Natl Acad Sci U S A **106**(38): 16209-16214.

Nassir, F., B. Wilson, X. Han, R. W. Gross and N. A. Abumrad (2007). "CD36 Is Important for Fatty Acid and Cholesterol Uptake by the Proximal but Not Distal Intestine*." Journal of Biological Chemistry **282**(27): 19493-19501.

Nauli, A. M., F. Nassir, S. Zheng, Q. Yang, C. M. Lo, S. B. Vonlehmden, D. Lee, R. J. Jandacek, N. A. Abumrad and P. Tso (2006). "CD36 is important for chylomicron formation and secretion and may mediate cholesterol uptake in the proximal intestine." Gastroenterology **131**(4): 1197-1207.

Neeli, I., S. A. Siddiqi, S. Siddiqi, J. Mahan, W. S. Lagakos, B. Binas, T. Gheyi, J. Storch and C. M. Mansbach, 2nd (2007). "Liver fatty acid-binding protein initiates budding of pre-chylomicron transport vesicles from intestinal endoplasmic reticulum." J Biol Chem **282**(25): 17974-17984.

Nguyen, T. M., J. K. Sawyer, K. L. Kelley, M. A. Davis and L. L. Rudel (2012). "Cholesterol esterification by ACAT2 is essential for efficient intestinal cholesterol absorption: evidence from thoracic lymph duct cannulation." J Lipid Res **53**(1): 95-104.

Niot, I., H. Poirier, T. T. Tran and P. Besnard (2009). "Intestinal absorption of long-chain fatty acids: evidence and uncertainties." Prog Lipid Res **48**(2): 101-115.

Nolte, H., T. D. MacVicar, F. Tellkamp and M. Kruger (2018). "Instant Clue: A Software Suite for Interactive Data Visualization and Analysis." Sci Rep **8**(1): 12648.

Novak, E. A. and K. P. Mollen (2015). "Mitochondrial dysfunction in inflammatory bowel disease." Frontiers in cell and developmental biology **3**: 62-62.

Nunnari, J. and A. Suomalainen (2012). "Mitochondria: in sickness and in health." Cell **148**(6): 1145-1159.

Nurmi, H., P. Saharinen, G. Zarkada, W. Zheng, M. R. Robciuc and K. Alitalo (2015). "VEGF-C is required for intestinal lymphatic vessel maintenance and lipid absorption." EMBO Mol Med **7**(11): 1418-1425.

O'Hare, E. A., R. Yang, L. M. Yerges-Armstrong, U. Sreenivasan, R. McFarland, C. C. Leitch, M. H. Wilson, S. Narina, A. Gorden, K. A. Ryan, A. R. Shuldiner, S. A. Farber, G. C. Wood, C. D. Still, G. S. Gerhard, J. D. Robishaw, C. Sztalryd and N. A. Zaghloul (2017). "TM6SF2 rs58542926 impacts lipid processing in liver and small intestine." Hepatology **65**(5): 1526-1542.

Obrowsky, S., P. G. Chandak, J. V. Patankar, T. Pfeifer, S. Povoden, R. Schreiber, G. Haemmerle, S. Levak-Frank and D. Kratky (2012). "Cholesteryl ester accumulation and accelerated cholesterol absorption in intestine-specific hormone sensitive lipase-null mice." Biochim Biophys Acta **1821**(11): 1406-1414.

Obrowsky, S., P. G. Chandak, J. V. Patankar, S. Povoden, S. Schlager, E. E. Kershaw, J. G. Bogner-Strauss, G. Hoefler, S. Levak-Frank and D. Kratky (2013). "Adipose triglyceride lipase is a TG hydrolase of the small intestine and regulates intestinal PPARα signaling." J Lipid Res **54**(2): 425-435.

Olzmann, J. A. and P. Carvalho (2019). "Dynamics and functions of lipid droplets." Nature Reviews Molecular Cell Biology **20**(3): 137-155.

Pakos-Zebrucka, K., I. Koryga, K. Mnich, M. Ljujic and A. Samali (2016). "The integrated stress response." **17**(10): 1374-1395.

Pan, X. and M. M. Hussain (2012). "Gut triglyceride production." Biochim Biophys Acta **1821**(5): 727-735.

Pan, X., M. K. Munshi, J. Iqbal, J. Queiroz, A. A. Sirwi, S. Shah, A. Younus and M. M. Hussain (2013). "Circadian regulation of intestinal lipid absorption by apolipoprotein AIV involves forkhead transcription factors A2 and O1 and microsomal triglyceride transfer protein." J Biol Chem **288**(28): 20464-20476.

Papa, S., P. L. Martino, G. Capitanio, A. Gaballo, D. De Rasmo, A. Signorile and V. Petruzzella (2012). "The oxidative phosphorylation system in mammalian mitochondria." Adv Exp Med Biol **942**: 3-37.

Park, C. B., J. Asin-Cayuela, Y. Cámara, Y. Shi, M. Pellegrini, M. Gaspari, R. Wibom, K. Hultenby, H. Erdjument-Bromage, P. Tempst, M. Falkenberg, C. M. Gustafsson and N. G. Larsson (2007). "MTERF3 is a negative regulator of mammalian mtDNA transcription." Cell **130**(2): 273-285.

Pascual-Itoiz, M. A., A. Peña-Cearra, I. Martín-Ruiz, J. L. Lavín, C. Simó, H. Rodríguez, E. Atondo, J. M. Flores, A. Carreras-González, J. Tomás-Cortázar, D. Barriales, A. Palacios, V. García-Cañas, A. Pellón, A. Fullaondo, A. M. Aransay, R. Prados-Rosales, R. Martín, J. Anguita and L. Abecia (2020). "The mitochondrial negative regulator MCJ modulates the interplay between microbiota and the host during ulcerative colitis." Scientific Reports **10**(1): 572.

Pasparakis, M. and P. Vandenabeele (2015). "Necroptosis and its role in inflammation." Nature **517**(7534): 311-320.

Pavlic, M., C. Xiao, L. Szeto, B. W. Patterson and G. F. Lewis (2010). "Insulin acutely inhibits intestinal lipoprotein secretion in humans in part by suppressing plasma free fatty acids." Diabetes **59**(3): 580-587.

Pentinmikko, N., S. Iqbal, M. Mana, S. Andersson, A. B. Cognetta, R. M. Suciu, J. Roper, K. Luopajärvi, E. Markelin, S. Gopalakrishnan, O.-P. Smolander, S. Naranjo, T. Saarinen, A. Juuti, K. Pietiläinen, P. Auvinen, A. Ristimäki, N. Gupta, T. Tammela, T. Jacks, D. M. Sabatini, B. F. Cravatt, Ö. H. Yilmaz and P. Katajisto (2019). "Notum produced by Paneth cells attenuates regeneration of aged intestinal epithelium." Nature **571**(7765): 398-402.

Perekatt, A. O., M. J. Valdez, M. Davila, A. Hoffman, E. M. Bonder, N. Gao and M. P. Verzi (2014). "YY1 is indispensable for Lgr5⁺ intestinal stem cell renewal." Proceedings of the National Academy of Sciences **111**(21): 7695-7700.

Peretti, N., A. Sassolas, C. C. Roy, C. Deslandres, M. Charcosset, J. Castagnetti, L. Pugnet-Chardon, P. Moulin, S. Labarge, L. Bouthillier, A. Lachaux and E. Levy (2010). "Guidelines for the diagnosis and management of chylomicron retention disease based on a review of the literature and the experience of two centers." Orphanet J Rare Dis **5**: 24.

Perez-Riverol, Y., A. Csordas, J. Bai, M. Bernal-Llinares, S. Hewapathirana, D. J. Kundu, A. Inuganti, J. Griss, G. Mayer, M. Eisenacher, E. Perez, J. Uszkoreit, J. Pfeuffer, T. Sachsenberg, S. Yilmaz, S. Tiwary, J. Cox, E. Audain, M. Walzer, A. F. Jarnuczak, T. Ternent, A. Brazma and J. A. Vizcaino (2019). "The PRIDE database and related tools and resources in 2019: improving support for quantification data." Nucleic Acids Res **47**(D1): D442-D450.

Pfanner, N., B. Warscheid and N. Wiedemann (2019). "Mitochondrial proteins: from biogenesis to functional networks." Nature Reviews Molecular Cell Biology **20**(5): 267-284.

Pitceathly, R. D. S. and J.-W. Taanman (2018). "NDUFA4 (Renamed COXFA4) Is a Cytochrome-c Oxidase Subunit." Trends in Endocrinology & Metabolism **29**(7): 452-454.

Pollard, P. J., M. El-Bahrawy, R. Poulsom, G. Elia, P. Killick, G. Kelly, T. Hunt, R. Jeffery, P. Seedhar, J. Barwell, F. Latif, M. J. Gleeson, S. V. Hodgson, G. W. Stamp, I. P. Tomlinson and E. R. Maher (2006). "Expression of HIF-1alpha, HIF-2alpha (EPAS1), and their target genes in paraganglioma and pheochromocytoma with VHL and SDH mutations." J Clin Endocrinol Metab **91**(11): 4593-4598.

Qin, X., C. Li, T. Guo, J. Chen, H. T. Wang, Y. T. Wang, Y. S. Xiao, J. Li, P. Liu, Z. S. Liu and Q. Y. Liu (2017). "Upregulation of DARS2 by HBV promotes hepatocarcinogenesis through the miR-30e-5p/MAPK/NFAT5 pathway." J Exp Clin Cancer Res **36**(1): 148.

Quiroga, A. D., J. Lian and R. Lehner (2012). "Carboxylesterase1/Esterase-x regulates chylomicron production in mice." PLoS One **7**(11): e49515.

Quirós, P. M. and M. A. Prado (2017). "Multi-omics analysis identifies ATF4 as a key regulator of the mitochondrial stress response in mammals." **216**(7): 2027-2045.

Raabe, M., L. M. Flynn, C. H. Zlot, J. S. Wong, M. M. Véniant, R. L. Hamilton and S. G. Young (1998). "Knockout of the abetalipoproteinemia gene in mice: reduced lipoprotein secretion in heterozygotes and embryonic lethality in homozygotes." Proc Natl Acad Sci U S A **95**(15): 8686-8691.

Rajendran, V., P. Kalita, H. Shukla, A. Kumar and T. Tripathi (2018). "Aminoacyl-tRNA synthetases: Structure, function, and drug discovery." Int J Biol Macromol **111**: 400-414.

Ramachandran, A., U. Basu, S. Sultana, D. Nandakumar and S. S. Patel (2017). "Human mitochondrial transcription factors TFAM and TFB2M work synergistically in promoter melting during transcription initiation." Nucleic Acids Res **45**(2): 861-874.

Rambold, A. S., S. Cohen and J. Lippincott-Schwartz (2015). "Fatty acid trafficking in starved cells: regulation by lipid droplet lipolysis, autophagy, and mitochondrial fusion dynamics." Dev Cell **32**(6): 678-692.

Rappsilber, J., M. Mann and Y. Ishihama (2007). "Protocol for micro-purification, enrichment, pre-fractionation and storage of peptides for proteomics using StageTips." Nat Protoc **2**(8): 1896-1906.

Read, A. D., R. E. T. Bentley, S. L. Archer and K. J. Dunham-Snary (2021). "Mitochondrial iron–sulfur clusters: Structure, function, and an emerging role in vascular biology." Redox Biology **47**: 102164.

Remis, N. N., T. Wiwatpanit, A. J. Castiglioni, E. N. Flores, J. A. Cantú and J. García-Añoveros (2014). "Mucolipin Co-deficiency Causes Accelerated Endolysosomal Vacuolation of Enterocytes and Failure-to-Thrive from Birth to Weaning." PLOS Genetics **10**(12): e1004833.

Ren, Z., T. Ding, Z. Zuo, Z. Xu, J. Deng and Z. Wei (2020). "Regulation of MAVS Expression and Signaling Function in the Antiviral Innate Immune Response." Frontiers in Immunology **11**.

Repa, J. J., K. K. Buhman, R. V. Farese, Jr., J. M. Dietschy and S. D. Turley (2004). "ACAT2 deficiency limits cholesterol absorption in the cholesterol-fed mouse: impact on hepatic cholesterol homeostasis." Hepatology **40**(5): 1088-1097.

Robertson, M. D., M. Parkes, B. F. Warren, D. J. Ferguson, K. G. Jackson, D. P. Jewell and K. N. Frayn (2003). "Mobilisation of enterocyte fat stores by oral glucose in humans." Gut **52**(6): 834-839.

Rodriguez-Colman, M. J., M. Schewe, M. Meerlo, E. Stigter, J. Gerrits, M. Pras-Raves, A. Sacchetti, M. Hornsveld, K. C. Oost, H. J. Snippert, N. Verhoeven-Duif, R. Fodde and B. M.

Burgering (2017). "Interplay between metabolic identities in the intestinal crypt supports stem cell function." Nature **543**(7645): 424-427.

Rodriguez, C. I., F. Buchholz, J. Galloway, R. Sequerra, J. Kasper, R. Ayala, A. F. Stewart and S. M. Dymecki (2000). "High-efficiency deleter mice show that FLPe is an alternative to Cre-loxP." Nat Genet **25**(2): 139-140.

Rong, X., B. Wang, M. M. Dunham, P. N. Hedde, J. S. Wong, E. Gratton, S. G. Young, D. A. Ford and P. Tontonoz (2015). "Lpcat3-dependent production of arachidonoyl phospholipids is a key determinant of triglyceride secretion." **4**.

Rorbach, J., R. Richter, H. J. Wessels, M. Wydro, M. Pekalski, M. Farhoud, I. Kühl, M. Gaisne, N. Bonnefoy, J. A. Smeitink, R. N. Lightowlers and Z. M. Chrzanowska-Lightowlers (2008). "The human mitochondrial ribosome recycling factor is essential for cell viability." Nucleic Acids Res **36**(18): 5787-5799.

Ross, J. M. (2011). "Visualization of mitochondrial respiratory function using cytochrome c oxidase/succinate dehydrogenase (COX/SDH) double-labeling histochemistry." Journal of visualized experiments : JoVE(57): e3266-e3266.

Rowland, A. A. and G. K. Voeltz (2012). "Endoplasmic reticulum-mitochondria contacts: function of the junction." Nat Rev Mol Cell Biol **13**(10): 607-625.

Rumyantseva, A., E. Motori and A. Trifunovic (2020). "DARS2 is indispensable for Purkinje cell survival and protects against cerebellar ataxia." Hum Mol Genet **29**(17): 2845-2854.

Saddar, S., V. Carriere, W. R. Lee, K. Tanigaki, I. S. Yuhanna, S. Parathath, E. Morel, M. Warrier, J. K. Sawyer, R. D. Gerard, R. E. Temel, J. M. Brown, M. Connelly, C. Mineo and P. W. Shaul (2013). "Scavenger receptor class B type I is a plasma membrane cholesterol sensor." Circ Res **112**(1): 140-151.

Saito, K., M. Maeda and T. Katada (2017). "Regulation of the Sar1 GTPase Cycle Is Necessary for Large Cargo Secretion from the Endoplasmic Reticulum." Frontiers in Cell and Developmental Biology **5**(75).

Sané, A., L. Ahmarani, E. Delvin, N. Auclair, S. Spahis and E. Levy (2019). "SAR1B GTPase is necessary to protect intestinal cells from disorders of lipid homeostasis, oxidative stress, and inflammation." J Lipid Res **60**(10): 1755-1764.

Sané, A. T., E. Seidman, N. Peretti, M. L. Kleme, E. Delvin, C. Deslandres, C. Garofalo, S. Spahis and E. Levy (2017). "Understanding Chylomicron Retention Disease Through Sar1b Gtpase Gene Disruption: Insight From Cell Culture." Arterioscler Thromb Vasc Biol **37**(12): 2243-2251.

Santhanam, S., S. Rajamanickam, A. Motamarry, B. S. Ramakrishna, J. G. Amirtharaj, A. Ramachandran, A. Pulimood and A. Venkatraman (2012). "Mitochondrial electron transport chain complex dysfunction in the colonic mucosa in ulcerative colitis." Inflamm Bowel Dis **18**(11): 2158-2168.

Santhanam, S., A. Venkatraman and B. S. Ramakrishna (2007). "Impairment of mitochondrial acetoacetyl CoA thiolase activity in the colonic mucosa of patients with ulcerative colitis." Gut **56**(11): 1543-1549.

Saraste, J. and K. Prydz (2019). "A New Look at the Functional Organization of the Golgi Ribbon." Frontiers in Cell and Developmental Biology **7**(171).

Sasaki, N., N. Sachs, K. Wiebrands, S. I. J. Ellenbroek, A. Fumagalli, A. Lyubimova, H. Begthel, M. van den Born, J. H. van Es, W. R. Karthaus, V. S. W. Li, C. López-Iglesias, P. J. Peters, J. van Rheenen, A. van Oudenaarden and H. Clevers (2016). "Reg4+ deep crypt secretory cells function as epithelial niche for Lgr5+ stem cells in colon." Proceedings of the National Academy of Sciences of the United States of America **113**(37): E5399-E5407.

Sato, H., L. S. Zhang, K. Martinez, E. B. Chang, Q. Yang, F. Wang, P. N. Howles, R. Hokari, S. Miura and P. Tso (2016). "Antibiotics Suppress Activation of Intestinal Mucosal Mast Cells and Reduce Dietary Lipid Absorption in Sprague-Dawley Rats." Gastroenterology **151**(5): 923-932.

Sato, T., J. H. van Es, H. J. Snippert, D. E. Stange, R. G. Vries, M. van den Born, N. Barker, N. F. Shroyer, M. van de Wetering and H. Clevers (2011). "Paneth cells constitute the niche for Lgr5 stem cells in intestinal crypts." Nature **469**(7330): 415-418.

Sazanov, L. A. (2015). "A giant molecular proton pump: structure and mechanism of respiratory complex I." Nature Reviews Molecular Cell Biology **16**(6): 375-388.

Scheper, G. C., T. van der Klok, R. J. van Andel, C. G. van Berkel, M. Sissler, J. Smet, T. I. Muravina, S. V. Serkov, G. Uziel, M. Bugiani, R. Schiffmann, I. Krageloh-Mann, J. A. Smeitink, C. Florentz, R. Van Coster, J. C. Pronk and M. S. van der Knaap (2007). "Mitochondrial aspartyl-tRNA synthetase deficiency causes leukoencephalopathy with brain stem and spinal cord involvement and lactate elevation." Nat Genet **39**(4): 534-539.

Schiffmann, L. M., J. P. Werthenbach, F. Heintges-Kleinhofer, J. M. Seeger, M. Fritsch, S. D. Günther, S. Willenborg, S. Brodesser, C. Lucas, C. Jüngst, M. C. Albert, F. Schorn, A. Witt, C. T. Moraes, C. J. Bruns, M. Pasparakis, M. Krönke, S. A. Eming, O. Coutelle and H. Kashkar (2020). "Mitochondrial respiration controls neoangiogenesis during wound healing and tumour growth." Nature Communications **11**(1): 3653.

Schneider, C., C. E. O'Leary and R. M. Locksley (2019). "Regulation of immune responses by tuft cells." Nature Reviews Immunology **19**(9): 584-593.

Schon, E. A., S. DiMauro and M. Hirano (2012). "Human mitochondrial DNA: roles of inherited and somatic mutations." Nat Rev Genet **13**(12): 878-890.

Schwarzer, R., H. Jiao, L. Wachsmuth, A. Tresch and M. Pasparakis (2020). "FADD and Caspase-8 Regulate Gut Homeostasis and Inflammation by Controlling MLKL- and GSDMD-Mediated Death of Intestinal Epithelial Cells." Immunity **52**(6): 978-993.e976.

Seiferling, D., K. Szczepanowska, C. Becker, K. Senft, S. Hermans and P. Maiti (2016). "Loss of CLPP alleviates mitochondrial cardiomyopathy without affecting the mammalian UPRmt." **17**(7): 953-964.

Sergushichev, A. A. (2016). "An algorithm for fast preranked gene set enrichment analysis using cumulative statistic calculation." bioRxiv: 060012.

Seth, R. B., L. Sun, C.-K. Ea and Z. J. Chen (2005). "Identification and Characterization of MAVS, a Mitochondrial Antiviral Signaling Protein that Activates NF-κB and IRF3." Cell **122**(5): 669-682.

Sharma, P., E. Maklashina and G. Cecchini (2020). "The roles of SDHAF2 and dicarboxylate in covalent flavinylation of SDHA, the human complex II flavoprotein." **117**(38): 23548-23556.

Shew, T., N. E. Wolins and V. Cifarelli (2018). "VEGFR-3 Signaling Regulates Triglyceride Retention and Absorption in the Intestine." Front Physiol **9**: 1783.

Shi, Y. and D. Cheng (2009). "Beyond triglyceride synthesis: the dynamic functional roles of MGAT and DGAT enzymes in energy metabolism." Am J Physiol Endocrinol Metab **297**(1): E10-18.

Shiau, Y. F., D. A. Popper, M. Reed, C. Umstetter, D. Capuzzi and G. M. Levine (1985). "Intestinal triglycerides are derived from both endogenous and exogenous sources." Am J Physiol **248**(2 Pt 1): G164-169.

Shim, J., C. L. Moulson, E. P. Newberry, M. H. Lin, Y. Xie, S. M. Kennedy, J. H. Miner and N. O. Davidson (2009). "Fatty acid transport protein 4 is dispensable for intestinal lipid absorption in mice." J Lipid Res **50**(3): 491-500.

Siddiqi, S. and C. M. Mansbach, 2nd (2012). "Phosphorylation of Sar1b protein releases liver fatty acid-binding protein from multiprotein complex in intestinal cytosol enabling it to bind to endoplasmic reticulum (ER) and bud the pre-chylomicron transport vesicle." J Biol Chem **287**(13): 10178-10188.

Siddiqi, S., U. Saleem, N. A. Abumrad, N. O. Davidson, J. Storch, S. A. Siddiqi and C. M. Mansbach, 2nd (2010). "A novel multiprotein complex is required to generate the prechylomicron transport vesicle from intestinal ER." Journal of lipid research **51**(7): 1918-1928.

Siddiqi, S., S. A. Siddiqi and C. M. Mansbach, 2nd (2010). "Sec24C is required for docking the prechylomicron transport vesicle with the Golgi." J Lipid Res **51**(5): 1093-1100.

Siddiqi, S. A., F. S. Gorelick, J. T. Mahan and C. M. Mansbach, 2nd (2003). "COPII proteins are required for Golgi fusion but not for endoplasmic reticulum budding of the pre-chylomicron transport vesicle." J Cell Sci **116**(Pt 2): 415-427.

Siddiqi, S. A., F. S. Gorelick, J. T. Mahan and C. M. Mansbach, II (2003). "COPII proteins are required for Golgi fusion but not for endoplasmic reticulum budding of the pre-chylomicron transport vesicle." Journal of Cell Science **116**(2): 415-427.

Siddiqi, S. A., J. Mahan, S. Siddiqi, F. S. Gorelick and C. M. Mansbach, 2nd (2006). "Vesicle-associated membrane protein 7 is expressed in intestinal ER." J Cell Sci **119**(Pt 5): 943-950.

Siddiqi, S. A. and C. M. Mansbach, 2nd (2008). "PKC zeta-mediated phosphorylation controls budding of the pre-chylomicron transport vesicle." J Cell Sci **121**(Pt 14): 2327-2338.

Siddiqi, S. A., S. Siddiqi, J. Mahan, K. Peggs, F. S. Gorelick and C. M. Mansbach, 2nd (2006). "The identification of a novel endoplasmic reticulum to Golgi SNARE complex used by the prechylomicron transport vesicle." J Biol Chem **281**(30): 20974-20982.

Sifroni, K. G., C. R. Damiani, C. Stoffel, M. R. Cardoso, G. K. Ferreira, I. C. Jeremias, G. T. Rezin, G. Scaini, P. F. Schuck, F. Dal-Pizzol and E. L. Streck (2010). "Mitochondrial respiratory chain in the colonic mucosal of patients with ulcerative colitis." Mol Cell Biochem **342**(1-2): 111-115.

Sissler, M., L. E. González-Serrano and E. Westhof (2017). "Recent Advances in Mitochondrial Aminoacyl-tRNA Synthetases and Disease." Trends in Molecular Medicine **23**(8): 693-708.

Smits, P., J. Smeitink and L. van den Heuvel (2010). "Mitochondrial Translation and Beyond: Processes Implicated in Combined Oxidative Phosphorylation Deficiencies." Journal of Biomedicine and Biotechnology **2010**: 737385.

Spang, A., J. H. Saw, S. L. Jørgensen, K. Zaremba-Niedzwiedzka, J. Martijn, A. E. Lind, R. van Eijk, C. Schleper, L. Guy and T. J. G. Ettema (2015). "Complex archaea that bridge the gap between prokaryotes and eukaryotes." Nature **521**(7551): 173-179.

Spinelli, J. B. and M. C. Haigis (2018). "The multifaceted contributions of mitochondria to cellular metabolism." Nature Cell Biology **20**(7): 745-754.

Srivillibhuthur, M., B. N. Warder, N. H. Toke, P. P. Shah, Q. Feng, N. Gao, E. M. Bonder and M. P. Verzi (2018). "TFAM is required for maturation of the fetal and adult intestinal epithelium." Developmental biology **439**(2): 92-101.

Srivillibhuthur, M., B. N. Warder, N. H. Toke, P. P. Shah, Q. Feng, N. Gao, E. M. Bonder and M. P. Verzi (2018). "TFAM is required for maturation of the fetal and adult intestinal epithelium." Dev Biol **439**(2): 92-101.

Stahl, A. (2004). "A current review of fatty acid transport proteins (SLC27)." Pflügers Archiv **447**(5): 722-727.

Storch, J., Y. X. Zhou and W. S. Lagakos (2008). "Metabolism of apical versus basolateral sn-2-monoacylglycerol and fatty acids in rodent small intestine." J Lipid Res **49**(8): 1762-1769.

Subramanian, A., P. Tamayo, V. K. Mootha, S. Mukherjee, B. L. Ebert, M. A. Gillette, A. Paulovich, S. L. Pomeroy, T. R. Golub, E. S. Lander and J. P. Mesirov (2005). "Gene set enrichment analysis: a knowledge-based approach for interpreting genome-wide expression profiles." Proc Natl Acad Sci U S A **102**(43): 15545-15550.

Sünderhauf, A., M. Hicken, H. Schlichting, K. Skibbe, M. Ragab, A. Raschdorf, M. Hirose, H. Schäffler, A. Bokemeyer, D. Bettenworth, A. G. Savitt, S. Perner, S. Ibrahim, E. I. Peerschke, B. Ghebrehiwet, S. Derer and C. Sina (2021). "Loss of Mucosal p32/gC1qR/HABP1 Triggers Energy Deficiency and Impairs Goblet Cell Differentiation in Ulcerative Colitis." Cellular and Molecular Gastroenterology and Hepatology **12**(1): 229-250.

Suomalainen, A. and B. J. Battersby (2018). "Mitochondrial diseases: the contribution of organelle stress responses to pathology." Nat Rev Mol Cell Biol **19**(2): 77-92.

Tait, S. W. G. and D. R. Green (2012). "Mitochondria and cell signalling." Journal of cell science **125**(Pt 4): 807-815.

Takimoto, A. (2021). "Rab7-Dependent Endocytic Pathways Play an Important Role in Nutrient Absorption during Pre-Weaning Growth." BPB Reports **4**(1): 27-35.

Taniguchi, M. and T. Okazaki (2020). "Ceramide/Sphingomyelin Rheostat Regulated by Sphingomyelin Synthases and Chronic Diseases in Murine Models." Journal of lipid and atherosclerosis **9**(3): 380-405.

Tarugi, P., M. Averna, E. Di Leo, A. B. Cefalù, D. Noto, L. Magnolo, L. Cattin, S. Bertolini and S. Calandra (2007). "Molecular diagnosis of hypobetalipoproteinemia: An ENID review." Atherosclerosis **195**(2): e19-e27.

Temel, R. E. and J. M. Brown (2015). "A new model of reverse cholesterol transport: enTICEing strategies to stimulate intestinal cholesterol excretion." Trends Pharmacol Sci **36**(7): 440-451.

Tetteh, P. W., H. F. Farin and H. Clevers (2015). "Plasticity within stem cell hierarchies in mammalian epithelia." Trends Cell Biol **25**(2): 100-108.

Theiss, A. L., M. Vijay-Kumar, T. S. Obertone, D. P. Jones, J. M. Hansen, A. T. Gewirtz, D. Merlin and S. V. Sitaraman (2009). "Prohibitin is a novel regulator of antioxidant response that attenuates colonic inflammation in mice." Gastroenterology **137**(1): 199-208, 208.e191-196.

Tiwari, S. and S. A. Siddiqi (2012). "Intracellular trafficking and secretion of VLDL." Arterioscler Thromb Vasc Biol **32**(5): 1079-1086.

Tormos, K. V., E. Anso, R. B. Hamanaka, J. Eisenbart, J. Joseph, B. Kalyanaraman and N. S. Chandel (2011). "Mitochondrial complex III ROS regulate adipocyte differentiation." Cell Metab **14**(4): 537-544.

Treuting, P. M., M. A. Valasek and S. M. Dintzis (2012). 11 - Upper Gastrointestinal Tract. Comparative Anatomy and Histology. P. M. Treuting and S. M. Dintzis. San Diego, Academic Press**:** 155-175.

Trifunovic, A. and N. G. Larsson (2008). "Mitochondrial dysfunction as a cause of ageing." J Intern Med **263**(2): 167-178.

Tsuchida, T., S. Fukuda, H. Aoyama, N. Taniuchi, T. Ishihara, N. Ohashi, H. Sato, K. Wakimoto, M. Shiotani and A. Oku (2012). "MGAT2 deficiency ameliorates high-fat diet-induced obesity and insulin resistance by inhibiting intestinal fat absorption in mice." Lipids Health Dis **11**: 75.

Tsukihara, T., H. Aoyama, E. Yamashita, T. Tomizaki, H. Yamaguchi, K. Shinzawa-Itoh, R. Nakashima, R. Yaono and S. Yoshikawa (1996). "The whole structure of the 13-subunit oxidized cytochrome c oxidase at 2.8 A." Science **272**(5265): 1136-1144.

Uchida, A., M. N. Slipchenko, T. Eustaquio, J. F. Leary, J. X. Cheng and K. K. Buhman (2013). "Intestinal acyl-CoA:diacylglycerol acyltransferase 2 overexpression enhances postprandial triglyceridemic response and exacerbates high fat diet-induced hepatic triacylglycerol storage." Biochim Biophys Acta **1831**(8): 1377-1385.

Valnot, I., J. C. von Kleist-Retzow, A. Barrientos, M. Gorbatyuk, J. W. Taanman, B. Mehaye, P. Rustin, A. Tzagoloff, A. Munnich and A. Rötig (2000). "A mutation in the human heme A:farnesyltransferase gene (COX10) causes cytochrome c oxidase deficiency." Hum Mol Genet **9**(8): 1245-1249.

van Berge, L., E. M. Hamilton, T. Linnankivi, G. Uziel, M. E. Steenweg, P. Isohanni, N. I. Wolf, I. Krägeloh-Mann, N. J. Brautaset, P. I. Andrews, B. A. de Jong, M. al Ghamdi, W. N. van Wieringen, L. R. Group, B. A. Tannous, E. Hulleman, T. Würdinger, C. G. M. van Berkel, E. Polder, T. E. M. Abbink, E. A. Struys, Scheper, Gert C. and M. S. van der Knaap (2014). "Leukoencephalopathy with brainstem and spinal cord involvement and lactate elevation: clinical and genetic characterization and target for therapy." Brain **137**(4): 1019-1029.

van der Flier, L. G. and H. Clevers (2009). "Stem cells, self-renewal, and differentiation in the intestinal epithelium." Annu Rev Physiol **71**: 241-260.

Van Dyck, F., C. V. Braem, Z. Chen, J. Declercq, R. Deckers, B. M. Kim, S. Ito, M. K. Wu, D. E. Cohen, M. Dewerchin, R. Derua, E. Waelkens, L. Fiette, A. Roebroek, F. Schuit, W. J. Van de Ven and R. A. Shivdasani (2007). "Loss of the PlagL2 transcription factor affects lacteal uptake of chylomicrons." Cell Metab **6**(5): 406-413.

van Es, J. H., A. Haegebarth, P. Kujala, S. Itzkovitz, B. K. Koo, S. F. Boj, J. Korving, M. van den Born, A. van Oudenaarden, S. Robine and H. Clevers (2012). "A critical role for the Wnt effector Tcf4 in adult intestinal homeostatic self-renewal." Mol Cell Biol **32**(10): 1918-1927.

van Lidth de Jeude, J. F., B. J. Meijer, M. C. B. Wielenga, C. N. Spaan, B. Baan, S. L. Rosekrans, S. Meisner, Y. H. Shen, A. S. Lee, J. C. Paton, A. W. Paton, V. Muncan, G. R. van den Brink and J. Heijmans (2017). "Induction of endoplasmic reticulum stress by deletion of Grp78 depletes Apc mutant intestinal epithelial stem cells." Oncogene **36**(24): 3397-3405.

van Roy, F. and G. Berx (2008). "The cell-cell adhesion molecule E-cadherin." Cellular and Molecular Life Sciences **65**(23): 3756-3788.

Van Vranken, Jonathan G., Daniel K. Bricker, N. Dephoure, Steven P. Gygi, James E. Cox, Carl S. Thummel and J. Rutter (2014). "SDHAF4 Promotes Mitochondrial Succinate Dehydrogenase Activity and Prevents Neurodegeneration." Cell Metabolism **20**(2): 241-252.

Vankoningsloo, S., M. Piens, C. Lecocq, A. Gilson, A. De Pauw, P. Renard, C. Demazy, A. Houbion, M. Raes and T. Arnould (2005). "Mitochondrial dysfunction induces triglyceride accumulation in 3T3-L1 cells: role of fatty acid β-oxidation and glucose." Journal of Lipid Research **46**(6): 1133-1149.

Vlantis, K., A. Polykratis, P. S. Welz, G. van Loo, M. Pasparakis and A. Wullaert (2016). "TLR-independent anti-inflammatory function of intestinal epithelial TRAF6 signalling prevents DSS-induced colitis in mice." Gut **65**(6): 935-943.

Vlantis, K., A. Wullaert, A. Polykratis, V. Kondylis, M. Dannappel, R. Schwarzer, P. Welz, T. Corona, H. Walczak, F. Weih, U. Klein, M. Kelliher and M. Pasparakis (2016). "NEMO Prevents RIP Kinase 1-Mediated Epithelial Cell Death and Chronic Intestinal Inflammation by NF-κB-Dependent and -Independent Functions." Immunity **44**(3): 553-567.

Wai, T. and T. Langer (2016). "Mitochondrial Dynamics and Metabolic Regulation." Trends Endocrinol Metab **27**(2): 105-117.

Waldschmitt, N., E. Berger, E. Rath, R. B. Sartor, B. Weigmann, M. Heikenwalder, M. Gerhard, K. P. Janssen and D. Haller (2014). "C/EBP homologous protein inhibits tissue repair in response to gut injury and is inversely regulated with chronic inflammation." Mucosal Immunology **7**(6): 1452-1466.

Wallace, D. C. (2007). "Why do we still have a maternally inherited mitochondrial DNA? Insights from evolutionary medicine." Annu Rev Biochem **76**: 781-821.

Wang, J., M. A. Mitsche, D. Lütjohann, J. C. Cohen, X. S. Xie and H. H. Hobbs (2015). "Relative roles of ABCG5/ABCG8 in liver and intestine." J Lipid Res **56**(2): 319-330.

Wang, L. C., F. Nassir, Z. Y. Liu, L. Ling, F. Kuo, T. Crowell, D. Olson, N. O. Davidson and L. C. Burkly (2002). "Disruption of hedgehog signaling reveals a novel role in intestinal morphogenesis and intestinal-specific lipid metabolism in mice." Gastroenterology **122**(2): 469-482.

Welz, P. S., A. Wullaert, K. Vlantis, V. Kondylis, V. Fernández-Majada, M. Ermolaeva, P. Kirsch, A. Sterner-Kock, G. van Loo and M. Pasparakis (2011). "FADD prevents RIP3-mediated epithelial cell necrosis and chronic intestinal inflammation." Nature **477**(7364): 330-334.

Westermann, B. (2010). "Mitochondrial fusion and fission in cell life and death." Nature Reviews Molecular Cell Biology **11**(12): 872-884.

Wheaton, W. W., S. E. Weinberg, R. B. Hamanaka, S. Soberanes, L. B. Sullivan, E. Anso, A. Glasauer, E. Dufour, G. M. Mutlu, G. S. Budigner and N. S. Chandel (2014). "Metformin inhibits mitochondrial complex I of cancer cells to reduce tumorigenesis." Elife **3**: e02242.

Whitcomb, D. C. and M. E. Lowe (2007). "Human Pancreatic Digestive Enzymes." Digestive Diseases and Sciences **52**(1): 1-17.

Wilfling, F., J. T. Haas, T. C. Walther and R. V. Farese, Jr. (2014). "Lipid droplet biogenesis." Curr Opin Cell Biol **29**: 39-45.

Willenborg, S., D. E. Sanin, A. Jais, X. Ding, T. Ulas, J. Nüchel, M. Popović, T. MacVicar, T. Langer, J. L. Schultze, A. Gerbaulet, A. Roers, E. J. Pearce, J. C. Brüning, A. Trifunovic and S. A. Eming (2021). "Mitochondrial metabolism coordinates stage-specific repair processes in macrophages during wound healing." Cell Metab **33**(12): 2398-2414.e2399.

Wu, M., J. Gu, R. Guo, Y. Huang and M. Yang (2016). "Structure of Mammalian Respiratory Supercomplex I(1)III(2)IV(1)." Cell **167**(6): 1598-1609.e1510.

Xiao, C., S. Dash, C. Morgantini and G. F. Lewis (2013). "Novel role of enteral monosaccharides in intestinal lipoprotein production in healthy humans." Arterioscler Thromb Vasc Biol **33**(5): 1056-1062.

Xiao, C., S. Dash, C. Morgantini, B. W. Patterson and G. F. Lewis (2014). "Sitagliptin, a DPP-4 inhibitor, acutely inhibits intestinal lipoprotein particle secretion in healthy humans." Diabetes **63**(7): 2394-2401.

Xiao, C., P. Stahel, A. L. Carreiro, K. K. Buhman and G. F. Lewis (2018). "Recent Advances in Triacylglycerol Mobilization by the Gut." Trends Endocrinol Metab **29**(3): 151-163.

Xiao, C., P. Stahel, A. L. Carreiro, Y. H. Hung, S. Dash, I. Bookman, K. K. Buhman and G. F. Lewis (2019). "Oral Glucose Mobilizes Triglyceride Stores From the Human Intestine." Cell Mol Gastroenterol Hepatol **7**(2): 313-337.

Xiao, C., P. Stahel and G. F. Lewis (2018). "Regulation of Chylomicron Secretion: Focus on Post Assembly Mechanisms." Cellular and Molecular Gastroenterology and Hepatology.

Xiao, C., P. Stahel, A. Nahmias and G. F. Lewis (2020). "Emerging Role of Lymphatics in the Regulation of Intestinal Lipid Mobilization." Frontiers in Physiology **10**(1604).

Xie, Y., E. P. Newberry, S. G. Young, S. Robine, R. L. Hamilton, J. S. Wong, J. Luo, S. Kennedy and N. O. Davidson (2006). "Compensatory increase in hepatic lipogenesis in mice with conditional intestine-specific Mttp deficiency." J Biol Chem **281**(7): 4075-4086.

Yen, C. E., D. W. Nelson and M. I. Yen (2015). "Intestinal triacylglycerol synthesis in fat absorption and systemic energy metabolism." J Lipid Res **56**(3): 489-501.

Yen, C. L., M. L. Cheong, C. Grueter, P. Zhou, J. Moriwaki, J. S. Wong, B. Hubbard, S. Marmor and R. V. Farese, Jr. (2009). "Deficiency of the intestinal enzyme acyl CoA:monoacylglycerol acyltransferase-2 protects mice from metabolic disorders induced by high-fat feeding." Nat Med **15**(4): 442-446.

Young, S. G., C. M. Cham, R. E. Pitas, B. J. Burri, A. Connolly, L. Flynn, A. S. Pappu, J. S. Wong, R. L. Hamilton and R. V. Farese, Jr. (1995). "A genetic model for absent chylomicron formation: mice producing apolipoprotein B in the liver, but not in the intestine." The Journal of clinical investigation **96**(6): 2932-2946.

Yu, G., L. G. Wang, Y. Han and Q. Y. He (2012). "clusterProfiler: an R package for comparing biological themes among gene clusters." OMICS **16**(5): 284-287.

Zechner, R., F. Madeo and D. Kratky (2017). "Cytosolic lipolysis and lipophagy: two sides of the same coin." Nat Rev Mol Cell Biol **18**(11): 671-684.

Zhang, F. and G. Zarkada (2018). "Lacteal junction zippering protects against diet-induced obesity." **361**(6402): 599-603.

Zhang, L. J., C. Wang, Y. Yuan, H. Wang, J. Wu, F. Liu, L. Li, X. Gao, Y. L. Zhao, P. Z. Hu, P. Li and J. Ye (2014). "Cideb facilitates the lipidation of chylomicrons in the small intestine." J Lipid Res **55**(7): 1279-1287.

Zhang, P., L. S. Csaki, E. Ronquillo, L. J. Baufeld, J. Y. Lin, A. Gutierrez, J. R. Dwyer, D. N. Brindley, L. G. Fong, P. Tontonoz, S. G. Young and K. Reue (2019). "Lipin 2/3 phosphatidic acid phosphatases maintain phospholipid homeostasis to regulate chylomicron synthesis." J Clin Invest **129**(1): 281-295.

Zhu, J., B. Lee, K. K. Buhman and J.-X. Cheng (2009). "A dynamic, cytoplasmic triacylglycerol pool in enterocytes revealed by ex vivo and in vivo coherent anti-Stokes Raman scattering imaging[S]." Journal of Lipid Research **50**(6): 1080-1089.

6. Acknowledgments

I would like to heartily thank Prof. Dr. Manolis Pasparakis for providing me with the great opportunity to conduct my doctoral thesis in his lab. I immensely thank you for allowing me to work on such a fascinating project. Due to the interdisciplinary nature of this project, I learned how to be an independent, hard-working member of a team and highly productive under pressure. Thank you for believing in me from the very beginning, tolerating my stubbornness and constantly supporting every single step that I took during the last 5 years in your lab. In spite of the fact that this work was completely different from your scientific expertise, you have always shown great interest in my project and you were constantly available for fruitful meetings and helpful discussions that highly contributed to the progress of this challenging project. Thank you for teaching me how to critically interpret my data and effectively communicate my work. I am grateful for your scientific guidance, mentoring and constant encouragement that helped me to become a better scientist. I feel very lucky for being part of your team during the last 5 years!

Next, I would like to express my deep gratitude to Prof. Dr. Aleksandra Trifunovic for her great commitment to this project. I am very thankful to you Sandra for all your amazing support and mentoring during these years. Thank you for listening to my problems and considering me as a member of your lab. I would also like to heartily thank you for taking the time and effort to proofread my thesis. This project would not be possible without your help and input!

Furthermore, I would like to thank Prof. Dr. Elena Rugarli for the insightful, long discussions during our TAC meetings. I am grateful to Prof. Dr. Thomas Langer for kindly agreeing to be a second reviewer of my PhD thesis and for providing me with constructive feedback. Many thanks to Prof. Dr. Jan Riemer for being the chair of my thesis committee and third reviewer of my PhD thesis.

Special thanks to Dr. Vangelis Kondylis for his endless support during these years. Vangeli, thank you so much for always being willing to listen to my numerous work and personal – related problems that I encountered during my PhD and I apologize for being annoying sometimes. I would also like to warmly thank you for your invaluable help with my lab work.

Furthermore, I would like to thank Dr. Karolina Szczepanowska for her amazing intellectual contribution during my PhD and her willingness to share her broad scientific knowledge.

I am very grateful to Prof. Dr. Christian Frezza and his team, particularly Dr. Ming Yang and Dr. Christina Schmidt for their precious help with the analysis and the interpretation of the metabolomics, proteomics and transcriptomics data. Additionally, many thanks to Prof. Dr. Joerg Heeren and his team for the outstanding willingness to help us with the postprandial mouse experiments and for accommodating me in his lab. Special thanks to my great friend Giannis Evangelakos for his crucial help with the metabolic tracing experiments and for the amazing time that we've spent in Hamburg.

Moreover, I would like to thank all former and present lab members of the Pasparakis lab for the incredible, unique working atmosphere and particularly Dr. Robin Schwarzer for spending his time teaching me how to work with the intestine. I am extremely lucky

for beeing part of the “Gut-Lab”! Lastly, I deeply thank Dr. Lucie Laurien for being such a great lab partner and good friend.

I highly appreciate the invaluable, excellent technical assistance provided by our technicians; Jennifer Kuth, Claudia Uthoff-Hachenberg, Elza Gareus, Edeltraud Stade and Julia von Rhein. Elza and Edi, thank you so much for spending endless hours cutting my paraffin and cryosections. You are the best! Many thanks to Silke Röpke, Martin Hafner and Johannes Winkler for helping me with administrative and bureaucratic issues.

I am immensely thankful to Dr. Katerina Vlantis, the scientific manager of the Mito-RTG/CRC 1218 for her thoughful advice considering professional and personal issues. Thank you so much Katerina for always being kind and willing to listen and help me out. I am grateful for your support in this matter.

To my great friend Dr. Andreia Correia:
Um agradecimento muito especial a ti, minha querida amiga Andreia. Obrigada por todo o suporte e paciência durante todo este tempo. Obrigada pela tua generosidade e pureza, pelo cuidado pela minha saúde, partilhando sempre um petisco cozinhado por ti e o Antônia (especialmente lentilhas!). Sinto-me tão grata por te ter conhecido! Muitos beijinhos!

I am extremely thankful to my very close friends Machi, Lisonia and Danae and to all my amazing long-lasting friends in Greece, Sweden and in the Netherlands; Marilena, Alexandros, Nikolas and Vangelis who were always super supportive and patient after so many years. I love you guys!

I would like to express my immense gratitude to Constantinos for his endless support during all these years. Thank you for always being there for me and perfectly handling my mood swings and my immaturity. You have helped me enormously! Thank you for not getting tired with my dramatic attitude and for pulling me up when I am down. I owe you a lot!

Last but not least, my warmest thanks to my beloved family, Mom, Dad, Lena, Christos, my aunt Christina and my lovely grandma Chrysanthi. You are my ultimate source of inspiration and motivation. Thank you for your understanding and for always believing in me and never giving up on me. Without you, I might not be the person I am today. Thank you for everything! Σας αγαπώ πολύ και σας ευχαριστώ για όλα!

Erklärung zur Dissertation

Erklärung zur Dissertation

gemäß der Promotionsordnung vom 12. März 2020

„Hiermit versichere ich an Eides statt, dass ich die vorliegende Dissertation selbstständig und ohne die Benutzung anderer als der angegebenen Hilfsmittel und Literatur angefertigt habe. Alle Stellen, die wörtlich oder sinngemäß aus veröffentlichten und nicht veröffentlichten Werken dem Wortlaut oder dem Sinn nach entnommen wurden, sind als solche kenntlich gemacht. Ich versichere an Eides statt, dass diese Dissertation noch keiner anderen Fakultät oder Universität zur Prüfung vorgelegen hat; dass sie - abgesehen von unten angegebenen Teilpublikationen und eingebundenen Artikeln und Manuskripten - noch nicht veröffentlicht worden ist sowie, dass ich eine Veröffentlichung der Dissertation vor Abschluss der Promotion nicht ohne Genehmigung des Promotionsausschusses vornehmen werde. Die Bestimmungen dieser Ordnung sind mir bekannt. Darüber hinaus erkläre ich hiermit, dass ich die Ordnung zur Sicherung guter wissenschaftlicher Praxis und zum Umgang mit wissenschaftlichem Fehlverhalten der Universität zu Köln gelesen und sie bei der Durchführung der Dissertation zugrundeliegenden Arbeiten und der schriftlich verfassten Dissertation beachtet habe und verpflichte mich hiermit, die dort genannten Vorgaben bei allen wissenschaftlichen Tätigkeiten zu beachten und umzusetzen. Ich versichere, dass die eingereichte elektronische Fassung der eingereichten Druckfassung vollständig entspricht."

Teilpublikationen:

Datum, Name und Unterschrift

18/03/22, Chrysanthi Moschandrea

CMoschandrea